CONSTRAINED INVERSION OF GRAVITY DATA OVER THE OVOID AND MINI-OVOID IN THE VOISEY'S BAY Ni-Cu-Co DEPOSIT, LABRADOR

MICHAEL R. ASH

Constrained Inversion of Gravity Data over the Ovoid and Mini-Ovoid in the Voisey's Bay Ni-Cu-Co Deposit, Labrador

by

© Michael R. Ash, B.Sc. (Honours)

A thesis submitted to the School of Graduate Studies in partial fulfillment of the requirements for the degree of
Master of Science

Department of Earth Sciences
Memorial University of Newfoundland
October 2007

St. John's Newfoundland and Labrador

Abstract

The Voisey's Bay Nickel-Copper-Cobalt deposit provides a unique opportunity to test the latest minimum-structure gravity inversion program developed by the University of British Columbia-Geophysical Inversion Facility (UBC-GIF). The success of generating geologically meaningful results depends on the inherent uncertainty and spatial properties of the raw gravity data set, and on the statistical properties and spatial distribution of the rock density data. The objective of this study is to examine the effects of the initial survey configuration and the knowledge of subsurface parameters on the refinement of the inversion models. Density models derived using geostatistical methods can be assigned weights which reflect model confidence and spatial correlations. The spatial distribution of the borehole samples and the developed geostatistical models control the lateral and vertical resolution of the inversion.

The constraints applied in the gravity inversion were in the form of data from a significant number of drill holes penetrating the Ovoid and Mini-Ovoid. From these, refined models of the depth of the overburden and of the density distribution within the body were developed. To explore the utility of gravity inversion as a forecasting and planning tool, inversions were constrained using density models derived from 50%, 25% and 5% of the original number of drill logs. Reasonable models of the Ovoid were obtained when the thickness of the overburden was constrained. The inversion results indicate that incorporating drill log information into the inversion process, early in a drilling program, can improve our knowledge of the subsurface density distribution.

Acknowledgements

First and foremost I would like to thank my supervisor, Hugh Miller, for his direction, encouragement and support throughout my project. I would also like to thank Colin Farquharson for his guidance and input. Many thanks are extended to Brian Bengert and Robert Wheeler of Voisey's Bay Nickel Company for their help throughout this project. I would also like to thank the Inco Innovation Centre for funds and support for this work. In addition, I would like to thank the University of British Columbia-Geophysical Inversion Facility for providing the forward modeling and inversion software used throughout this project. Special thanks are extended to Chuck Hurich, Jeremy Hall, Jim Wright and all other faculty/staff at Memorial who provide constant support for students. Finally, Krista thank you for everything.

List of Figures

Chapter 1

Chapter 2

Chapter 5

Table of Contents

List of Abbreviations:

CVRD- Companhia Vale do Rio Doce
ENGN- Enderbitic Gneiss
MASU- Massive Sulphide
NAD83- North American Datum 1983
OB- Overburden
TR-Troctolite
UBC-GIF -University of British Columbia-Geophysical Inversion Facility
VBNC-Voisey's Bay Nickel Company Limited
WGS84- World Geodetic System 1984

Chapter 1: Introduction

1.1 Objective

A major objective of this study is to examine methods in which reliable geological models can be used to constrain geophysical inversions of gravity data. Geostatistical methods are used to create multiple geological models which can then be then incorporated into the inversion process. In most exploration projects, it is common to see a greater database of geophysical observations at the surface than the number of geological samples below the surface. As a result, inversions are typically completed using little or no geological information, although capability exists in current inversion software for incorporating geological information.

An extensive drilling program since 1995 has provided a database, in the area of the Ovoid and Mini-Ovoid, for which derived density was available from geochemical and assay results. Using the three-dimensional modelling and geostatistical capabilities of Gocad, a cellular model of the Ovoid and Mini-Ovoid was generated from the extensive density database. This geocellular model was incorporated into a typical minimum-structure gravity inversion program as an initial model, a reference model or a boundary model. Cell weighting models were designed using common geostatistical methods and incorporated into the inversion process. Little research has been carried out on the benefits, uses and limitations of incorporating substantial amounts of geological information into typical state-of-the-art inversion programs using the cell weights generated from the statistical information in the database.

This study examines if gravity inversions can be used in conjunction with a drilling program to better refine the geological model of the subsurface. This is accomplished by systematically reducing the number of drill logs from the original dataset. The minimum number of drill logs needed to constrain the gravity inversion, yet still producing a reasonable geological model, will yield valuable information on the applicability of using gravity data early in exploration programs to determine the subsurface density distribution to guide subsequent drilling. The minimum number of drill logs required to build a reasonable geological model will primarily depend on the geometry and scale of the anomaly.

1.2 The Voisey's Bay Discovery

The Voisey's Bay Nickel-Copper-Cobalt deposit, located on the northeast coast of Labrador approximately 30km southeast of Nain (Figure 1.1), has been interpreted as one of the most significant mineral discoveries in Canada in the past 40 years (Naldrett et al., 1996). In 1993, Albert Chislett and Chris Verbiski of Archean Resources Ltd., while in an exploration program looking for diamonds, examined an exposed gossan and noted the presence of several indicator minerals for an ore deposit. The original grab samples returned assay results up to 6% Cu and 3% Ni (Naldrett et al., 1998). The results obtained from what is now known as Discovery Hill prompted Diamond Field Resources Incorporated, a junior diamond exploration company, to begin a grass roots exploration program for nickel at Voisey's Bay in the summer of 1994.

The geophysical data obtained from a helicopter electromagnetic survey encouraged Diamond Field resources to begin a four-hole diamond drill program in late

1994. The large 1200m long conductive feature observed in the electromagnetic survey data was consequently determined to be from a mineralized body of semi-massive to massive sulphide ore. The second drill hole of the program intersected 41m of mineralized core grading 2.96% Ni, 1.89 Cu and 0.16% Co. The following year, an intensive drilling program resulted in the delineation of a world class nickel deposit, known as the Ovoid, marked by a 104m thick intersection of massive sulphide in diamond drill hole VB95007. Currently, the Ovoid deposit is believed to contain proven and probable reserves of 30 million tonnes grading 2.85% Ni, 1.68% Cu and 0.14% Co. In the fall of 1995 a second major discovery, known as the Eastern Deeps, was intersected during a step-out drilling program (Evans-Lamswood et al., 2000) one kilometre east of the Ovoid. In 1997, the most recent discovery was the Reid Brook zone, which is located one kilometre west of Discovery Hill. This increased the known mineralized east-west trend to roughly six kilometres in length. With the addition of the Reid Brook zone and Eastern Deeps, the mineral reserve is estimated to increase to 54 million tonnes of indicated mineral resources and 16 million tonnes of inferred mineral resources grading 1.53% Ni, 0.70% Cu, 0.09% Co, and 1.6% Ni, 0.80% Cu, 0.1% Co respectively.

1.3 Regional Geology

The major litho-tectonic units building the regional framework of Labrador and Quebec geology are the Superior, Churchill, Nain, Makkovik, and Grenville provinces illustrated in Figure 1.2. The Voisey's Bay Ni-Cu-Co deposit is a part of the Nain Plutonic Suite (NPS), comprising intrusions of granite, anorthosite, ferrodioritie, and troctolitie (Evans-Lamswood et al., 2000). The troctolite is gabbro rich in olivine and

plagioclase feldspar. These intrusions lie along the Nain-Churchill boundary which separates the eastern (2.5 Ga) Archean Nain province from the western (1.8 Ga) Proterozoic Churchill province (Figure 1.2). The Voisey's Bay troctolite, host of the Ni-Cu-Co deposit, straddles the Nain-Churchill boundary and is believed to be associated with the 1.8 Ga collisional suture between the two provinces (Naldrett et al., 1996) known as the Torngat orogen.

The evolution of the Torngat orogen began with the subduction of oceanic crust beneath the Rae continent prior to 1.8 Ga (Ryan, 2000) as depicted in Figure 1.2. The subduction of the oceanic crust initiated arc magmatism on the overriding Rae continent along with the accretion of sediment along the continental margin of the overriding plate. Collision of the continents between 1.8 Ga to 1.84 Ga (Rivers and Mengel, 1994; Funck and Louden, 1998) resulted in a thickening of the continental crust and subsequent large-scale metamorphism. The Paleoproterozoic Tasiuyak gneiss located along the eastern edge of the Churchill province is believed to be highly metamorphosed sediment derived from the subduction of the oceanic lithosphere (Ryan, 2000; Van Kranendonk et al., 1993). The Abloviak shear zone located in northern Labrador marks the final stages of the collisional event, dated between 1.73 Ga to 1.75 Ga (Figure 1.2a and 1.2d).

1.4 Voisey's Bay Intrusion

The Voisey's Bay intrusion lies between the Archean Nain orthogneisses of igneous derivation to the north and the Proterozoic Tasiuayak paragneisses of sedimentary derivation to the south. The intrusion consists mainly of weakly layered gabbros and troctolites that date between 1330 Ma (Evans-Lamswood et al., 2000;

Amelin et al., 1999) and 1338 Ma (Ryan et al., 1995). According to Li et al. (2000), the intrusion is thought to consist of an upper chamber (Eastern Deeps chamber) connected to a lower chamber (Reid Brook chamber) through a conduit system of varying thickness (Figure 1.3). Contained within the troctolite intrusion are five zones of mineralization. The zones hosting Ni-Cu-Co deposits consist of the Reid Brook zone, Discovery Hill zone, Mini-Ovoid, Ovoid and the Eastern Deeps from west to east respectively (Figure 1.3). The base of the Eastern Deeps chamber consists of fine-grained gabbros and intrusive troctolite breccias overlain by disseminated to semimassive sulphides (Evans-Lamswood et al., 2000), overlain by sequences of variable-textured troctolites and normal troctolites. The Eastern Deeps chamber is primarily a sub-vertical sheet having a horizontal feeder system with mineralization occurring at depths up to a kilometre.

Approximately one kilometre west of the Eastern Deeps, the Ovoid is located beneath 20m to 30m of overburden and is commonly viewed as a "bowl-shaped" accumulation of massive sulphide ore. Having horizontal dimensions of 650m by 350m and a maximum thickness of 120m, the Ovoid overlies a thin breccia sequence followed by troctolite and enderbitic orthogneiss. The Ovoid, Mini-Ovoid and Discovery Hill zones are all mineralized along vertical to sub-vertical domain of the feeder dyke system. Further west, the Reid Brook complex is located at a depth of 400m and extends to depths in excess of 2km.

As discussed above, the Voisey's Bay deposit is believed to be a complex system consisting of two chambers. The genetic model of the deposit is believed to consist of three stages (Nalderett, 2004). The first stage is believed to have occurred when the magma of the lower chamber rose within the Tasiuyak gneiss. Magma reacted with the

overlying gneiss and was saturated with sulphides. The second stage of the Voisey's Bay intrusion was a second wave of magma pushing the first pulse up through the Enderbitic gneiss into the Nain orthognesis. Varying degrees of nickel concentration could be a result of re-equilibration of nickel between the first and second pulse of magma (Naldrett et al., 2000). As the second pulse pushed material through the conduit, sulphides were deposited due to changes in dyke geometry (Evans-Lamswood et al., 2000) The third and final stage was the continuation of magma through the system carrying reacted gneiss inclusions to the base of the upper chamber (Nalderett, 2004).

1.5 Data

The gravity and density data used in this study were supplied by the Voisey's Bay Nickel Company (VBNC) a subsidiary of Inco Limited now a wholly-owned subsidiary of Companhia Vale do Rio Doce (CVRD). The gravity dataset was collected by Eastern Geophysics Limited beginning in February 1996 and ending in May 1997. The field gravity data were reduced to terrain corrected Bouguer anomalies following usual corrections for latitude and elevation effects using the standard crustal density of 2.67 g/cc. The final dataset available for the present study included GPS measurements (UTMX, UTMY), line and station number, elevation, and terrain corrected Bouguer gravity. All positions were determined using the 1983 North American Datum.

The subsurface density database is derived from over 500 drill logs collected since the beginning of the Voisey's Bay project in 1995. The density database was determined from regression analysis of the geochemical assays. VBNC did provide the equations used to calculate the density values; however, they were not willing to release the

information regarding the procedures used in deriving the density equations. No rock samples were available to check the validity of the derived density. The drill log dataset supplied by VBNC included the borehole identification number, UTM coordinates, depth in borehole and calculated density value. In addition to the calculated density value, VBNC also included the assay results of nickel, copper, cobalt, iron and sulphur collected during the drilling program. The analysis of the geochemical data is the subject of a PhD thesis at Memorial University by Michelle Huminicki which is near completion.

1.6 Gravity Inversion Program

The minimum-structure gravity inversion program used throughout this study was supplied by the University of British Columbia Geophysical Inversion Facility (UBC-GIF). The thee-dimensional inversion program operates by simultaneously minimizing a model objective function while generating a synthetic dataset that adequately fits the collected data. The collected data are normally reduced using standard regional-residual separation techniques such as wavelength filtering. The inversion is performed until the synthetic data agrees with the collected data to a degree of misfit calculated by the statistical attributes of the data. In addition, the model objective function is minimized by generating a density anomaly that is close to the reference model and is smooth in three spatial directions. The UBC-GIF inversion code incorporates a depth weighting function which counteracts the natural decay of the kernels (Li and Oldenburg, 1998a).

The model objective function allows the user to incorporate prior geological information through the reference and cell weighting models. The reference model could be a simple uniform half-space or a complex three-dimensional model. Cells within the

reference model can be weighted according to the confidence level of the value assigned to each cell. Cells intersected by drill logs can be assigned high cell weights while cells located at a greater distance from a drill log have a lower confidence and can be assigned a low cell weight. Although this project only examines the minimum-structure inversion program provided by UBC-GIF, research is currently being conducted at Memorial on blocky-style inversions (Farquharson, 2006).

1.7 Thesis Organization

The study is organized following the same standard procedures used by a geophysicist when processing and inverting gravity data. In Chapter 2 the collection of gravity data, survey configuration, and standard processing techniques used to remove the regional field and visualize data are examined. Since all reduction to gravity anomalies were completed before the data was provided by VBNC, the majority of the chapter will be focused on regional-residual separation techniques and further processing. The borehole data, calculation of the density data and methods used to generate three-dimensional models of the subsurface which will be incorporated into the inversion process are discussed in Chapter 3. The majority of the chapter will be focused on the building of the three-dimensional density models in Gocad.

The background information on the UBC inversion method, programs and file configurations are in Chapter 4. With the fundamental concepts of gravity inversion in place, the inversion of gravity at Voisey's Bay is investigated in Chapter 5 which is basically an integration of the previous chapters. The chapter investigates the inversion of gravity data discussed in Chapter 2, using the methods and inversion programs

discussed in Chapter 4. In addition, the inversions are constrained using the three-dimensional density models generated in Chapter 3. The results obtained from the previous chapters are summarized in Chapter 6.

Figure 1.1: A map illustrating the location of the Voisey's Bay Ni-Cu-Co deposit.

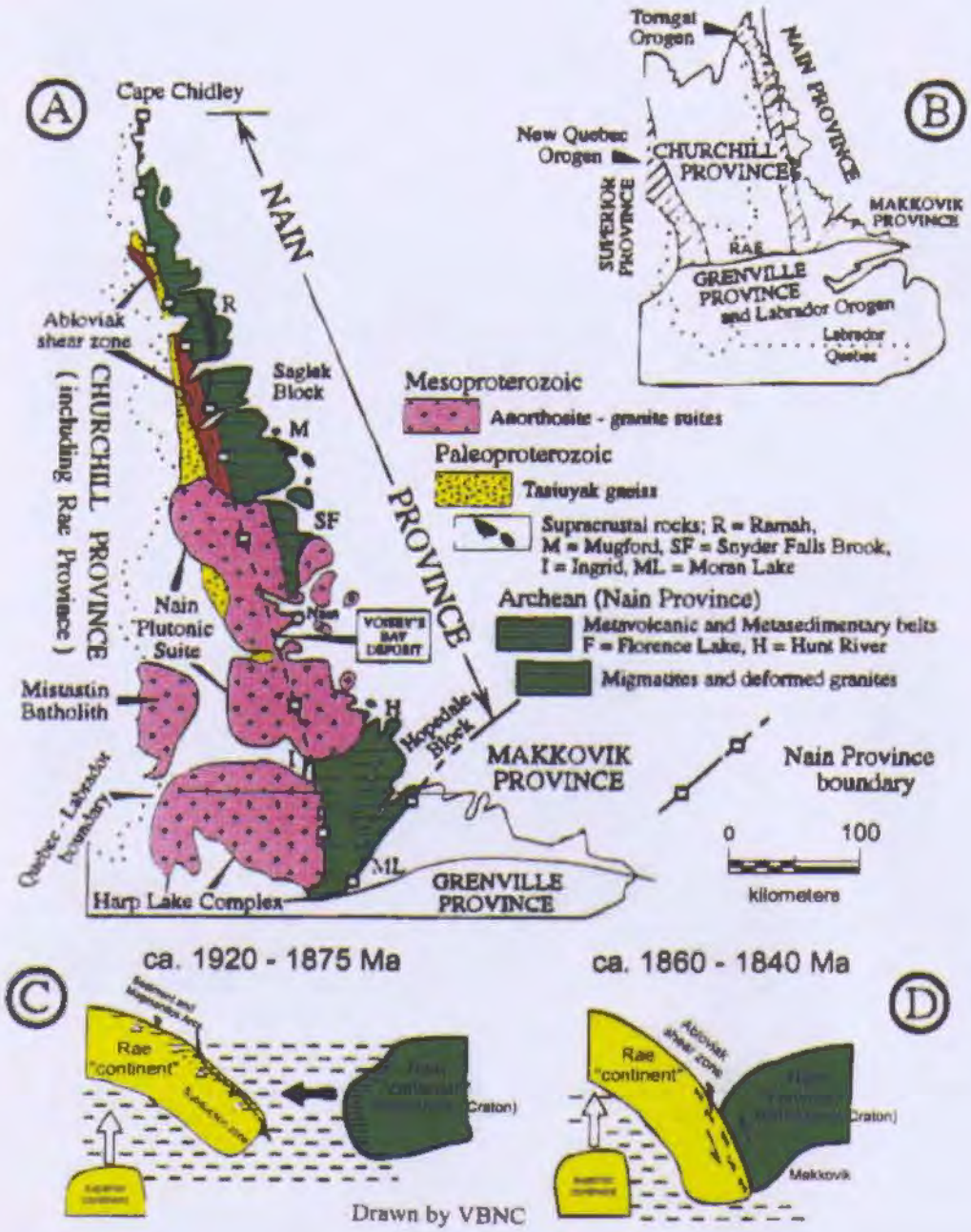

Figure 1.2: Regional geology of Northern Labrador (after International Geological Correlation Programme Projects No.290 and No. 315, 1994); A: major geological units; B: major lithotectonic units; C: postulated plate tectonic setting between 1920 and 1875 Ma; D: postulated plate tectonic setting between 1860-1840 Ma. The figure was drawn and provided by VBNC.

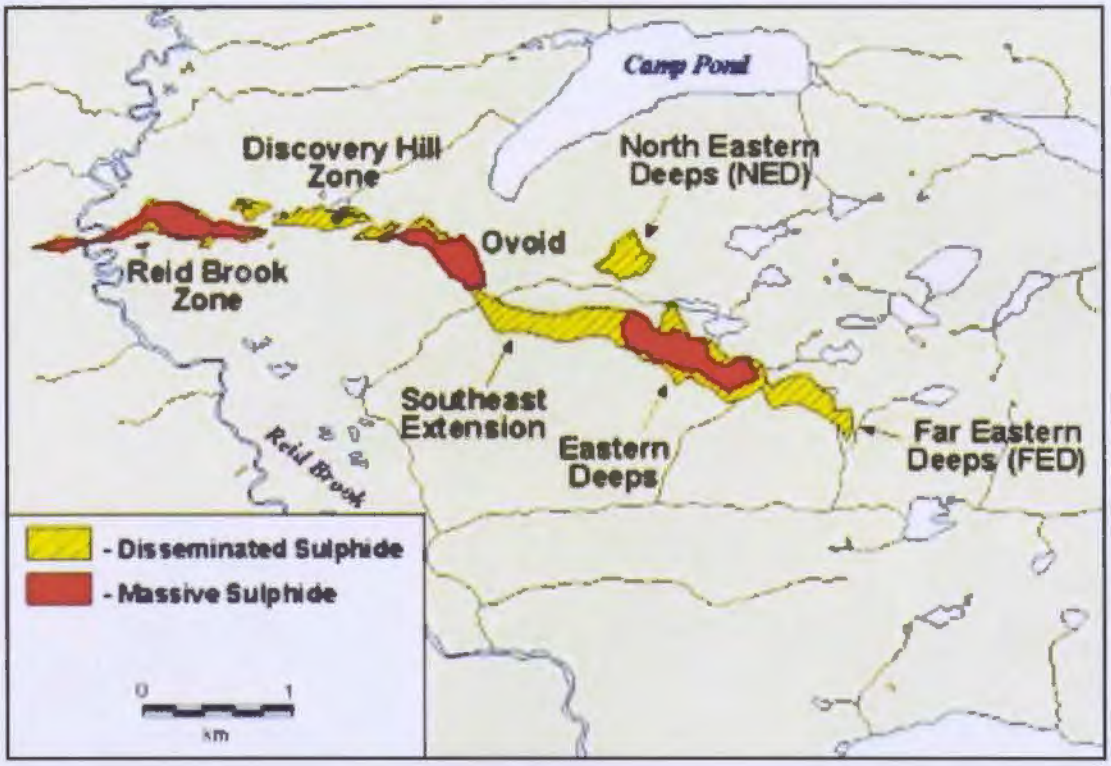

(Drawn by VBNC)

Figure 1.3: Simplified geological map of the Voisey's Bay Ni-Cu-Co deposit illustrating the distribution of disseminated and massive sulphide zones projected to the surface. The figure was drawn and provided by VBNC.

Chapter 2: Gravity

2.1 Introduction

Gravity methods applied to geophysical exploration have been refined over the past seventy years. The processing techniques can be subdivided into three major categories (Blakely, 1995): *field enhancement and display*, *forward modelling* and *inverse modelling*. This chapter will primarily deal with field enhancement and display, leaving other methods to be discussed in subsequent chapters.

The goal of this chapter is to describe the process used to generate a residual gravity dataset which can be used to interpret near surface geological features and to be incorporated into the minimum-structure inversion codes as input data. The chapter will begin with background information on the collection of gravity data, survey specifications and gravity reduction processing. The second section will focus on the survey layout and examine the distribution of gravity observations relative to known geological features which has important consequences. The third section will discuss the gridding methods used to generate maps and prepare the data for interpretation and further processing. The fourth section will provide a mathematical review of the techniques used in regional-residual separation and discuss the application of these techniques to the gravity data. The fifth and final section will discuss the results obtained from each regional-residual separation technique when applied to the gravity data at Voisey's Bay.

2.2 Gravity Data Collection and Reduction

The gravity data used in this study were collected for VBNC by Eastern Geophysics during a five-phase ground exploration program. The first phase of the gravity survey began on February 9th, 1996. The fifth and final phase of the gravity survey ended on May 30th, 1997. A LaCoste and Romberg model G gravimeter and a Lecia SR 299 Geodetic Real Time Differential Global Positioning System were used. Survey specifications required that the elevation was measured to within (+/-) 0.05m. All positions were determined using the 1983 North American Datum (NAD83) Zone 21. In addition, the global geodetic system chosen for the survey and later corrections was the WGS84. Survey specifications for gravity collection required that the daily loop closures and station repeat variations were less than 0.05 mGal. The recorded data included line and station number, date and time of meter reading, height of meter above ground, the gravity meter reading, and GPS coordinates.

Standard Bouguer and terrain corrections were applied to the dataset in 1996, using the universally accepted Bouguer reduction density of 2.67 g/cm^3. Data required for inner Hammer zone terrain corrections were collected in the field by the geophysical technician while outer terrain corrections were calculated using topographic datasets contoured at 5m intervals. Outer terrain corrections were computed using five rings with incremental radii of 500m to a maximum radius of 2500m. Further information pertaining to the survey procedures and calculation of the Bouguer gravity anomaly at Voisey's Bay may be obtained from the logistics report and operator journal supplied by Eastern Geophysics Limited and Excel Geophysics Inc (1997).

2.3 Survey Layout

Approximately 10000 gravity readings were taken during the Voisey's Bay gravity project covering an approximate area of 285km^2 (Figure 2.1). The dataset contains 105 lines with 97 of those directed north-south and 8 directed east-west. The station spacing along the lines ranged from 25m to 50m, depending on their location. The east-west lines were located above 6245000m north and lay between 554000m and 564000m east with a maximum length of 10km. All of the east-west lines had a station spacing of 50m and a line separation of 1km. The east-west lines were orientated perpendicular to three main geological units shown in Figure 2.1, which are from west to east, the Makhavinekh Lake Granite, Nain Gneiss and Kangeklualuk Anorthosite. In addition to the main geological units, small intrusions such as the Mushuau Intrusions (North, Central and Southern), have elongated axes in plan view in the north-south direction.

The north-south lines shown in Figure 2.1 can be separated into three groups based on their position within the study area. The first group of lines located within the study area is a group of 13 lines centred at 560000m east and 6250000m north. Each line in this group had a station spacing of 50m and a main line separation of 200m. The most eastern and western lines were separated by 1km from the main group. The positions of the lines correlated with the position of the northern and central segment of the Mushuau Intrusion. The second group of north-south lines is concentrated at the centre and southeastern section of the study area. The line separation is approximately 200m with station spacing along the lines ranging between 25m to 50m. Lines containing 25m spacings are related to the position of Reid Brook Zone, Discovery Hill Zone, Mini-

Ovoid, Ovoid, Voisey's Bay Troctolite and Voisey's Bay Granite from west to east respectively. The 50m intervals were positioned along lines over the Voisey's Bay Granite to the east. The third and final group of lines were located over the Ashley Intrusion in the southwest. The lines had a separation of 300m and a station spacing of 50m.

2.4 Gridding

In the majority of gravity surveys, data are collected along a series of lines where the distance between the lines is greater than the station spacing along the line. In order to utilize common processing and filtering techniques available, the data must be imposed onto an equally spaced coordinate system in the easting and northing directions. Most processing packages require an equally spaced dataset, since most of the techniques are applied in the Fourier domain to decrease processing times. These techniques will be covered later within this chapter. Choosing a gridding interval is simply deciding an appropriate distance where we are maximizing the use of the data collected without losing signal or generating artefacts. The shortest spatial wavelength λ_n, which can accurately reconstructed from a series of equally spaced points (Δx) is defined by

$$\lambda_n = 2\Delta x . \qquad (2.1)$$

The Nyquist sample interval (λ_n) is also considered as the minimum sample interval required to achieve error free reconstruction of a band limited function (Naidu and

Mathew, 1998). Wavelengths less than the Nyquist sample interval will be combined with larger wavelengths in the signal.

2.4.1 Application to Gravity Data:

To investigate the effects of using various grid intervals, the raw gravity data were gridded using the minimum curvature algorithm in the Oasis Montaj package (Oasis Montaj™ 6.4) at a spacing of 100m, 200m, and 500m. From the computed 100m, 200m, and 500m grid (.grd) files, a suite of maps was produced (Figure 2.2, Figure 2.3, and Figure 2.4). Choosing a gridding interval is effectively defining the lower limit (minimal scale) in the local system. In this study the smallest, yet most important, geological feature investigated is the Ovoid. The Ovoid has approximate maximum north-south and east-west dimensions of 340m and 280m as illustrated in Figure 2.5. To examine the effects of gridding at different intervals, the three north-south profiles (VB01, VB02 andVB03) over the known position of the Ovoid were selected. A comparison (Figure 2.6) can be made between the raw un-gridded data and gridded data by projecting the gravity field obtained from the various grid surfaces to the position of the collected data. This method was accomplished by using a four step process;

1. Generate a grid(s) of the raw gravity data using the Oasis Montaj^{tm} software, and export the grid in a common .txt format.
2. Import the raw gravity data and generated grids separately into the Gocad geomodeling software package as pointsets.
3. Generate surfaces using liner triangulation from the gridded data and fix surfaces to the elevations contained within the raw gravity pointset.

4. Using the vertical projection capabilities in Gocad, project the gravity information from the surfaces to the raw gravity pointset. The raw gravity pointset will now contain the raw and gridded Bouguer gravity values.

The best-suited grid interval for the purpose of regional-residual separation was chosen to be 100m. This grid interval is a 'happy' medium between the spatial distribution of gravity readings in the north-south and east-west directions. The VB02 and VB03 gravity profiles shown in Figure 2.6 demonstrate that the 100m-grid interval reproduces the gravitational field over the Ovoid to within 0.5 mGal. Larger grid intervals result in a significant decrease in amplitude over the Ovoid. Smaller grid intervals result in gravitational highs being centred over the survey lines, commonly known as the "bull's eye" effect.

2.5 Regional Residual Separation

Potential field theory indicates that any observed gravitational field is a complex combination of fields generated from multiple source bodies (Telford et al., 1990). The frequency spectra obtained from gravity maps are usually declining functions, whose rate of decay is largely determined by the depth and thickness of anomaly producing bodies (Spector and Grant, 1970). As a result, multiple source bodies located at different depths can be separated based on the frequency spectra (Odegrad and Berg, 1965).

Wavelength filtering is based on the principle that deep lying bodies produce long wavelengths while shallow sources are characterized by short wavelengths. Immediately a connection between wavelength filtering and regional-residual separation can be seen. Regional scale features are mostly dominated by long wavelengths while residual bodies

are primarily dominated by short wavelengths. However, it must be noted that every potential field anomaly is composed of the entire spectrum of frequencies (Odegrad and Berg, 1965).

2.5.1 Mathematical Review:

In the early 1800's, Jean Baptiste Fourier suggested that any periodic signal could be reconstructed by superimposing a series of sine and cosine waves. The Fourier series is commonly defined as (James, 2002),

$$F(t) = \frac{A_0}{2} + \sum_{n=1}^{\infty} A_n \cos(2\pi n f_0 t) + B_n \sin(2\pi n f_0 t) \qquad (2.2)$$

where f_0 is the fundamental frequency and t is time. In Fourier analysis, time (t) and displacement (x) are interchangeable allowing Fourier techniques to be applied to spatially distributed points. One significant disadvantage to the Fourier series is that it must be applied to a periodic wave. In geophysical sciences, no measurable wave is truly periodic. Using a Fourier series to approximate a non-periodic wave, results in an inaccurate reconstruction of the original wave (James, 2002). Geophysical and geological data are usually collected in a two dimensional coordinate system (u,v), with u and v representing the eastern and northern directions. The two-dimensional Fourier transform $\underline{F}(f_u,f_v)$ of a signal $F(u,v)$ can be expressed as (Pan and Harris, 2000),

$$\underline{F}(f_u, f_v) = \int_{-\infty}^{\infty}\int_{-\infty}^{\infty} F(u,v) e^{-i(f_u u + f_v v)} du dv \qquad (2.3)$$

and

$$F(u,v) = \int_{-\infty}^{\infty}\int_{-\infty}^{\infty} \overline{F}(f_u, f_v) e^{i(f_u u + f_v v)} df_u df_v \tag{2.4}$$

where, e is the base of the natural logarithm, i is the imaginary unit of the complex number system, f_u is the spatial frequency in the eastern direction, and f_v is the frequency in the northing direction. The benefit of the Fourier integral over the Fourier series is that the Fourier integral is applicable to non-periodic waveforms (Ramirez, 1985).

Another characteristic of geophysical data is that the data are collected at discreet points within a survey. Discrete surveys having m lines and n stations along each line are transformed into the frequency domain using the equation (Pan and Harris, 2000),

$$\overline{Z}(k,l) = \sum_{\alpha=1}^{m}\sum_{\beta=1}^{n} Z(\alpha,\beta) e^{-2\pi i\left(\frac{k\alpha}{m} + \frac{l\beta}{n}\right)} \tag{2.5}$$

where, k and l are the wavenumbers and α and β are the indices of spatial locations. A commonly exploited property of the Fourier transform is that the transform simplifies calculations of many linear filter operations (Naidu and Mathew, 1998). In signal processing, the original signal is convolved with a filter creating the output signal or filtered signal $y(x)$. The convolution theorem in the spatial domain is (Spiegel, 1999),

$$y(x) = \int_{-\infty}^{\infty} f(x-\tau) s(\tau) d\tau \tag{2.6}$$

where, $s(\tau)$ is the signal and $f(x)$ is the filter. Convolutions require many computations to produce an output signal. In the frequency domain, the Fourier Transform of the convolution of two functions $s(\tau)$ and $f(x)$ is equal to the product of their Fourier transforms,

$$\bar{y}(f_u, f_v) = \bar{s}(f_u, f_v) \times \bar{f}(f_u, f_v). \tag{2.7}$$

Calculating a convolution in the frequency domain, results in a reduction in the total number of computations and time.

2.5.1.1 High/Low-Pass Filters:

Frequency filtering is a common processing tool (Bhattacharya, 1966; Parker, 1973; Oldenburg, 1974) whereby the processor selects a frequency and passes or rejects all frequencies above or below the selected cutoff frequency (f_c). The high-pass filter passes all frequencies higher than the cutoff frequency and is expressed as (Pan and Harris, 2000),

$$\begin{aligned} \bar{F}(f_u, f_v) &= 1. \quad \text{if } \sqrt{f_u^2 + f_v^2} \geq f_c \\ &= 0. \quad \textit{otherwise} \end{aligned} \tag{2.8}$$

Conversely, low-pass filters pass all frequencies below the cutoff frequency and may be expressed as (Pan and Harris, 2000),

$$\begin{aligned} \bar{F}(f_u, f_v) &= 1. \quad \text{if } \sqrt{f_u^2 + f_v^2} \leq f_c \\ &= 0. \quad \textit{otherwise} \end{aligned} \tag{2.9}$$

2.5.1.2 Band-Pass Filters:

Band-pass filters are similar to high and low-pass filters since they limit the frequencies viewed in map display. The band of frequencies is limited to those frequencies that lie between a selected high cut (f_{hc}) and low cut (f_{lc}) frequency. The filter may be expressed as (Pan and Harris, 2000),

$$\overline{F}(f_u, f_v) = 1. \quad if \quad f_{hc} \le \sqrt{f_u^2 + f_v^2} \ge f_{lc}$$
$$= 0. \quad otherwise \qquad (2.10)$$

2.5.1.3 Field Continuation Methods:

The upward continuation of a gravitational field is a process that determines the smoothing which would be expected if the gravity field were measured at a new elevation from the observed plane. If the gravitational field is calculated above the observed plane, the process is called *upward continuation*. Conversely, if the computed field is below the plane of observation, the process is called *downward continuation*. In the Fourier domain, the gravitational field may be expressed as an exponential function and computed by (Pan and Harris, 2000),

$$\overline{F}(f_u, f_v) = e^{2\pi h\sqrt{f_u^2 + f_v^2}} \qquad (2.11)$$

where h is the continuation height from the observed plane. A positive and negative value for h in Equation 2.11 will execute the downward and upward continuation of the observed gravity field gravity field.

2.5.2. Application to the Voisey's Bay Gravity Data:

The purpose of this subsection is to apply each of the frequency based processing techniques to the gravity data set, in order to determine the gravity contribution on a local and regional scale. In the process of regional-residual separation, it will be assumed that

the frequency spectra of near surface bodies will be dominated by short wavelengths while deep sources are dominated by long wavelengths. The degree of regional-residual separation will be simplified such that the separation that produces the least correlation with the near surface local geology will be defined as the "best" representation of the regional field (Hearst and Morris, 2001). A problem with this simplification is that most of the geological units throughout the study area vary in geometry and depth. As an example, the Ovoid will have different regional-residual criteria than the larger Voisey's Bay Troctolite. The best estimate of the regional field will be considered to have been achieved when no gravitational contribution from the Mushuau Intrusion is present within the filtered data. The Mushuau Intrusion (Northern Lobe) produces the largest gravitational anomaly of approximately 9mGal (Figure 2.2). Removal of the anomaly ensures that the gravitational contributions of other near surface geological bodies are preserved in the residual field. Enhancing the gravitational signature over the Ovoid will be examined in Chapter 5.

2.5.2.1. Band-Pass Filters:

Two major obstacles in wavelength filtering are the spectral overlap that exists between bodies in the frequency spectra and the loss of spatial information (phase) when the data is cast into the wavenumber domain. To correlate components of the frequency spectrum with gravity anomalies located throughout the study area, a series of band-pass filters was applied to the 100m-grid dataset. The benefit of using a series of band-pass filters is that maps in the spatial domain can be used to correlate frequency ranges with geological features. With the use of Oasis Montaj™, four band-pass filters were designed

with bandwidths of 20km to 10km, 10km to 2km, 5km to 1km, and 2km to 200m. The Oasis Montaj™ user manual does not specify whether the band-pass filters are tapered. Each filter was applied to the Bouguer 100m-grid data to produce a suite of maps illustrated in Figure 2.7, Figure 2.8, Figure 2.9 and Figure 2.10.

Regional features with wavelengths between 20km and 10km illustrated in Figure 2.7 have a major north-south component with a high over the Nain Gneiss. This result is expected since the Nain-Churchill boundary is a major north-south trending boundary, separating the Nain and Churchill Provinces shown in Figure 2.1. Wavelengths contained between 10km and 2km (Figure 2.8) correlate with the position of sub-regional geological features like the Mushuau Intrusion, Voisey's Bay Troctolite, Ashley Intrusion and Sections of the Voisey's Bay Granite. Similarly for wavelengths between 5km and 1km (Figure 2.9), although several of the sub-regional geological units like the Mushuau Intrusion are resolved with greater detail. The final band-pass filter, which has a range between 2km and 200m (Figure 2.10), results in a high signature over the Ovoid and other small scale features in the south.

2.5.2.2. High/Low-Pass Filters:

A series of low-pass filters were applied to the Bouguer gravity dataset using cutoff wavelengths of 5km, 3km, 2km and 750m. All wavelengths above the cutoff wavelengths of 5km, 3km, 2km and 750m are illustrated in Figure 2.11, Figure 2.12, Figure 2.13 and Figure 2.14. Limiting wavelengths above 5km, results in a major north-south trending gravitational anomaly as shown in Figure 2.11. The north-south regional trend has a slight gradient toward the west, with an average of 52mGal in the east and

44mGal in the west. A positive anomaly exists over the position of the Mushuau Intrusion (Northern Lobe) and Voisey's Bay Granite. This is consistent with the results obtained from band-pass filtering at larger wavelengths. At a cutoff of 5km, the equipotential lines run predominantly north-south. The equipotential lines are pulled east, toward the Enderbitic Gneiss (Figure 2.1) as smaller wavelengths are introduced into the dataset as shown in Figure 2.13 and Figure 2.14. The residual field was not calculated given that the gravitational field over the Mushuau Intrusion was still present at wavelengths greater than 5km.

2.5.2.3. Upward Continuation:

Upward continuation methods were applied to the Bouguer gravity dataset at continuation distances of 500m, 1.5km, 3km and 5km (Figure 2.15, Figure 2.16, Figure 2.17 and Figure 2.18). The upward continuation method generates smooth models since it suppresses noise as the distance from the observed plane increases. One downside to the upward continuation of potential data is that small-scale anomalies may be coalesced together forming a large broad scale anomaly (Hearst and Morris, 2001).

At the first continuation level of 0.5km, shown in Figure 2.15, the gravitational field is dominated by three anomalous highs, from north to south (Figure 2.15), correlating with the position of the Mushuau Intrusion (Northern Lobe), Mushuau Intrusion (Southern Lobe) and Voisey's Bay Granite. Influence from the Voisey's Bay Troctolite is still apparent in the data, as it draws the north-south contours to the west. The gravitation field over the Ovoid is significantly reduced having little effect on the overall field distribution. At the continuation level of 1.5km and 3km, the gravitational

contribution of local geological units begins to decrease as illustrated in Figure 2.16 and Figure 2.17. Many of the features are removed or drastically modified from the original field. The three major anomalies present at the continuation level of 0.5km are no longer present in the data at a continuation level of 3km. Contour lines are now trending in a northeast-southwest direction with a gradient decreasing toward the northwest. The Mushuau Intrusion has little impact on the gravitational field. Finally, at the fourth continuation stage of 5km (Figure 2.18), there is no correlation with the near-surface geological units.

The residual field was computed using the equation,

$$\textit{Residual Field} = (\textit{Bouguer Gravity Data}) - (\textit{Upward Continued Data}). \qquad (2.12)$$

With the use of Equation 2.12, residual maps for continuation levels of 500m, 3km and 5km were created (Figure 2.19, Figure 2.20 and Figure 2.21). The first continuation level of 500m (Figure 2.19) results in a residual field outlining the major geological units. At a continuation level of 500m, amplitudes from the high frequency near surface features are removed. The loss of wanted signal is a result of overestimating the regional field. In map display, the residual field calculated at a continuation level of 3km produces smooth, continuous, isolated anomalies as illustrated by the shaded relief map in Figure 2.22. Major geological units like the Mushuau Intrusion (North, Central, Southern), Voisey's Bay Troctolite, and Voisey's Bay Granite are all well defined. Similarly, small-scale structures like the Ovoid and Ashley Intrusion are also represented by isolated gravitational highs.

2.5.2.4 Trend-Surface Analyses:

A simple approach in regional-residual separation is to fit a polynomial surface to a dataset using statistical methods. The methodology behind this approach is based on the assumption that the gravitational field produced from large-scale regional features varies smoothly over the survey area. Consequently, the regional field may be represented by a low-order polynomial surface. This simplistic view of the regional field provides a quick method to determine the gravity contribution of near surface bodies. Caution must be used when generating polynomial surfaces with datasets containing large ranges (Zurflueh, 1967), as pseudo-anomalies are commonly incorporated in the estimate of the residual field. A second issue arises when data sets have areas containing a high concentration of data points. If a polynomial surface is created from all points within a dataset, the trend-surface may be drawn towards the highly concentrated areas (Hearst and Morris, 2001). In such cases, the polynomial surfaces may be computed by using only the edge points of the dataset.

With the use of Oasis Montaj, a number of polynomial surfaces were generated from the gridded data using least squares fitting. The modelling program allows the user to select if all points or edge points are used in the least squares fitting process. A 1^{st} order polynomial surface was removed from the Bouguer gravity data using both all points and edge points (Figure 2.23 and Figure 2.24). When choosing all the observation points, the generated planar surface has a greater north-south component. In map display, the residual field calculated from the edge points, results in a smoother anomaly distribution. As an example, southern anomalies shown in Figure 2.24 have a greater correlation with geological bodies shown in Figure 2.1. A second order polynomial

surface, using only the edge points, was applied to the gravity dataset shown in Figure 2.25. The second order regional field is highly influenced by the Mushuau Intrusion, pulling the regional field to the northwest.

2.6 Results

Each regional-residual processing method has its advantages and disadvantages in the calculation of the regional and residual field. The best estimate of the regional field is completely subjective and may vary depending on the geological target chosen. In this chapter, identification of the best estimate of the regional field was taken to be when no gravitational contribution from the Mushuau Intrusion is present in the data. This criterion was based solely on the fact that the Mushuau Intrusion contains a range of wavelengths, greater than any other near-surface geological source, as shown through various band-pass filters.

Upward continuation and trend-surface analysis using only the edge points provided the best estimate of the regional field. At a continuation level of 3km, no correlation could be made with near surface geological features. A similar result was obtained from a 1st order polynomial surface using edge points. When all observation points were used in the trend surface analysis, the major positive anomaly over the Mushuau Intrusion (Northern Lobe) influenced the outcome of the calculated regional field. As a result, pseudo-anomalies distorted the residual field in map display. Low-pass filters were unable to successfully remove the regional field due to the wide range of wavelengths contained within the Mushuau anomaly. From the suite of residual maps created, it was difficult to correlate gravity anomalies with geological bodies in the south.

The difficulty is due to the complex configuration and the low density contrast between individual units. In summary, the upward continued data at a continuation level of 3km produced the best estimate of the regional field. The residual data calculated from this continuation level best represents the gravitational field of near surface geological bodies throughout the Voisey's Bay area.

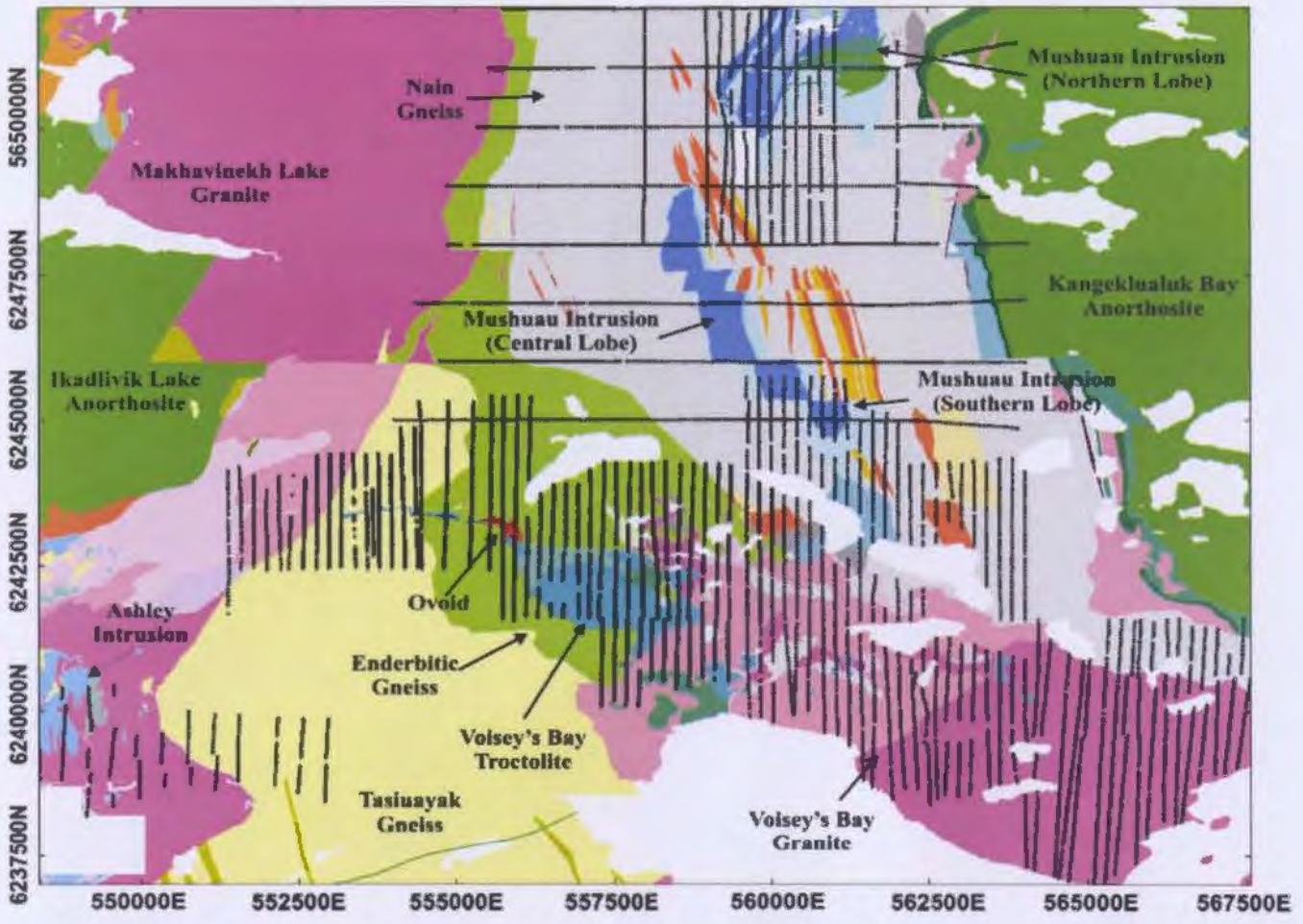

Figure 2.1: A map illustrating the position of major geological units and the location of gravity readings at Voisey's Bay. Data supplied by VBNC. Coordinates are in UTM meters relative to NAD83 (Zone 21). Scale can be inferred from coordinate annotations.

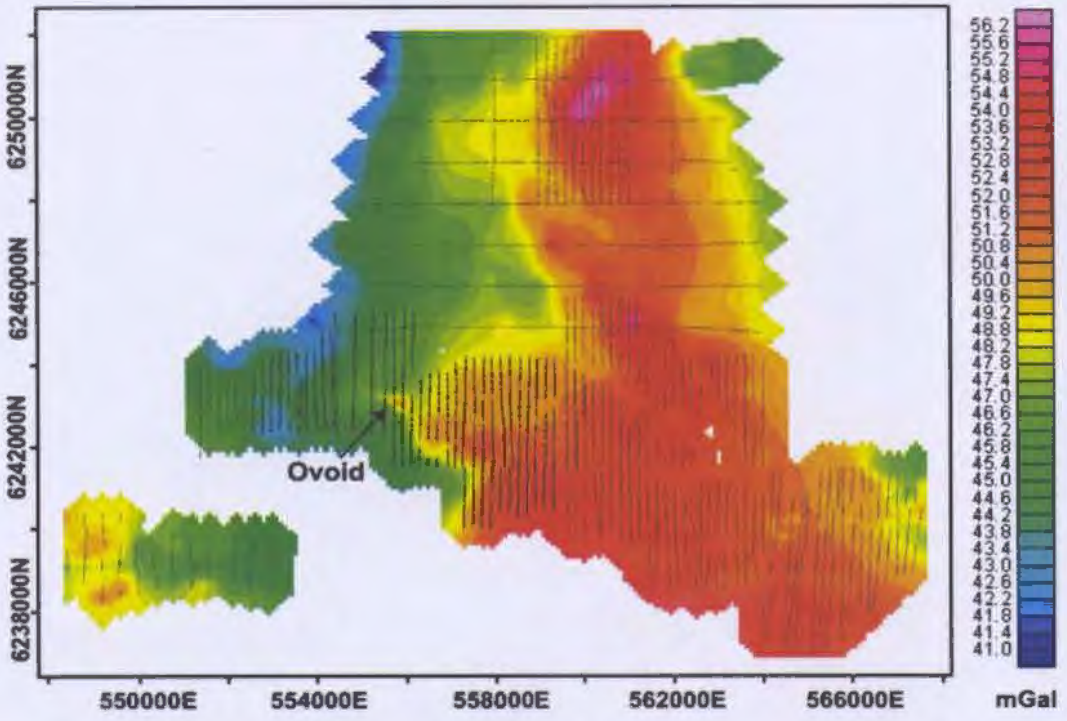

Figure 2.2: Bouguer gravity distribution gridded at 100m. The location of the Ovoid is shown by the black arrow. Coordinates are in UTM meters relative to NAD83 (Zone 21). Scale can be inferred from coordinate annotations.

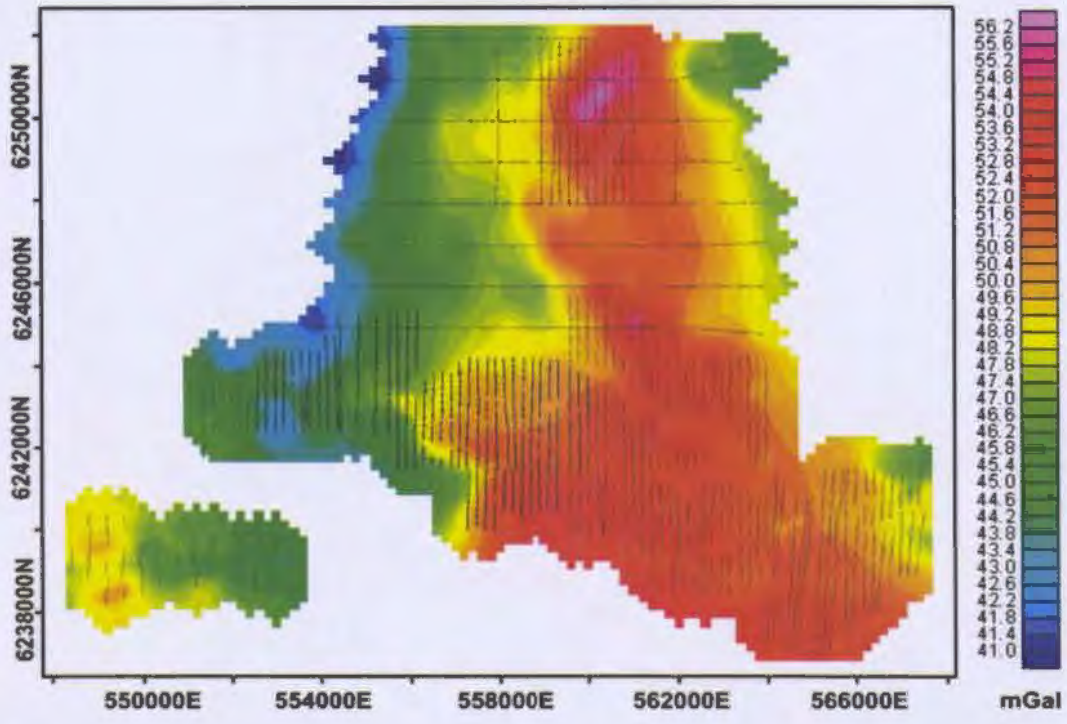

Figure 2.3: Bouguer gravity distribution gridded at 200m. Coordinates are in UTM meters relative to NAD83 (Zone 21). Scale can be inferred from coordinate annotations.

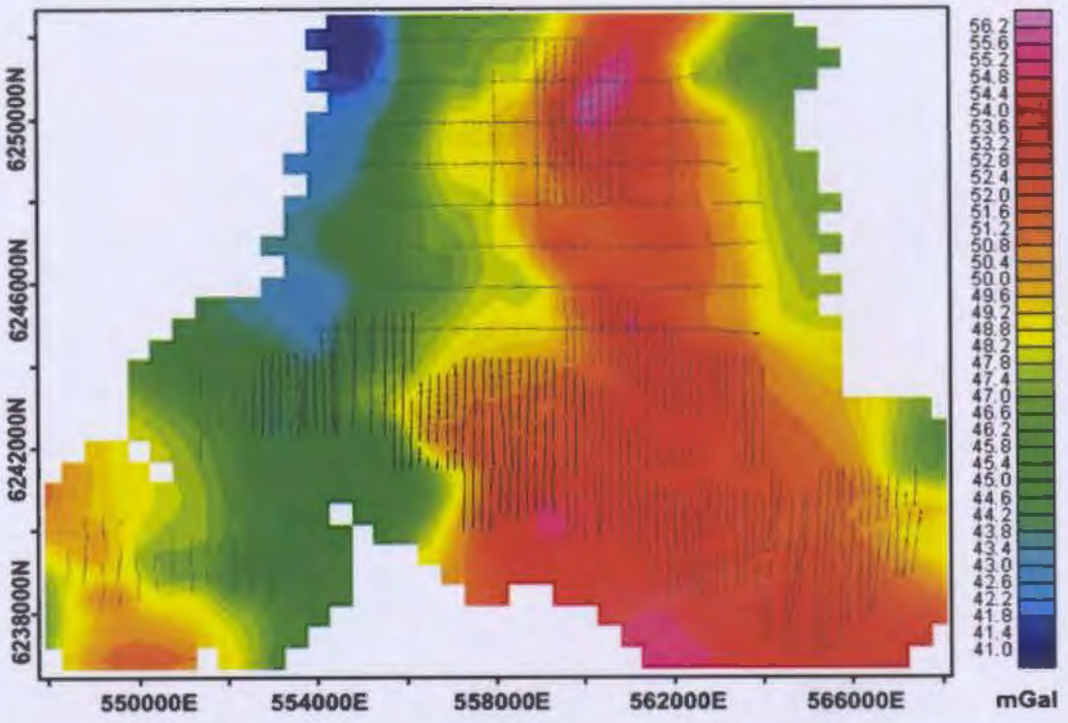

Figure 2.4: Bouguer gravity distribution gridded at 500m. Coordinates are in UTM meters relative to NAD83 (Zone 21). Scale can be inferred from coordinate annotations.

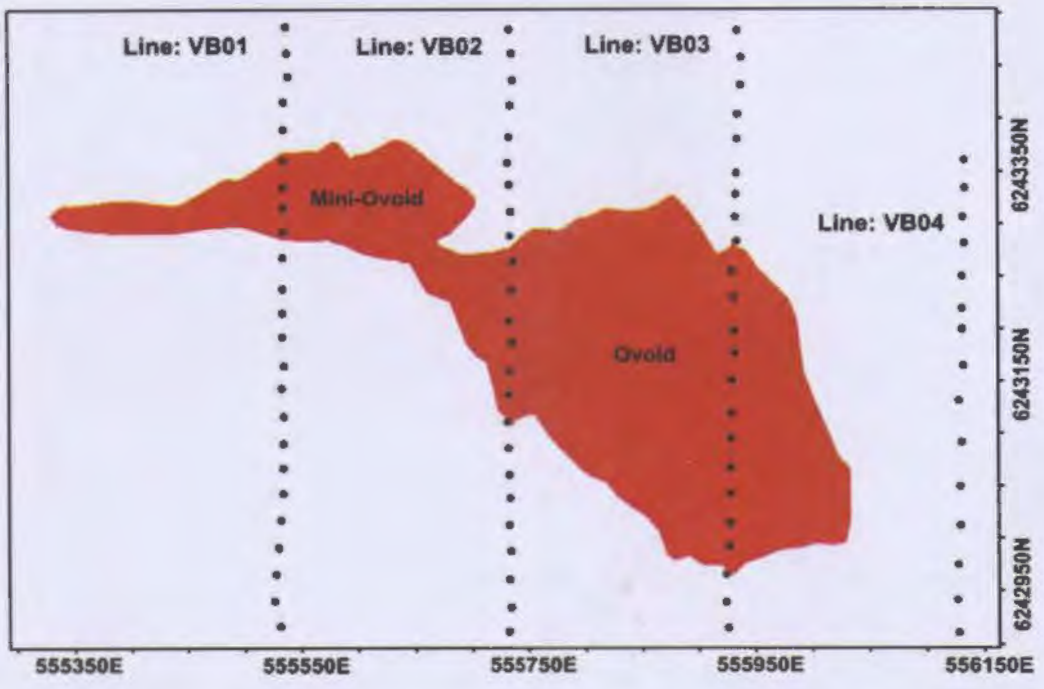

Figure 2.5: A map illustrating the projection of the Ovoid and Mini-Ovoid wireframe to the surface. Superimposed are the locations of survey lines VB01, VB02, VB03 and VB04. Coordinates are in UTM meters relative to NAD83 (Zone 21). Scale can be inferred from coordinate annotations.

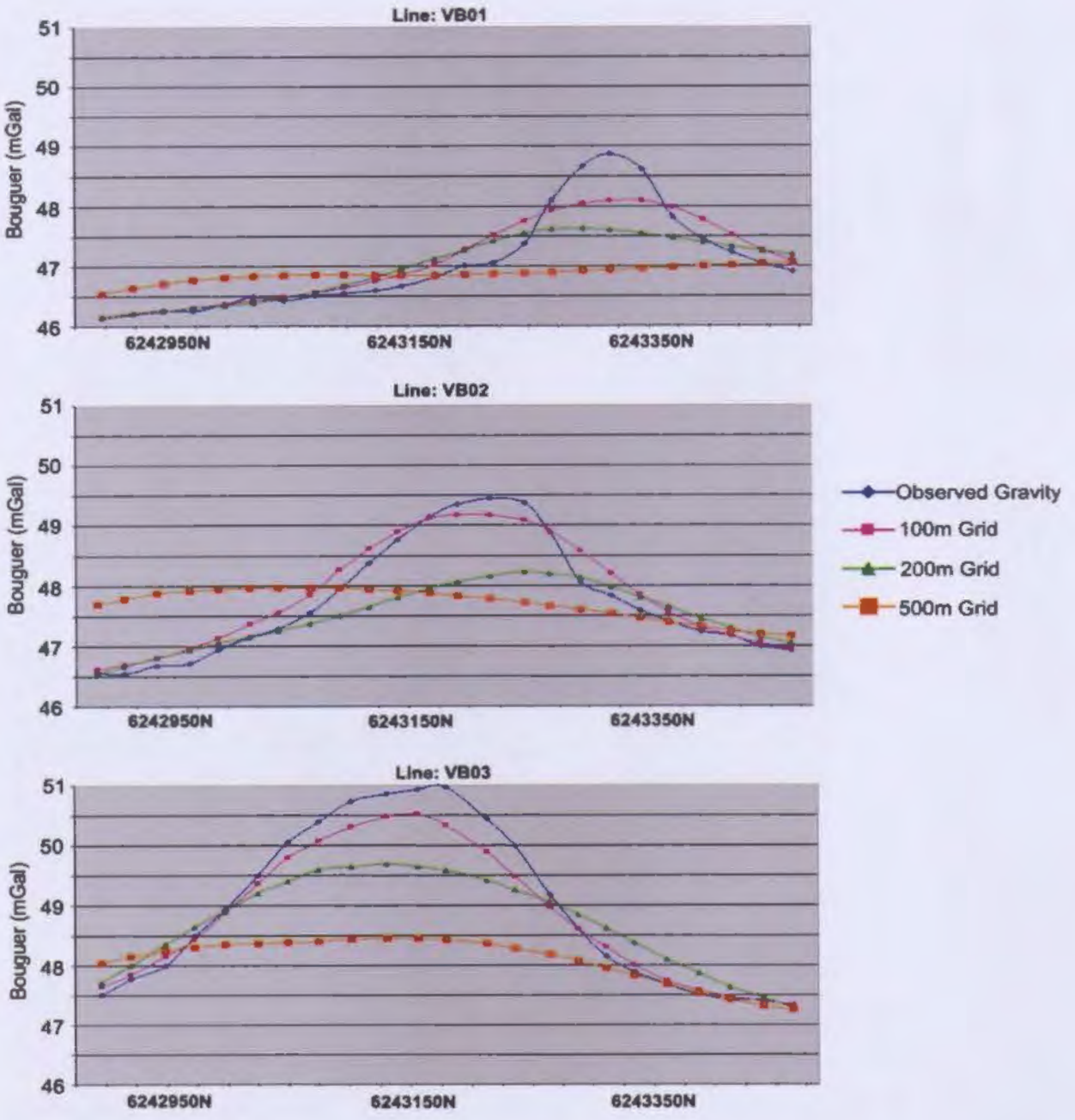

Figure 2.6: Profiles crossing the Ovoid and Mini-Ovoid along lines VB01, VB02 and VB03 comparing 100m, 200m, and 500m grid surfaces vertically projected to the location of the collected gravity data. Profile locations are illustrated on Figure 2.5. Coordinates are in UTM meters relative to NAD83 (Zone 21). Scale can be inferred from coordinate annotations.

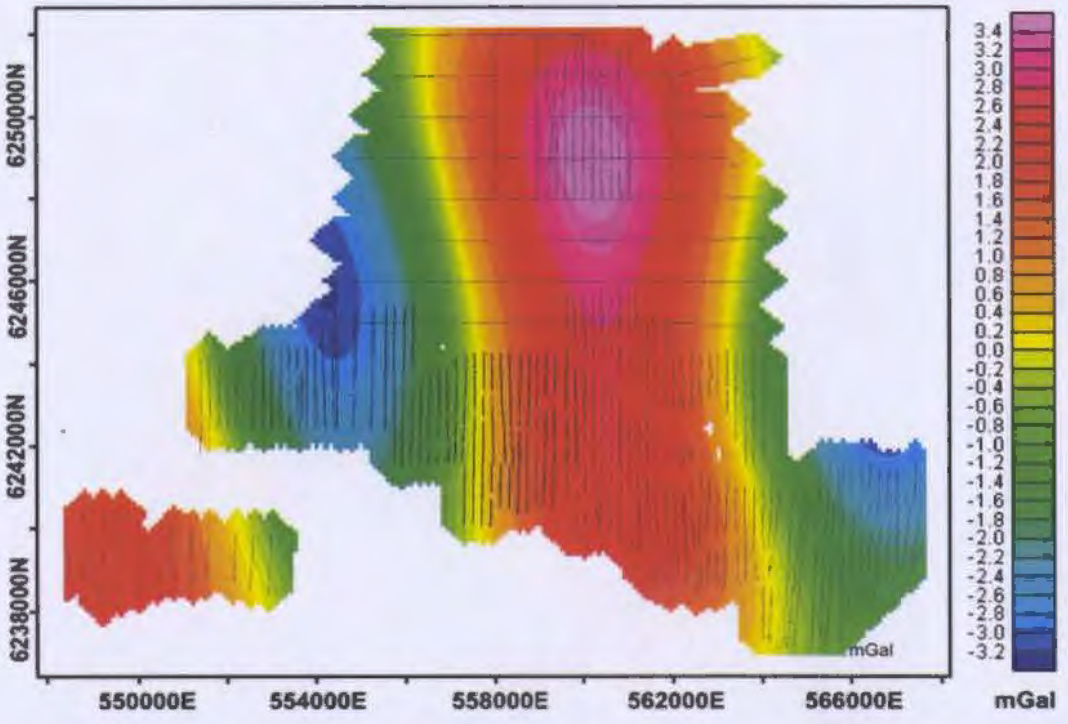

Figure 2.7: A map illustrating gravity wavelengths between 20km and 10km. Coordinates are in UTM meters relative to NAD83 (Zone 21). Scale can be inferred from coordinate annotations.

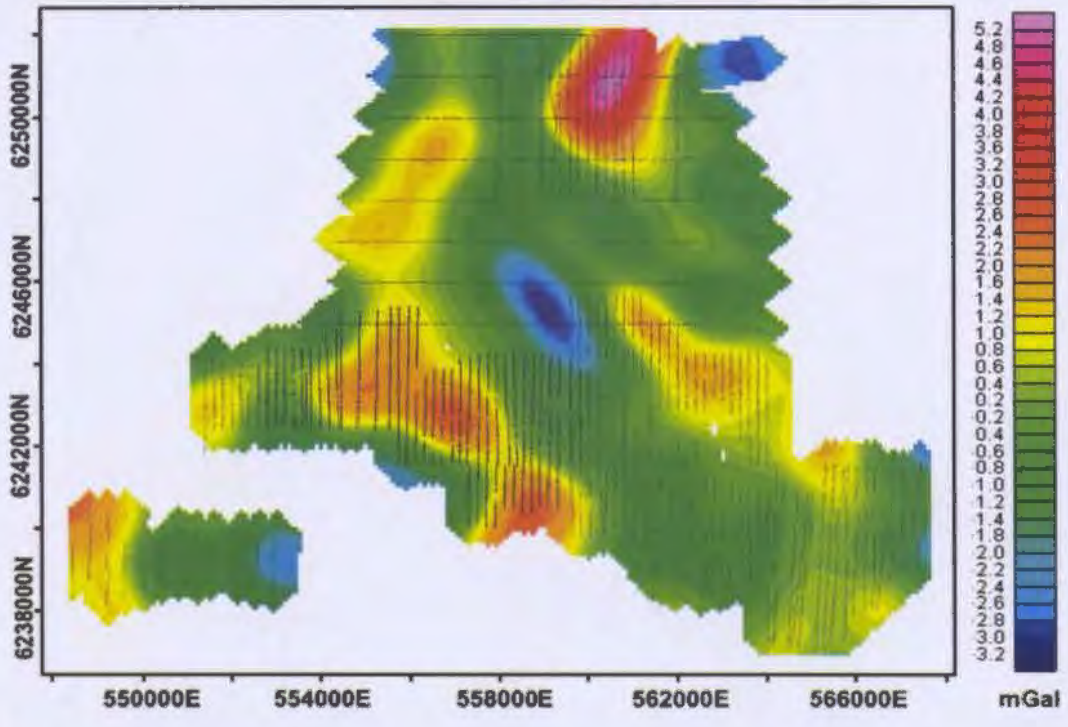

Figure 2.8: A map illustrating gravity wavelengths between 10km and 2km. Coordinates are in UTM meters relative to NAD83 (Zone 21). Scale can be inferred from coordinate annotations.

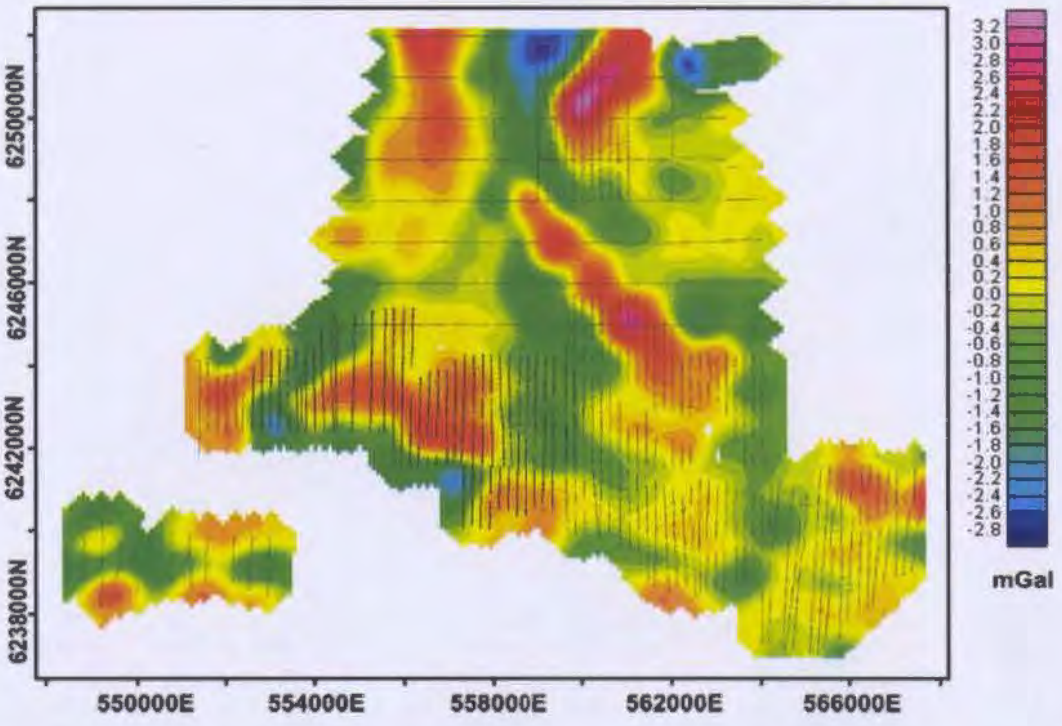

Figure 2.9: A map illustrating gravity wavelengths between 5km and 1km. Coordinates are in UTM meters relative to NAD83 (Zone 21). Scale can be inferred from coordinate annotations.

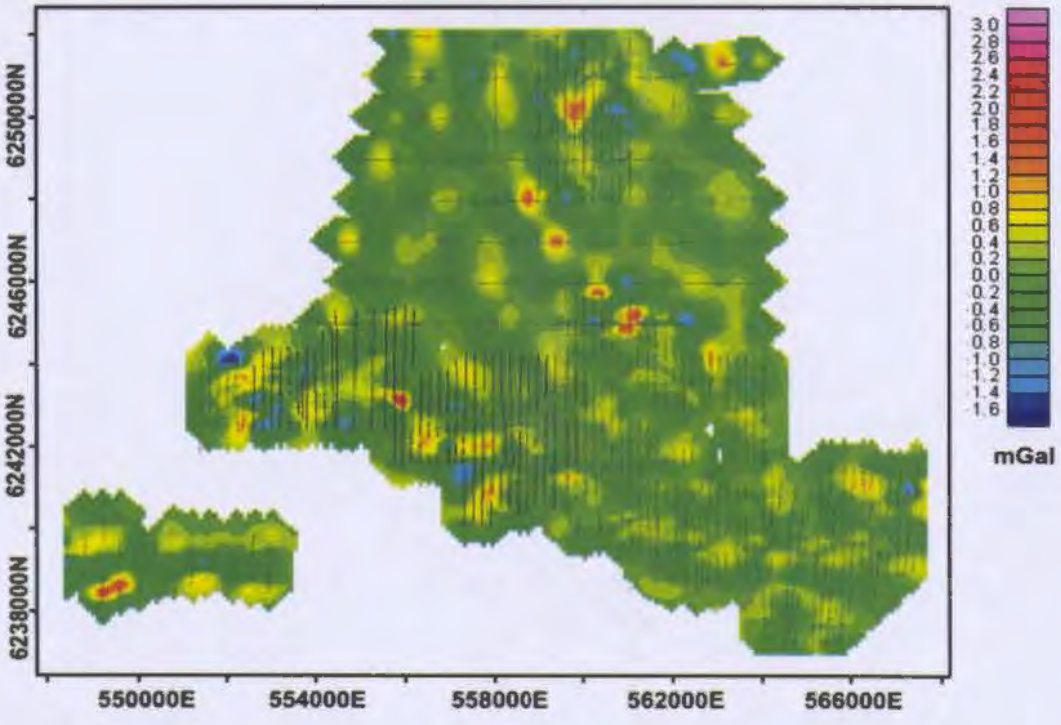

Figure 2.10: A map illustrating gravity wavelengths between 1km and 0.2km. Coordinates are in UTM meters relative to NAD83 (Zone 21). Scale can be inferred from coordinate annotations.

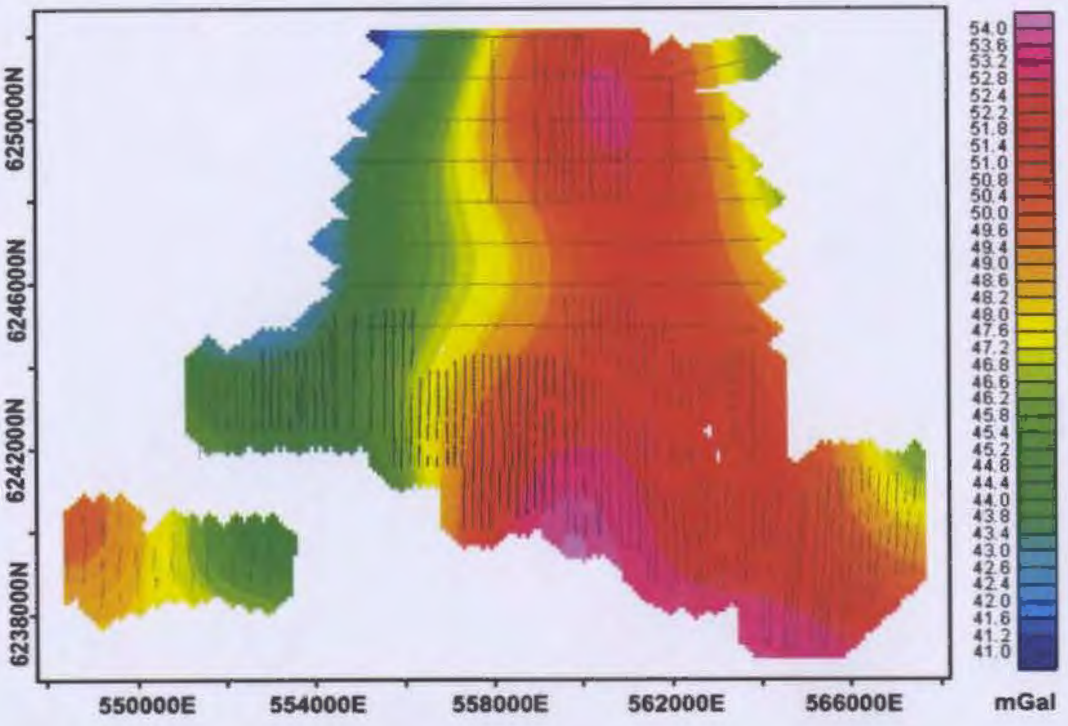

Figure 2.11: A map illustrating gravity wavelengths greater than 5km. Coordinates are in UTM meters relative to NAD83 (Zone 21). Scale can be inferred from coordinate annotations.

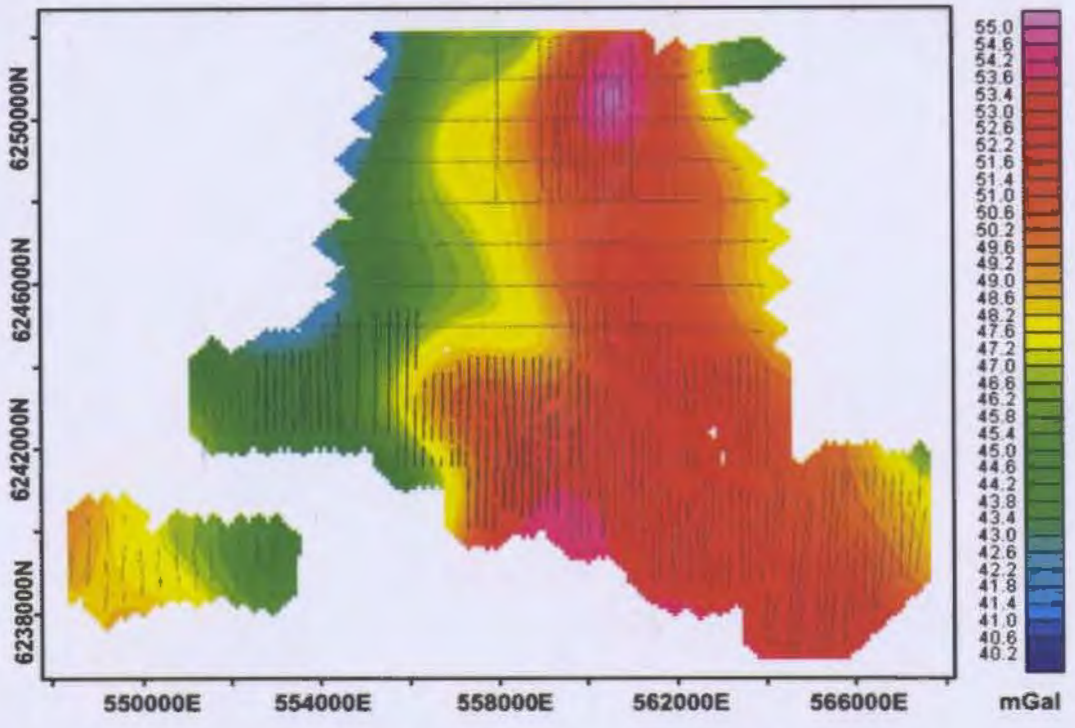

Figure 2.12: A map illustrating gravity wavelengths greater than 3km. Coordinates are in UTM meters relative to NAD83 (Zone 21). Scale can be inferred from coordinate annotations.

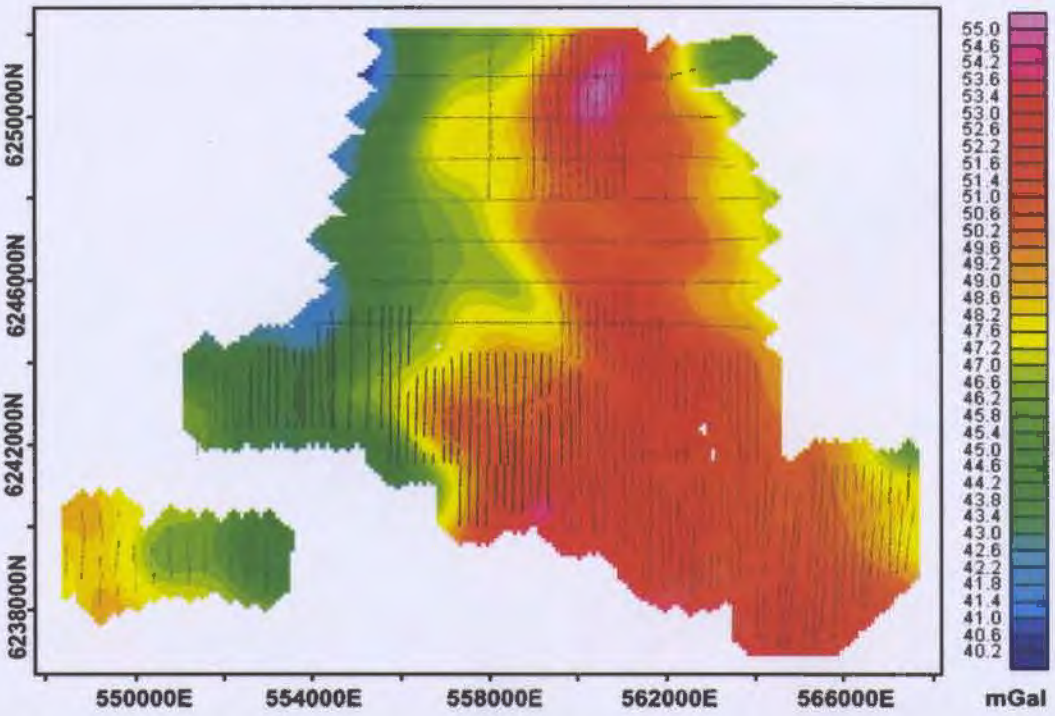

Figure 2.13: A map illustrating gravity wavelengths greater than 2km. Coordinates are in UTM meters relative to NAD83 (Zone 21). Scale can be inferred from coordinate annotations.

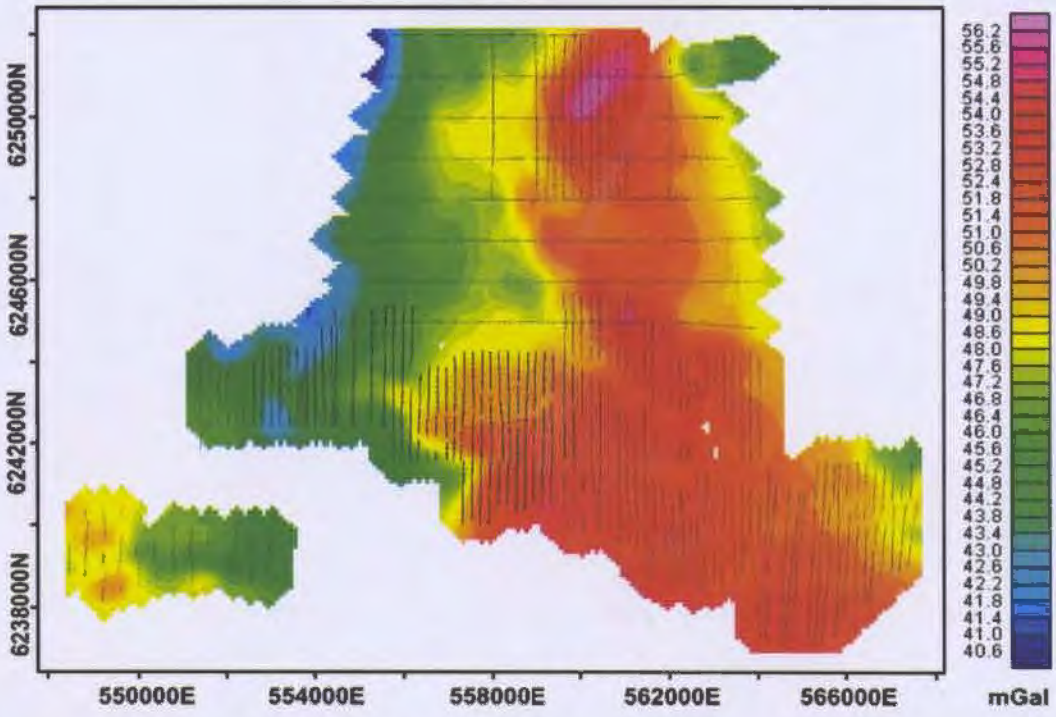

Figure 2.14: A map illustrating gravity wavelengths greater than 0.75km. Coordinates are in UTM meters relative to NAD83 (Zone 21). Scale can be inferred from coordinate annotations.

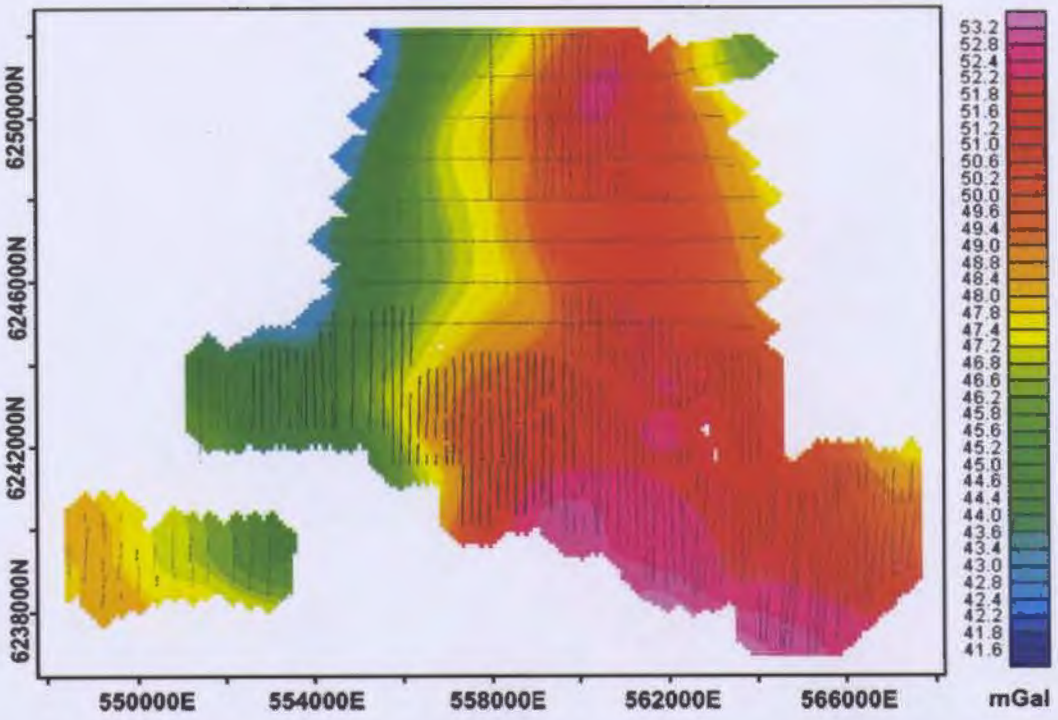

Figure 2.15: A map illustrating the gravity field upward continued 0.5km. Coordinates are in UTM meters relative to NAD83 (Zone 21). Scale can be inferred from coordinate annotations.

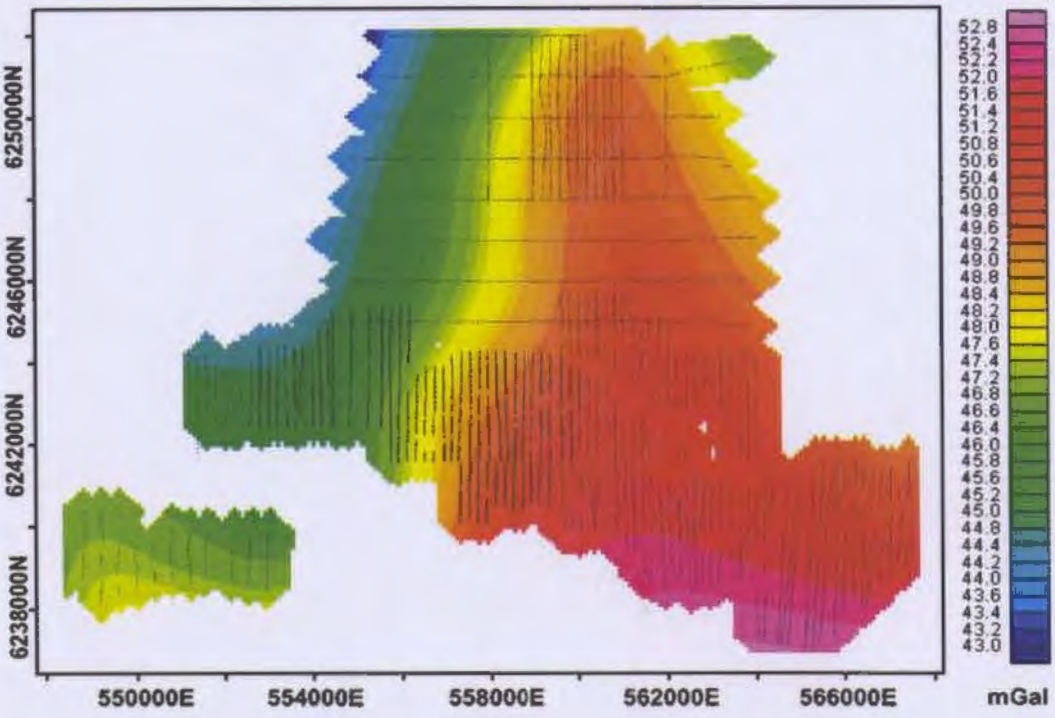

Figure 2.16: A map illustrating the gravity field upward continued 1.5km. Coordinates are in UTM meters relative to NAD83 (Zone 21). Scale can be inferred from coordinate annotations.

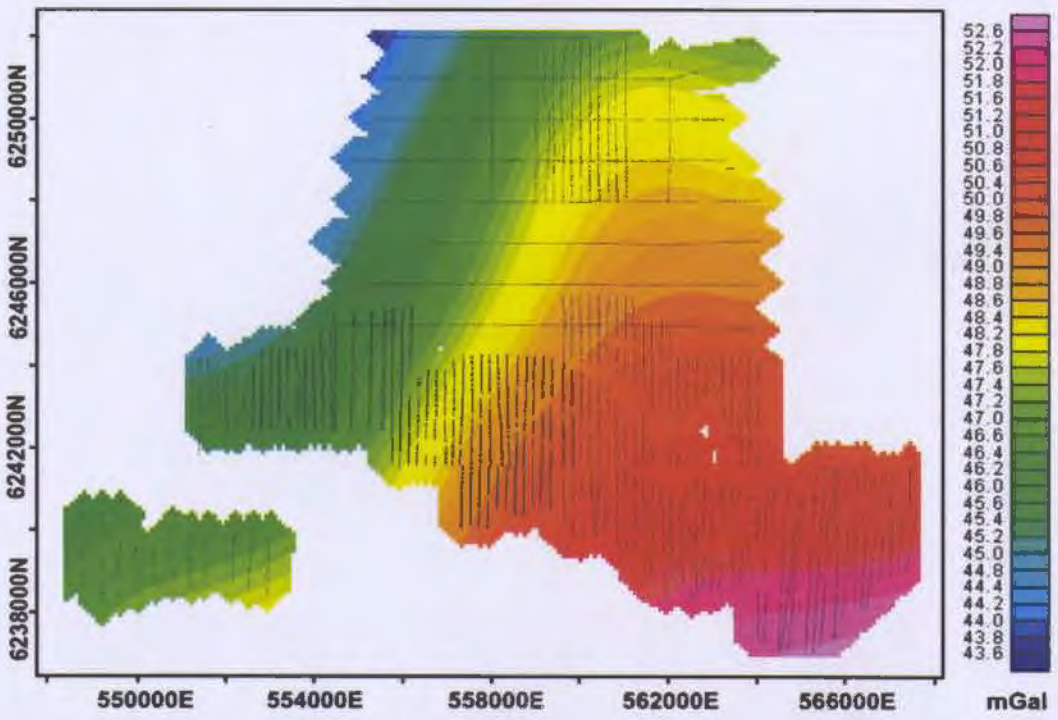

Figure 2.17: A map illustrating the gravity field upward continued 3km. Coordinates are in UTM meters relative to NAD83 (Zone 21). Scale can be inferred from coordinate annotations.

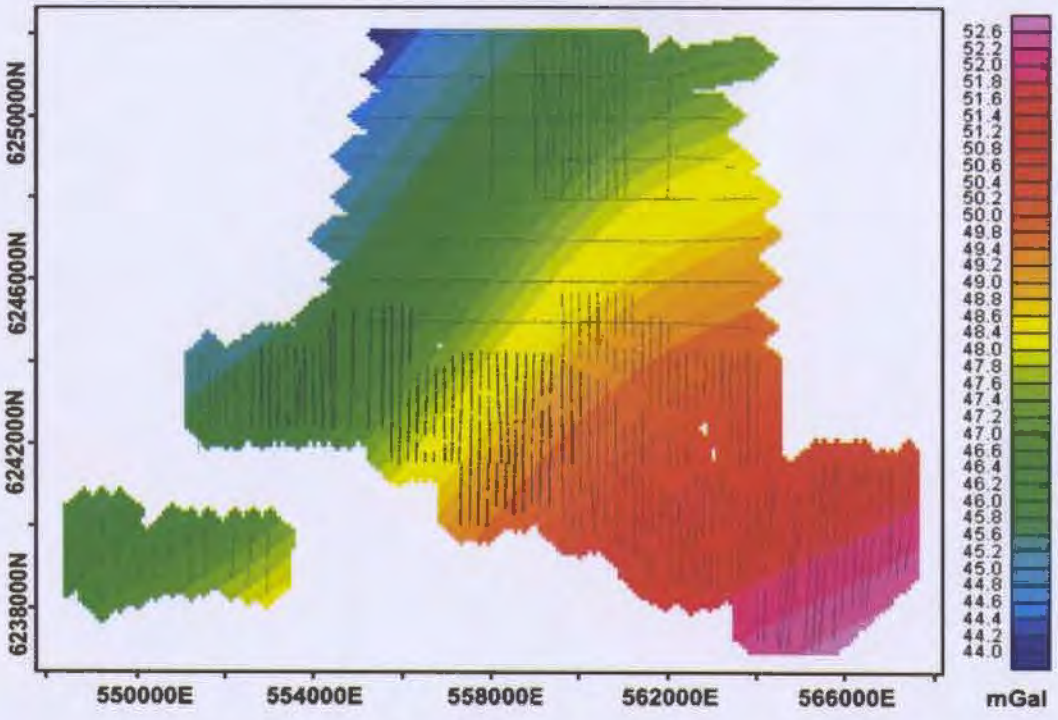

Figure 2.18: A map illustrating the gravity field upward continued 5km. Coordinates are in UTM meters relative to NAD83 (Zone 21). Scale can be inferred from coordinate annotations.

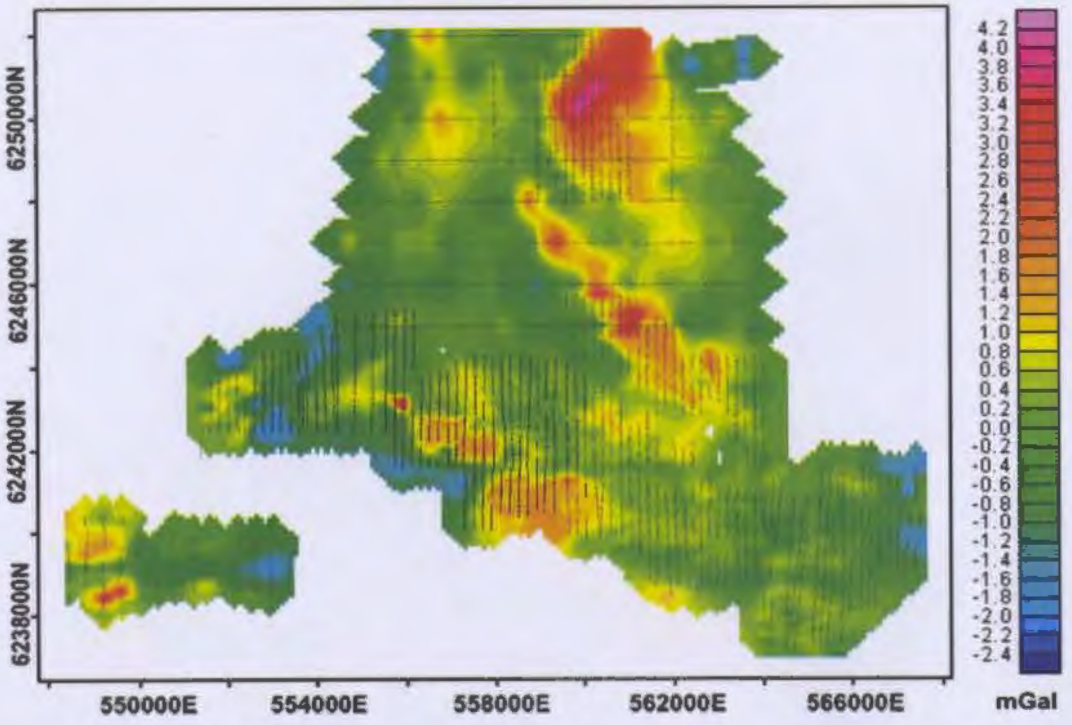

Figure 2.19: A map illustrating the residual gravity field calculated by subtracting Figure 2.15 from Figure 2.2 (raw data – upward continued 0.5km). Coordinates are in UTM meters relative to NAD83 (Zone 21). Scale can be inferred from coordinate annotations.

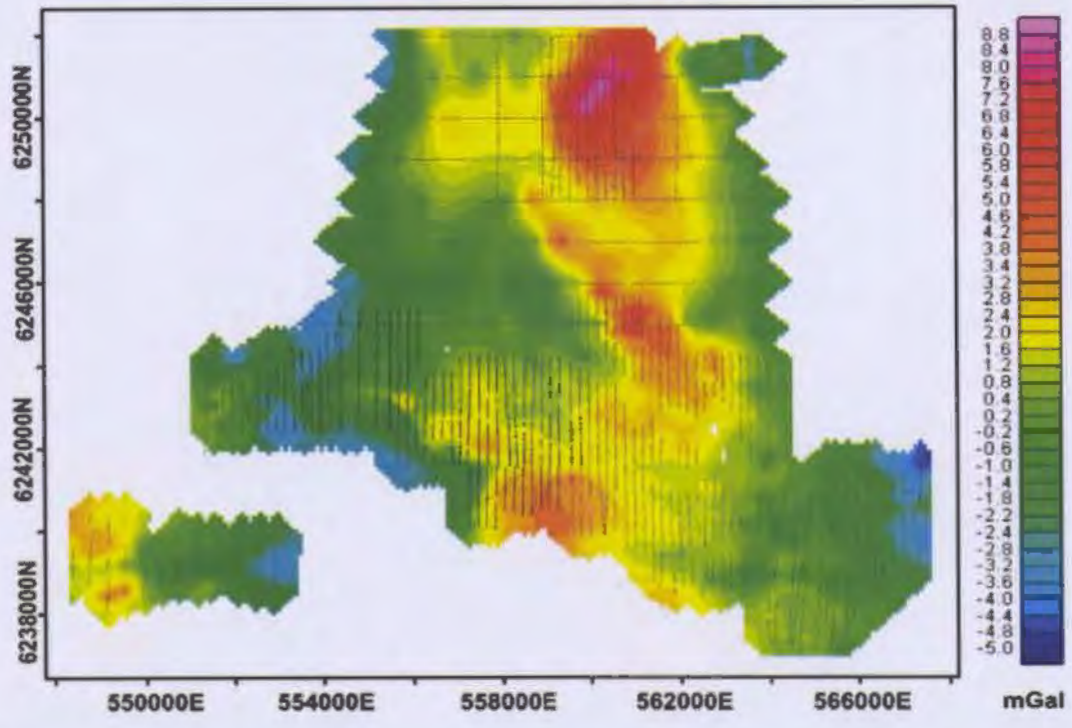

Figure 2.20: A map illustrating the residual gravity field calculated by subtracting Figure 2.17 from Figure 2.2 (raw data – upward continued 3km). Coordinates are in UTM meters relative to NAD83 (Zone 21). Scale can be inferred from coordinate annotations.

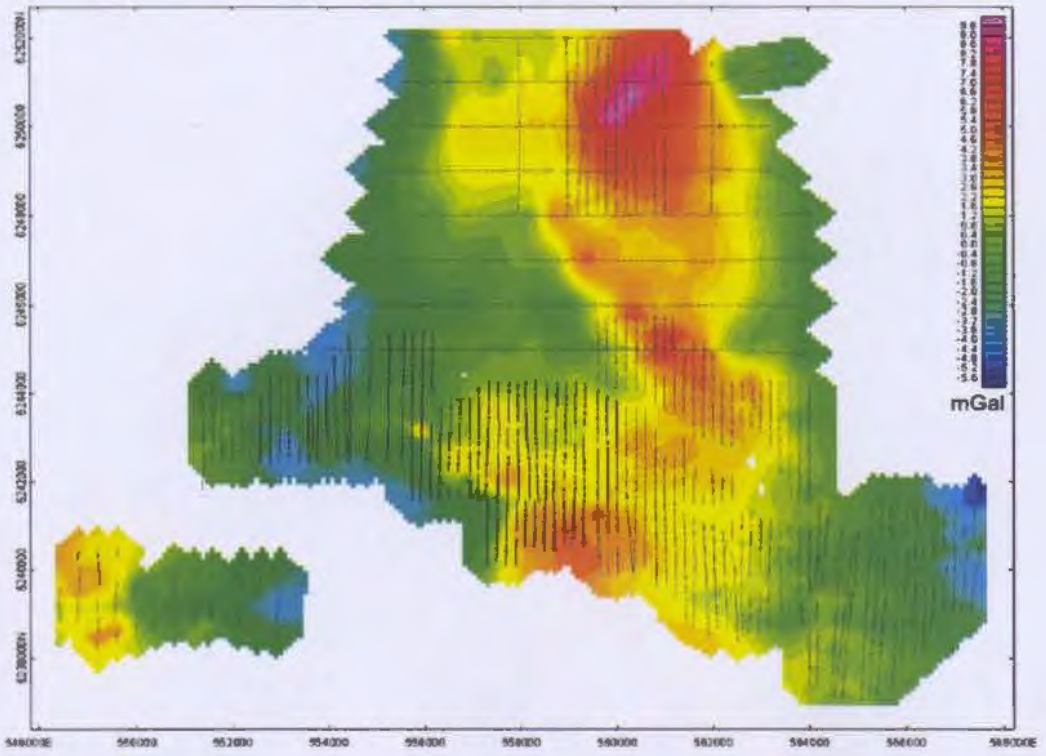

Figure 2.21: A map illustrating the residual gravity field calculated by subtracting Figure 2.18 from Figure 2.2(raw data – upward continued 5km). Coordinates are in UTM meters relative to NAD83 (Zone 21). Scale can be inferred from coordinate annotations.

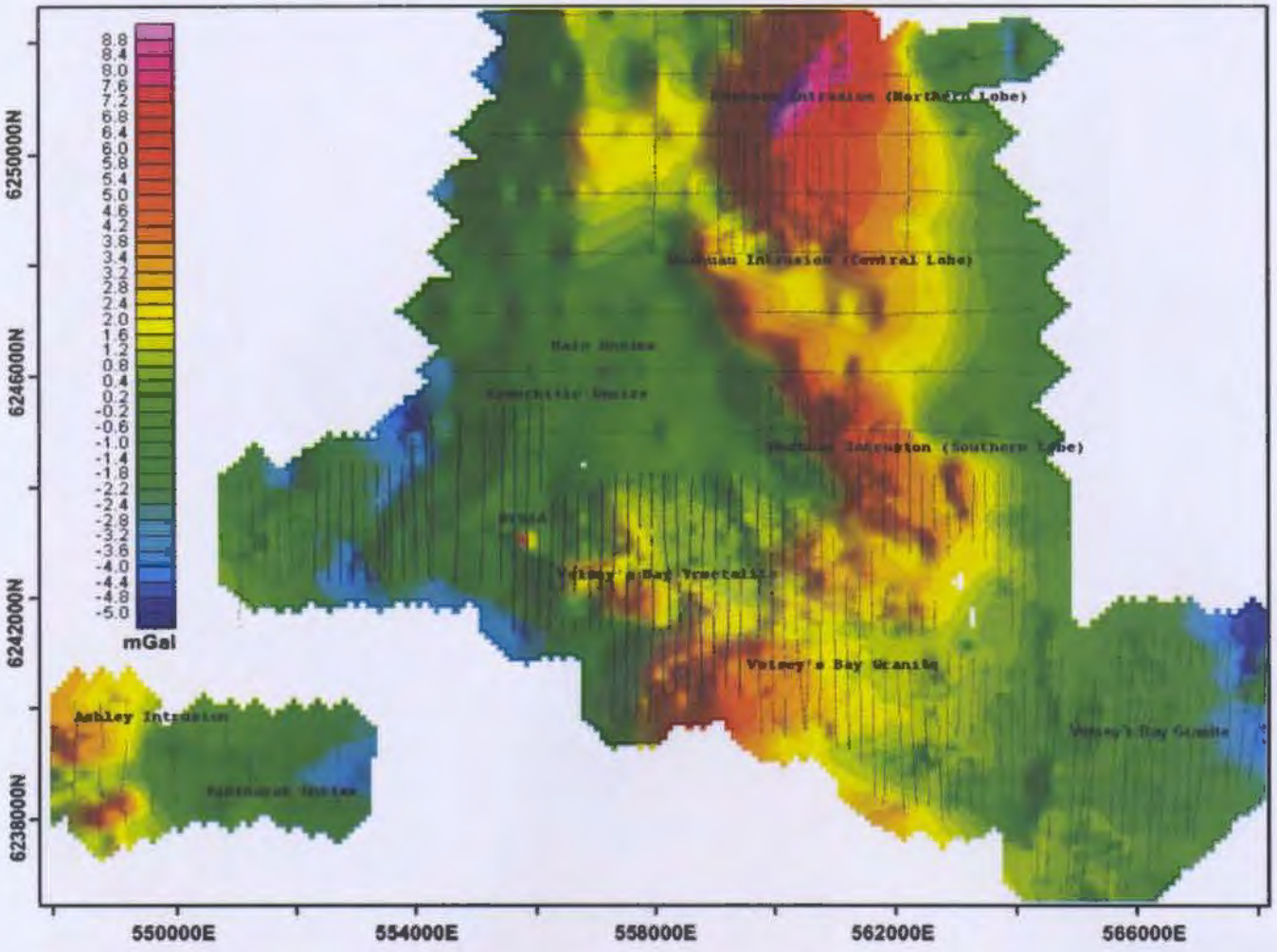

Figure 2.22: A shaded relief map illustrating the residual field shown in Figure 2.20 (raw data – upward continued 3km). Major geological units corresponding to Figure 2.1 are shown in black. Coordinates are in UTM meters relative to NAD83 (Zone 21). Scale can be inferred from coordinate annotations.

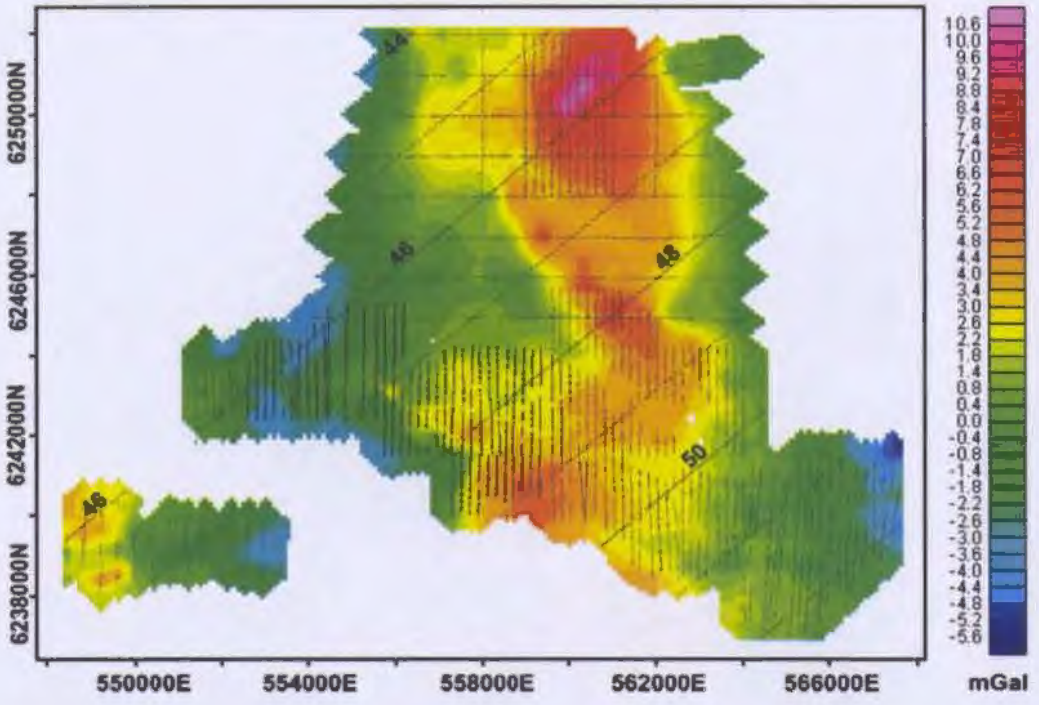

Figure 2.23: A map illustrating the residual gravity field calculated by subtracting a 1st order polynomial surface (2 mGal contours) using all data points. Coordinates are in UTM meters relative to NAD83 (Zone 21). Scale can be inferred from coordinate annotations.

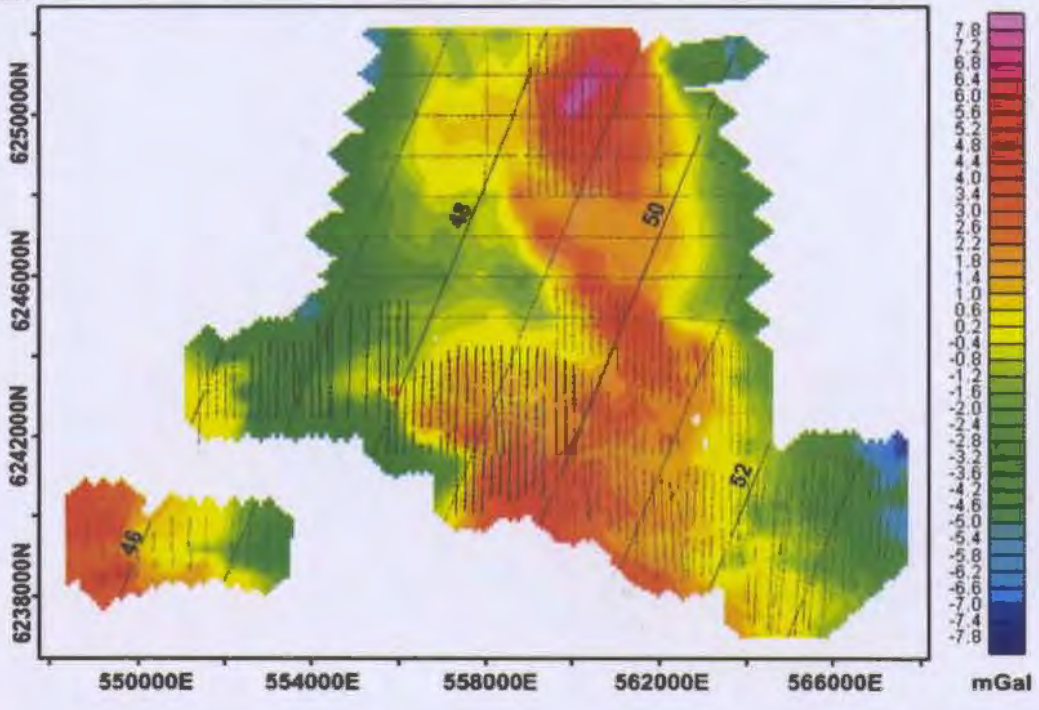

Figure 2.24: A map illustrating the residual gravity field calculated by subtracting a 1st order polynomial surface (2 mGal contours) using only edge points. Coordinates are in UTM meters relative to NAD83 (Zone 21). Scale can be inferred from coordinate annotations.

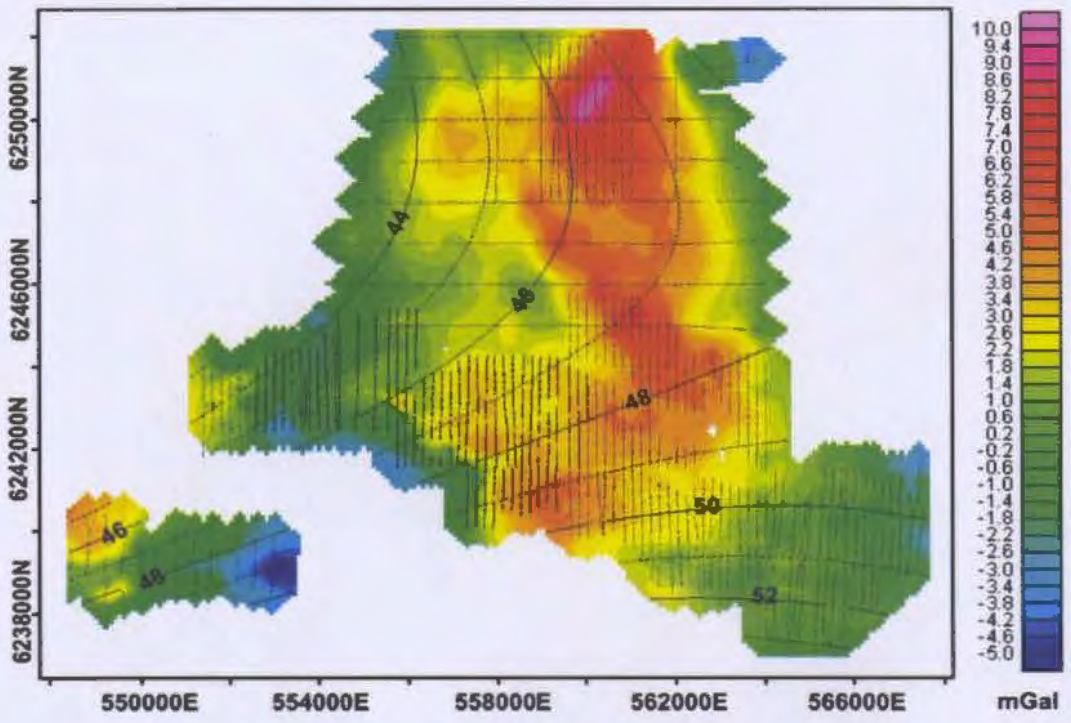

Figure 2.25: A map illustrating the residual gravity field calculated by subtracting a 2nd order polynomial surface (2 mGal contours) using only edge points. Coordinates are in UTM meters relative to NAD83 (Zone 21). Scale can be inferred from coordinate annotations.

Chapter 3: Creation of the Geocellular Model

3.1 Introduction

Placing an irregularly spaced three-dimensional dataset into a regularly spaced orthogonal grid is a common processing technique used to manipulate and visualize geophysical data. This chapter is simply a three-dimensional analog of section 2.4. In this study, the objective is to create a geocellular model that will be used as an initial and/or reference model during the inversion process. Many geostatistical techniques have been developed to determine the optimum estimation of block grades derived from drilling programs. These techniques are designed to model the spatial relationships that exist in a geological dataset. Measuring the spatial continuity of a dataset provides valuable information about the nature of the geological property under investigation. Measuring the spatial continuity of density will reveal information about the distribution of ore throughout the Voisey's Bay deposit. The first section in this chapter will examine the density data provided by VBNC. The second section will examine the spatial variability of the density data through variogram analysis. After quantifying the spatial variability through a series of variogram models, the final section will discuss the generation of a three-dimensional density model using Kriging.

3.2 Density Data

The density data used in this study was calculated from three conditional equations derived by VBNC from the regression analysis of geochemical data. The dataset includes samples from the Reid Brook zone, Discovery Hill zone, Mini-Ovoid, Ovoid and Eastern Deeps. The three empirical equations used to calculate the specific gravity (SG) values are given by:

If Fe (%) < 20 then $SG = 2.6079 + 0.0373 \times Fe\ (\%) - 0.011 \times S\ (\%)$ [3.1]

If Fe (%) ≥ 20 and < 51 then $SG = 2.493 + 0.0125 \times Cu\ (\%) + 0.0340 \times Fe\ (\%)$ [3.2]

If Fe (%) ≥ 51 then $SG = 3.0282 + 0.009 \times Cu\ (\%) + 0.0332 * Ni\ (\%) + 0.0286 \times Fe\ (\%) - 0.0037 \times S\ (\%)$ [3.3]

where Fe (%), S (%), Cu (%) are the assay percentages of iron, sulphur, and copper of selected borehole samples. VBNC were unwilling to provide the particulars of how the equations were derived. Every effort was made to obtain rock samples in order to test the accuracy of the formulated equations; however, ultimately no drill core samples were available.

The dataset provided by VBNC included the drill log name, distance of sample from the drill collar, pseudo-easting, pseudo-northing, elevation and calculated density value. The absolute coordinates for the drill log data was obtained by adding 500000 and 6400000 to the easting and northing of the drill log dataset. In addition, the vertical component was adjusted by subtracting 5000 from the drill log elevations. These corrections are necessary since the models generated using the drill log dataset will be incorporated into the inversion process as reference and/or initial models, and therefore must have absolute coordinates.

A detailed analysis of the specific gravity values for the given drill logs indicates that some of the values do not correspond properly to the assigned rock type. These improperly assigned values are commonly found at boundaries along the drill path. Figure 3.1 illustrates the specific gravity values along diamond drill hole VB95027. This drill log contains four boundaries (highlighted in red) where two very different rock samples are assigned the same specific gravity value. As an example, the contact between the massive sulphide unit (MASU) and the mafic dyke (MFDK) lies approximately 37m to 38m below the drill collar. At this location the MASU and MFDK rock units are assigned the same specific gravity value of 4.23 g/cc. Assigning a specific gravity value of 4.23 g/cc for a mafic rock is not realistic since all of the other MFDK measurements lie between 2.88 g/cc to 2.89 g/cc. A second example ean be shown at the contact between the troctolite-gneiss having 15-40% massive sulphide (TGM4) and enderbitic gneiss (ENGN) located at a depth between 62.8m and 63.5m below the drill collar. At this location both rock types are assigned a specific gravity value of 3.28 g/cc. This value is acceptable for the TGM4 unit, however is unaeceptable for the ENGN unit. All the specific gravity values below the contact for the ENGN have values that lie between 2.75 g/cc and 2.78 g/cc.

In order to develop a database that contains the statistical attributes of each rock type only, all of the samples that have been assigned an incorrect specific gravity value must be removed from the dataset. This was accomplished by removing all of the data values that contain a similar specific gravity value for two unlike rock units located at a geological contact. Of the 51436 data points contained in the original dataset, 5378 data points were removed. The mean, standard deviation and variance were calculated for

each rock type using the edited dataset. The results are summarized in Appendix A. Removing the questionable values has little effect on the overall mean values due to the large number of data points. However, a noticeable difference is observed in the standard deviation and range. As an example, the MASU originally had a mean and standard deviation of 4.54 g/cc and 0.29 g/cc. Removing the uncertain values located near contacts results in a mean and standard deviation of 4.61 g/cc and 0.11 g/cc. The edited dataset will be used for future computation, processing and interpretation.

A detailed examination of the specific gravity dataset revealed that there were 251 repeated density calculations derived from the geochemical percentages tabulated in Appendix B. From the repeated measurements the specific gravity values were recomputed and compared to the original values. Taking the difference between the original and repeated value at each of the 251 locations will provide information on the repeatability of the specific gravity calculation. The mean and standard deviation of the differences were determined to be approximately 0.002 g/cc and 0.05 g/cc respectively. A mean close to zero indicates that there is no bias in the repeated values. The standard deviation is a measure of the degree of dispersion of the data from the mean value. In this case, the standard deviation of the repeated values indicates that there is an average variation of 0.05 g/cc from the mean. It is important to note that the mean calculated is not a direct measure of the uncertainty of equations [3.1], [3.2] and [3.3]. The standard deviation calculated from the repeated measurements indicates that the regression method developed by VBNC is able to repeat calculated density values to 0.05 g/cc, which can be considered a measure of the uncertainty within the log interval. Since all data provided

by VBNC was rounded to the nearest 0.01 g/cc, all subsequent estimates will be rounded to the nearest 0.01 g/cc.

A detailed examination of the calculated average densities (Appendix A) reveals a general correlation between the amount of sulphides and mean density. Rock types that have a mean density below 3.2 g/cc are commonly associated with rocks that contain less than 15% sulphides. Rocks that have a mean density between 3.2 g/cc and 4.6 g/cc are observed to correlate with rocks containing approximately 40% to 75% sulphides. Finally, rocks containing a mean density greater than 4.6 g/cc are indicative of massive sulphides. Although these are very general observations, they may be used to relate subsurface density distributions inferred from inversion of gravity data with specific rock type, and degree of mineralization.

3.3 Variogram Modeling

This section will briefly introduce geostatistical methods used to quantitatively measure the spatial relationships contained in the density dataset. These statistical methods will then be applied to the drill log data obtained from the Ovoid and Mini-Ovoid and surrounding host rock.

3.3.1 Theoretical Background:

Spatial association is an inherent feature observed in most geological environments. In a sulphide deposit, one would expect to see high density ore surrounded by a host rock of lower density. Variogram modeling is based on the simple notion that samples closer together contain more similarities than samples located further apart. By

measuring the "similarity" in various directions, directional weights can be integrated into the interpolation process. The spatial correlation techniques were originally developed in order to determine a "linear unbiased estimator" applicable to a gold deposit in South Africa (Krige, 1976).

The basic variogram formula was designed to calculate the spatial correlation of a distribution of points, also known as a pointset. The variogram (2γ) of regularly spaced pointset is calculated by (Pan and Harris, 2000),

$$2\gamma(\vec{k}_{ij}) = \frac{1}{N(\vec{k}_{ij})}\sum_{i=1}^{n}[(Z(\vec{x}) - Z(\vec{x}+\vec{k}_{ij})]^2 \qquad [3.4]$$

where,

$$\vec{k}_{ij} = \vec{x}_i - \vec{x}_j = (u_i - u_j, v_i - v_j, w_i - w_j) \qquad [3.5]$$

and N is the number of sample pairs separated by the vector **k**. The separation distance used in the variogram calculation is commonly referred as the *lag* distance. One downside of Equation 3.4 is that the sample locations must be collected on a regularly spaced grid. This is not a practical assumption when dealing with geophysical surveys or data collected in drill holes having variable spacings. In order to calculate a variogram on an irregularly spaced grid, the above equation must be modified to allow tolerances within the lag distance and angle. This is accomplished in one-, two- and three-dimensions by counting pairs within a line segment, area or volume. In two-dimensions, a typical approach is to define a wedge illustrated in Figure 3.2A. Allowing a separation

vector (**k**) to vary over a tolerance distance and tolerance angle, a point X_1 will be paired with any point within the shaded region depicted in Figure 3.2A. Larger tolerance angles increase the amount of smoothing that occurs in the variogram computation. In most cases, the data points are transformed into a polar-coordinate gird (Figure 3.3A). In a two-dimensional grid, the separation distance (k) and polar angle (Θ_p) are represented by

$$k = \sqrt{(x_2 - x_1)^2 - (y_2 - y_1)^2} \qquad [3.6]$$

and,

$$\theta_p = \arctan\left(\frac{y_2 - y_1}{x_2 - x_1}\right). \qquad [3.7]$$

In three-dimensions, the volume is depicted by rotating the wedge along the separation vector illustrated in Figure 3.2B. Any point lying within this volume shown in Figure 3.2B is paired with the point located at X_1. The modified formula may be expressed as (after Pan and Harris, 2000),

$$2\gamma(\vec{k}_{ij}) = \frac{1}{N(\vec{k})} \sum_{(i,j)\vec{k}_{ij} \approx \vec{k}}^{n} [(Z(\vec{x}_i) - Z(\vec{x}_j)]^2 \qquad [3.8]$$

where, x_i and x_j are two sample locations separated by a vector **k.**

In order to develop a variogram model, the data is displayed in a series of two-dimensional plots. These two dimensional plots represent a slice of the polar-coordinate system. A hypothetical variogram is calculated along an azimuth of 45° with a 15° tolerance, shown in Figure 3.3A. Three major components contained in a typical

variogram are the sill, range, and nugget depicted in Figure 3.3B. The range is the maximum distance in which a given dataset can be spatially correlated. The major range is typically chosen along the direction of maximum correlation. The maximum correlation is represented by a linear increase with increasing lag. At the point which no further correlation is visible, the range plateaus at a constant variance and is then referred as the sill. The nugget effect is a value that reflects the lower limit of the range, meaning the spatial variations that occur at distances closer than the sample spacing. Simple variogram models (Figure 3.3B) are commonly used to model the complex spatial variability found in practical datasets. The four most common models are the spherical, exponential, Gaussian and linear models. The choice of which model to use is highly dependent on the nature of the dataset. As an example, density is a property that has small range in possible values. As a result, we would expect a slight variation at small lag distances. Spherical models are commonly used since they behave linearly at small separation distances and begin to flatten out as the separation distance increases.

3.3.2 Application: Ovoid and Mini-Ovoid

The spatial correlation techniques discussed in the previous section were applied to the drill logs used in this study. The density dataset was reduced to those logs that lie between the eastings and northings of 555297.5E to 555617.5E and 6242847.5N to 6243457.5N respectively. This region focuses in the area surrounding the Ovoid and Mini-Ovoid. The density logs were further subdivided based on rock type. In the region of the Ovoid and Mini-Ovoid, the main geological units are the ENGN, TR, MASU and

Overburden (OB). Although there are other geological units present in the selected area, they are insignificant when compared to the four main geological units. Due to the limited number of data points, and spatial variability of the ENGN samples, a constant density was assigned to the ENGN unit. The density value chosen is examined in a later section. In addition, no density measurements of the OB unit were provided by VBNC, therefore a constant density was also applied. As a result, no variogram models were required for the ENGN and OB units. A vertical and a three-dimensional variogram were calculated for the TR and MASU units. Vertical variograms were calculated using an incremental lag distance of 2m while three-dimensional variograms were calculated using a lag distance of 10m. The three-dimensional variograms were orientated at 0°, 30°, 45°, 60°, 90°, 120° and 135° with a tolerance of 30°. In addition to those parameters, the variograms were calculated at a dip of 15° with a tolerance of 30°.

3.3.2.1 Troctolite (TR)

The vertical and three-dimensional variograms calculated for the troctolite are illustrated in Figure 3.4. The three-dimensional variograms shown in Figure 3.4 clearly demonstrate that the density data is complex and non-stationary. The spatial variability in the vertical direction (Figure 3.4A) suggests a range of 20m, along with a nugget 0.2 and a sill approaching 0.8. The three-dimensional distribution reveals a high spatial correlation along an azimuth of 120° (Figure 3.4B) with an estimated sill of 1.0 and a nugget of 0.25. A high spatial correlation is represented by a linear increase with

increasing lag. The major range correlating along this direction was estimated to be approximately 100m. The minor range calculated along an azimuth of 45° was determined to be approximately 35m while the vertical range was estimated to be 20m. The nugget estimate observed for the three-dimensional variogram is greater than the nugget observed for the vertical variogram. The discrepancy in nugget values are a result of the variation is data distribution. The cyclicity observed in many of the three-dimensional variogram plots is most likely due to the limited data in the horizontal direction. In addition, the vertical variogram reaches a lower sill which is possibly caused by the additional between log variances. The model variogram (VM-TR01) estimated from the experimental variograms has a major, minor and vertical range of 110m, 45m, and 20m respectively. The model variogram will be incorporated into the Kriging process discussed in a later section.

3.3.2.2 Massive Sulphide (MASU)

The vertical and three-dimensional variograms calculated for the MASU unit is illustrated in Figure 3.5. The vertical distribution (Figure 3.5A) suggests a maximum range of 45m, along with a nugget and still estimated to be 0.1 and 1.0 respectively. A secondary, less dominant, feature is captured in the vertical variogram at a lag of 25m. This may be associated with internal variations within the Ovoid. The three-dimensional variogram illustrated in Figure 3.5B suggests a dominant trend at 135° with a maximum range of 100m. The minor range orientated at 45° was estimated to be 70m. The cyclic

behaviour is most prevalent in the direction of data sampling orientated at 90°. The nugget effect was difficult to estimate due to the lack of data points in the horizontal direction. The model variogram (VM-MASU01) designed from the experimental variograms was orientated at 135°, along the direction of maximum correlation, with a major, minor and vertical range of 100m, 70m, and 45m respectively. The nugget was estimated to be 0.1.

3.4 Kriging

The following section will combine the information gathered from the spatial correlation techniques and incorporate the spatial trends into a three-dimensional gridding algorithm. The section will be subdivided into two subsections. The first subsection will provide a brief introduction into the fundamental concepts of Kriging. The second will include a discussion on the construction of the geocellular model, using geological information provided by VBNC.

3.4.1 Theoretical Background:

Kriging is an interpolation method that incorporates spatial structure into the interpolation algorithm. Based on a variogram model, optimum weights are assigned to known values in order to calculate unknown values. In geostastics, Kriging is commonly referred as a method that determines "the best linear unbiased estimator" (B.L.U.E) of a point. Unbiased estimator means that a point estimated is neither overestimated nor

underestimated. The method simply minimises the variance of the error of the estimated point.

The fundamental idea of Kriging is to estimate a value Z(x) at a point (point kriging) using a series of weighted linear estimators (λ_i) defined by,

$$z(x) = \sum_{i=1}^{n} \lambda_i \bullet Z(x_i) \qquad [3.9]$$

where $Z(x_i)$ are the known data values. Another common from of kriging is to estimate the value of a block instead of a point, known as block kriging. Point kriging is straightforward since it only involves some distance computation. Block kriging requires two calculations, the covariance of a point and the covariance of a block. Since the derivation of the solution is beyond the scope of this study, and found in most geostatistical textbooks (Stein, 1999; Kitanidis, 1999; Pan and Harris, 2000 etc.), the solution in matrix form is defined as (Pan and Harris, 2000)

$$\begin{pmatrix} C & 1 \\ 1^T & 0 \end{pmatrix} \begin{pmatrix} \lambda \\ \mu \end{pmatrix} = \begin{pmatrix} C_0 \\ 1 \end{pmatrix} \qquad [3.10]$$

where

$$C = \begin{pmatrix} c_{11} & \cdots & c_{1n} \\ \vdots & \ddots & \vdots \\ c_{m1} & \cdots & c_{mn} \end{pmatrix} C_0 = \begin{pmatrix} c_{10} \\ c_{20} \\ \vdots \\ c_{n0} \end{pmatrix} \qquad [3.11]$$

and $\mathbf{C_0}$ is a vector of point sample covariances, **C** is the sample-sample covariances, μ is a Lagrange multiplier, and **1** is a column vector containing n ones. The variogram measures the sample-point and sample-sample covariances leaving the directional weights (λ), and the Lagrange multiplier to be solved by a process of Gaussian elimination (Press, 1989).

The two most common forms of kriging are ordinary kriging and simple kriging. Ordinary kriging is more accurate in the interpolation process than simple kriging since it only uses the averages of the points next to the interpolation point. Simple kriging uses the global average, resulting in a smoother distribution of interpolated points. Another fundamental difference between ordinary and simple Kriging is the way directional weights are managed. Ordinary Kriging makes use of the unbiasedness condition, meaning that all directional weights sum to one. Simple Kriging does not constrain the weights and works with the residual from of the mean (data values minus the mean).

A useful by product of Kriging is the ability to use the variogram to compute the expected error of estimation at each interpolation point. This is possible since the error of estimation is a function of distance from the surrounding scatter points. The Kriging coefficients are obtained by minimizing the estimation variance. Replacing the unknown weights with estimated values, information about the precision of the Kriging process can be determined. The variance σ^2_v is calculated by the equation (Stein, 1999)

$$\sigma_v^2 = Sill - \mu - \sum_{i=1}^{n} \lambda_i C_i . \qquad [3.12]$$

3.4.2 Geocellular Model: Ovoid and Mini-Ovoid

A geocellular model of the Ovoid and Mini-Ovoid was developed using the Kriging procedure described in the previous section. This subsection will define the cellular mesh and describe the procedures used to develop cell regions based on geological information provided by VBNC. Once the cell regions are defined, the Kriging process was applied to the density data.

3.4.2.1 Cellular Mesh:

The top southwest corner of the mesh (MESH01) was placed at UTM's 555297.5E, 6242847.5N and at an elevation of 172.5 meters above sea level as illustrated in Figure 3.6. The top of the mesh was positioned above topography to ensure all topographic effects are included in the geocellular model. The mesh extends 610 meters north, 870 meters east and 540 meters vertically. The cell dimensions chosen were 10 meters by 10 meters in the horizontal direction, and 5 meters in the vertical direction. These dimensions were chosen based on the distribution of drill log data. Generally, the drill logs are separated by 50 meters in the north-south and east-west directions, with samples collected at 1 metre intervals in the vertical or sub vertical directions. The total number of cells in the mesh is 286,578. Once the cellular mesh is populated with specific densities, the cell size may be reduced by simply dividing the rectangular cell into two equal cubes with a length of 5 meters. This method is beneficial since it does not change the statistical attributes of the data.

3.4.2.2 Geological Regions:

The first stage in the modelling process was to segregate the geocellular grid based on known geological information. VBNC provided three wireframes containing the outline of the massive sulphide body (Figure 3.7), along with the surrounding mineralized and un-mineralized troctolite envelopes. The mineralized and un-mineralized troctolite (Figure 3.7) will be combined into one region due to the limited number of data points collected. In addition to the wireframes, topography and bedrock files were also supplied by VBNC and are illustrated in Figure 3.8A. Overburden thicknesses were calculated by taking the difference in elevation between the topographic and bedrock surface. The resulting values were then projected to the topographic surface representing the overburden thickness as shown in Figure 3.8B. Four regions representing the overburden, enderbitic gneiss, troctolite and massive sulphide zones were developed using a multiple stage process. The process has 7 sequential steps summarized below;

1. Generate a region (RG01) that contains all cells that lie in contact with or below the topography layer, and above or in contact with the bedrock layer. This region contains all cells classified as OB unit (Figure 3.9B).
2. Generate a region (RG02) that contains all cells that lie below the OB layer.
3. Generate a region (RG03) that contains all cells that lie within or in contact with the troctolite wireframe.
4. Generate a region (RG04) that contains all cells that lie within or in contact with the massive sulphide wireframe. The new region now contains all cells classified as the MASU unit (Figure 3.9B).

5. Subtract RG01 from RG02, RG03 and RG04. This subtraction will remove all overlapping cells
6. Generate a region (RG05) by subtracting RG03 from RG02. The new region now contains all cells classified as the ENGN unit (Figure 3.9B).
7. Generate a region (RG06) by subtracting RG04 from RG03. The new region now contains all cells classified as the TR unit (Figure 3.9B).

3.4.3 Model Population: Kriging:

The estimated values will be placed at the centre of each cell contained within the cellular mesh defined in Section 3.4.2.2. To ensure the best possible estimate at an un-sampled location, the spatial continuity will be incorporated into the Kriging process via the variogram models generated in section 3.3.2. The variogram models will be paired with the appropriate geological region. Ordinary Kriging was the chosen Kriging method, since it accounts for spatial trends and local variations. Simple Kriging is commonly applied when no spatial trends are present in the data. If more than one sample is located inside a cell, only the average of the data points will be used. All cells in the overburden region were simply assigned a constant density of 1.92 g/cc (Telford et al,, 1990). The Kriging algorithm in Gocad was applied to the troctolite (RG06) and massive sulphide (RG04) regions using the appropriate variogram models VM-TR01 and VM-MASU01. Using the statistical capabilities in Gocad, it was determined that 677 density values are contained within the ENGN region (RG05), summarized in Figure 3.10A. The 677 density values have a mean density of 2.81 g/cc, which is similar to the overall mean density calculated from 2340 data points tabulated in Appendix A. This density value

was assigned to each cell in the ENGN region. The histogram distributions were also calculated for the density data points contained in the regions RG06 and RG04 regions illustrated in Figure 3.10B and Figure 3.10C respectively. The populated regions were then combined to construct a final block model DEN01 illustrated in Figure 3.11. Histogram distributions for the estimated densities are shown in Figure 3.12 and were compared to the VBNC borehole calculated densities summarized in Figure 3.10. The kriged MASU data has a lower global range compared to the calculated drill log data contained within the MASU region. The lower range is most likely due to smoothing which occurs when multiple drill log data points are contained within a cell. These localized variations are confined within each drill log and therefore have no lateral spatial continuity. The kriged TR data (Figure 3.12A) on the other hand contain a greater proportion of higher densities compared to the drill log data (Figure 3.10B). This observation may be explained by the existence of a mineralized halo surrounding the MASU region. The mineralized halo has a greater continuity laterally that vertically. As a result, cells connecting drill logs will be populated with higher densities, resulting in a greater proportion of higher densities. A series of horizontal slices displaying the high density variations observed within the Ovoid are illustrated in Figure 3.13, Figure 3.14, Figure 3.15, Figure 3.16 and Figure 3.17.

The variance model was built using a similar approach as the density model. The variance estimates determined from the Kriging process were combined into a single model illustrated in Figure 3.18. The variances are normalized such that the data has a variance range of 0.0 to 1.0. Due to the number of drill logs and inherent lateral continuity of the topographic and bedrock layers, a constant variance of 0.0 was assigned

to all cells contained within this region (RG01). The ENGN region (RG05) was assigned a constant variance of 1.0 due to the limited number of samples collected. The overall between-well variances of the TR region are slightly lower than the between-well variances observed in the MASU region as depicted in Figure 3.18. This is a result of the greater horizontal ranges in the TR variogram (VM_TR01) compared to the MASU variogram (VM_MASU01).

3.5 Results

The kriged density model (DEN01) illustrated in Figure 3.11 suggests that a significant density contrast exists between the ENGN and MASU regions. The average density of the TR and MASU regions were estimated to be approximately 3.18 g/cc and 4.63 g/cc (Figure 3.10). The Kriged density model suggests that there is a non-uniform density distribution within the Ovoid. At an elevation of 62.5m (Figure 3.13A), a high density region of approximately 4.80 g/cc is located at an easting and northing of 555825m and 6243250m. A second high density region is observed at an elevation of 52.5m (Figure 3.13B) located at an easting and nothing of 555825m and 6243100m. These high density areas have a maximum north-south and east-west extent of 100m and 150m respectively. The two anomalous regions merge at a elevation 32.5m (Figure 3.14B) extending to a elevation of 12.5m (Figure 3.15B) at UTM nothing and easting 6243150m and 555875m. The distribution of densities greater than 4.7 g/cc suggest channelling of high density sulphides within the Ovoid. These density variations do not follow classical gravitational settling models marked by a gradation of higher densities

toward the base of the chamber. The modelled distribution of densities provides further evidence that the emplacement of the Ovoid is a result of multiple waves of magma (Naldrett, 2004; Naldrett et al., 2000) through a complex conduit system (Evans-Lamswood et al, 2000; Evens-Lamswood, 1998).

Diamond Drill Hole: VB9527

Collar Location: 555781.8E 6443057.8N

Elevation: 31.8m

FROM	TO	ROCK	SG	FROM	TO	ROCK	SG
28.0	29.0	MASU	4.65	58.5	59.5	TGM2	2.95
29.0	30.0	MASU	4.59	59.5	60.0	TGM2	2.87
30.0	31.0	MASU	4.60	60.0	60.5	TGM2	2.87
31.0	32.0	MASU	4.60	60.5	61.5	TGM2	2.94
32.0	33.0	MASU	4.61	61.5	62.5	TGM2	3.09
33.0	34.0	MASU	4.63	62.5	62.8	TGM2	3.28
34.0	35.0	MASU	4.60	62.8	63.4	TGM4	3.28
35.0	36.0	MASU	4.59	63.4	63.5	ENGN	3.28
36.0	37.0	MASU	4.66	63.5	64.5	ENGN	2.78
37.0	37.7	MASU	4.23	64.5	65.5	ENGN	2.76
37.7	38.0	MFDK	4.23	65.5	66.0	ENGN	2.76
38.0	39.0	MFDK	2.89	66.0	66.5	ENGN	2.76
39.0	40.0	MFDK	2.88	66.5	67.5	ENGN	2.75
40.0	41.0	MFDK	2.88				
41.0	41.7	MFDK	3.17				
41.7	42.0	TR5	3.17				
42.0	43.0	TR5	3.65				
43.0	44.0	TR5	3.65				
44.0	45.0	TR5	3.59				
45.0	46.0	TR5	3.49				
46.0	47.0	TR5	3.46				
47.0	47.2	TR5	3.44				
47.2	48.0	TR4	3.44				
48.0	49.0	TR4	3.54				
49.0	50.0	TR4	3.43				
50.0	51.0	TR4	3.38				
51.0	52.0	TR4	3.36				
52.0	53.0	TR4	3.18				
53.0	54.0	TR4	3.28				
54.0	55.0	TR4	3.22				
55.0	55.6	TR4	3.10				
55.6	55.7	TR4	3.10				
55.7	56.5	TGM2	3.10				
56.5	57.5	TGM2	2.92				
57.5	58.5	TGM2	2.94				

Figure 3.1: Specific gravity measurements along diamond drill hole VB9027. Values highlighted in red indicate locations of contacts where specific gravity values are similar for adjacent rock types.

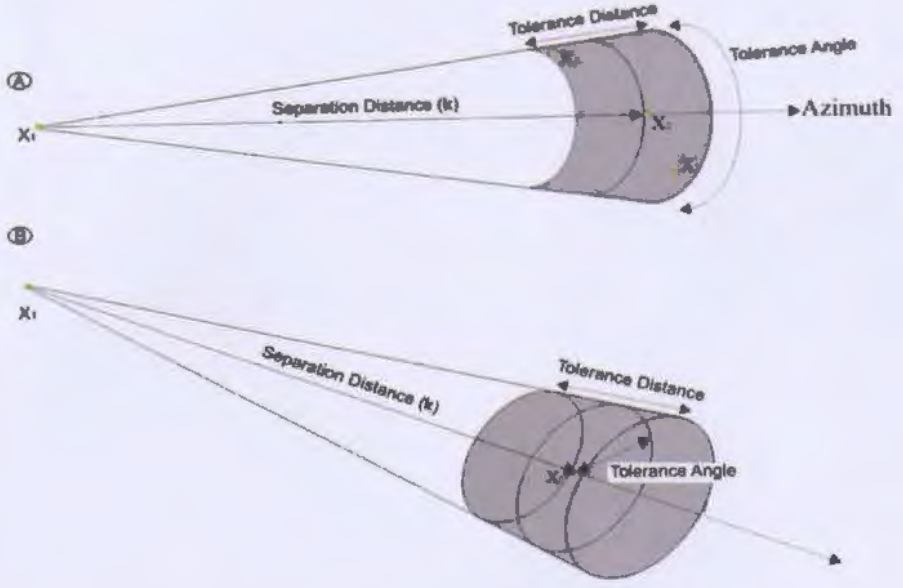

Figure 3.2: **A-** A wedge commonly used in two-dimensional variogram modelling. With the addition of tolerance angles and tolerance distances to a separation vector ***k***, a point X_1 will be paired with points X_2, X_3 and X_4. **B-** A three-dimensional variogram is calculated by revolving the wedge in **A**.

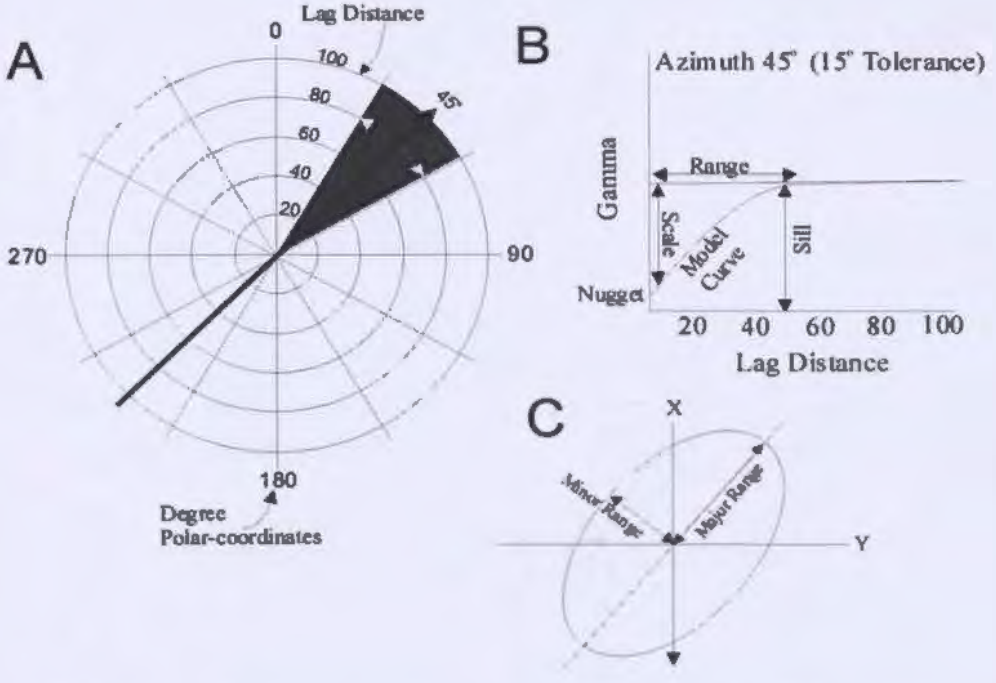

Figure 3.3: **A-** Polar coordinate system commonly used to reduce the total number of data points; **B-** Basic components of a variogram model; **C-** Variogram model with a major and minor range.

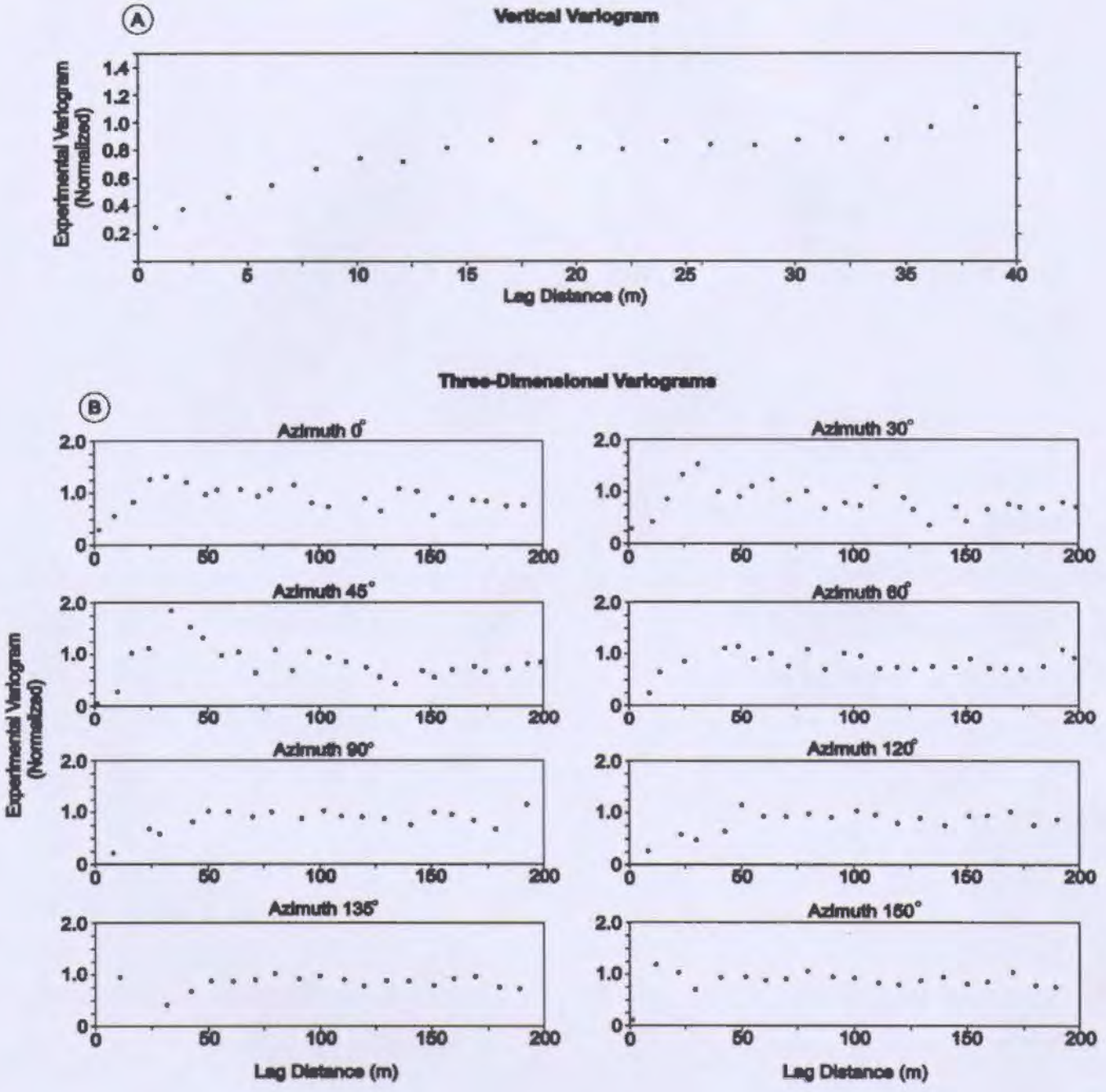

Figure 3.4: **A**- Vertical variogram calculated from the TR data using a lag unit distance of 2m. **B**- Three-dimensional variograms calculated from the TR data using a lag unit distance of 10m along an azimuth of 0°, 30°, 45°, 60°, 90°, 120°, 135° and 150° with a tolerance of 30°. The dip along each azimuth was 15° with a tolerance of 30°.

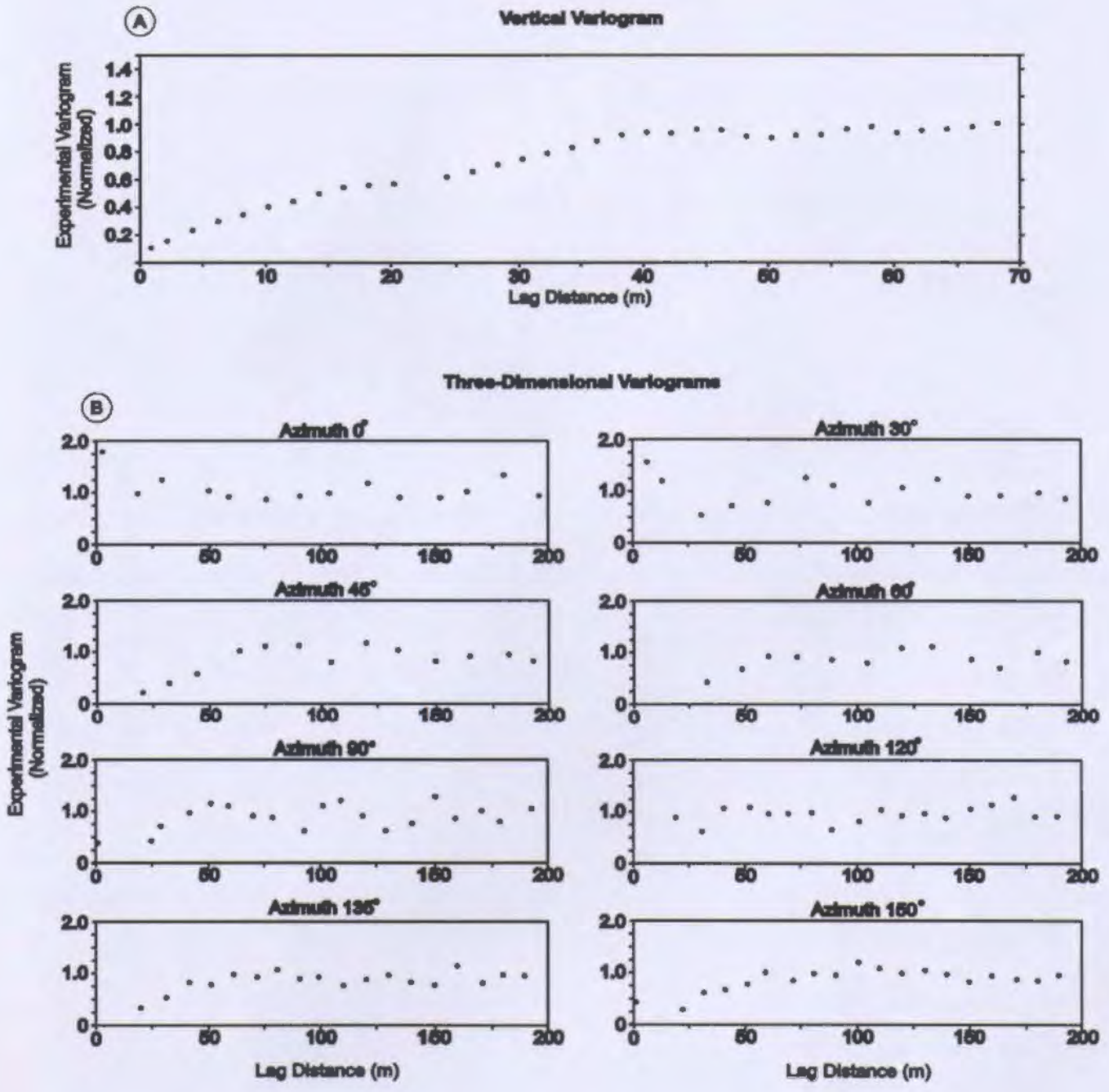

Figure 3.5: **A**- Vertical variogram calculated from the MASU data using a lag unit distance of 2m. **B**- Three-dimensional variograms calculated from the MASU data using a lag unit distance of 10m along an azimuth of 0°, 30°, 45°, 60°, 90°, 120°, 135° and 150° with a tolerance of 30°. The dip along each azimuth was 15° with a tolerance of 30°.

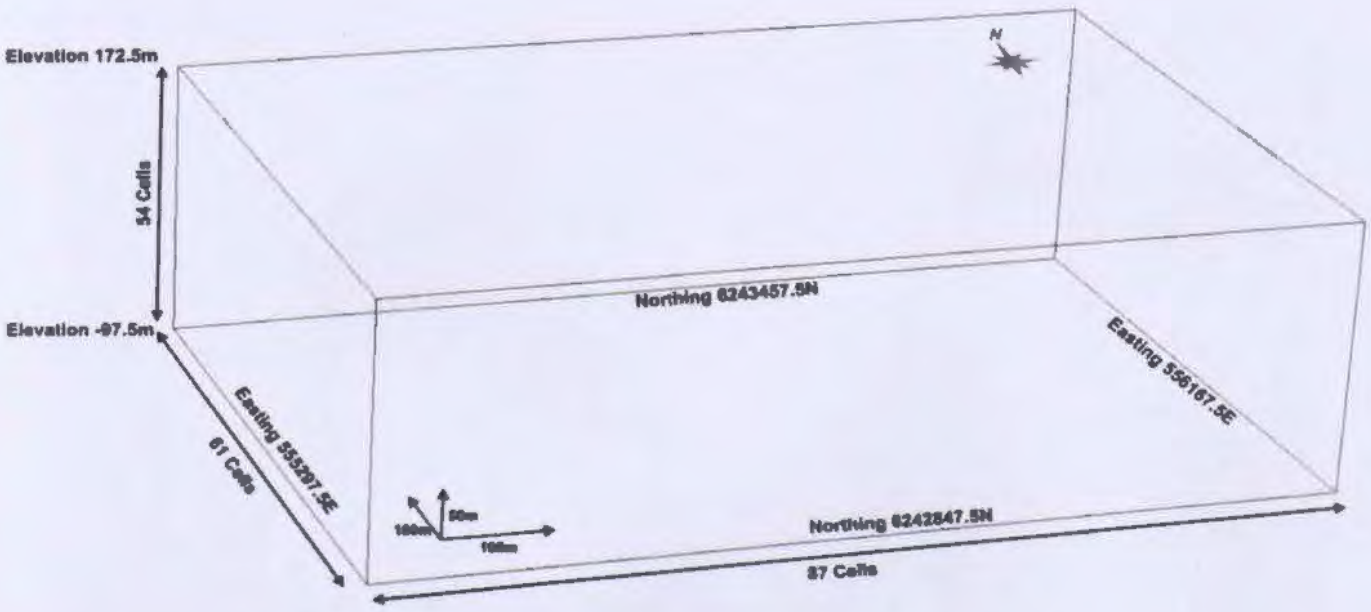

Figure 3.6: Mesh (MESH01) configuration for three-dimensional models. Coordinates are in UTM meters relative to NAD83 (Zone 21) and elevations are relative to sea level. Scale can be inferred from coordinate annotations.

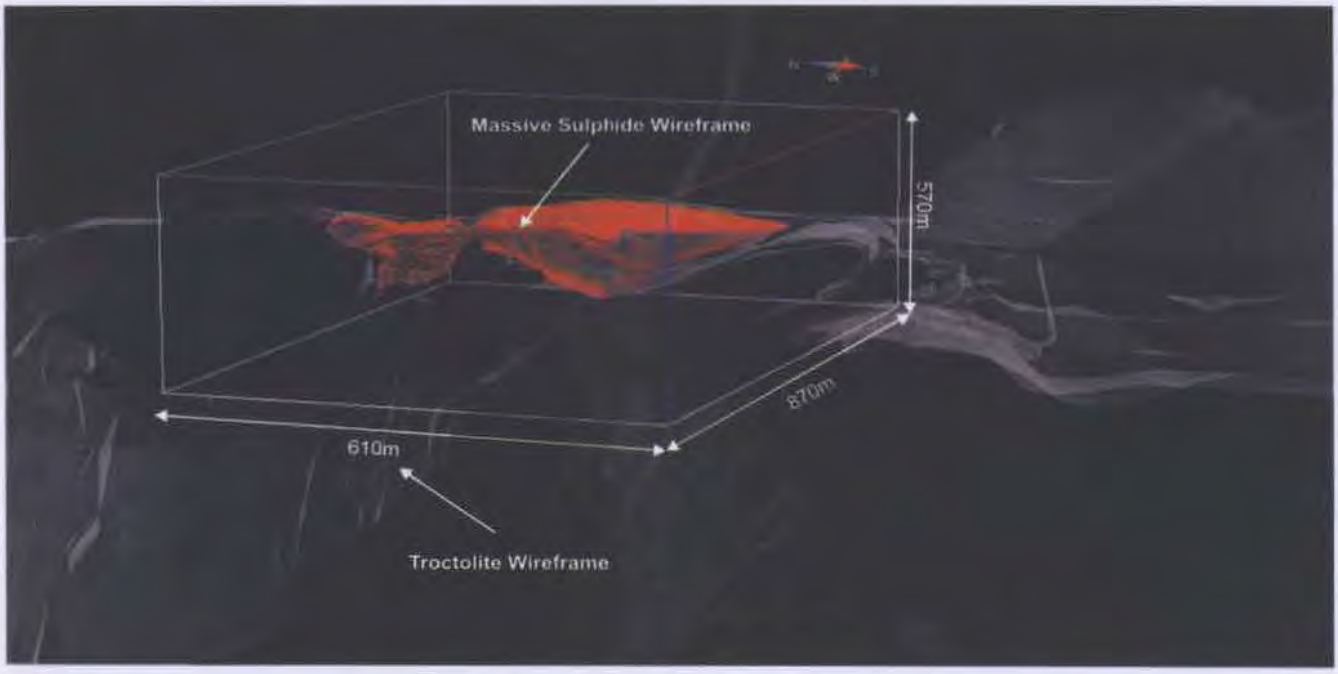

Figure 3.7: Three-dimensional image illustrating the TR (gray) and MASU (red) wireframes provided by VBNC. The dimensions of the mesh shown in the image are identical to the mesh shown in Figure 3.6.

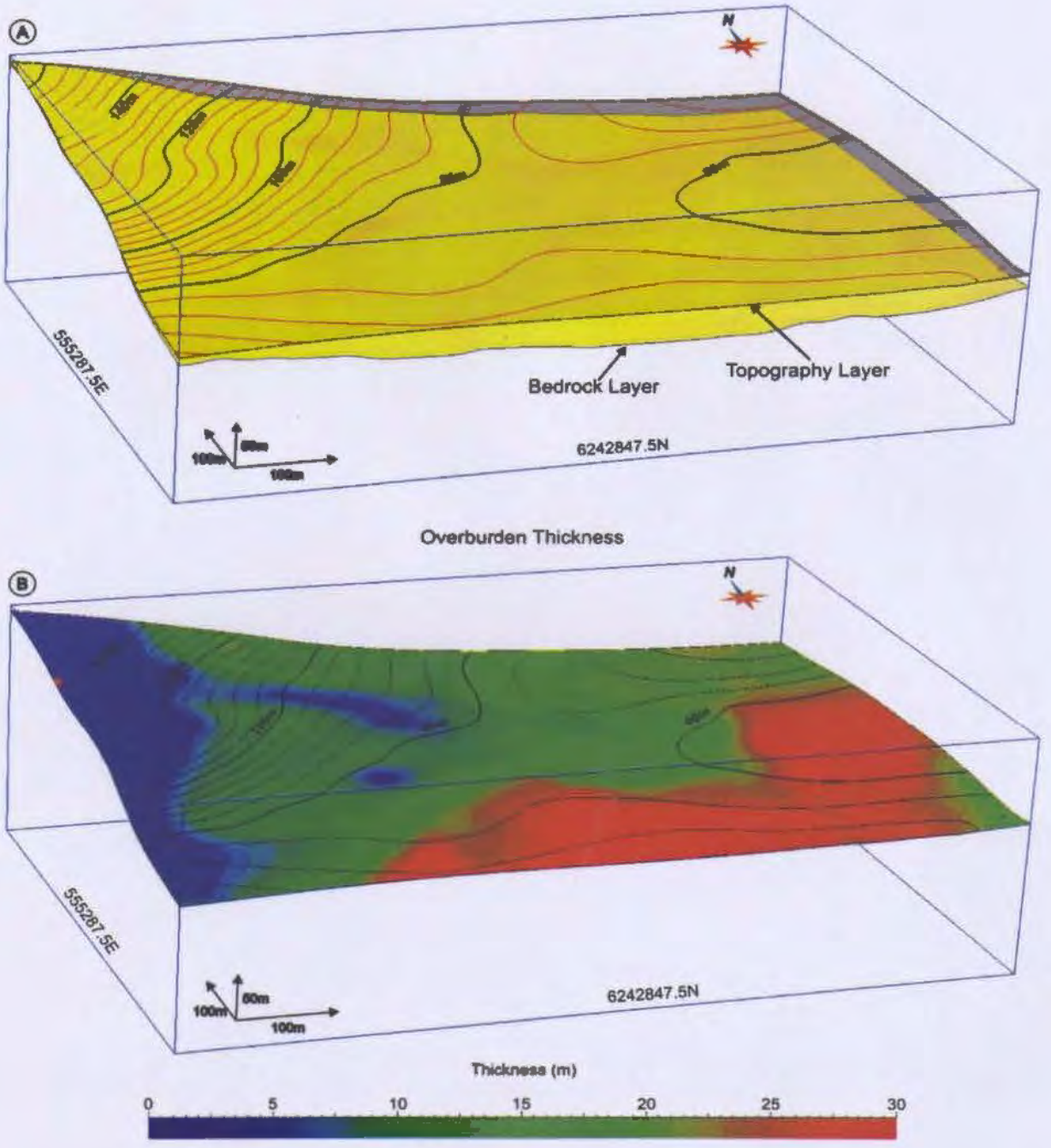

Figure 3.8: **A**- Three-dimensional image illustrating the location of the topographic and bedrock layers. **B**- The overburden thickness calculated by taking the difference between the topographic and bedrock elevations. The resulting thickness values represent metres below the topographic surface. Elevations are contoured at 5m intervals. Coordinates are in UTM meters relative to NAD83 (Zone 21). Scale can be inferred from coordinate annotations.

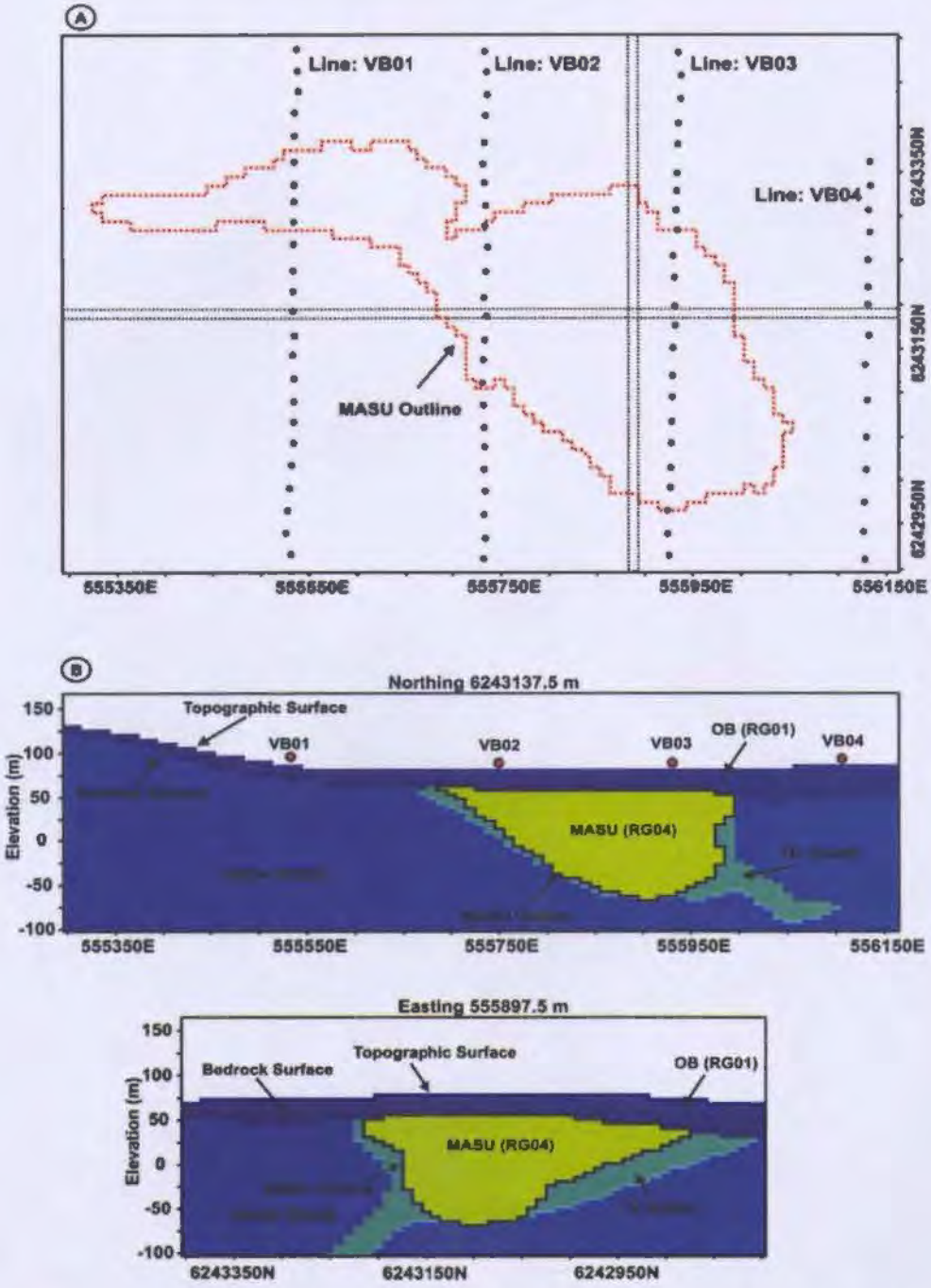

Figure 3.9: **A**- Map illustrating the MASU outline projected to surface. Gravity lines VB01, VB02, VB03 and VB04 are superimposed. **B**- Sections along northing 6243137.5m and easting 555897.5m illustrating the major surfaces and regions used during model construction. Regions were created from wireframes (Figure 3.7) and surfaces (Figure 3.8A) provided by VBNC. Positions of the gravity lines VB01, VB02, VB03 and VB04 perpendicular to east-west section are shown in red. Coordinates are in UTM meters relative to NAD83 (Zone 21) and elevation are relative to sea level. Scale can be inferred from coordinate annotations.

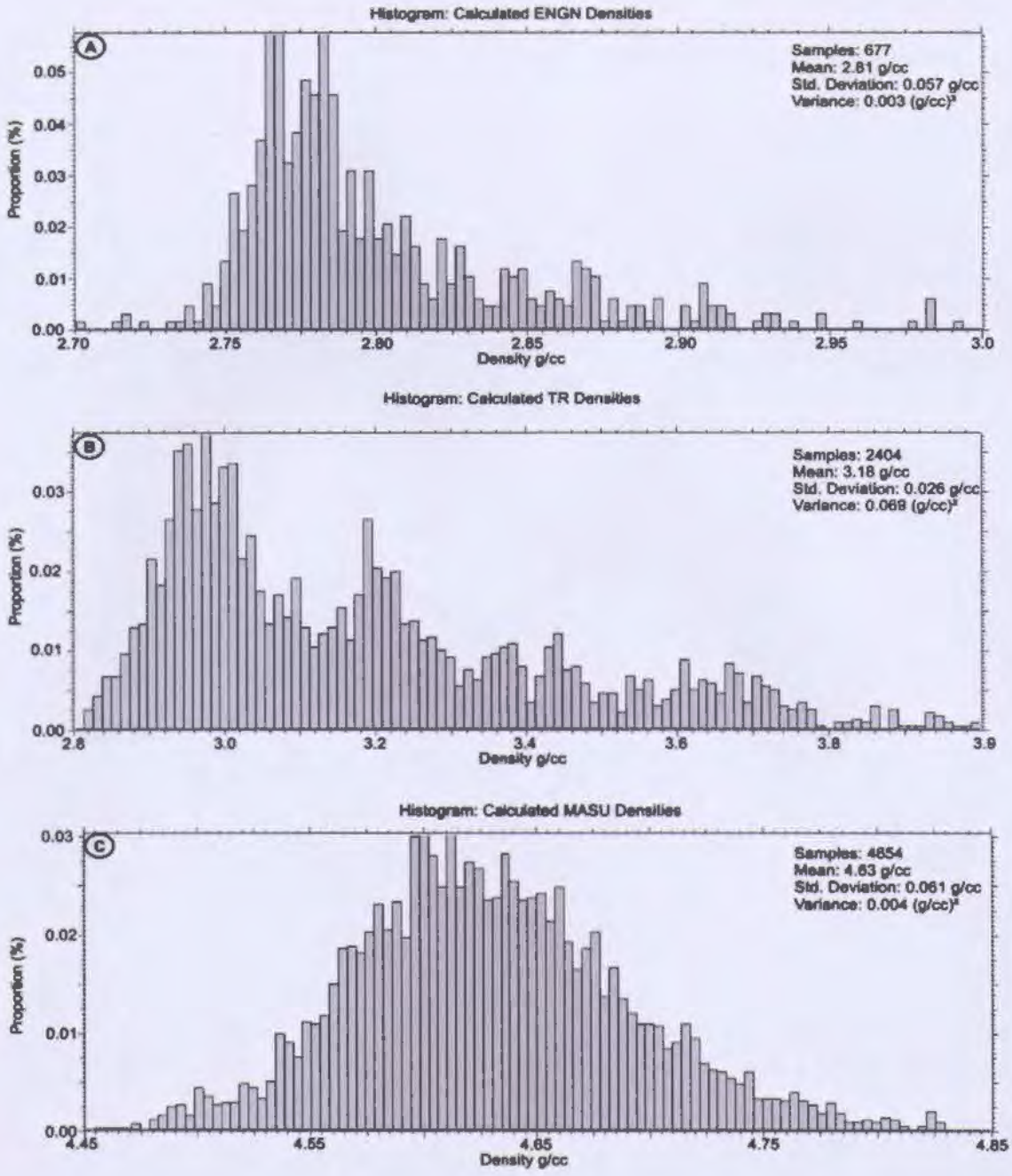

Figure 3.10: Histograms illustrating the proportion of calculated densities (g/cc) contained within the (**A**) ENGN, (**B**) TR and (**C**) MASU regions. All data points outside the regions are excluded from the histograms.

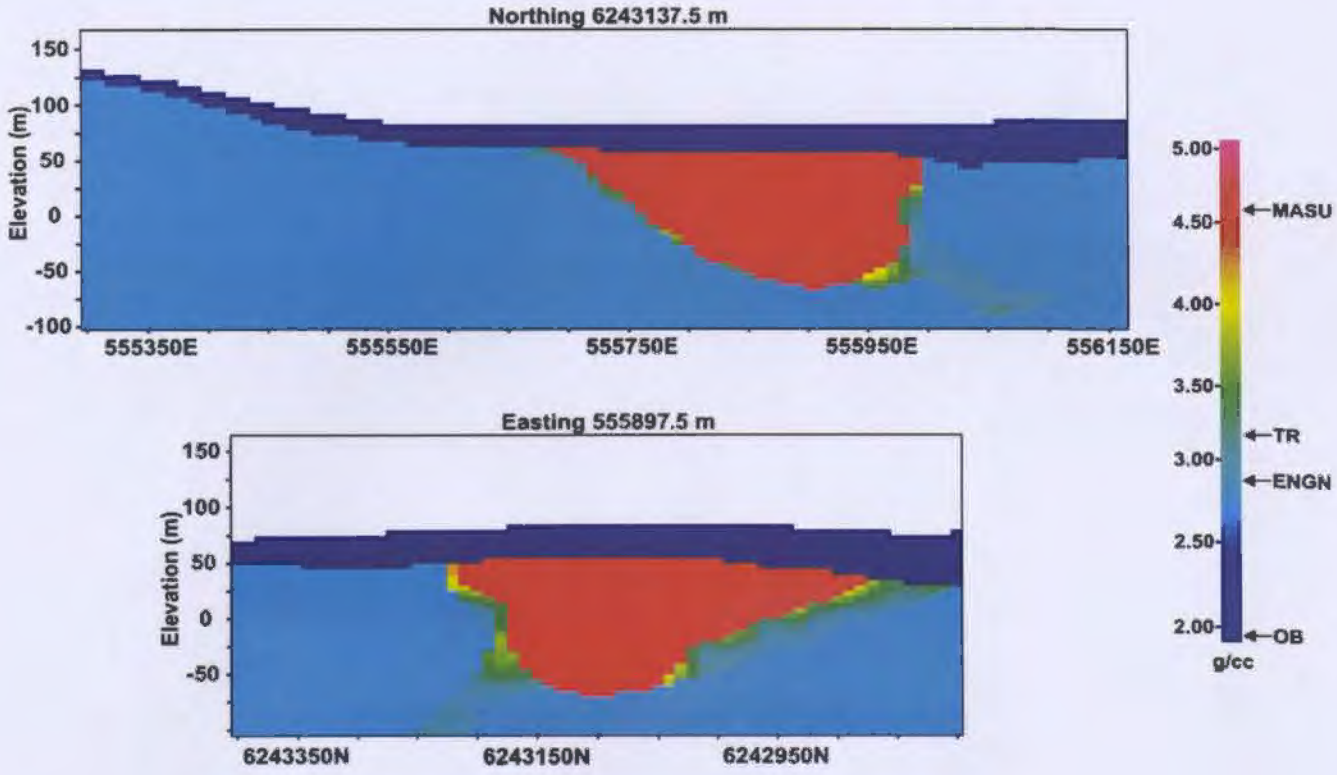

Figure 3.11: Sections along northing 6243137.5m and easting 555897.5m illustrating the Kriged density models DM01 from the associated regions in Figure 3.9B. The OB region (RG01) and ENGN region (RG05) were assigned a constant density of 1.92 g/cc and 2.81 g/cc respectively. The average densities of the OB, ENGN, TR and MASU densities are positioned along the colour bar. The MASU region is outlined in black. Estimated position of gravity lines VB01, VB02, VB03 and VB04 perpendicular to east-west section are shown in red. Coordinates are in UTM meters relative to NAD83 (Zone 21) and elevations are relative to sea level. Scale can be inferred from coordinate annotations.

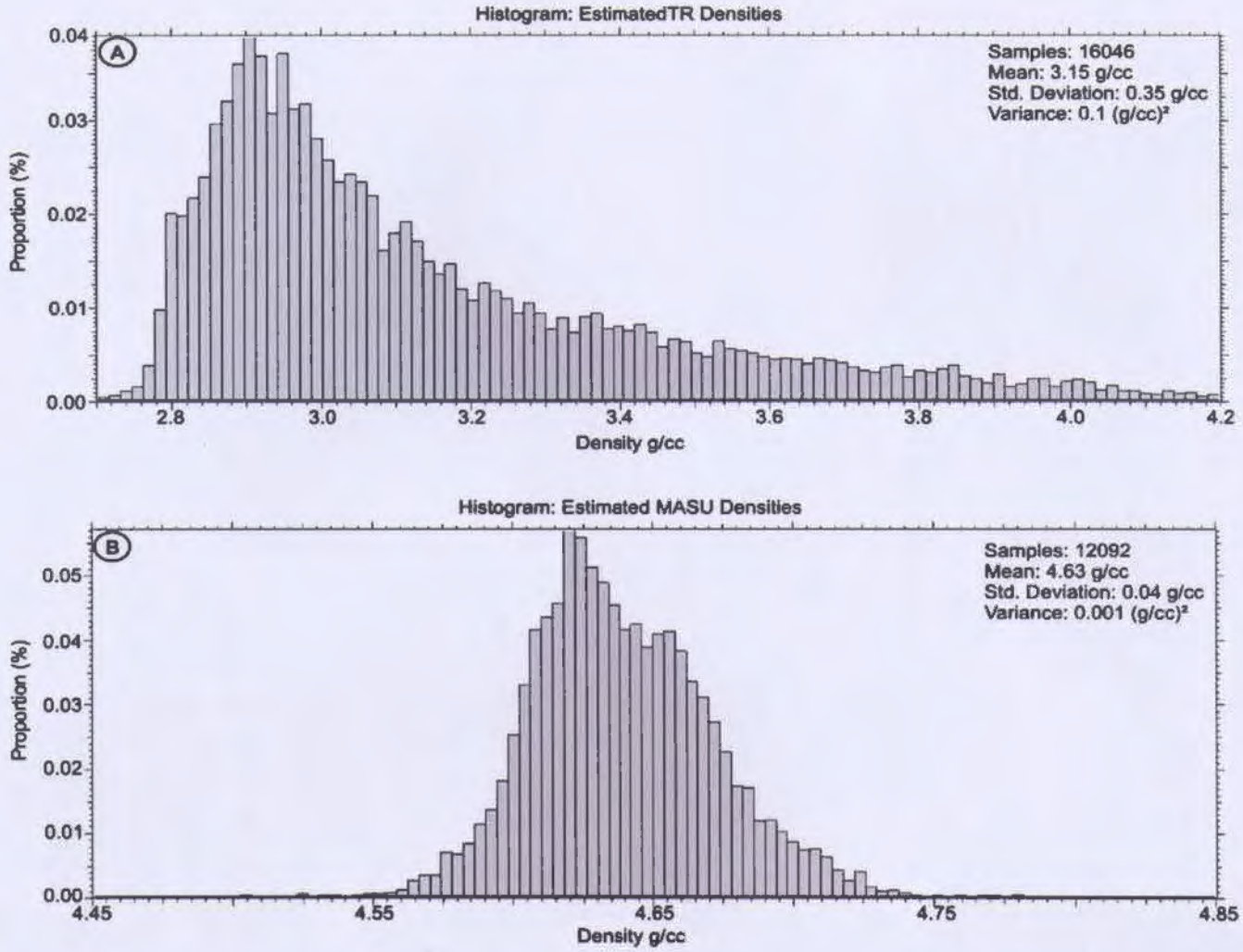

Figure 3.12: Histogram distributions for the Kriged data points contained in the TR (A) and MASU (B) regions.

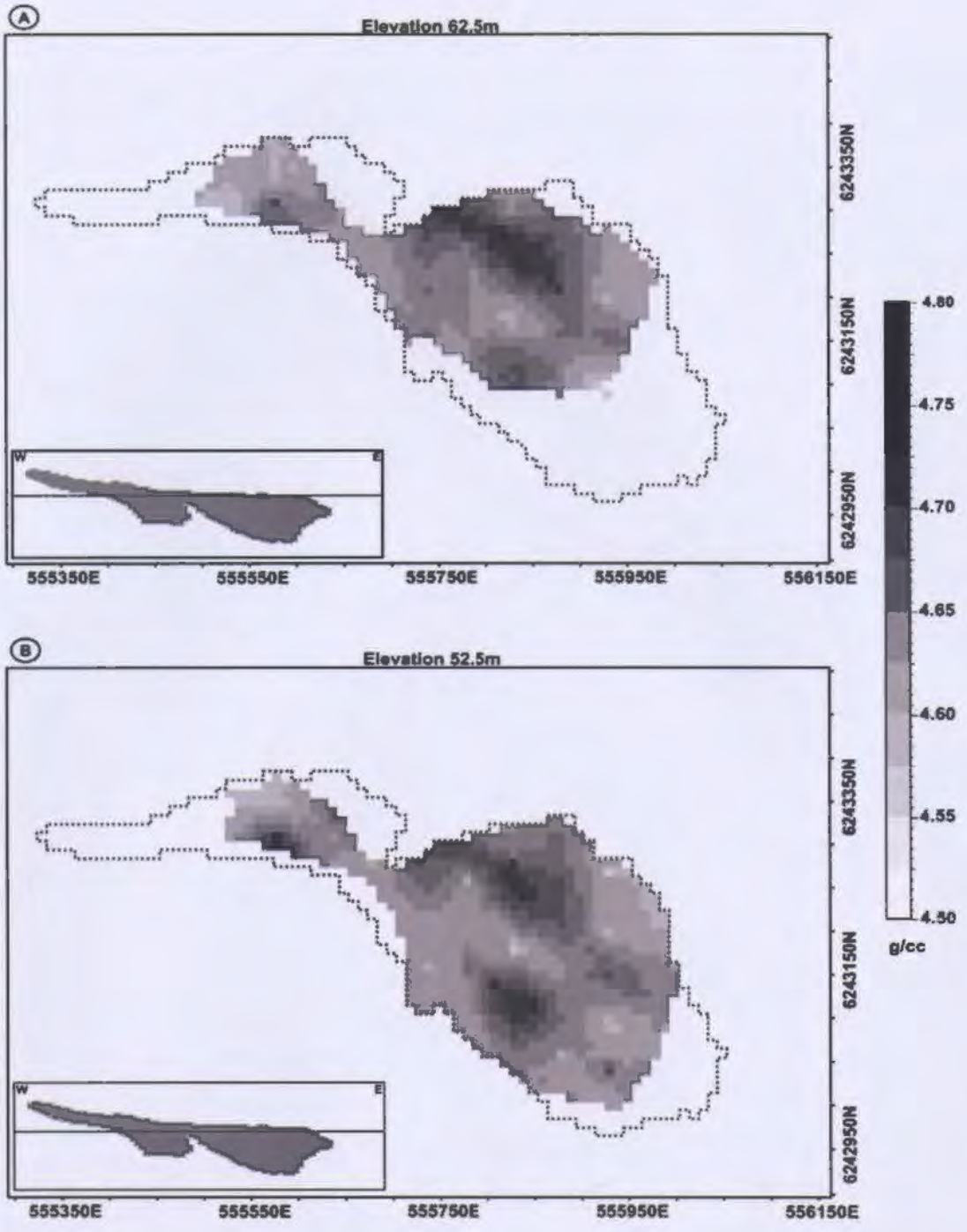

Figure 3.13: Horizontal slices at an elevation of 62.5m (A) and 52.5m (B) highlighting the high density regions contained within the Ovoid. MASU region projected to surface is shown by the black dotted line. The north facing sections are showing the location of the depth slices in relation to the position of the MASU regions (shaded). Coordinates are in UTM meters relative to NAD83 (Zone 21) and elevations are relative to sea level. Scale can be inferred from coordinate annotations.

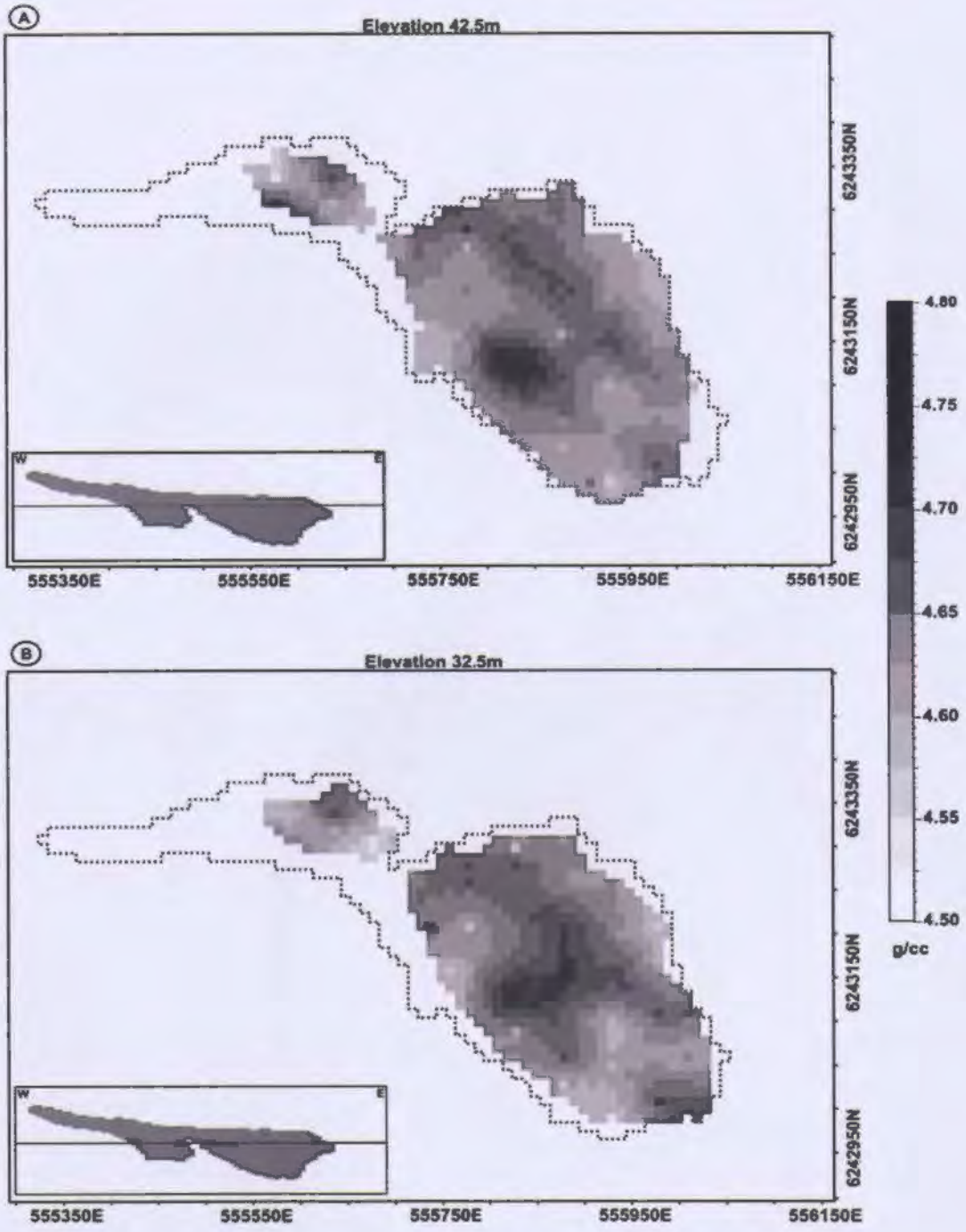

Figure 3.14: Horizontal slices at an elevation of 42.5m (A) and 32.5m (B) highlighting the high density regions contained within the Ovoid. MASU region projected to surface is shown by the black dotted line. The north facing sections are showing the location of the depth slices in relation to the position of the MASU region (shaded) and elevations are relative to sea level. Coordinates are in UTM meters relative to NAD83 (Zone 21). Scale can be inferred from coordinate annotations.

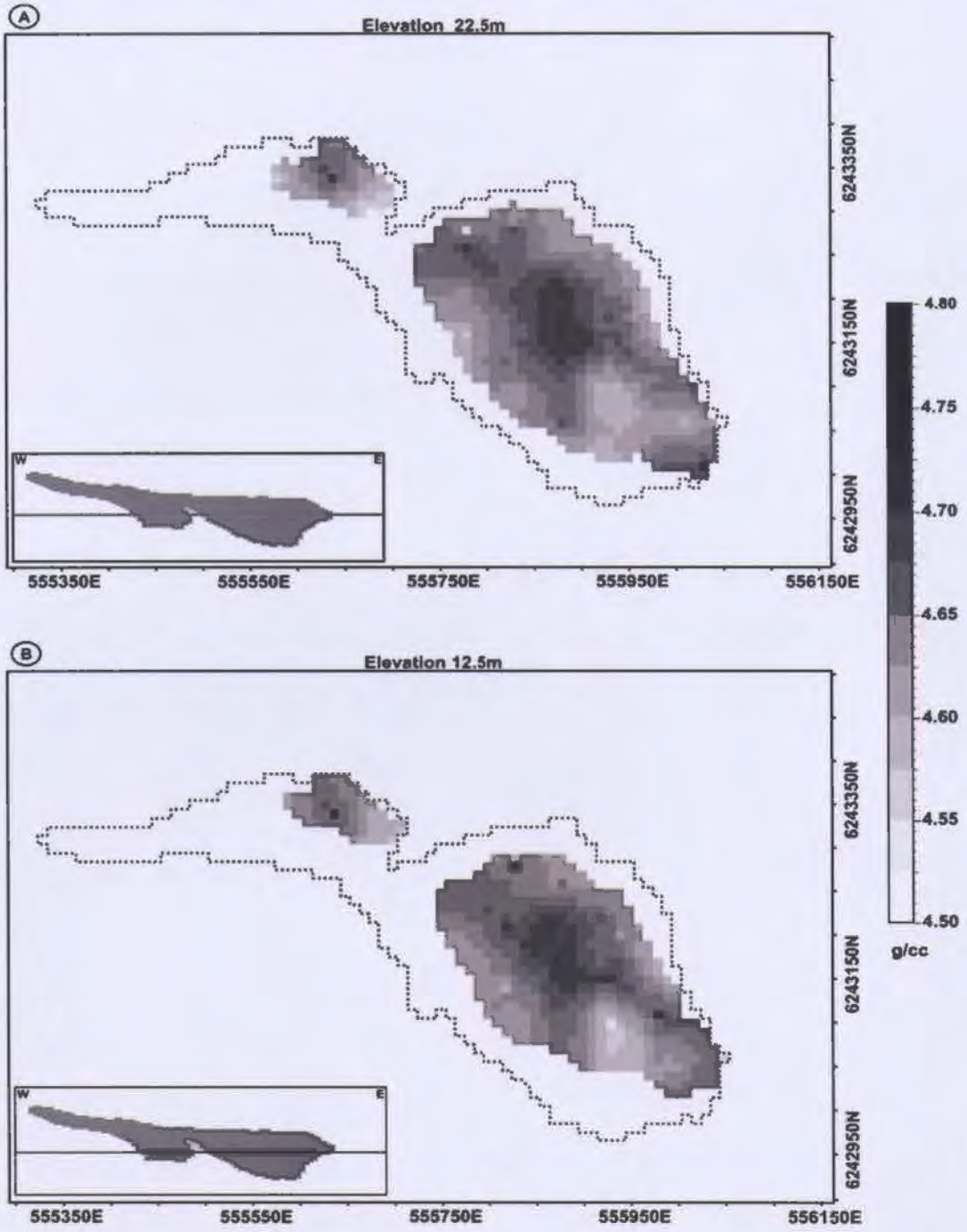

Figure 3.15: Horizontal slices at an elevation of 22.5m (A) and 12.5m (B) highlighting the high density regions contained within the Ovoid. MASU region projected to surface is shown by the black dotted line. The north facing sections are showing the location of the depth slices in relation to the position of the MASU regions (shaded). Coordinates are in UTM meters relative to NAD83 (Zone 21) and elevations are relative to sea level. Scale can be inferred from coordinate annotations.

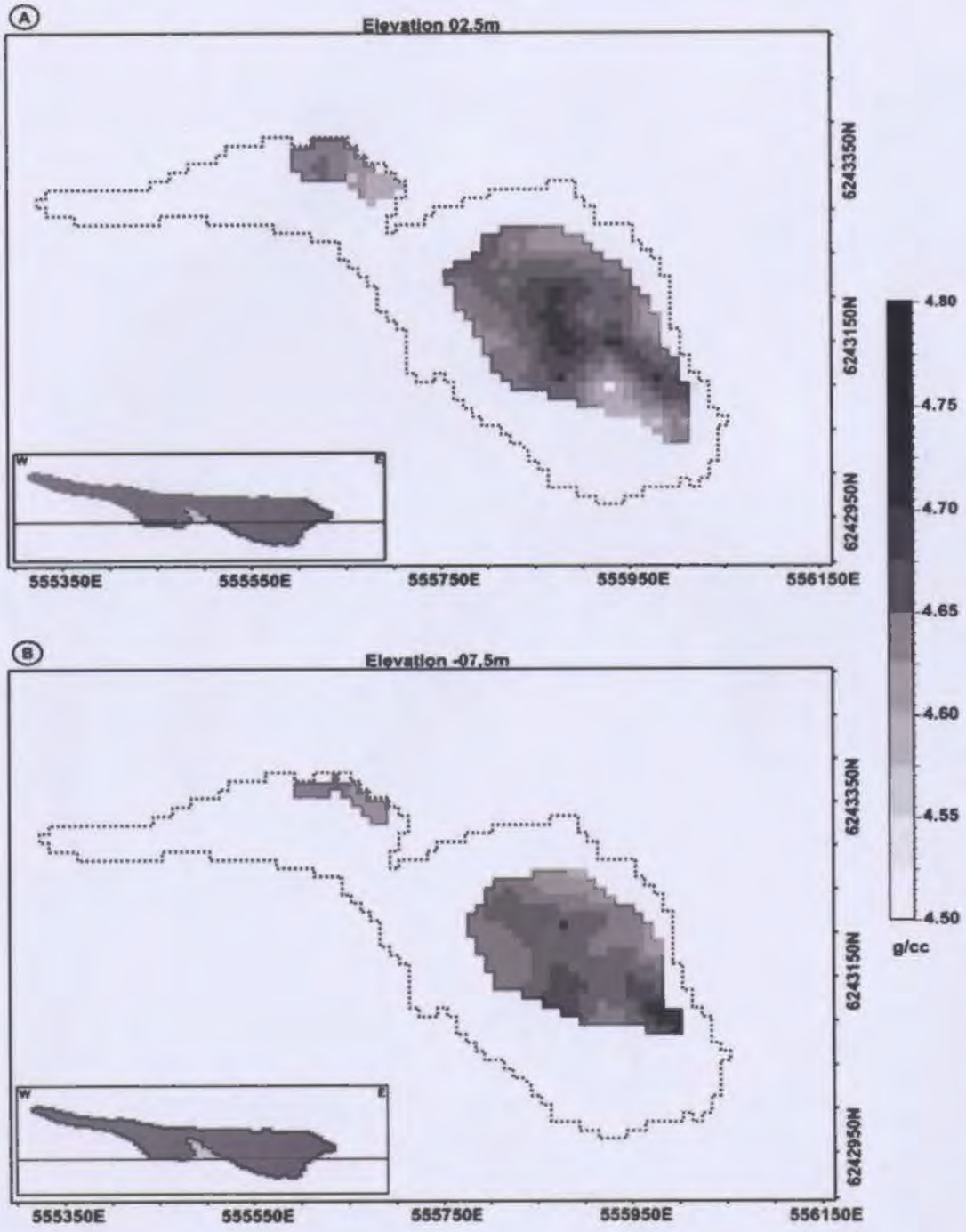

Figure 3.16: Horizontal slices at an elevation of 02.5m (A) and -07.5m (B) highlighting the high density regions contained within the Ovoid. MASU region projected to surface is shown by the black dotted line. The north facing sections are showing the location of the depth slices in relation to the position of the MASU region (shaded). Coordinates are in UTM meters relative to NAD83 (Zone 21) and elevations are relative to sea level. Scale can be inferred from coordinate annotations.

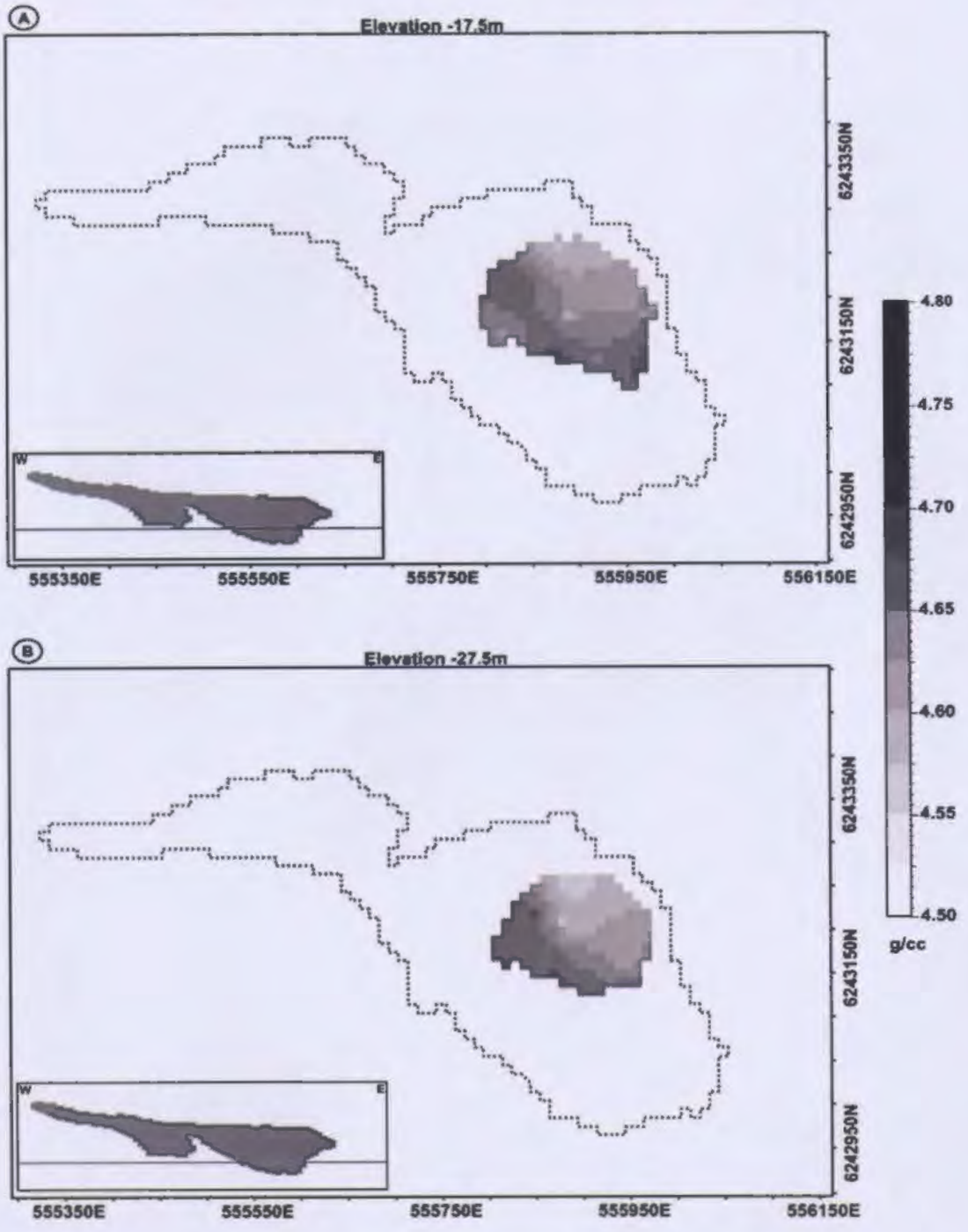

Figure 3.17: Horizontal slices at an elevation of -17.5m (A) and -27.5m (B) highlighting the high density regions contained within the Ovoid. MASU region projected to surface is shown by the black dotted line. The north facing sections are showing the location of the depth slices in relation to the position of the MASU region (shaded). Coordinates are in UTM meters relative to NAD83 (Zone 21) and elevations are relative to sea level. Scale can be inferred from coordinate annotations.

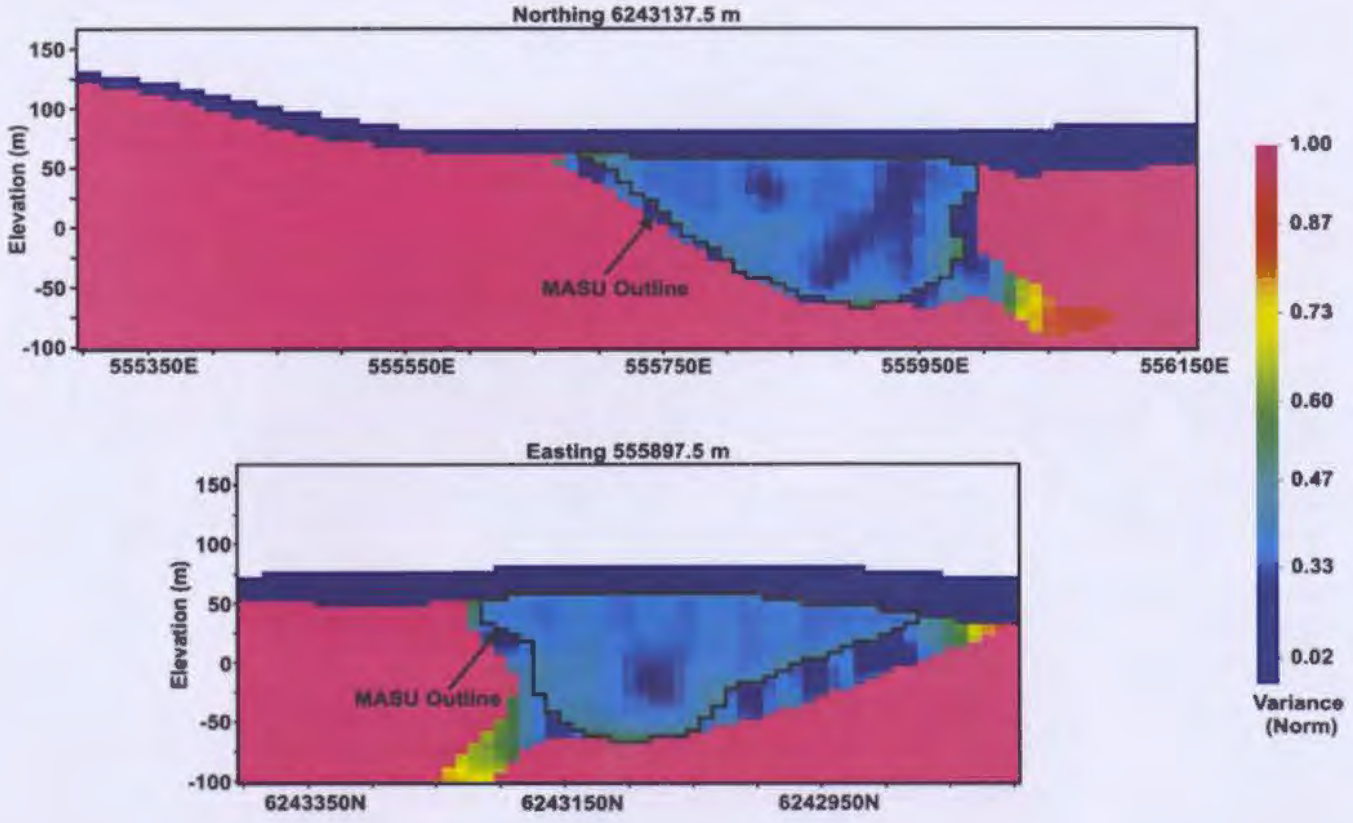

Figure 3.18: Sections along northing 6243137.5m and easting 555897.5m illustrating the normalized variances obtained from the Kriged density models illustrated in Figure 3.11. The OB region (RG01) and ENGN region (RG05) shown in Figure 3.9B were assigned constant variances of 0.0 and 1.0 respectively. The MASU region is outlined in black. Coordinates are in UTM meters relative to NAD83 (Zone 21) and elevations are relative to sea level. Scale can be inferred from coordinate annotations.

Chapter 4: Fundamentals of Gravity Inversion

Inverse techniques involve the quantitative interpretation of geophysical survey data via the generation of an Earth model that reproduces the observed gravity data. This chapter provides an overview of the essential components of a gravity inversion process, particularly investigating the 3-D inversion procedures supplied by the UBC-Geophysical Inversion Facility. The discussion consists of a brief mathematical review of the inverse problem and solution described by Li and Oldenburg (1996, 1998a). The review focuses on the basic elements of the Grav3D program that was used to invert the gravity data collected at Voisey's Bay.

4.1 The General Inverse Problem

Inverting a gravity dataset requires gravity measurements at the surface and an estimate of uncertainty at each location. The uncertainty assigned at each data point depends on the uncertainty associated with both the collection of gravity data and the Bouguer reduction techniques. The inversion reconstructs a model of the subsurface which adequately reproduces the data within the estimated uncertainty. One downside of inverting gravity data is the issue of nonuniqueness of static potential fields. An infinite number of possible models can be generated to match the observed response (Blakely, 1995). Constraints must be incorporated into the inversion algorithm to ensure that the resulting model is geologically reasonable. The algorithm incorporates a generic model objective function, which may be used to incorporate existing geological information into

the inversion algorithm. The inverse problem is solved by determining a model which minimizes the model objective function while fitting the data to within specified tolerance. The model objective function contains terms that ensure that the resultant model is close to a reference model, which is specified by the user, and smooth in three spatial directions. A "simple" or smooth model is desired when little is known about the subsurface geology.

4.2 Theoretical Background

The following section will provide a brief overview of the major theoretical components discussed in this chapter. The section will be subdivided into three main subsections. The first section will define the gravitational field and its forward solution. The second section will examine the depth weighting parameters used to counteract the natural decay of the gravitational field with depth. The final subsection will focus on the global objective function, consisting of the model objective function and data misfit function.

4.2.1 Gravity Field:

A typical gravity survey consists of measuring the vertical component of the gravity field at a location on the Earth's surface. The vertical component of the gravity field at the i^{th} observation point is defined as (Nagy, 1966; Nagy, 1973; Li and Oldenburg, 1998),

$$g_z(\bar{r}_i) = \gamma \int_V \rho(\bar{r}) \frac{z - z_i}{(\bar{r} - \bar{r}_i)} dv \qquad [4.1]$$

where V represents the volume of the anomalous mass $\rho(\boldsymbol{r})$ and γ is the universial gravitational constant. A right handed coordinate system with the z-axis pointing vertically downward is assumed. Equation [4.1] can be used to determine the gravitational field due to a known density distribution. This forward solution is determined by discretizing the subsurface density distribution into cells using a three-dimensional orthogonal mesh (Li and Oldenburg, 1998a). With the Earth divided into a set of three-dimensional prismatic cells, the gravitational field at the N observation points can be determined by solving the matrix (Li and Oldenburg, 1998a),

$$\mathbf{d} = \mathbf{F}\boldsymbol{\rho}, \qquad [4.2]$$

where $\mathbf{d} = (d_1,...,d_M)^T$ is the vector containing the N gravitational field values, $\boldsymbol{\rho} = (\rho_1,...,\rho_M)^T$ is a vector containing the densities of the M cells, and $\mathbf{F}$ is a matrix defining the gravitational contribution to the i^{th} datum of the j^{th} cell. The contribution at the i^{th} datum and j^{th} cell is given by,

$$F_{ij} = \gamma \int_{\Delta V_j} \frac{z - z_i}{|r - r_i|^3} dv \qquad [4.3]$$

where ΔV_j is the volume of the j^{th} cell, ρ_j is the density of the j^{th} cell and γ is the gravitational constant. The derivation of the closed form expression of Equation [4.3] was presented by Nagy (1973) for a three dimensional orthogonal cell.

4.2.2 The Global Objective Function:

The observed and predicted gravity responses are matched using a suitable minimization algorithm. The Grav3d codes make use of a global objective function (Φ) which is a combination of the model objective function (Φ_m) and the data misfit function (Φ_d) defined as.

$$\phi = \phi_d + \beta\phi_m \qquad [4.4]$$

where $0 < \beta < \infty$. β is the regularization parameter that influences the relative importance of the data misfit and model objective functions. This subsection will examine each function separately and discuss the ways in which these functions can incorporate geological information. In addition, this section will briefly examine the optimization approach, which is commonly used to describe the solution of the inverse problem.

4.2.2.1 Data Misfit Function:

The gravity value measured at the Earth's surface is a combination of the true gravitational value and associated measurement errors. The inversion algorithm must generate a predicted dataset that fits the data within the estimated error. The data misfit function can be written in its discrete from as (Grav3D User Manual),

$$\phi_d = \left\| W_d \left(\boldsymbol{d} - \boldsymbol{d}^{obs} \right) \right\|^2 \qquad [4.5]$$

where $\boldsymbol{d}^{obs}$ and $\boldsymbol{d}$ are the collected and predicted data vectors respectively, and W_d is a diagonal N x N matrix with elements $1/\varepsilon_i$, where ε_i is the standard deviation of the estimated noise of the i^{th} datum. The data misfit function is a chi-squared random variable, whose expected value is equal to the number of data.

4.2.2.2 Model Objective function:

The model objective function has the ability to incorporate prior geological information into the inversion process. The objective function is defined as (Grav3d User Manual)

$$\begin{aligned} \phi_m = {} & \alpha_s \int_V \omega_s \omega^2(z)(\rho - \rho_0)^2 + \alpha_x \int_V \omega_x \left(\frac{\partial \omega(z)(\rho - \rho_0)}{\partial x} \right)^2 dV \\ & + \alpha_y \int_V \omega_y \left(\frac{\partial \omega(z)(\rho - \rho_0)}{\partial y} \right)^2 dV + \alpha_z \int_V \omega_z \left(\frac{\partial \omega(z)(\rho - \rho_0)}{\partial z} \right)^2 dV \end{aligned} , \qquad [4.6]$$

where ω_s, ω_x, ω_y and ω_z are the weighting functions, and α_s, α_x, α_y, and α_z scaling coefficients that effect the smoothness of the resulting model, and ρ_0 is the vector of densities of the cells in the reference model. The first term in Equation [4.6] measures the closeness of the reference model to the estimated model. This term will be exploited throughout this study as various reference models will be used during the inversion process. The last three terms in Equation [4.6] compare the relative smoothness of the

estimated to the reference model. The user can control the smoothness of the estimated model through the use of length scales. The length scales along the x-, y- and z-axes may be written as

$$L_x = \sqrt{\frac{\alpha_x}{\alpha_s}}, \qquad [4.7]$$

$$L_y = \sqrt{\frac{\alpha_y}{\alpha_s}}, \qquad [4.8]$$

and

$$L_z = \sqrt{\frac{\alpha_z}{\alpha_s}}. \qquad [4.9]$$

The length scales can be chosen to influence the smoothness in various directions. The choice of length scales depends primarily on the surface gravity data distribution and knowledge of the subsurface geology. Typically, large length scales are assigned in areas with sparse data coverage and in areas where information on subsurface structure is limited. In these cases, smooth models are desired since they limit unwanted complexity.

The weighting functions in Equation [4.6] may also be manipulated to incorporate known geological information into the inversion process. The weighting functions influence the cell weights of the smallest model and the interfaces perpendicular to the easting, northing and vertical directions. When cell estimates in the reference model are considered to be accurate, a high ω_s value ensures that the cell estimate in the inverted model matches the cell estimate in the reference model. In regions of the reference model where little information is available, a low ω_s value allows the inversion program to manipulate the cell values while fitting the observed data.

4.2.2.3 The Optimization Approach:

The inversion is performed by minimizing Equation [4.5] described in Section 4.2.2. The outcome will primarily depend on the choice of the model objective function and the data misfit function. The process is iterative and must be solved numerous times in order to determine the optimum regularization parameter and final subsurface model. Grav3d uses a logarithmic barrier method with a conjugate gradient technique to solve the inverse problem (Grav3d User Manual). The logarithmic barrier method incorporates bounds into the minimization using a modified model objective function given by,

$$\phi = \phi_d + \beta\phi_m - 2\lambda\sum_{j=1}^{M}[ln(\rho_j - \rho_j^{min}) + ln(\rho_j^{max} - \rho_j)] \qquad [4.10]$$

where λ is the barrier parameter, ρ_j^{min} is the minimum user-defined density for the j^{th} cell, and ρ_j^{max} is the maximum user-defined density for the j^{th} cell. The barrier parameter is reduced during the iteration process while the regularization parameter β remains constant. The general inverse algorithm begins with an initial estimate of the regularization parameter and density model. The initial density model may be as simple as a uniform half-space or a complex density model. The model objective function is evaluated using these initial estimates then compared to the collected data. The process is iterative and usually begins by reducing the data misfit first. Once the data misfit approaches the target misfit Φ_d^*, the iterative processes continues until the model norm is reduced.

4.2.3 Depth Weighting:

As noted in the previous section, the contribution to the gravitational field from a cell is inversely proportional to the distance squared from the cell. The gravitation contribution of a cell at the surface is greater than the gravitational contribution of a cell having similar dimensions located at a greater depth. The Grav3d inversion codes utilize a depth weighting function which simply cancels this natural decay. Incorporating a depth weighting function into the algorithm insures that the cells at a greater depth have an equal chance of entering the solution as those cells located near the surface. The depth weighting function of the jth cell located at $\boldsymbol{r}_j$, has the form (Grav3d User Manual)

$$w(\boldsymbol{r}_j) = \left[\frac{1}{\Delta z_j} \int_{\Delta z_j} \frac{dz}{(z + z_0)^2} \right]^{1/2} \quad j = 1,..., M \qquad [4.11]$$

where Δz_j is the cell thickness and $(z + z_0)^{-2}$ approximates the natural decay of the kernels. This function is commonly applied to datasets with horizontal topographic surfaces. In areas with significant topographic variations, a three-dimensional weighting function is used to account for the gravitational decay. The generalized three-dimensional distance weighting function is expressed as (Grav3d User Manual),

$$w(\boldsymbol{r}_j) = \frac{1}{\sqrt{\Delta v_j}} \left[\sum_{i=1}^{N} \left(\int_{\Delta v_j} \frac{dv}{(R_{ij} + R_0)^2} \right)^2 \right]^{1/4} \quad j = 1,..., M \qquad [4.12]$$

where Δv_j is the volume of the jth cell, and R_{ij} is the distance between the ith observation point and a point in Δv_j. R_0 is a constant, chosen to be a quarter of the smallest cell size, which is used to clearly define the integral. In both Equations 4.11 and 4.12, the weighting functions are normalized in order to have a maximum value of unity.

4.3 Elements of the UBC-GIF Inversion Program

Grav3D consists of three programs, Gzfor3d, Gzsen3d and Gzinv3d. Gzfor3d is a forward modeling program that calculates the surface gravity field based on a specified density model. The Gzsen3d program calculates the sensitivity matrix, defined as **F** in Equation 4.2, while Gzinv3d inverts the gravity data. The following section will discuss the fundamental file configuration and examine the application of each program.

4.3.1 File Configurations:

4.3.1.1 Mesh .txt Files:

The mesh.txt file defines the three-dimensional orthogonal mesh used throughout the Grav3d program. The configuration of the mesh file is summarized in Figure 4.1. The NE, NN, and NV values contain the number of cells in the east-west, north-south and vertical directions. E_0, N_0 and V_0 are the easting, northing, and vertical locations of the top south-west corner of the mesh. The ΔE, ΔN, ΔV are the cell dimensions in the east-west, north-south and vertical directions. An example shown in Figure 4.2, illustrates the mesh configuration used for the subsurface density model illustrated in Figure 3.11.

4.3.1.2 Topography **.dat** Files:

The topo.dat file contains the surface topography data within the study area. The configuration of the topo.dat file is illustrated in Figure 4.3. The first row contains the number of data points (npt) in the topography file. The three columns starting below the first row contain the easting (E), northing (N) and elevation (Ele) of each data point. It is important to note that although the cells above the topographic surface are removed from the model, they should still be incorporated in all input models. All cells above the topographie surface are assigned a constant value of -100 and ignored from all calculations. The data distribution of the topography file should be able to adequately map the topographie surface. Direct triangulation is the interpolation method used to determine the topographic surface value above each column of cells. Elevations specified in the topo.dat file should have the same reference as the elevations contained in the mesh.txt file.

4.3.1.3 Observation **.loc** Files:

The obs.loc file is used to specify the observation locations. The structure of the obs.loc file is similar to the topo.dat configuration shown in Figure 4.3. All observation locations should be positioned over the topographic surface. The elevations contained in the obs.loc file should have the same reference as the mesh.txt and topo.dat files.

4.3.1.4 Observation **.grv** Files:

This file is similar to the obs.loc file with the addition of the gravity anomaly data (Grav) and the standard deviation (Err) of each gravity value summarized in Figure 4.4.

The observed gravity values contain only the residual anomalies after regional-residual processing techniques were applied to the Bouguer gravity data.

4.3.1.5 Model **.den** Files:

The .den file contains the density contrast values of each cell specified in the mesh.txt file. The density contrast values must be specified in g/cc. The file contains only one column of density contrast values starting in the top southwest corner of the mesh illustrated in Figure 4.4. The data values are sorted by ascending easting, ascending northing and descending elevation. All density data points above the topographic surface must be included in the density model. These values are typically assigned a large negative value and are not incorporated into the inversion process. The initial (*ini.den*) and reference (*ref.den*) models use the same file structure as the model.den file.

4.3.1.6 Boundary **.den** Files:

Bounds files contain the upper and lower bounds of the inverted density model. The inverted density must lie between the specified lower bound and upper bound. The structure of the bounds.den files is similar to the model.den file. The file contains two columns of density contrast values. The first column contains the lower bound while the second column contains the upper bound. Once again, the values above the topographic surface are ignored and should be assigned a large negative value.

4.3.1.7 Weighting **.dat** Files:

Weighting files contain the cell weights for each cell in the mesh.txt file. In addition, this file contains the weights for the interfaces perpendicular to the easting, northing and vertical directions. The values can be placed as a series of lines having the same order as the model.den file. The first line contains the cell weights for the model while the second, third and forth lines contains the cell weights for the interfaces perpendicular to the easting, northing and vertical directions. Given that the cell weights perpendicular to the interface are a derivative, they have one fewer values compared to the cell weights for the model. If no weighting file is specified all cell weights are equal to one.

4.3.2 Gzfor3d:

Gzfor3d is an executable command which calculates the gravitational effect from an input density model. The executable requires a file to compute the gravitational response. If no topography file is included the surface is treated as being flat. The command line used to run the program is **gzfor3d** *mesh.txt obs.loc model.den topo.dat*. The output file (gzfor3d.grv) contains the calculated gravity anomaly data without including error estimates.

4.3.3 Gzsen3d:

Gzsen3d is an executable program which performs the sensitivity and depth weighting calculations. The mesh.txt, obs.loc file, and a topo.dat files are required for the control file gzsen3d.inp. The control file shown in Figure 4.5 contains parameters which

allow the user to change the depth weighting function and matrix compression. A depth weighting or distance weighting function can be selected by the user depending on the model topography. A depth weighting function is commonly applied to models with little topographic variations, whereas distance weighting functions are typically applied to models with moderate to significant topographic variations. The control parameters, *beta* and *znot* allow the user to adjust the rate of decay of the weighting function. The parameters *wvlet*, *itol*, and *eps* define the type of wavelet used to compress the sensitivity matrix and the wavelet threshold. Wavelet compression is used to solve the linear system of equations which makes it possible to solve realistic large sized problems. The command line used to run the program is **gzsens3d** *gzsen3d.inp*.

4.3.4 Gzinv3d:

The Gzinv3d executable performs the 3D gravity inversion. The control file (gzinv3d.inp) illustrated in Figure 4.6 contains the parameters required to execute the program. The required input files are the obs.grv and the gzinv3d.mtx matrix file calculated by gzsen3d. Optional input files are the initial model (ini.den), reference model (ref.den), boundary model (bounds.den) and weighting model (w.dat). The control parameters allow the user to specify the choice of regularization parameter (*mode*), target misfit (*par*), misfit tolerance (*tolc*), and length scales (*Le*, *Ln*, and *Lz*). The two operational parameters *irest* and *idisk* specify the inversion starting procedure and sensitivity matrix accessibility. The inversion can be started from scratch or after an interruption by accessing the files gzinv3d.aux and gzinv3d.kap in the direetory of the previous inversion attempt.

Three modes exist for determining the regularization parameter. The first mode uses a line search to find the regularization parameter which gives the target value of misfit. The second mode allows the user to input the regularization parameter, while the third mode estimates the regularization through a generalized cross validation (GCV) technique. The length scale parameters determine the weighting coefficients in the model objective function (Equation 4.6). The length scales along the east-west (Le), north-south (Ln) and vertical (Lz) directions can be adjusted according to the cell dimensions. If no length scales are provided the program uses default values of two times the maximum cell width.

The output files of the gzinv3d program are gzinv3d.log, gzinv3d.den and gzinv3d.pre, gzinv3d.aux and gzinv3d.rho. Gzinv3d.log is a log file containing summary information of the inversion process. The gzinv3d.den and gzinv3d.pre files contain the recovered density model and predicted data. Finally, the gzinv3d.aux and gzinv3d.rho files contain information used for the purpose of restarting the inversion.

NE	NN	NV	
E_0	N_0	V_0	
E_1	E_2	...	E_{NE}
N_1	N_2	...	N_{NN}
V_1	V_2	...	V_{NV}

Figure 4.1: Mesh.txt file configuration used in the Grav3d inversion program.

87	61	54	
555297.5	6242847.5	175.5	
10	10	...	10
10	10	...	10
5	5	...	5

Figure 4.2: Mesh.txt file used to generate the subsurface density model shown in Figure 3.11.

npt		
E_1	N_1	Ele_1
E_2	N_2	Ele_1
⋮	⋮	⋮
E_{npt}	N_{npt}	Ele_{npt}

Figure 4.3: Topography.dat file configuration used in the Grav3d inversion program.

npt				
E_1	N_1	Ele_1	Grv_1	Err_1
E_2	N_2	Ele_1	Grv_2	Err_1
⋮	⋮	⋮	⋮	⋮
E_{npt}	N_{npt}	Ele_{npt}	Grv_{npt}	Err_{npt}

Figure 4.4: Observation.grv file configuration used in the Grav3d inversion program.

mesh
obs.grv
topo.dat
iwt
Beta znot
wvlet
itol eps

Figure 4.5: gzsen3d.inp file configuration required to calculate the sensitivity matrix and depth weighting function using gzsen3d.

irest
mode
par tolc
obs.grv
gzinv3d.mtx
initial.den
reference.den
bounds.den
L_E L_N L_V
w.dat
idisk

Figure 4.6: gzinv3d.inp file configuration required to run gzinv3d.

Chapter 5.0: Inversion of Gravity Data

The following chapter examines the inversion of the Voisey's Bay gravity data using the UBC inversion codes. The chapter begins by calculating the gravitational field from the Kriged density model generated in Chapter 3. Following the calculation of the forward model, the datasets used throughout the inversion process are described. The final section examines in detail various unconstrained and constrained inversions.

5.1 Forward Modeling

The gzfor3d program was used to calculate the gravitational effect of the density model generated in Section 3.4.3. Two density contrast models were created by removing 2.67 g/cc (DM02) and 2.81 g/cc (DM03) from the original density model (DM01). Removing a density of 2.67 g/cc was to correspond with the assumed density of the continental crust and the density used in the calculation of the Bouguer gravity field (Hinze, 2003). A density of 2.81 g/cc corresponds to the average value of the ENGN unit (Figure 3.10A). The gravity field was calculated using two observations files. The first observation file (OBS01) corresponds to the location of the collected gravity data shown in Figure 2.5. The second observation (OBS02) file contains data points generated from a 10m by 10m regular grid. The OBS02 file was generated as a result of an observation regarding the locations of the survey lines relative to the maximum density contrast and thickest section of the Kriged density model (Figure 3.11). The high density regions and thiekest section of the Ovoid are located between line VB02 and VB03. As a result, it

can be concluded that the current location of the survey lines does not adequately sample the gravitational effect over the Ovoid. If the gravity data collected were contoured and placed on a regular grid using a program such as Oasis Montaj™, the gravitational maximum would be contoured over survey line VB03. Grid points located between survey lines VB02 and VB03 would therefore have a lower gravitational value than one would expect from the observed density distribution, and ultimately influence the inversion.

To examine the effect of line positioning, four gravity models were calculated using the two density contrast models and the two observation files. The forward modeling runs are summarized below:

Run 1 (FM01): OBS01 and DM02

Run 2 (FM02): OBS01 and DM03

Run 3 (FM03): OBS02 and DM02

Run 4 (FM04): OBS02 and DM03

The gravitational field calculated at the observation locations along lines VB01, VB02 and VB03 for Run 1 and Run 2 are illustrated in Figure 5.1. Since both density contrast models are similar, except for a constant density difference of 0.14 g/cc, the resulting profiles have similar geometric characteristics with average offset of 0.71 mGal. Forward models FM03 and FM04 calculated the "observed" gravity on a 10m by 10m grid synthetic dataset using density models DM02 and DM03. As expected, the gravity distributions observed in both maps have similar geometric characteristics with an

average offset of 0.71 mGal. The gravitational maximum is located approximately 70m west of line VB03 with an amplitude variation of approximately 4.0 mGal. This is approximately 0.5 mGal larger that the amplitude variation measured along line VB03. Due to the spatial location of the collected data, a pseudo-gravity dataset was generated to capture a more representative gravitational anomaly over the Ovoid. The generation of the pseudo-gravity dataset will be examined in the following section.

5.2 Data Preparation

The input data used in the inversions will consist of two datasets. The first dataset (INDATA01) will consist of the residual field containing the residual gravitational field of the Ovoid generated as discussed in Chapter 2. A regional field was calculated by upward continuing the gravity data to 500m (Figure 2.15) and subtracted from the original data, tabulated in Appendix C, following the same procedures described in Section 2.5. In this example, the best estimate of the regional field was achieved when no gravitational contribution from the Ovoid is present in the data. The resulting observed regional and residual profiles are illustrated in Figure 5.3. A comparison between the residual profiles and the forward models FM01 and FM02 shown in Figure 5.1, indicate that the relative background density is closer to 2.67 g/ce rather than 2.81 g/cc. A background density of 2.67 used in the generation of FM01 matches the amplitude observed in the residual profiles. A background density of 2.81 g/cc results in negative tails away from the Ovoid. As a result, all inversions using the INDATA01 dataset will contain input models relative to 2.67 g/cc.

The second dataset (INDATA02) contains the forward model data FM03 (Figure 5.2), calculated from the density contrast model DM02 and the 10m by 10m grid locations for the "observation" data OBS02, a synthetic dataset, described in the previous section. In addition, these 4451 gravity data values were contaminated with random Gaussian noise with a standard deviation having a maximum of 0.05 mGal and 2% of the data value (Li and Oldenburg, 1998a) to give the synthetic data similar uncertainty as the true residual data. The INDATA02 dataset is displayed in Figure 5.4.The majority of examples illustrated in this chapter will consist of parallel inversions using both INDATA01 and INDATA02 datasets. The purpose of running parallel inversions is to compare the resulting models obtained from inverting a sparse dataset (INDATA01) compared to the models obtained from inverting a dense dataset (INDATA02) indicative of the expected gravity survey results on a denser grid. .

5.3 Unconstrained Inversions

Multiple inversion trials were carried out using the gravity data collected at Voisey's Bay. The UBC inversion algorithm provides the user with many parameters which may be adjusted based on the gravity data available and geological environment. Due to limited time constraints only a selection of the inversion parameters were adjusted. The parameters held constant throughout the study were; weighting function, type of wavelet used to compress the data and method of determining the regularization parameter. A depth weighting function was chosen given that topography data were included in each inversion. The type of wavelet and relative threshold were set to default, which uses the Daubechies-4 wavelet and a reconstruction error of 0.05. The default

regularization parameter is Mode 1 discussed in the section 4.3.4. In addition, all inverted models will be calculated without applying a positivity constraint since the overburden densities are negative relative to regional rock densities

The inversion process was started using only the gravity datasets, incorporating no prior geological knowledge into the algorithm. The following inversion examples will investigate the density distribution obtained from unconstrained inversions of the gravity datasets INDATA01 and INDATA02. A mesh (MESH02) was designed using the create mesh tool in the Grav3d user interface. The horizontal dimensions of the mesh varied from 20m by 20m at the center to 80m by 80m toward the edges. The vertical cell thickness ranged from 10m at the surface to 100m at the base.

The INDATA01 dataset was inverted to generate a subsurface density model. Length scales were adjusted to account for the variation in line and station spacing in the collected data. The length scales applied in the east-west, north-south and vertical directions were chosen to be 100m, 40m and 20m respectively. The distance weighting parameters were set to default. The density model (DEN01) recovered form inversion INV01, illustrated in Figure 5.6, reveals a single anomalous region of high density located at an easting, northing and elevation of 555900E, 6243150N and 25m. The high density region is located directly below the survey line VB03. The density contrast values recovered from the inversion are lower than the expected values. For a density contrast relative to 2.67 g/cc, the average density of the Ovoid was estimated to be 4.63 g/cc (Figure 3.10C) yielding an average density contrast of 1.96 g/cc. The maximum density contrast obtained from the inverted model is approximately 1.2 g/cc, with an average of 1.0 g/cc. The lower density contrast is most likely a result of the location of the survey

lines relative to the maximum thickness of the Ovoid and lack of overburden densities in the model. High densities are placed in near surface cells which should be populated with low density contrasts indicative of overburden. In addition, the high density region extends to a greater depth than the known position of the Ovoid. The cells containing a negative density contrast on the flanks of the high density region may be a result of overestimating the regional field. A profile along line VB03 shown in Figure 5.7 compares the calculated gravity anomaly produced by the density model DEN01 and the residual data INDATA01.

The density model DEN02 obtained by inverting the INDATA02 dataset is shown in Figure 5.8. The inversion INV02 was carried out using the same mesh as INV01. Both of the L_e and L_n length scales were set to 20m given that the dataset contains data points on a regular 10m by 10m grid. The resulting model places the maximum density at the center of the known position of the Ovoid with a maximum density contrast of 1.50 g/cc. A higher density contrast is achieved since the regular grid captured the maximum amplitude over the Ovoid. Since no overburden densities were included in the model, the high densities are placed in near surface cells which reduce the overall density contrast. The horizontal distribution of density obtained from the inverted model adequately outlines the edges of the Ovoid. The vertical distribution positions the high densities at the center of the Ovoid, but extends the anomalous region to a greater depth.

5.4 Constrained Inversions

Multiple constrained inversions were attempted in order to investigate methods of integrating geological data into the inversion process. The following section is

subdivided into three subsections based on the models used to constrain the gravity inversions. The first subsection will examine the effect of simply introducing a mesh to the inversion. The second section will include a series of inversions based on a simple two-layer geological model. The third and final subsection will provide a series of examples whereby the inversions are constrained using the densities obtained from drilling. The mesh MESH01, summarized in Section 3.4.2.1, was used during each inversion trial. The density models, gravity datasets and chosen parameters used in inversion are summarized in Figure 5.5.

5.4.1 Regional Constraint:

The unconstrained inversions INV01 and INV02 in the previous section were populated in a default type mesh generated by the Grav3d user interface. Using a mesh defined by the operator may be considered as a regional constraint, since it would allow the inversion to populate only those cells within the mesh. The following inversions will be constrained to cells that lie within the mesh MESH01 generated in Section 3.4.2.1. All other parameters chosen for inversions INV03 and INV04 are similar to those used for inversion INV01 and INV02 respectively. The recovered density models DEN03 and DEN04 for inversions INV03 and INV04 are illustrated in Figure 5.9 and Figure 5.10. In both examples the recovered amplitudes are lower than the expected values. However, the recovered amplitudes are closer to the expected values compared to inversions INV01 and INV02. As seen with INV01, the high density values recovered from INV03 with the "real" dataset OBS01 are placed close to line VB03. Due to the lack of data points, the edges are difficult to estimate from the smooth anomaly distribution in Figure 5.9. The

model DEN04 (Figure 5.10) recovered from inverting the synthetic dataset OBS02 provides a good estimate of the location of the high density region. The low density halo surrounding the high density region extends past the known position of the Ovoid. In both cases, the vertical dimensions of the Ovoid are difficult to estimate from the recovered models.

5.4.2 Overburden Constraint:

A simple two-layer regional model was constructed based on the known position of the overburden-bedrock contact. The regional model DM04 was constructed by assigning a constant density of 1.92 g/cc to region OB (RG01) and a constant density of 2.81 g/cc to region RG02 generated in Section 3.4.2.2. A density contrast model DM05 was created by removing a constant density of 2.67 g/cc from the regional model.

The inversions INV05 and INV06 were preformed to determine whether constraining the overburden cells would direct the inversion toward a more reasonable solution. The regional models were incorporated into the inversion via the reference model. Each cell within the mesh was weighted with upper and lower bounds of 2.30 g/cc and -0.75 g/cc reflecting the known density contrast range. With the exceptions of the reference model (DM05) and boundary model, all other parameters used during the INV05 and INV06 inversions are similar to the inversions INV03 and INV04. The density models DEN05 and DEN06 recovered from inverting the INDATA01 and INDATA02 datasets, using the regional model as a reference model, are illustrated in Figure 5.11 and Figure 5.12. Although the recovered density anomalies are centered at the known position of the Ovoid, it is difficult to estimate the horizontal extent of the

Ovoid. A large density halo of 1.0 g/cc surrounds a zone of high density with an approximate density of 1.5 g/cc. The reference model guides the inversion to generate a low density region consistent with the position of the overburden region. However, directly above the position of the Ovoid the overburden density is increased from -0.75 g/cc to 0.00 g/cc. The increase in densities over the Ovoid is a result of smoothing dictated by the length scales chosen in the model objective function. In both models, the anomaly has a major vertical component giving the anomalous region a rectangular appearance. Both DEN05 and DEN06 models provide little information on the vertical extent of the Ovoid.

In the previous examples, it was shown that the addition of a reference model guides the inversion to generate a low density region corresponding to the position of the overburden region. However, overburden cells located directly above the Ovoid are assigned a positive density contrast in the recovered models. To constrain the density value of the overburden cells, a cell weighting model (WDAT01) was created by assigning a constant weight of 1000 to region RG01 and a constant cell weight of 0.001 to region RG02 generated in Section 3.4.2.2. Assigning a high cell weight prevents the inversion from changing the values specified in the reference model for the OB cells. The inversion runs INV07 and INV08 use the same parameters as runs INV05 and INV06 with the addition of the regional variance model WDAT01. The resulting density models DEN07 and DEN08 recovered from INV07 and INV08 are shown in Figure 5.13 and Figure 5.14. A visual inspection clearly shows that the low density overburden cells contained in the reference model are recovered in the inverted models. The density amplitudes observed in the recovered models below the OB are similar to the amplitudes

estimated from Kriging the borehole data. Directly below the overburden region, the inversion algorithm generates a smooth transition which drives the top of the high density region to a greater depth.

To examine the effect of altering the length scales, a series of inversions were executed changing the length scale in the vertical direction. The synthetic dataset was inverted using a vertical length scale of 80m (INV09), 20m (INV10) and 5m (INV11) shown in Figure 5.15. The horizontal scales were kept at the default value of 20m. For regularity, all other parameters are similar to those used in INV08. Similarly, a series of inversions were executed varying only the horizontal length scales. The synthetic dataset was inverted using a horizontal length scale of 80m, 40m and 10m. The vertical scale was set at twice the cell thickness of 10m. The resulting inversions INV12, INV13 and INV14 are illustrated in Figure 5.16. As expected, larger length scales result in a greater amount of smoothing. A length scale of 5m in the vertical direction reduces the amount of smoothing occurring between the overburden layer and top of the Ovoid. In addition, a lower length scale pulls the high density cells toward the surface. Lowering the length scale reduces the transition between the high density cells to the low density background, reducing the halo surrounding the density anomaly. The smallest model was obtained by setting the vertical and horizontal length scales to 0m. Setting the length scales to 0m eliminates the last three terms in Equation 4.6. The resultant density model (DEN15) obtained from INV15 is illustrated in Figure 5.17. Removing the smoothing criteria from the inversion process, results in a model with a sharp density gradient between the OB-ENGN and OB-MASU interfaces.

The depth weighting function was adjusted to try and offset the result of constraining the overburden cells which push high densities to the base of the mesh. The synthetic data were inverted (INV16, INV17, INV18) using the same parameters and input files as INV08 adjusting only the depth weighting parameters. L_E, L_N and L_V length scales of 20m, 20m, and 5m were applied to the inversion since they reduce the amount of smoothing in the horizontal and vertical directions. The default parameter sets *beta* and *znot* to 2.0 and 1.25 respectively. To investigate the effect of changing the depth weighting parameter, the synthetic dataset INDATA02 was inverted using a *beta* of 1.75, 1.5 and 1.25. Decreasing the *beta* value places more emphasis on the gravitational contribution of near surface cells. The recovered models are summarized in Figure 5.18. As expected, decreasing the value of *beta* causes the high density cells to be placed closer to the base of the overburden region. Inverting the data using a *beta* of 1.5 and 1.25, yields a favorable density model with similar geometric characteristics as the Ovoid. The depth and width of the Ovoid can be reasonably estimated form the model. The average density contrast of 1.85 g/cc is also comparable to the average density contrast of the Ovoid which is approximately 1.96 g/cc (Figure 3.10C).

5.4.3 Borehole Constraints:

Multiple reference models were generated using the three dimensional capabilities in Gocad. The first reference model used to constrain the gravity inversion is the Kriged density model examined in Chapter 3 which incorporates all the drill hole data. The subsequent models will be derived from decimated drill log datasets. The three decimated

models used to constrain the inversions are derived from 50%, 25% and 5% of the drill logs.

5.4.3.1 Kriged Density Model:

Several inversions were performed using the Kriging density model as the reference model. The purpose of using the Kriging model is to recover the best estimate of the subsurface density distribution from inverting the gravity data. The first example (INV19) inverts the residual gravity dataset INDATA01 using the Kriged density model as the reference model and the regional weighting model (WDAT01) to constrain the overburden cells. The horizontal length scales were set to 20m while the vertical length scales were set to 5m. The depth weighting parameters *beta* and *znot* were set to 1.5 and 1.25. The recovered density model DEN19 shown in Figure 5.19 generates a model which correlates well with the known position of the Ovoid illustrated in Figure 5.20. The outline of the Ovoid is well preserved while the high density region within the body of the Ovoid is positioned beneath the location of line VB03.

Using the same parameters as INV19, the INDATA02 dataset was inverted to produce a recovered model (DEN20) illustrated in Figure 5.21. The recovered density distribution matches the overall density model obtained from Kriging. However, the high density cells are placed at the top and base of the body. The difference observed between the Kriged density model and the recovered model is most likely a result of the distance weighting parameters applied during the inversion. The INDATA02 dataset was inverted (INV21) using horizontal and vertical length scales of 0m, and a *beta* of 2.0. In addition, the overburden cells were constrained using the WDAT01 weighting model as in Figure

5.20. The high density regions within the recovered model, shown in Figure 5.22, are now comparable to the Kriged density model displayed in Figure 5.20. In order to recover a model with similar density variations within the Ovoid using the INDATA01 dataset, the reference model must be weighted according to the drill log locations.

The reference model (DM02) was weighted according to the Kriging variances calculated in Section 3.4.3. Cells with a variance between the range of 0 and 0.2 were weighted with a high cell weight of 1000. These variances correspond to the cells intersecting or adjacent to a drill log. Cells with a variance greater than 0.2 were assigned a cell weight of 0.001. The weightings along the cell interfaces were held constant, using the default value of 1.0. Using the same parameters as INV19, the resulting weighting model (WDAT02) was used to constrain inversion INV22. The recovered density anomaly illustrated in Figure 5.23 now has high density cells corresponding to the location of high density regions within the Ovoid.

5.4.3.2 Decimated Model 50% (DM06):

A density contrast model was generated using 56 drill logs or 50% of the drill logs (Figure 5.24) used to generate the original Kriged density model. A similar approach was used to build the density model as described in Section 3.3 and 3.4. Instead of Kriging the dataset using wireframes provided by VBNC, the model was Kriged using all data contained in the drill logs chosen. The density values were populated in only the cells located below the bedrock layer classified as the RG02 region (Section 3.4.2.2). Cells located in the OB region (RG01) were assigned a constant density of 1.92 g/cc. The three-dimensional variogram model was determined from the drill log data and estimated

to have a major, minor and vertical range of 120m, 80m, and 50m. The dominant direction and dip was orientated at 135° and 15° respectively. The procedures used to calculate the three dimensional variograms are summarized in Section 3.3.2. Using the variogram parameters, ordinary Kriging was used to populate the bedrock region (RG02). The density model was limited to only those cells with variances between 0 and 1.0 shown in Figure 5.25. Cells containing a greater variance than 1.0 or assigned a non data value were assigned a constant density of 2.81 g/ec. This method was chosen since a limited number of data points are contained in the ENGN region. The density contrast model DM06 (relative to 2.67 g/cc) shown in Figure 5.26 correctly positions high densities with the known position of the Ovoid. To constrain the inversion, a weighting model WDAT03 was designed based on the variances obtained from Kriging. High cell weights (1000) were applied to the to the OB region and to cells which had variances between 0 and 0.2 shown in Figure 5.25. This variance range corresponds to cells that are intersected or adjacent to cells that have been intersected by a drill log. Low cell weights (0.001) were assigned to any cell below the overburden region with variances greater than or equal to 0.2.

The density contrast model DM06 was incorporated into the inversion program as the reference model. The INDATA02 was inverted using a horizontal and vertical length scale of 20m and 5m respectively. The depth weighting parameters *beta* and *znot* were set to 2.0 and 1.25. The resulting density model DEN23 corresponding to inversion run INV23 is shown in Figure 5.27. The recovered model is similar to the reference model, but places higher densities at the center of the Ovoid. To constrain the densities within the Ovoid the weighting model was incorporated into the inversion INV24. Constraining

the inversion limits the high densities within the Ovoid and increases the width of the anomaly as shown in Figure 5.28. The recovered model does a better job matching the known position of the Ovoid. Due to the location and spatial variability of the collected data, the INDATA01 dataset was not inverted using DM06 as a reference model. The INDATA01 dataset will be inverted when the spatial resolution of the borehole data is less than the collected data.

5.4.3.3 Decimated Model 25% (DM07):

A density contrast model DM07 was generated using 28 drill logs or 25% of the drill logs (Figure 5.29) used to generate the original Kriged density model. The procedures used to generate the model follow those described in the previous Section 5.4.3.2. The major, minor and vertical range of the variogram model was estimated to be 120m, 50m and 40m. A constant density of 1.92 g/cc was applied to the OB region. In addition, cells containing a variance grater than 1.0 (Figure 5.30) were assigned a constant density of 2.81 g/cc. The resultant density model DM07 is illustrated in Figure 5.31. As in the previous section, the weighting model WDAT04 was designed based on the cell variances. High cell weights (1000) were applied to the OB region and to cells which had variances between 0.0 and 0.20 shown in Figure 5.30. This variance range corresponds to cells that are intersected or adjacent to cells that have been intersected by a drill log. Low cell weights (0.001) were assigned to any cell below the overburden region with variances greater than or equal to 0.2.

The density model was incorporated into the inversion program via the reference model. The INDATA02 was inverted (INV25) using the same parameters as INV23.

The recovered density anomaly illustrated in Figure 5.32 is comparable with the input reference model. The recovered amplitude is slightly higher than the reference model which reflects the density of the Ovoid. The DM07 model has a lower overall density contrast, which may be a result of smoothing the decimated dataset. Constraining the inversion using the weighting model WDAT04 causes high densities to be repositioned within the Ovoid (Figure 5.33). The high densities are concentrated at UTM easting and northing 555900m and 6243200m, similar to the position observed in the Kriged density contrast model (Figure 5.20). As described in Section 5.4.3.2, the INDATA01 dataset was not inverted due to the spatial distribution of the collected data. The dataset will be inverted in the following section.

5.4.3.4 Decimated Model 5% (DM08):

A density model was generated using 6 drill logs (Figure 5.34) or 5% of the drill logs used to generate the original Kriged density model. The spatial distribution in the vertical direction along the 6 drill logs were estimated using Gocad. Due to the limited number of drill logs, the spatial distribution in the horizontal direction can not be accurately estimated. The horizontal distribution was estimated from the INDATA02 gravity dataset. The half maximum of the gravitational anomaly can be used as a guide to estimate the approximate edge of the anomalous mass (Telford et al, 1990). From the FM01 gravity profiles shown in Figure 5.1, the half maximum is approximately located at 2.0 mGal. The 2.0 mGal contour of the INDATA02 dataset shown in Figure 5.4 follows the projected outline of the Ovoid. Using the gravity data as an estimate, the major and minor range is estimated to be approximately 240m by 180m orientated at 120°. Due to

the limited dataset, no dip information was incorporated into the variogram. The density model was designed using the same procedures as those described for density models DM06 and DM07. A constant density of 1.92 g/cc was applied to the OB region while cells containing a greater variance of 1.5 (Figure 5.35) were assigned a constant density of 2.81 g/cc. In this example, a variance of 1.5 was chosen since it coincides with the 2.0 mGal contour illustrated in Figure 5.4. The model displayed in Figure 5.36 provides a reasonable estimate of the high density region along the western and southern edges. The eastern and northern edges of the Ovoid are not well defined due to the location of the drill logs chosen to be incorporated into the model, as summarized in Figure 5.34. The weighting model WDAT05 was designed using the same method as the WDAT03 and WDAT04 models described in the previous two subsections.

The INDATA02 was inverted using the DM08 as a reference model. All other parameters are similar to those used for inversion INV23 and INV25. The recovered density anomaly shown in Figure 5.37 extends the high densities to the north and east relative to the reference model shown in Figure 5.36. The inversion populates cells with high densities that could not otherwise be estimated from Kriging methods. Incorporating a weighting model (WDAT05) into the inversion based on cell variances, guides the inversion to recover a model with many similarities when compared to the density distribution of the Ovoid. The anomaly recovered from INV28 (Figure 5.38) populates medium densities (~1.00 g/cc) at the base of the mesh. This is most likely a result of smoothing which occurs in the vertical direction due to the depth weighting and length scales. Overall, the maximum thickness, width and dip can be easily estimated from the recovered density anomaly.

The INDATA01 dataset was inverted to determine how the gravity data collected at Voisey's Bay could have contributed using the 6 drill logs chosen in this study. The depth weighting function *beta* and length scales were set to 1.50, and 100m, 40m and 20m respectively. The recovered model shown in Figure 5.39 is a slight improvement of the Kriged density model DM08. The recovered anomaly suggests that high densities in the east-west direction should be placed between line VB03 and VB04 illustrated by eastern dipping density anomaly of approximately 1.0 g/cc. However, due to the lack of data in the east west direction, the edges of the Ovoid can not be inferred from the recovered model. The recovered model in the north-south direction is also improved slightly. The recovered density anomaly has a greater amplitude and thickness compared to DEN08, which is more representative of the amplitude and thickness of the Ovoid shown in Figure 3.11.

5.5 Results

The multiple inversion trials carried out using the INDATA01 (Figure 5.6) and INDATA02 (Figure 5.7) datasets illustrate that geologically meaningful results can be achieved when geological information is incorporated into the inversion process. Unconstrained inversions INV01 and INV02 shown in Figure 5.6 and Figure 5.8 generate density models that provide reasonable estimates of the location of the Ovoid. The depth, maximum width and maximum thickness can be estimated from the density anomalies. The recovered amplitudes of the unconstrained inversions are lower than the known density contrasts due to cells having densities of approximately 0.60 g/cc being populated at a greater depth. The difference between the recovered models obtained from

unconstrained inversions of the INDATA01 and INDATA02 datasets are not all that significant. The differences become apparent when geological information is incorporated into the inversion.

Significant improvements were observed in the recovered models when the overburden densities were incorporated into the inversion. Weighting overburden cells resulted in anomalies containing correct amplitudes and geometric characteristics similar to the Ovoid when the proper parameters were adjusted. The parameters which had major influences on the resultant models were the length scales and depth weighting functions. Smaller length scales in the horizontal and vertical directions (Figure 5.15 and Figure 5.16) reduce the amount of smoothing observed in the models. In addition, the depth weighting parameter *beta* had to be reduced to account for the sharp contact between the OB and MASU regions illustrated in Figure 5.18. The sharp interfaces between the OB-MASU and ENGN-MASU are difficult to reproduce in typical minimum-structure inversion programs. Weighted reference models must be incorporated into the inversion to generate sharp interfaces.

The density logs were incorporated into the inversion program via a Kriged reference model generated in Gocad. The recovered density model from INV19 (Figure 5.19) exhibits excellent correlation with the boundaries of the Ovoid derived from Kriging the density data. However, internal variations are not well resolved when inverting the INDATA01 dataset. Inverting the INDATA01 dataset causes high densities to be located under line VB03 shown in Figure 5.19. This is a consequence of having the gravity data along lines that are offset from the thickest section of the Ovoid by approximately 70m. When the proper parameters are chosen, the inversion is able to

reproduce the internal density variations when the INDATA02 pseudo-dataset is inverted using the Kriging model as a referenee model.

Using decimated datasets can provide acceptable models when incorporated as reference models. The decimated models DM06 and DM07 generated from Kriging 56 and 28 density drill logs are relatively similar in amplitude and geometry. However, a noticeable improvement is observed when using the DM08 model, generated from Kriging 6 drill logs, as a reference model. Due to the position of the 6 drill logs (Figure 5.34), the northernmost and easternmost edges are not well defined in the Kriging model (DM08) observed in Figure 5.36. The inversion places high densities in these regions considerably improving the density model illustrated in Figure 5.37 and Figure 5.38. On the other hand, inverting the collected data (INDATA01) generates a smooth model DEN29 (Figure 5.39), providing only a slight improvement to the subsurface density distribution as illustrated in Figure 5.36. The northernmost and easternmost edges are difficult to estimate from the recovered model DEN29.

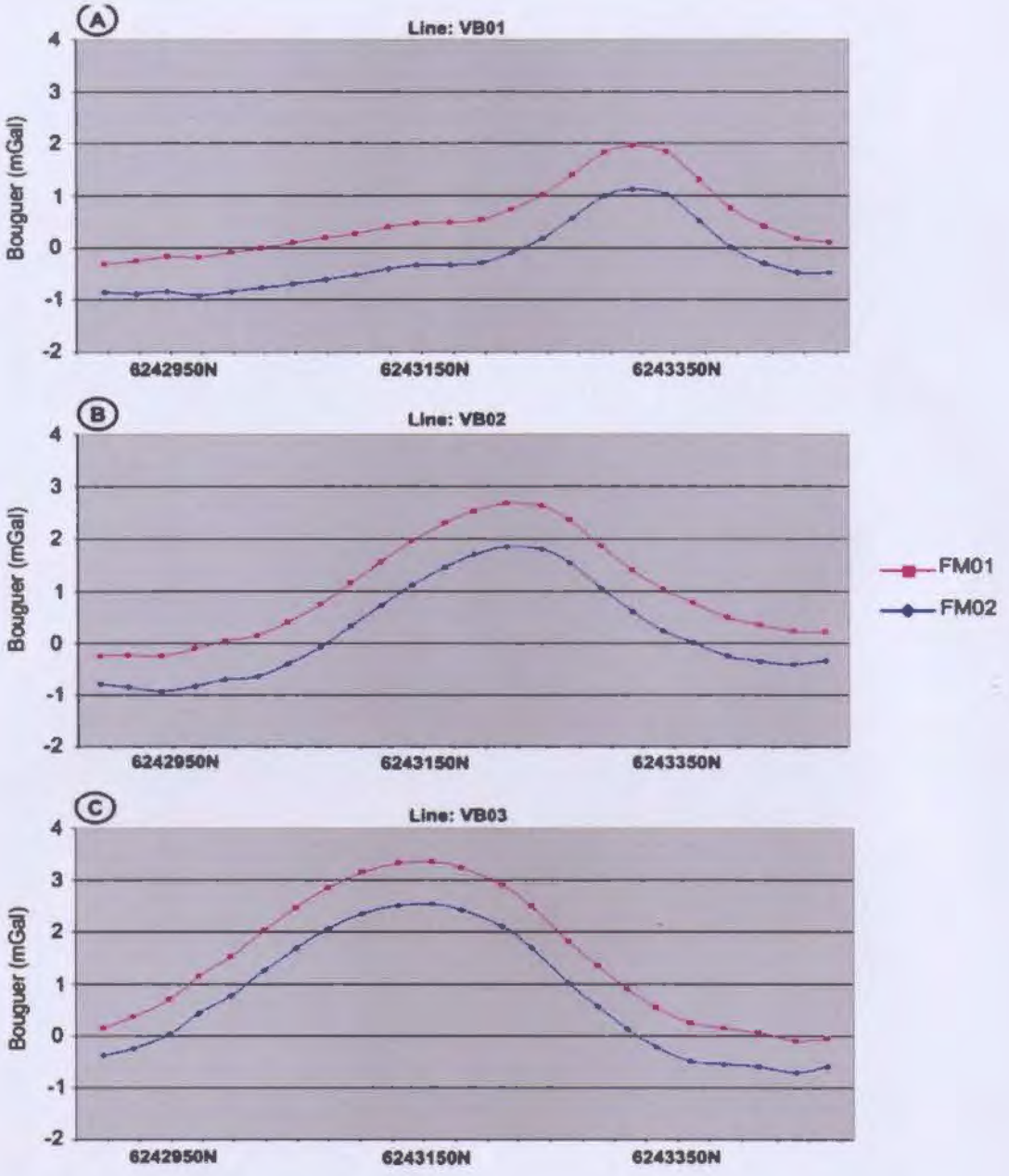

Figure 5.1: Calculated gravitational anomalies crossing the Ovoid along lines VB01 (A), VB02 (B) and VB03 (C) obtained from forward models FM01 and FM02. Coordinates are in UTM meters relative to NAD83 (Zone 21). Scale can be inferred from coordinate annotations.

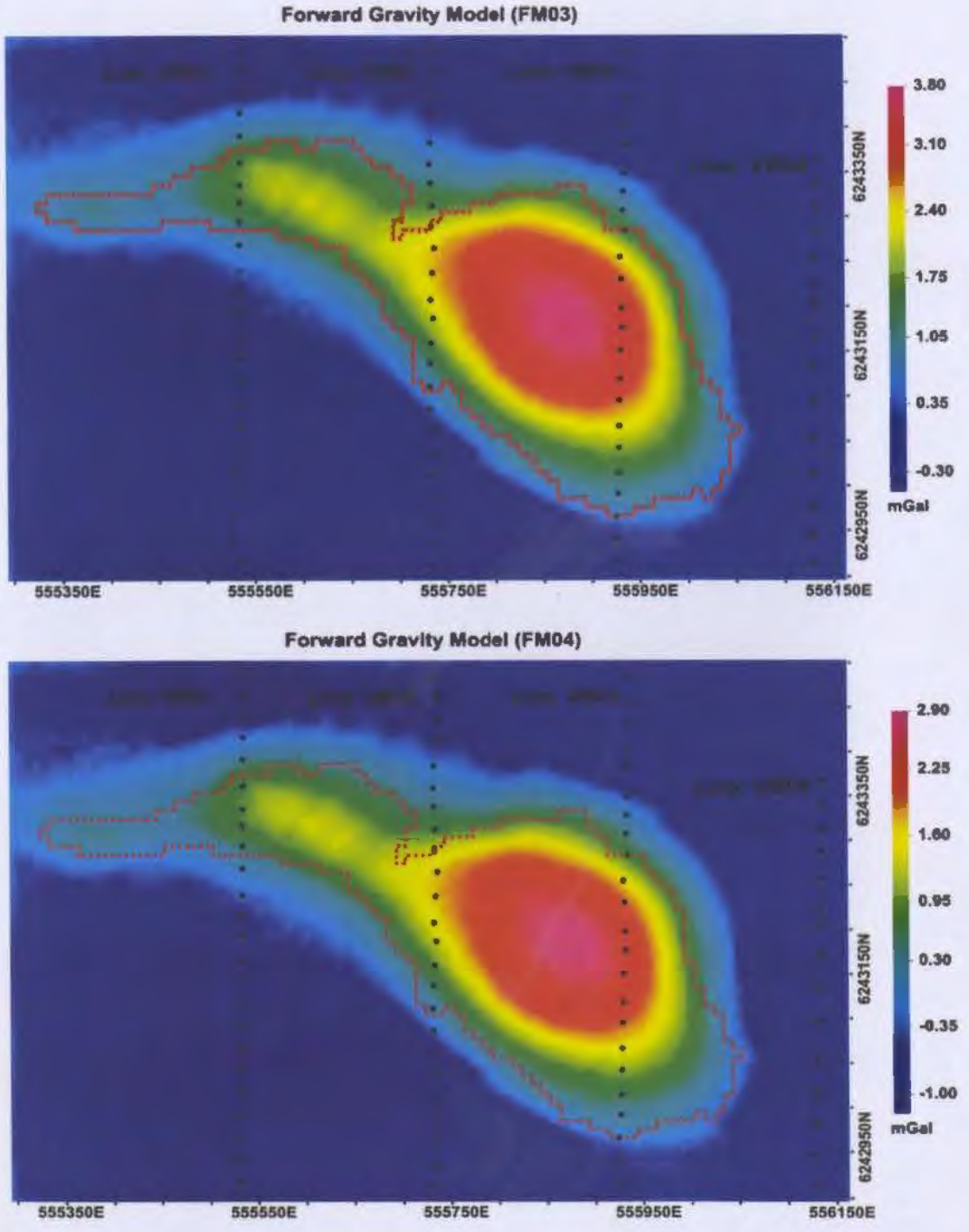

Figure 5.2: The calculated gravitational field obtained from the forward gravity models FM03 (top) and FM04 (bottom). The MASU unit projected to the surface is shown in red while the survey lines VB01, VB02, VB03 and VB04 are shown in black. Coordinates are in UTM meters relative to NAD83 (Zone 21). Scale can be inferred from coordinate annotations.

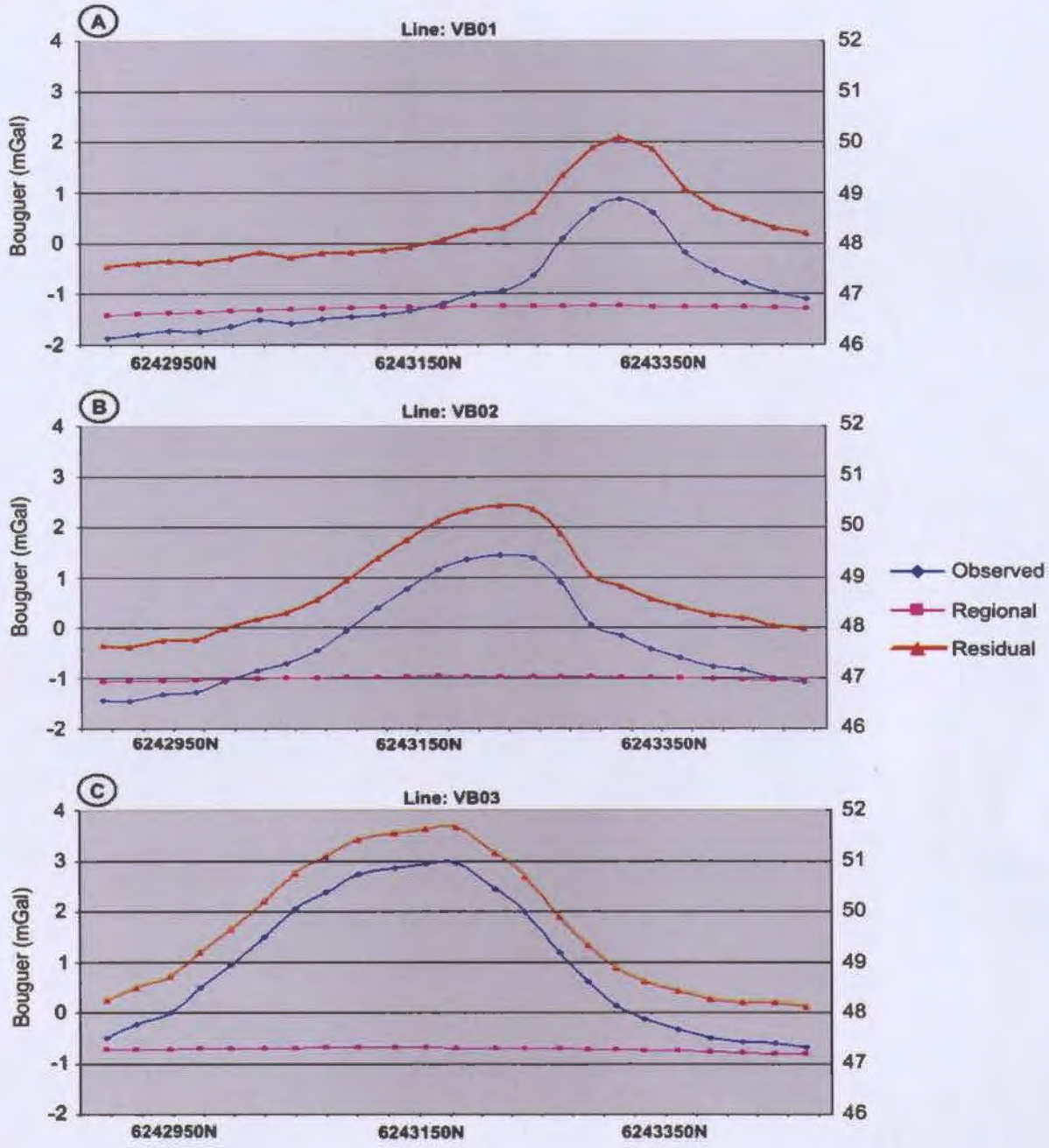

Figure 5.3: The observed, regional and residual (INDATA01) profiles along lines VB01 (A), VB02 (B) and VB03 (C). The observed and regional fields are relative to the right side axis. Residuals are relative to the left side axis. Coordinates are in UTM meters relative to NAD83 (Zone 21). Scale can be inferred from coordinate annotations.

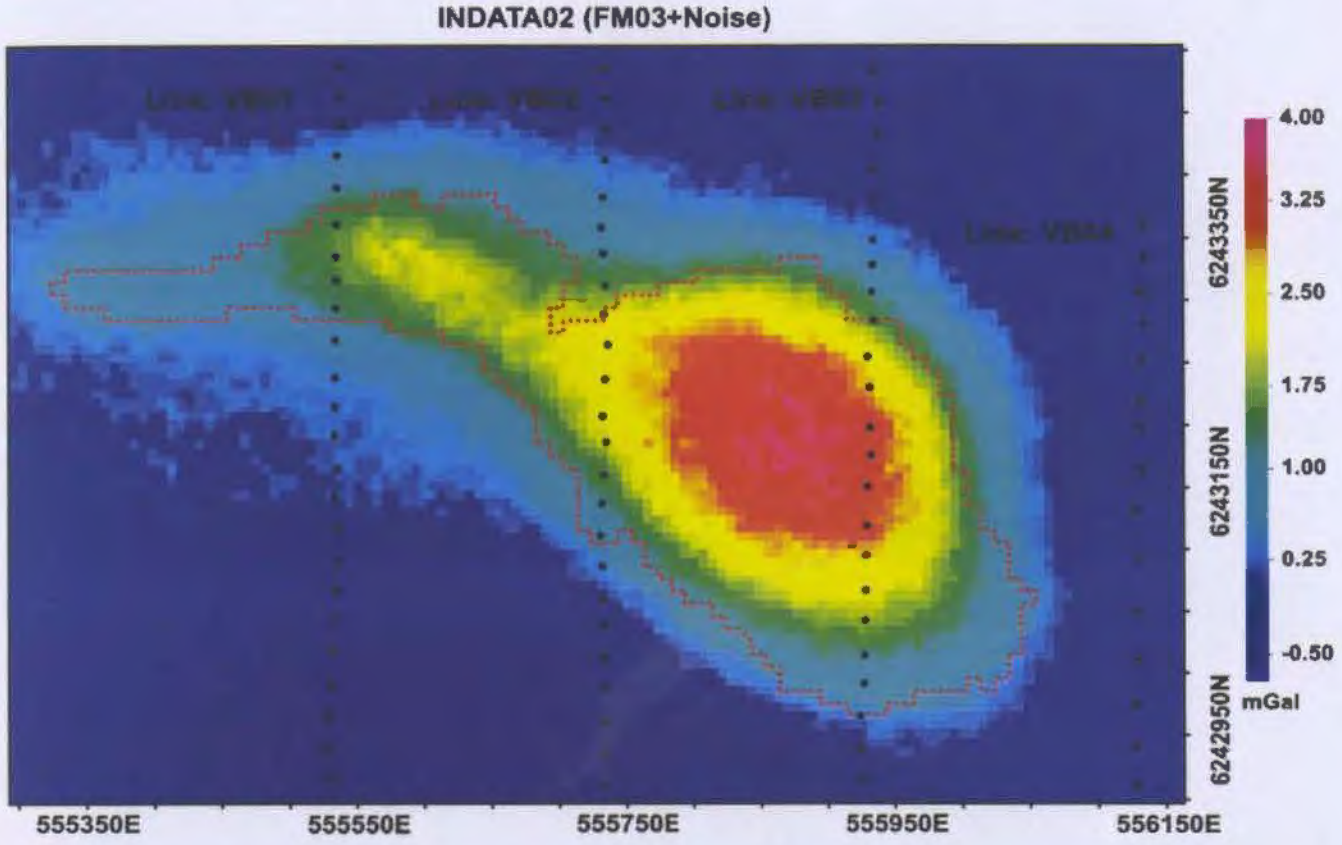

Figure 5.4: The INDATA02 dataset generated by adding Gaussian noise with a standard deviation of 0.05 mGal and 2% of the data value of the FM03 dataset. The MASU unit projected to the surface is shown in red while the survey lines VB01, VB02, VB03 and VB04 are shown in black. Coordinates are in UTM meters relative to NAD83 (Zone 21). Scale can be inferred from coordinate annotations.

Inversion	Mesh (MESH)	OBS.grv (INDATA)	Weights (beta,znot)	Ref.	Bounds (High, Low)	Length S. (Le, Ln, Lv)	W.dat	Model (DEN)	Figure
INV01	02	01	(2, 1.25)	none	null	100, 40, 20	none	1	5.06
INV02	02	02	(2, 1.25)	none	null	20, 20, 20	none	2	5.08
INV03	01	01	(2, 1.25)	none	null	100, 40, 20	none	3	5.09
INV04	01	02	(2, 1.25)	none	null	20, 20, 20	none	4	5.10
INV05	01	01	(2, 1.25)	DM05	(-0.75,2.3)	100, 40, 20	none	5	5.11
INV06	01	02	(2, 1.25)	DM05	(-0.75,2.3)	20, 20, 20	none	6	5.12
INV07	01	01	(2, 1.25)	DM05	(-0.75,2.3)	100, 40, 20	WDAT01	7	5.13
INV08	01	02	(2, 1.25)	DM05	(-0.75,2.3)	20, 20, 20	WDAT01	8	5.14
INV09	01	02	(2, 1.25)	DM05	(-0.75,2.3)	20, 20, 80	WDAT01	9	5.15A
INV10	01	02	(2, 1.25)	DM05	(-0.75,2.3)	20, 20, 20	WDAT01	0	5.15B
INV11	01	02	(2, 1.25)	DM05	(-0.75,2.3)	20, 20, 5	WDAT01	11	5.15C
INV12	01	02	(2, 1.25)	DM05	(-0.75,2.3)	80, 80, 10	WDAT01	12	5.16A
INV13	01	02	(2, 1.25)	DM05	(-0.75,2.3)	40, 40, 10	WDAT01	13	5.16B
INV14	01	02	(2, 1.25)	DM05	(-0.75,2.3)	10, 10, 10	WDAT01	14	5.16C
INV15	01	02	(2, 1.25)	DM05	(-0.75,2.3)	0, 0, 0	WDAT01	15	5.17
INV16	01	02	(1.75, 1.25)	DM05	(-0.75,2.3)	20, 20, 5	WDAT01	16	5.18A
INV17	01	02	(1.50, 1.25)	DM05	(-0.75,2.3)	20, 20, 5	WDAT01	17	5.18B
INV18	01	02	(1.25, 1.25)	DM05	(-0.75,2.3)	20, 20, 5	WDAT01	18	5.18C
INV19	01	01	(1.50, 1.25)	DM02	(-0.75,2.3)	20, 20, 5	WDAT01	19	5.19
INV20	01	02	(1.50, 1.25)	DM02	(-0.75,2.3)	20, 20, 5	WDAT01	20	5.21
INV21	01	02	(2, 1.25)	DM02	(-0.75,2.3)	0 ,0 ,0	WDAT01	21	5.22
INV22	01	02	(1.50, 1.25)	DM02	(-0.75,2.3)	20, 20, 5	WDAT02	22	5.23
INV23	01	02	(2, 1.25)	DM06	(-0.75,2.3)	20, 20, 5	WDAT01	23	5.27
INV24	01	02	(2, 1.25)	DM06	(-0.75,2.3)	20, 20, 5	WDAT03	24	5.28
INV25	01	02	(2, 1.25)	DM07	(-0.75,2.3)	20, 20, 5	WDAT01	25	5.32
INV26	01	02	(2, 1.25)	DM02	(-0.75,2.3)	20, 20, 5	WDAT04	26	5.33
INV27	01	02	(2, 1.25)	DM08	(-0.75,2.3)	20, 20, 5	WDAT01	27	5.37
INV28	01	02	(2, 1.25)	DM08	(-0.75,2.3)	20, 20, 5	WDAT05	28	5.38
INV29	01	01	(2, 1.25)	DM08	(-0.75,2.3)	100, 40, 20	WDAT05	29	5.39

Figure 5.5: A table illustrating the fundamental inversion parameters and input files used for each inversion trial. The input gravity data and weighting models are represented by OBS.grv and W.dat respectively.

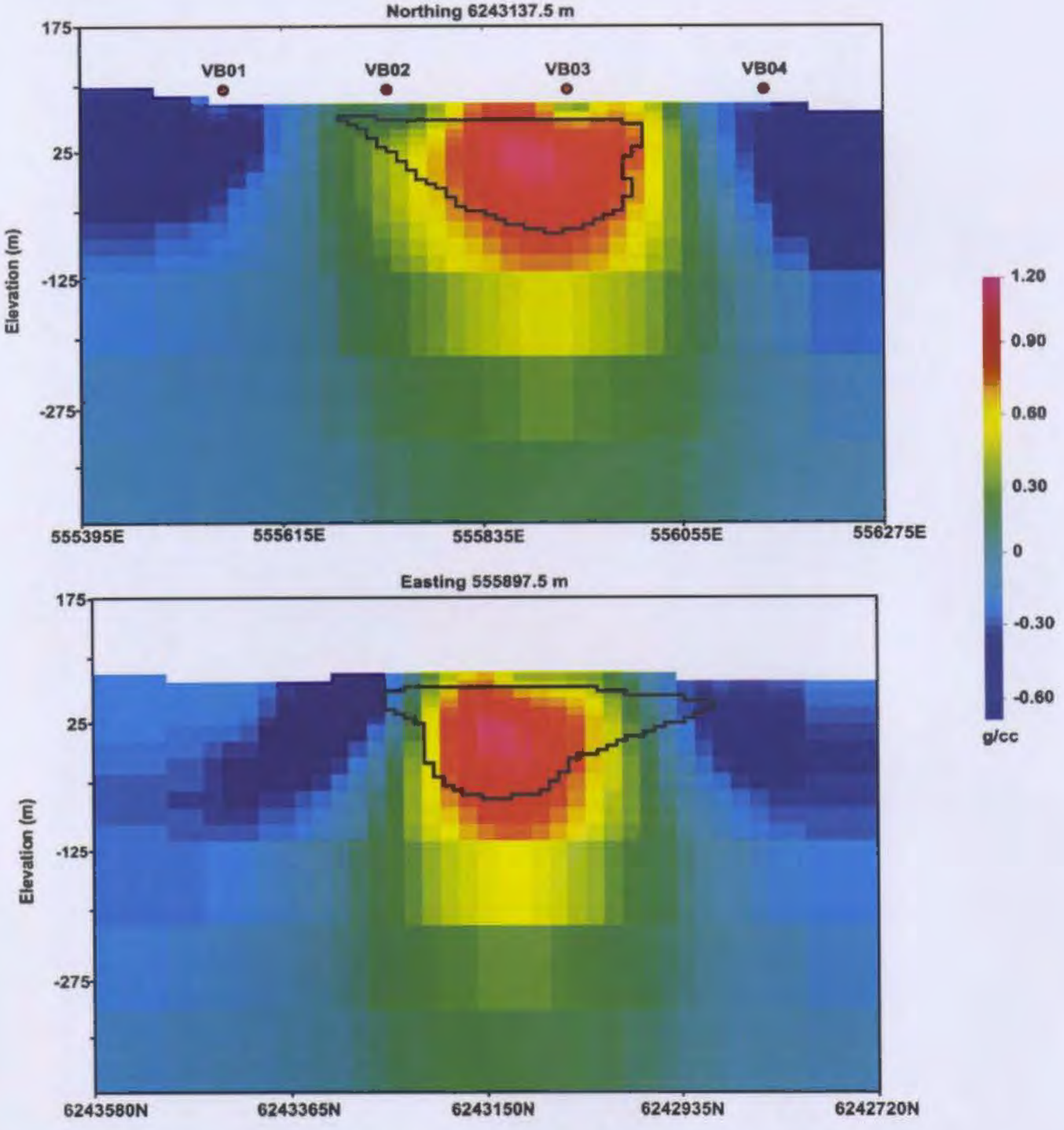

Figure 5.6: The density model DEN01 recovered from inversion INV01. Sections are along UTM northing 6243137.5m and easting 555897.5m (NAD83). The known position of the MASU unit is shown in black. The known position of gravity lines VB01, VB02, VB03 and VB04 perpendicular to east-west section are shown in red. Scale can be inferred from coordinate annotations.

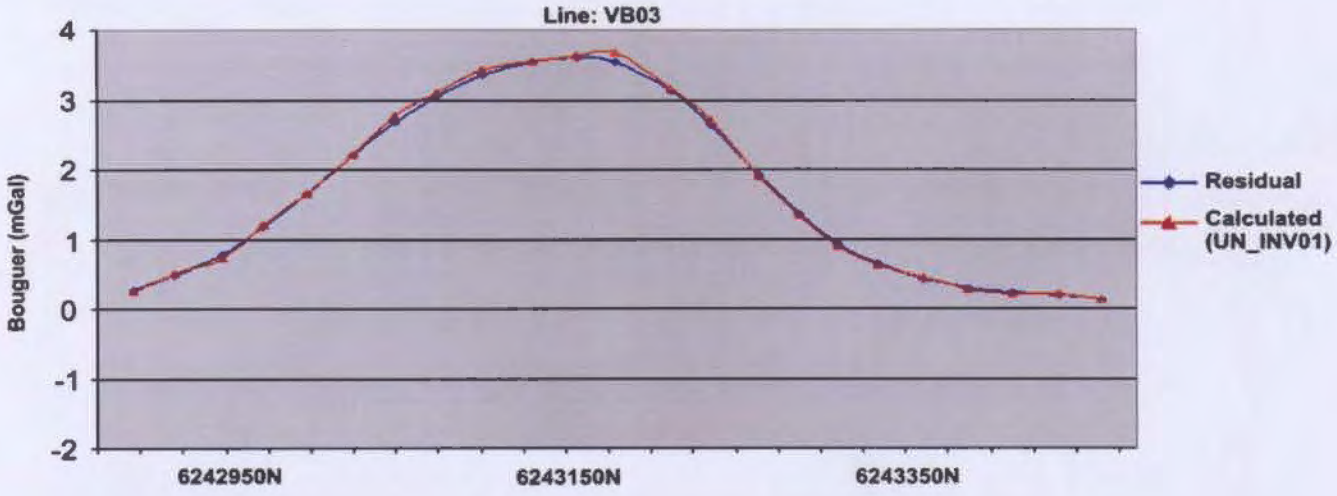

Figure 5.7: A profile along line VB03 comparing the calculated gravity anomaly produced by the density model shown in Figure 10 with the residual data (OBS01). Coordinates are in UTM meters relative to NAD83 (Zone 21). Scale can be inferred from coordinate annotations.

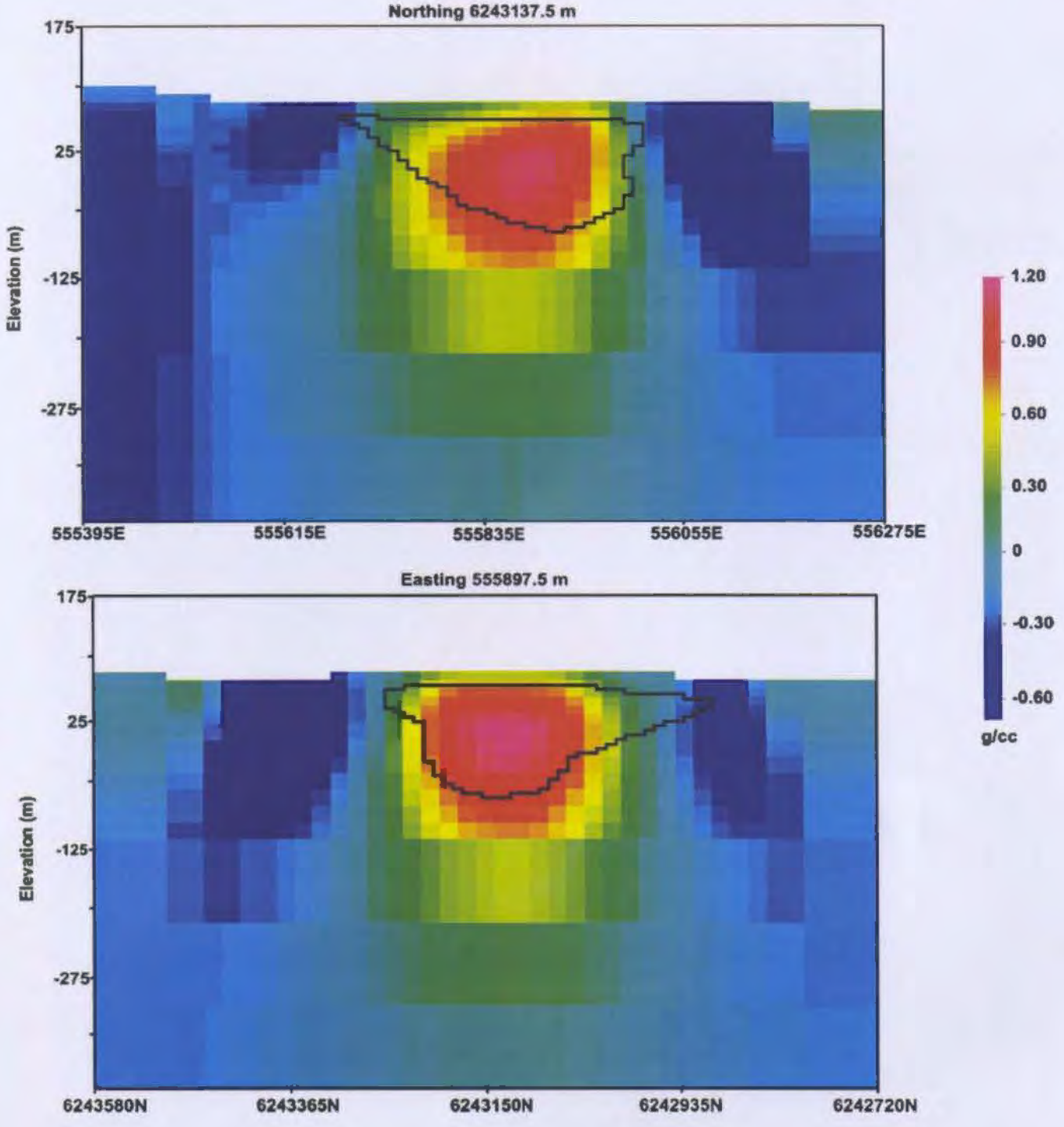

Figure 5.8: The density model DEN02 recovered from inversion INV02. Sections are along UTM northing 6243137.5m and easting 555897.5m (NAD83), with elevations relative to sea level. The known position of the Ovoid is shown in black. Scale can be inferred from coordinate annotations.

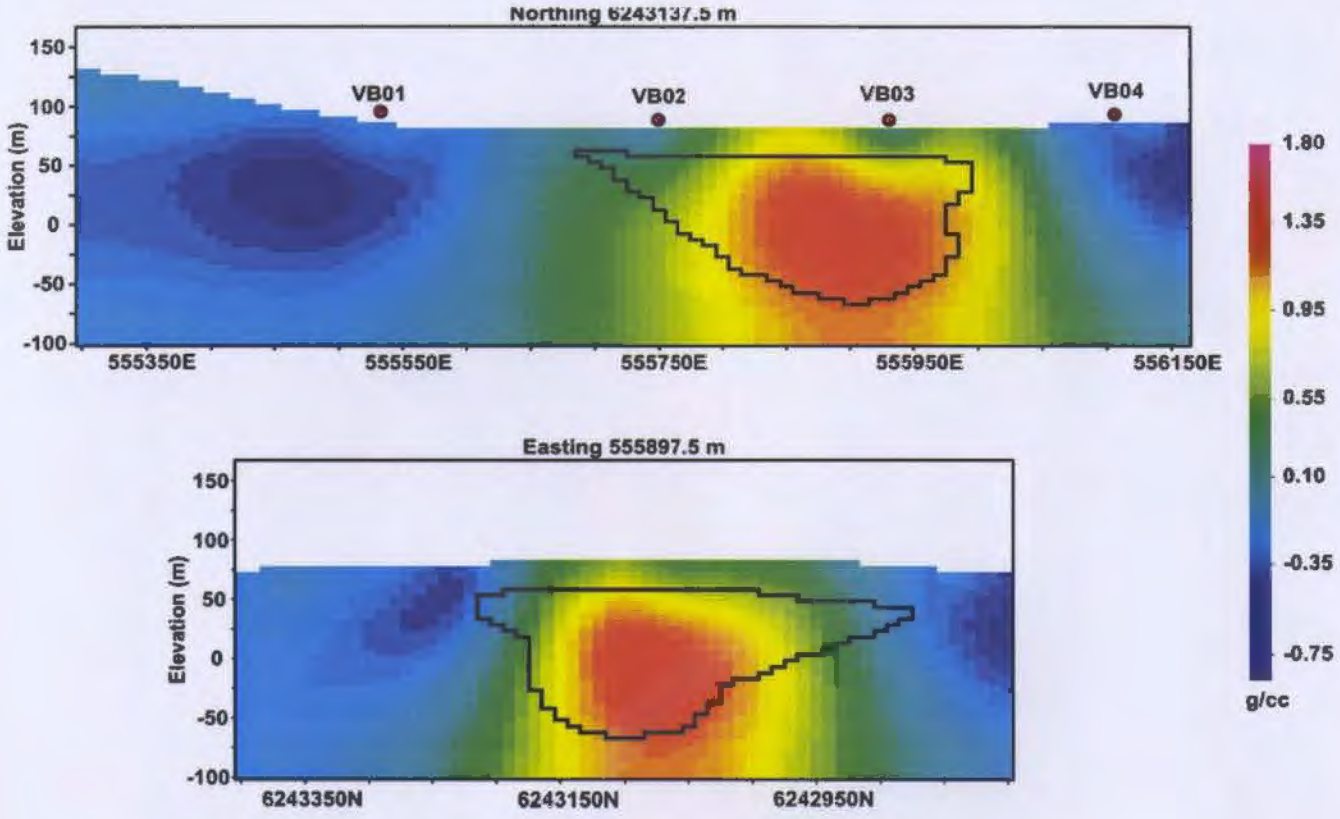

Figure 5.9: The density model DEN03 recovered from inversion INV03. Sections are along UTM northing 6243137.5m and easting 555897.5m (NAD83), with elevations relative to sea level. The known position of the Ovoid is shown in black. The position of gravity lines VB01, VB02, VB03 and VB04 perpendicular to east-west section are shown in red. Scale can be inferred from coordinate annotations.

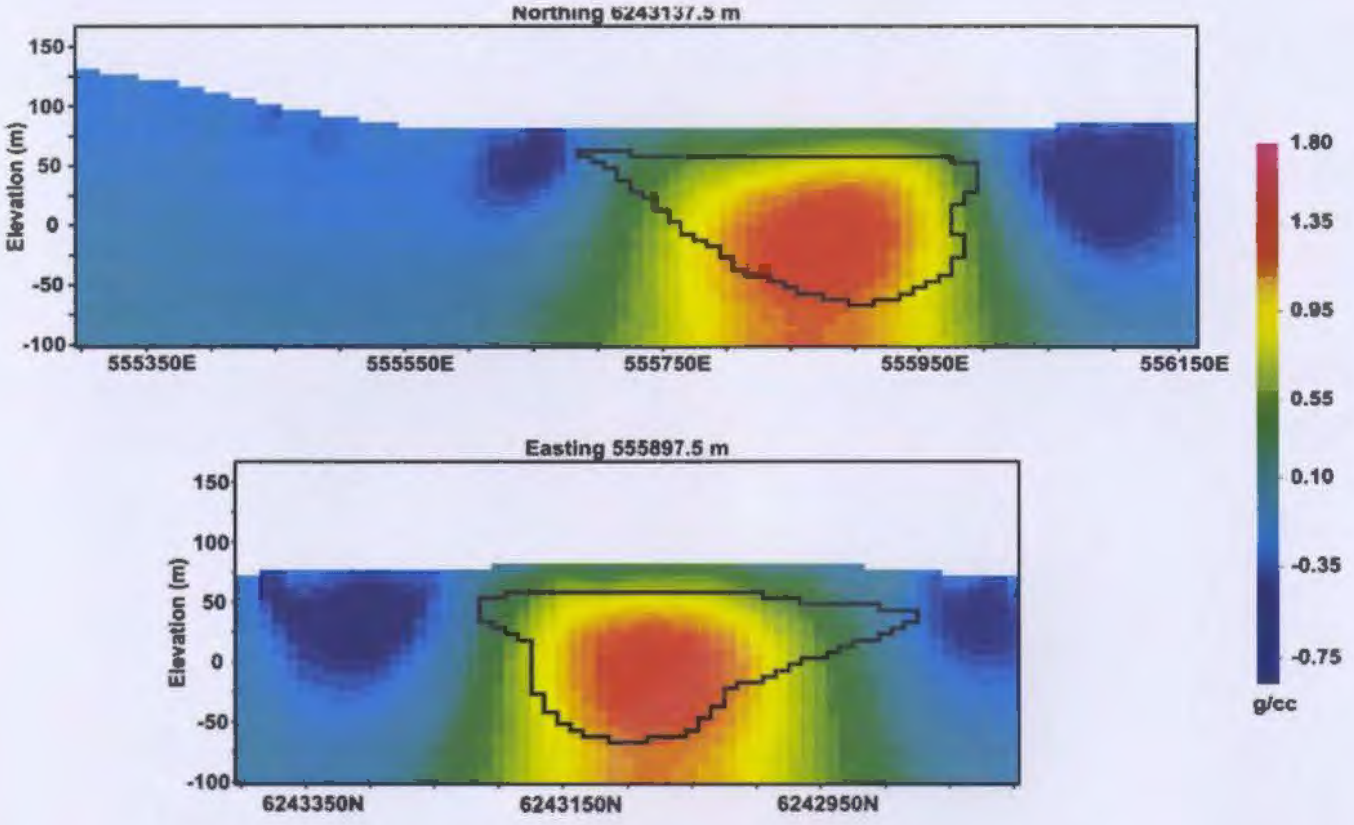

Figure 5.10: The density model DEN04 recovered from inversion INV04. Sections are along UTM northing 6243137.5m and easting 555897.5m (NAD83), with elevations relative to sea level. The known position of the Ovoid is shown in black. Scale can be inferred from coordinate annotations.

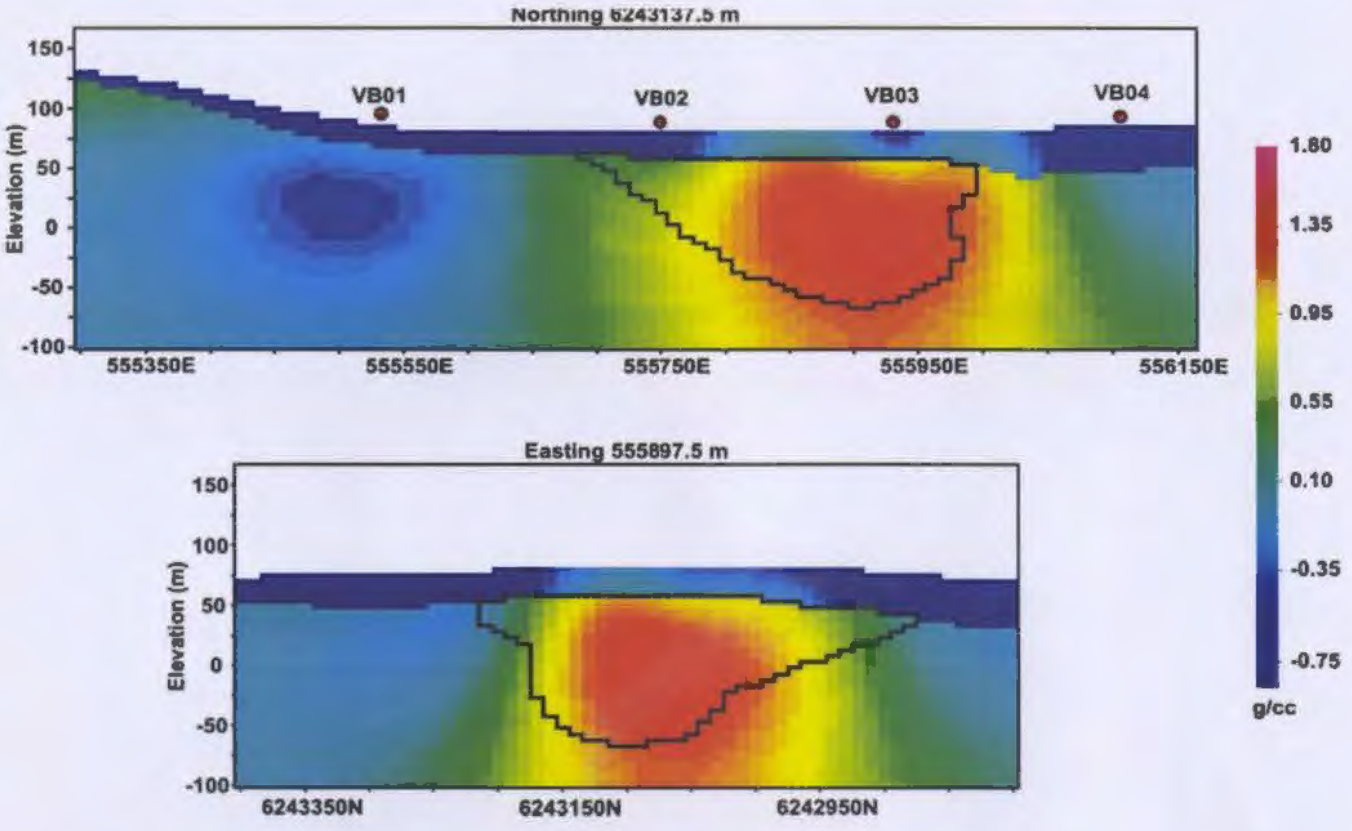

Figure 5.11: The density model DEN05 recovered from inversion INV05. Sections are along UTM northing 6243137.5m and easting 555897.5m (NAD83), with elevations relative to sea level. The known position of the Ovoid is shown in black. The position of gravity lines VB01, VB02, VB03 and VB04 perpendicular to east-west section are shown in red. Scale can be inferred from coordinate annotations.

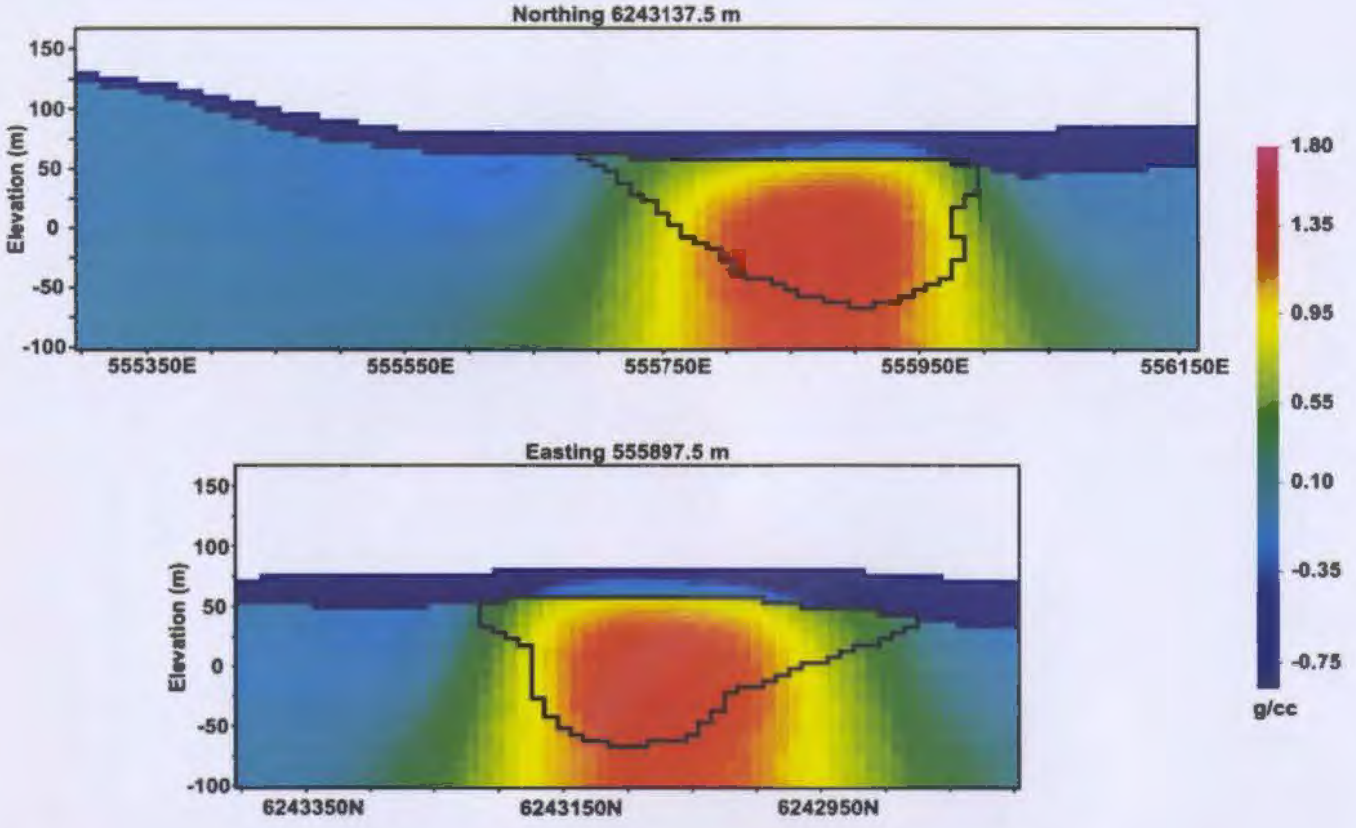

Figure 5.12: The density model DEN06 recovered from inversion INV06. Sections are along UTM northing 6243137.5m and easting 555897.5m (NAD83), with elevations relative to sea level. The known position of the Ovoid is shown in black. Scale can be inferred from coordinate annotations.

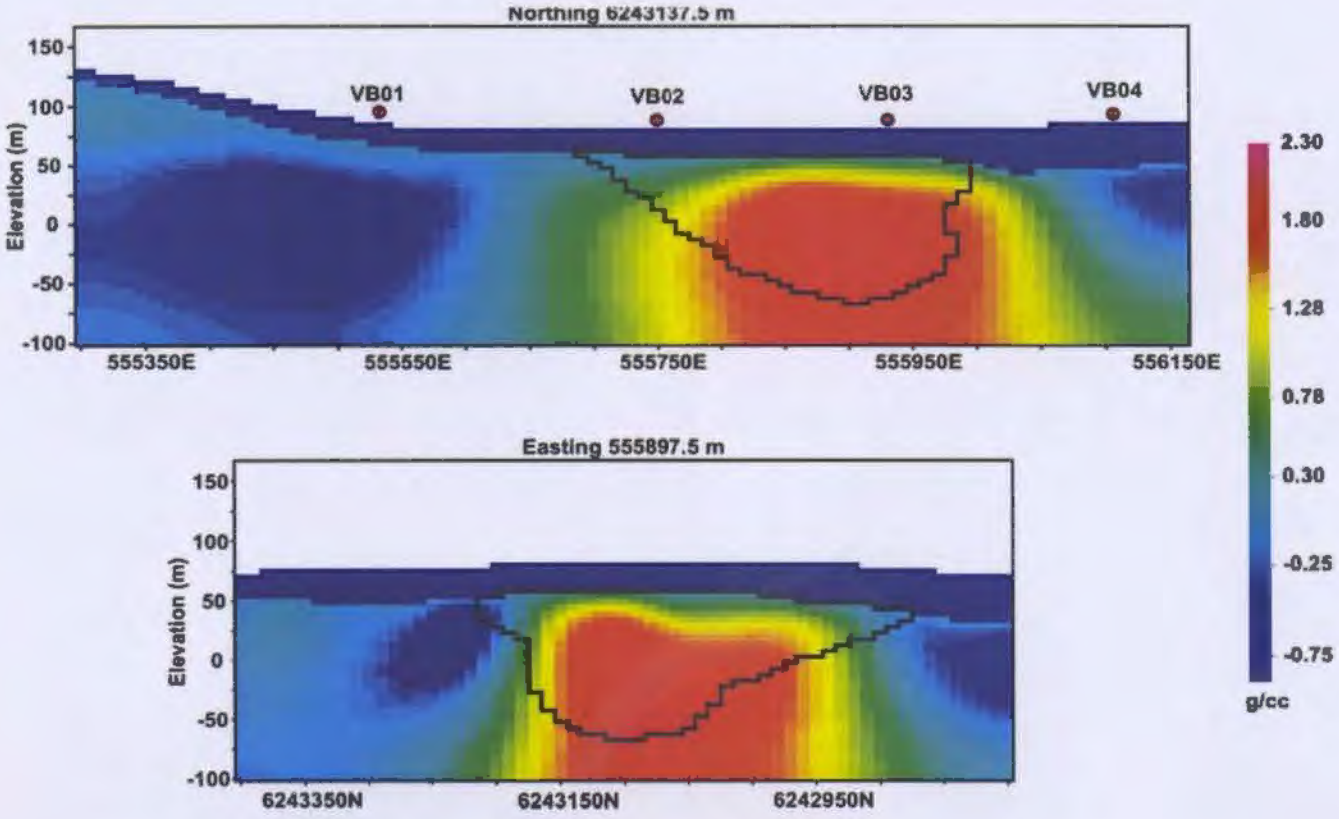

Figure 5.13: The density model DEN07recovered from inversion INV07. Sections are along UTM northing 6243137.5m and easting 555897.5m (NAD83), with elevations relative to sea level. The known position of the Ovoid is shown in black. The position of gravity lines VB01, VB02, VB03 and VB04 perpendicular to east-west section are shown in red. Scale can be inferred from coordinate annotations.

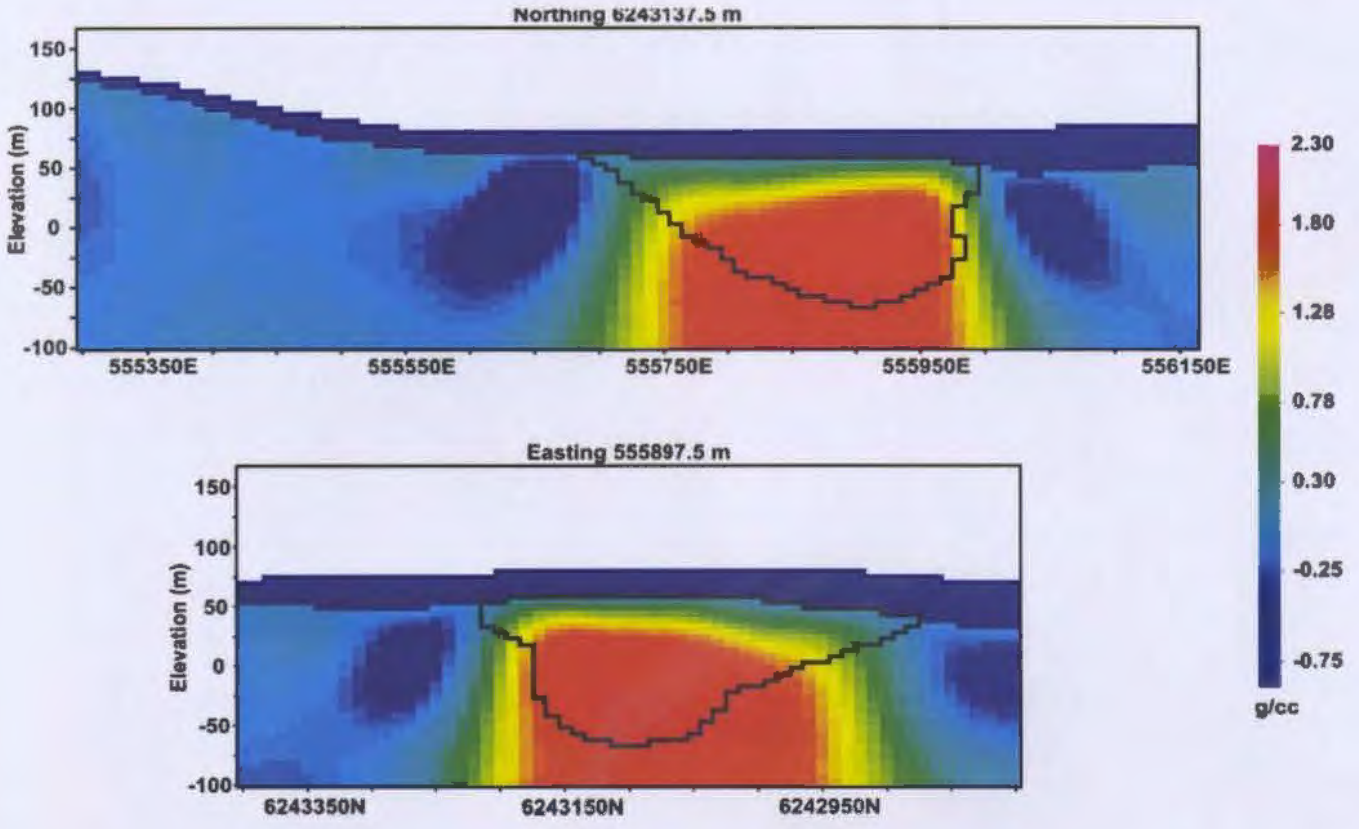

Figure 5.14: The density model DEN08 recovered from inversion INV08. Sections are along UTM northing 6243137.5m and easting 555897.5m (NAD83), with elevations relative to sea level. The known position of the Ovoid is shown in black. Scale can be inferred from coordinate annotations.

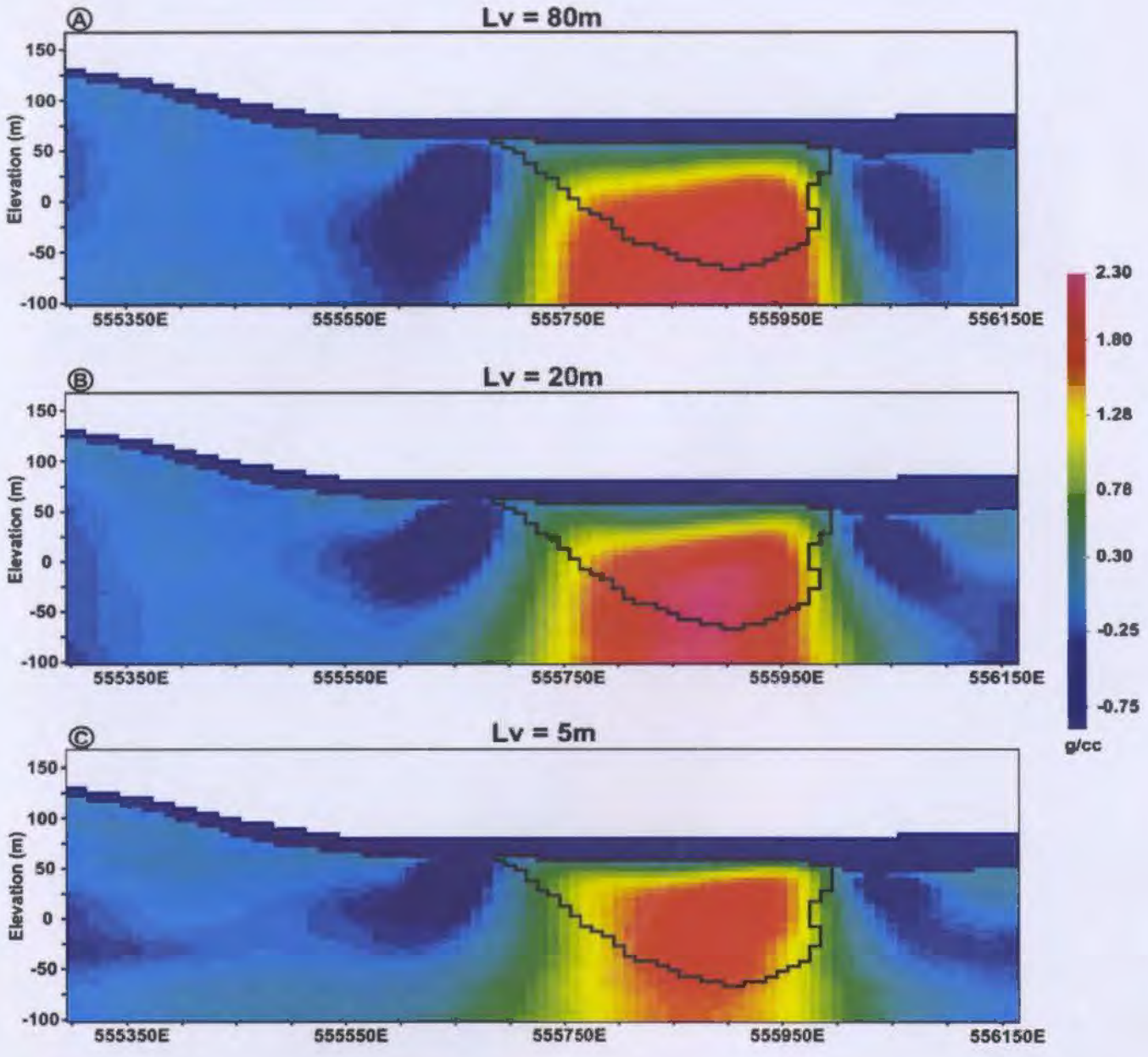

Figure 5.15: The density models DEN09 (**A**), DEN10 (**B**) and DEN11 (**C**) recovered from inversions INV09, INV10 and INV11. Vertical length scales of 80m, 20m and 5m were applied while all other parameters were held constant. The above sections are along UTM northing 6243137.5m (NAD83) and elevations are relative to sea level. The known position of the Ovoid is shown in black. Scale can be inferred from coordinate annotations.

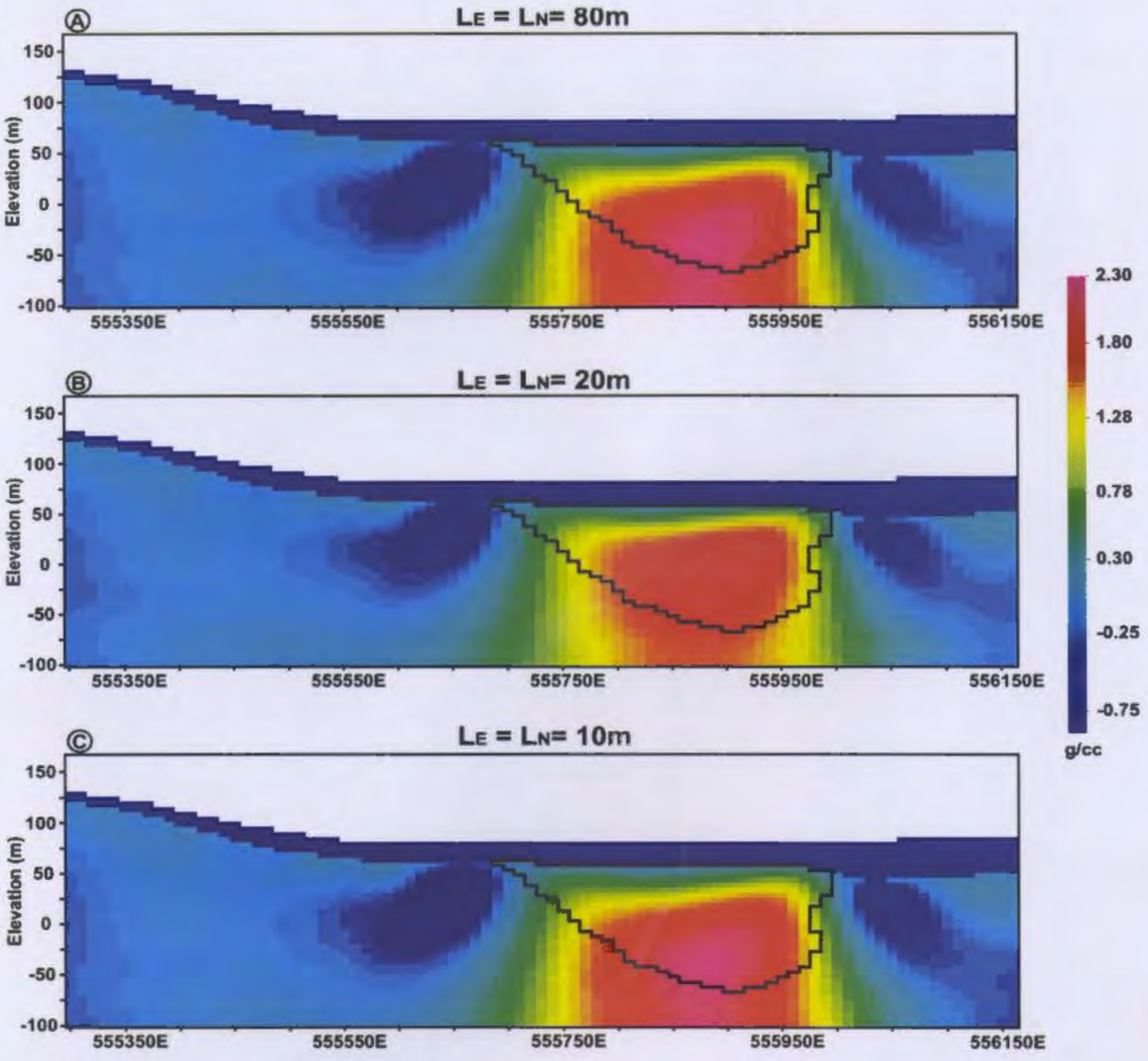

Figure 5.16: The density models DEN12 (**A**), DEN13 (**B**) and DEN14 (**C**) recovered from inversions INV12, INV13 and INV14. Horizontal length scales of 80m, 20m and 10m were applied while all other parameters were held constant. The above sections are along UTM northing 6243137.5m (NAD83) and elevations are relative to sea level. The known position of the Ovoid is shown in black. Scale can be inferred from coordinate annotations.

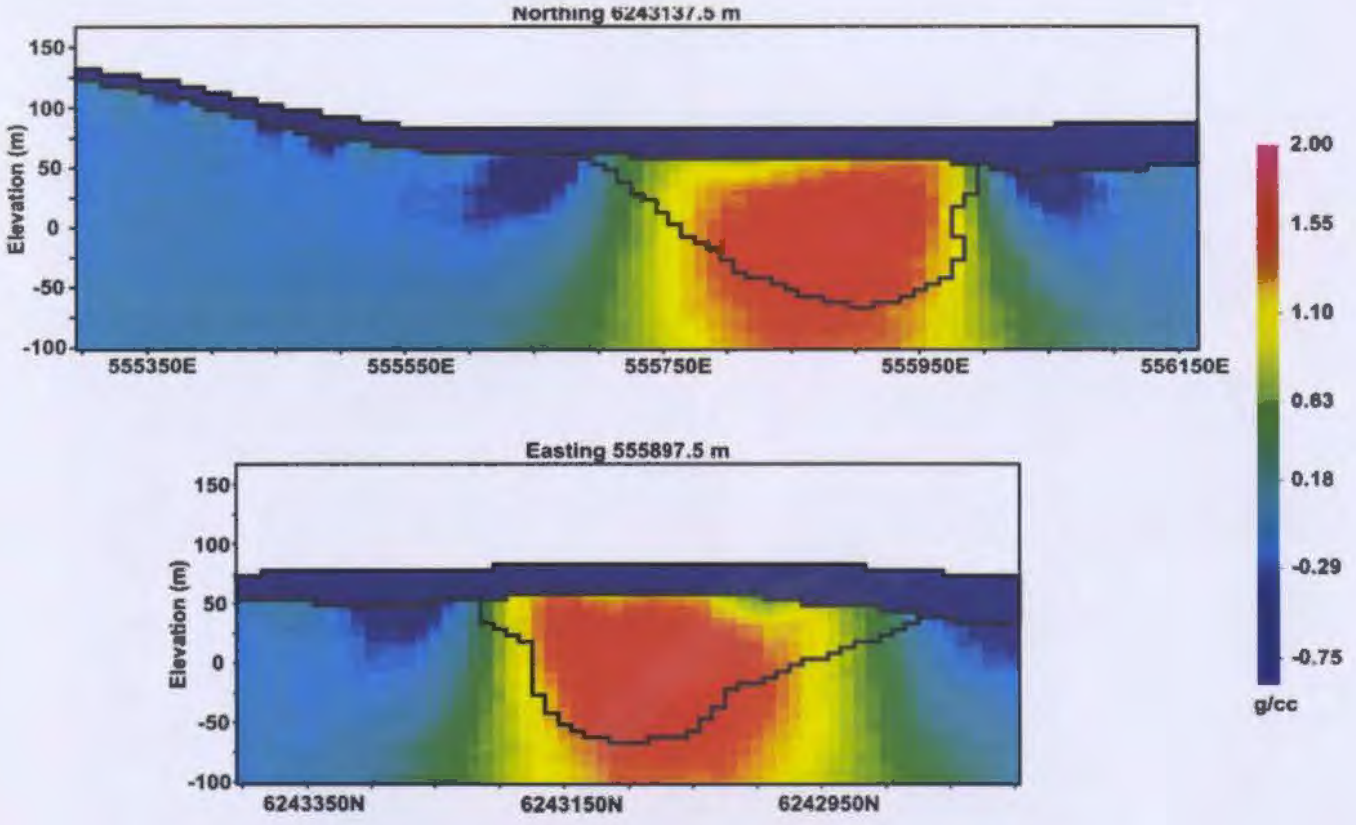

Figure 5.17: The density model DEN15 recovered from inversion INV15. Sections are along UTM northing 6243137.5m and easting 555897.5m (NAD83), with elevations relative to sea level. The known position of the Ovoid is shown in black. Scale can be inferred from coordinate annotations.

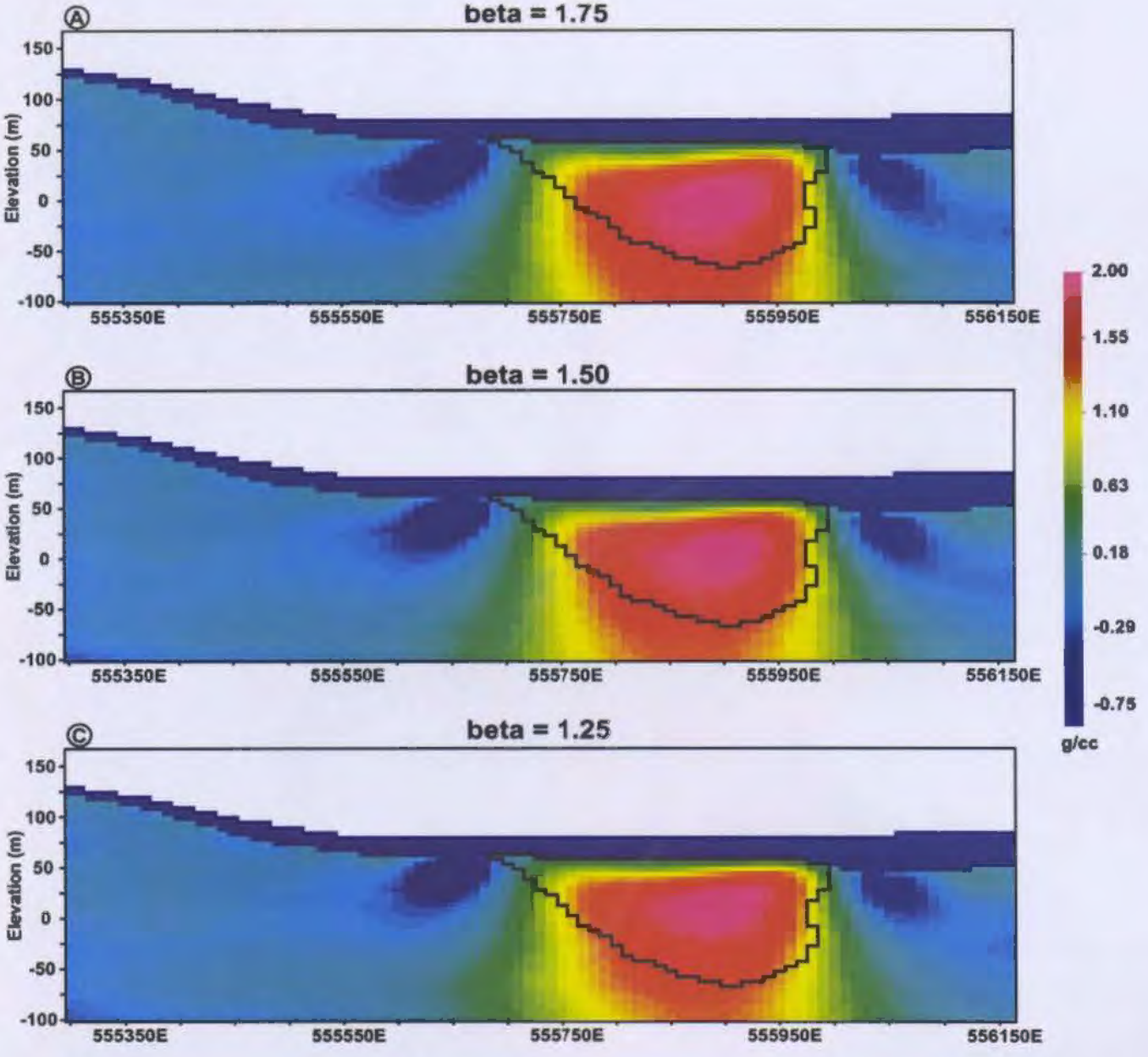

Figure 5.18: The density models DEN16 (**A**), DEN17 (**B**) and DEN18 (**C**) recovered from inversions INV16, INV17 and INV18. The depth weighting parameter beta was adjusted to 1.75, 1.50 and 1.25 while all other parameters were held constant. The above sections are along UTM northing 6243137.5m (NAD83) and elevations are relative to sea level. The known position of the Ovoid is shown in black. Scale can be inferred from coordinate annotations.

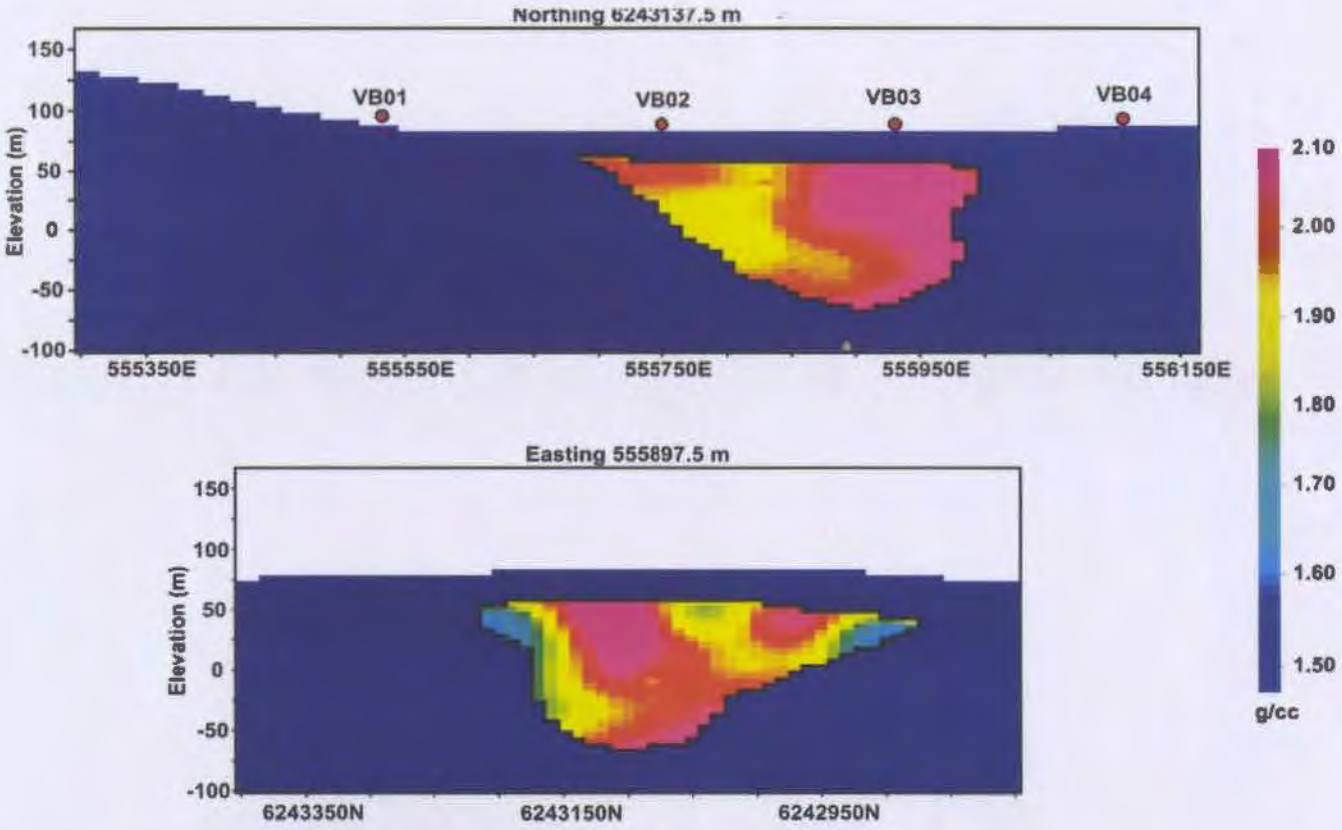

Figure 5.19: The density model DEN19 recovered from inversion INV19. Sections are along UTM northing 6243137.5m and easting 555897.5m (NAD83), with elevations relative to sea level. The known position of the Ovoid is shown in black. The position of gravity lines VB01, VB02, VB03 and VB04 perpendicular to east-west section are shown in red. Scale can be inferred from coordinate annotations.

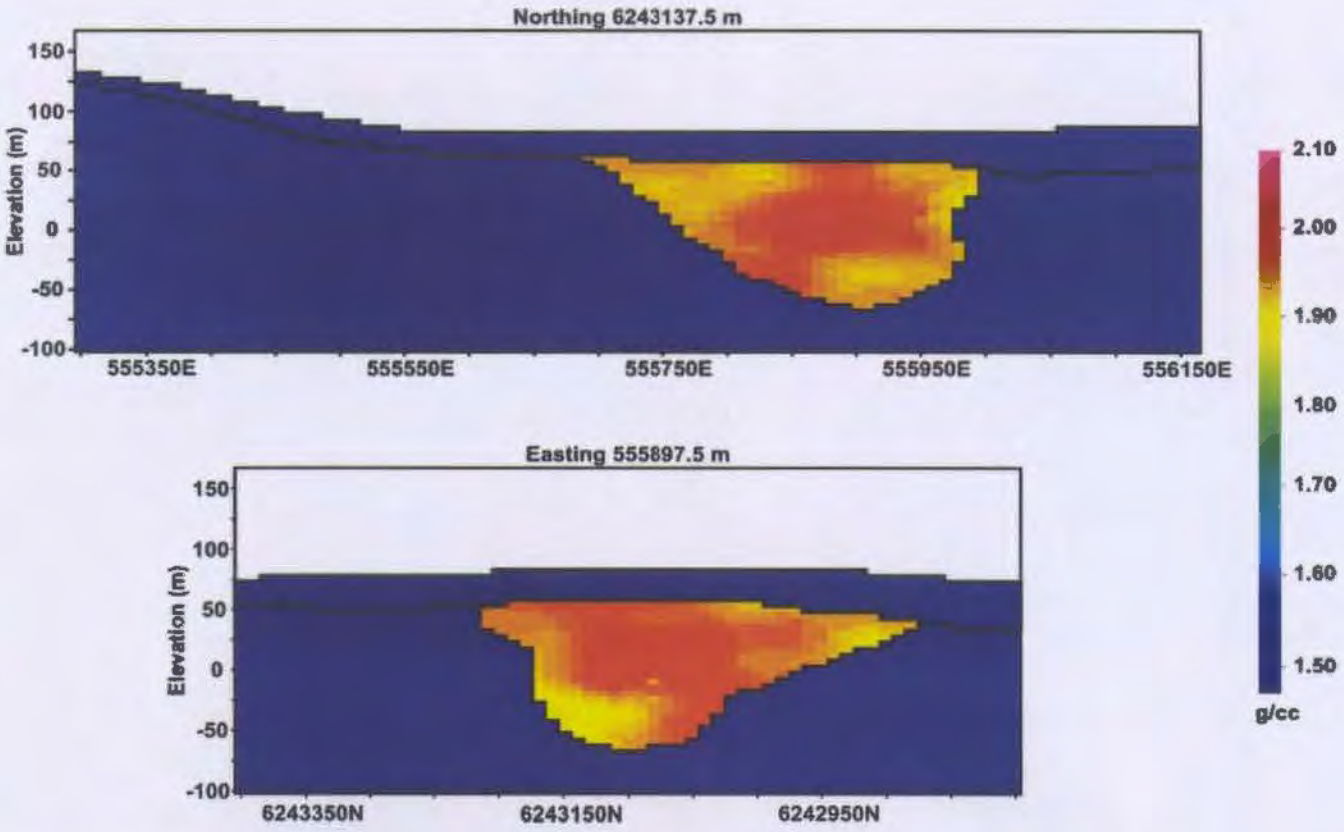

Figure 5.20: The kriged density contrast model DM02 generated in Section 3.4.3. Sections are along UTM northing 6243137.5m and easting 555897.5m (NAD83), with elevations relative to sea level. The known position of the overburden and Ovoid is shown in black. Scale can be inferred from coordinate annotations and the density contrast is relative to 2.67 g/cc.

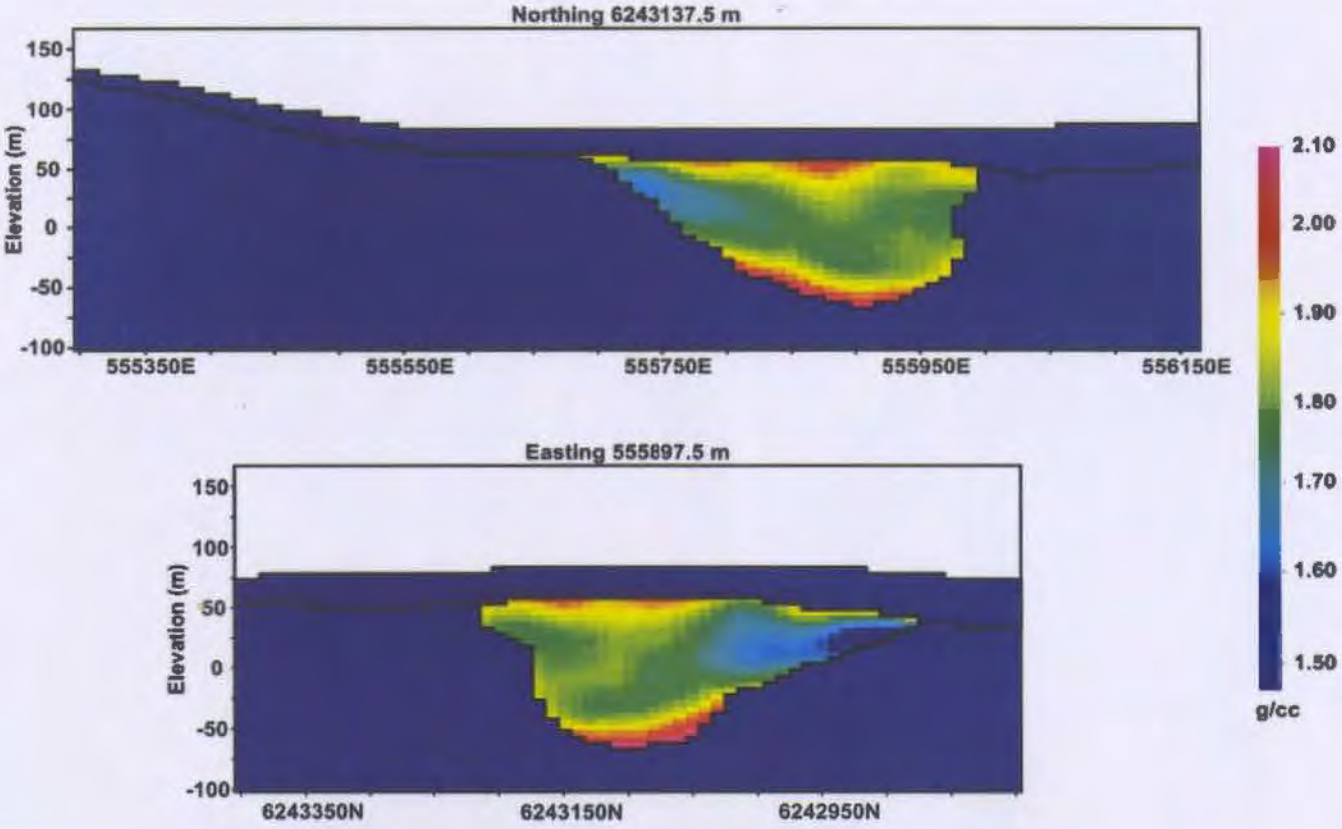

Figure 5.21: The density model DEN20 recovered from inversion INV20. Sections are along UTM northing 6243137.5m and easting 555897.5m (NAD83), with elevations relative to sea level. The known position of the overburden and Ovoid is shown in black. Scale can be inferred from coordinate annotations.

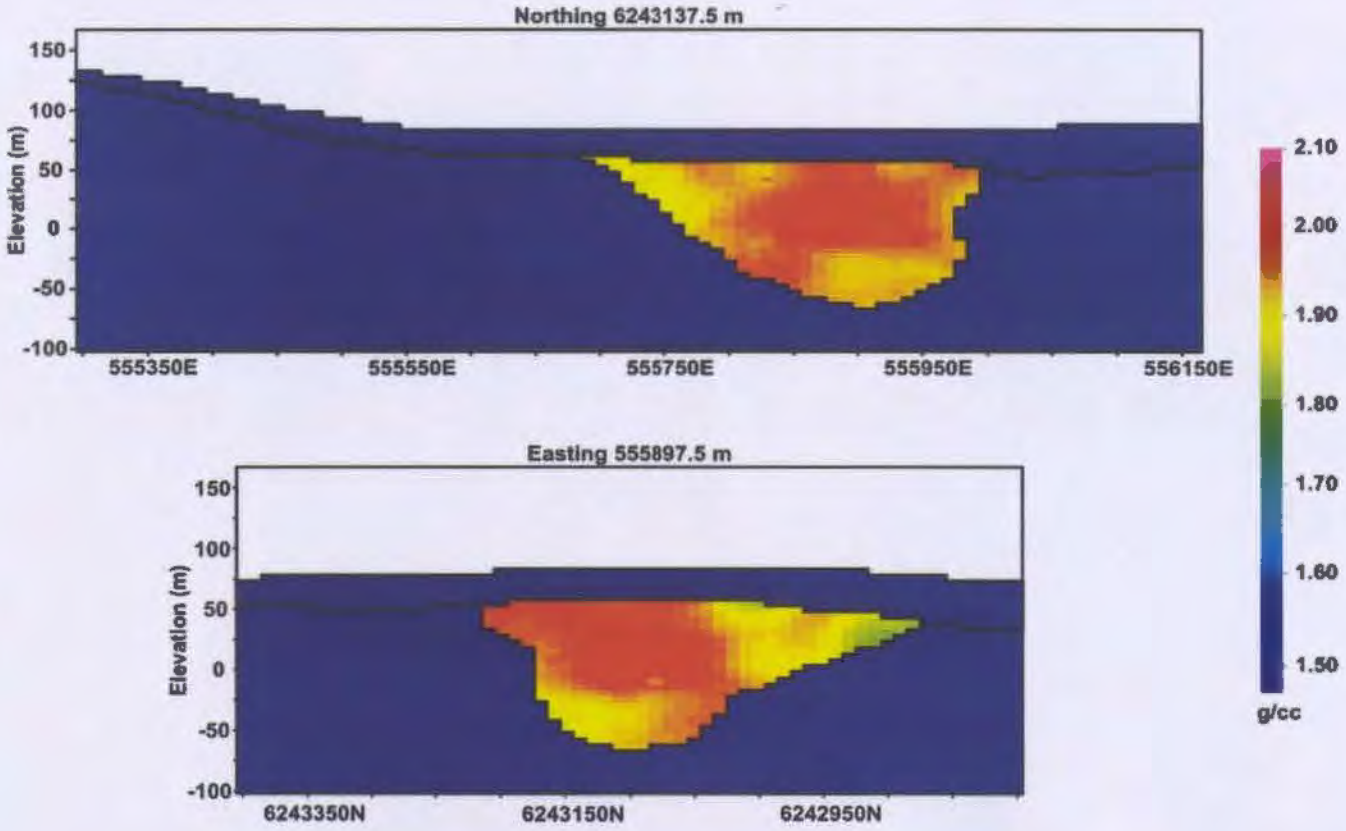

Figure 5.22: The density model DEN21 recovered from inversion INV21. Sections are along UTM northing 6243137.5m and easting 555897.5m (NAD83), with elevations relative to sea level. The known position of the overburden and Ovoid is shown in black. Scale can be inferred from coordinate annotations.

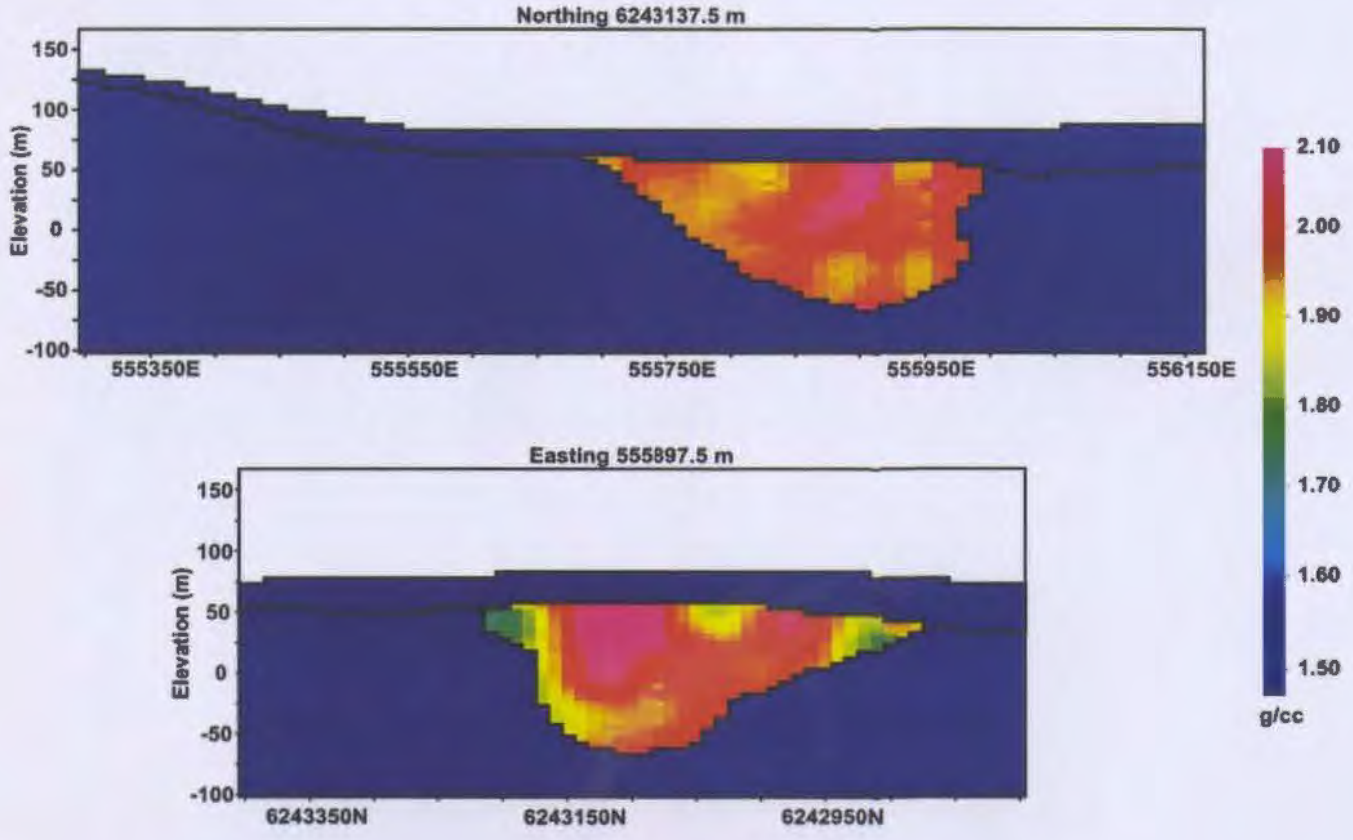

Figure 5.23: The density model DEN22 recovered from inversion INV22. Sections are along UTM northing 6243137.5m and easting 555897.5m (NAD83), with elevations relative to sea level. The known position of the overburden and Ovoid is shown in black. Scale can be inferred from coordinate annotations.

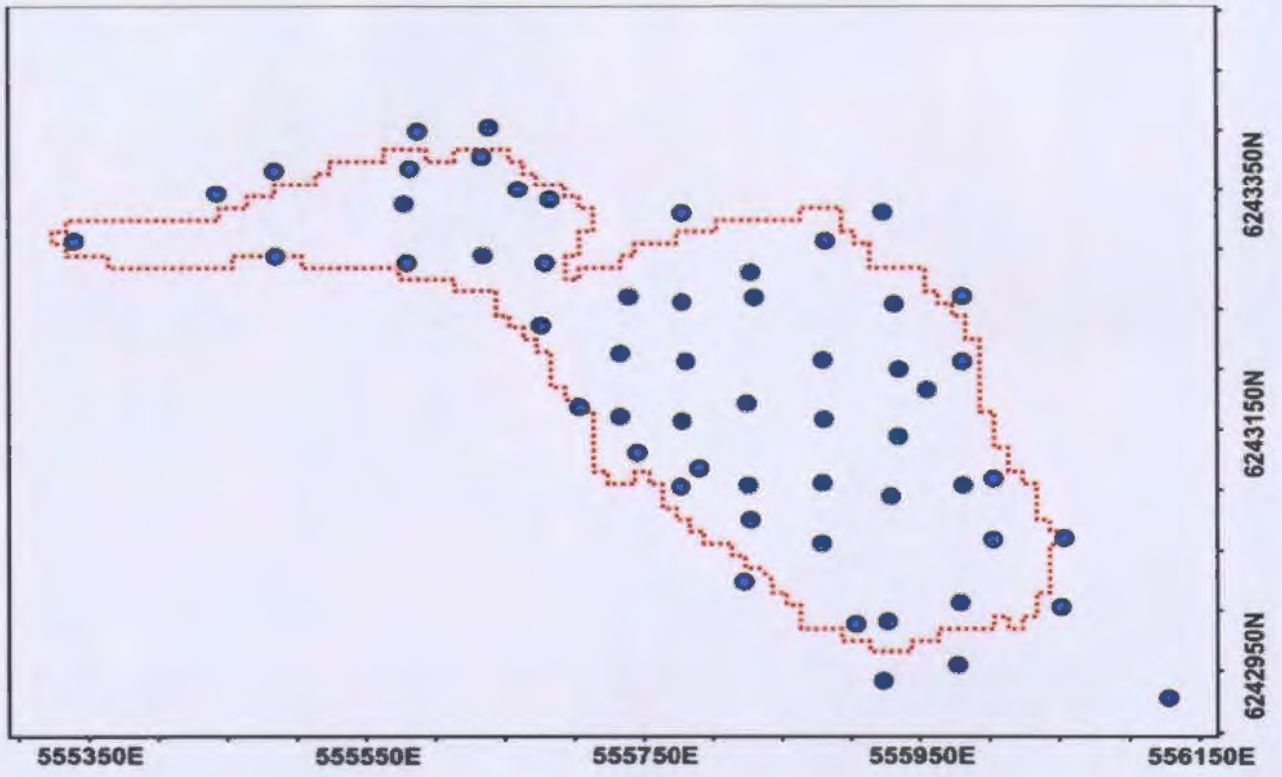

Figure 5.24: Drill collar locations of the density logs used to generate the 50% decimated density model DM06.The MASU unit projected to the surface is shown by the red dotted line. Coordinates are in UTM northings and eastings (NAD83). Scale can be inferred from coordinate annotations.

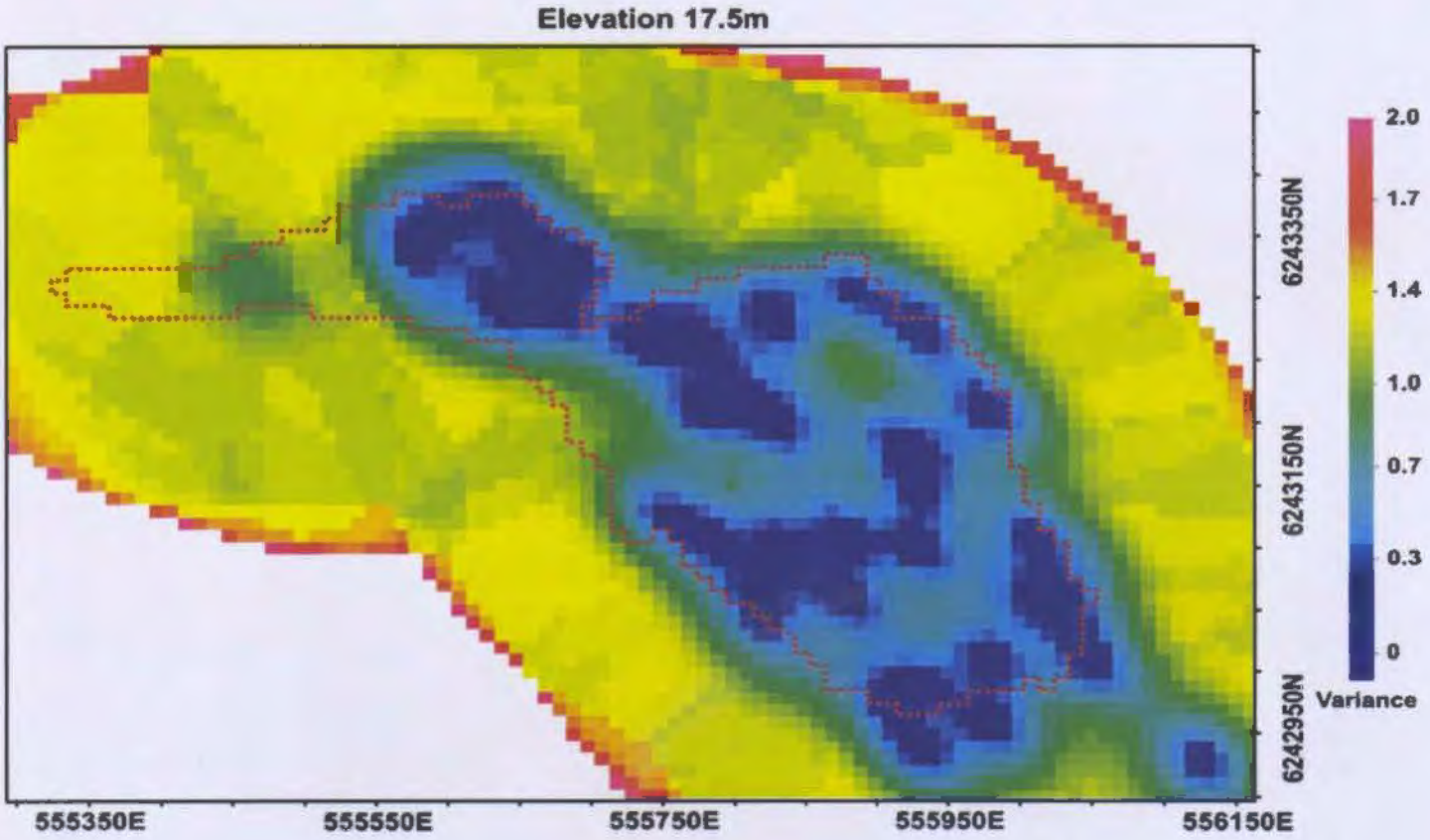

Figure 5.25: A horizontal slice at an elevation of 17.5m illustrating the cell variances obtained from Kriging 56 density logs. White areas containing no variances are assigned a no-data-value (NDV) in Gocad. The MASU unit projected to the surface is shown by the red dotted line. Coordinates are in UTM northings and eastings (NAD83). Scale can be inferred from coordinate annotations.

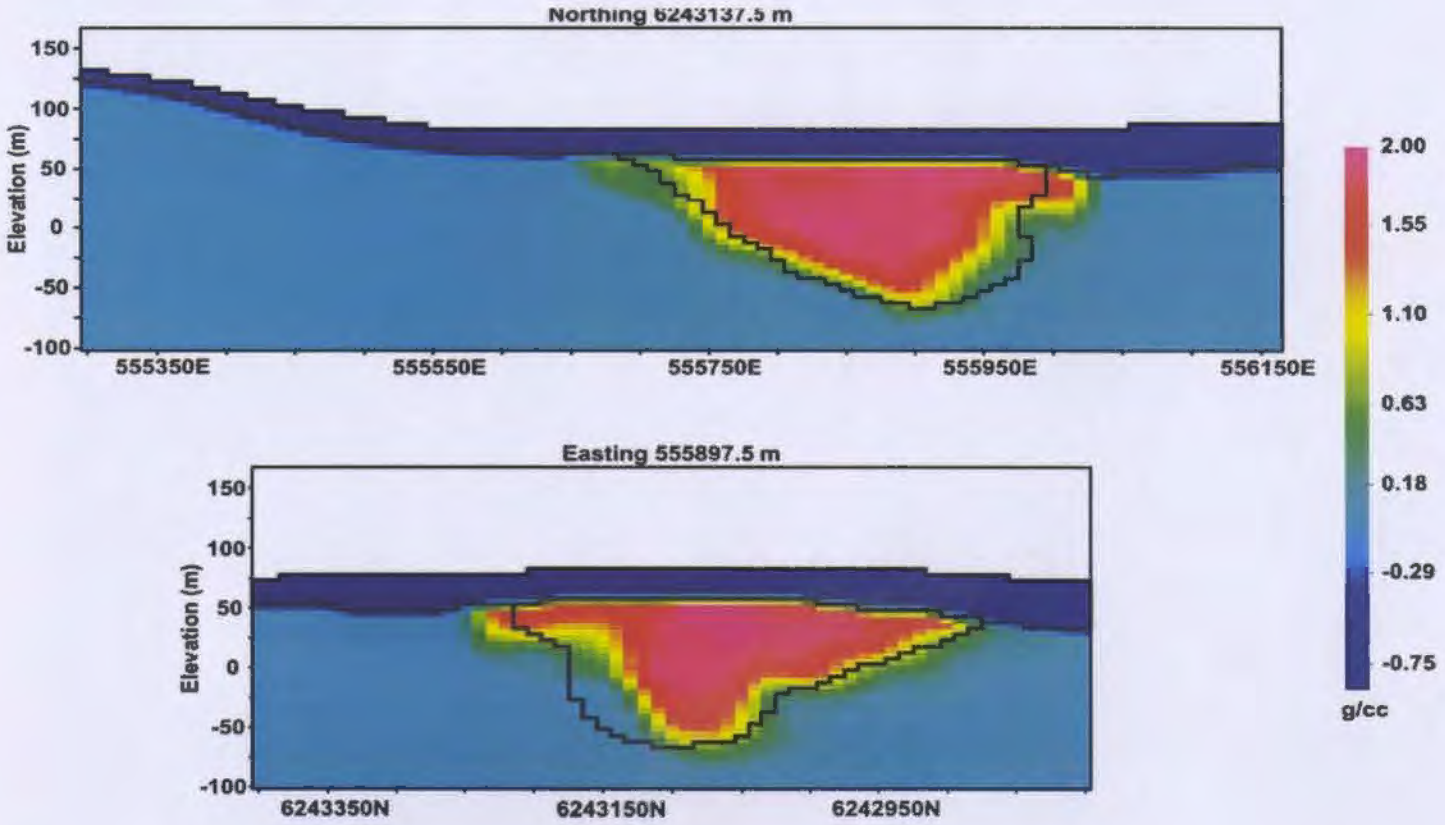

Figure 5.26: Sections along UTM northing 6243137.5m and easting 555897.5m illustrating the density model DM06 (50% decimated) obtained from kriging the drill logs illustrated in Figure 5.24. The OB region (RG01) was assigned a constant density of 1.92 g/cc and cells containing a variance range of 0.0 to 1.0 (Figure 5.25) are assigned a constant density of 2.81 g/cc The known position if the Ovoid is shown in black. Scale can be inferred from coordinate annotations.

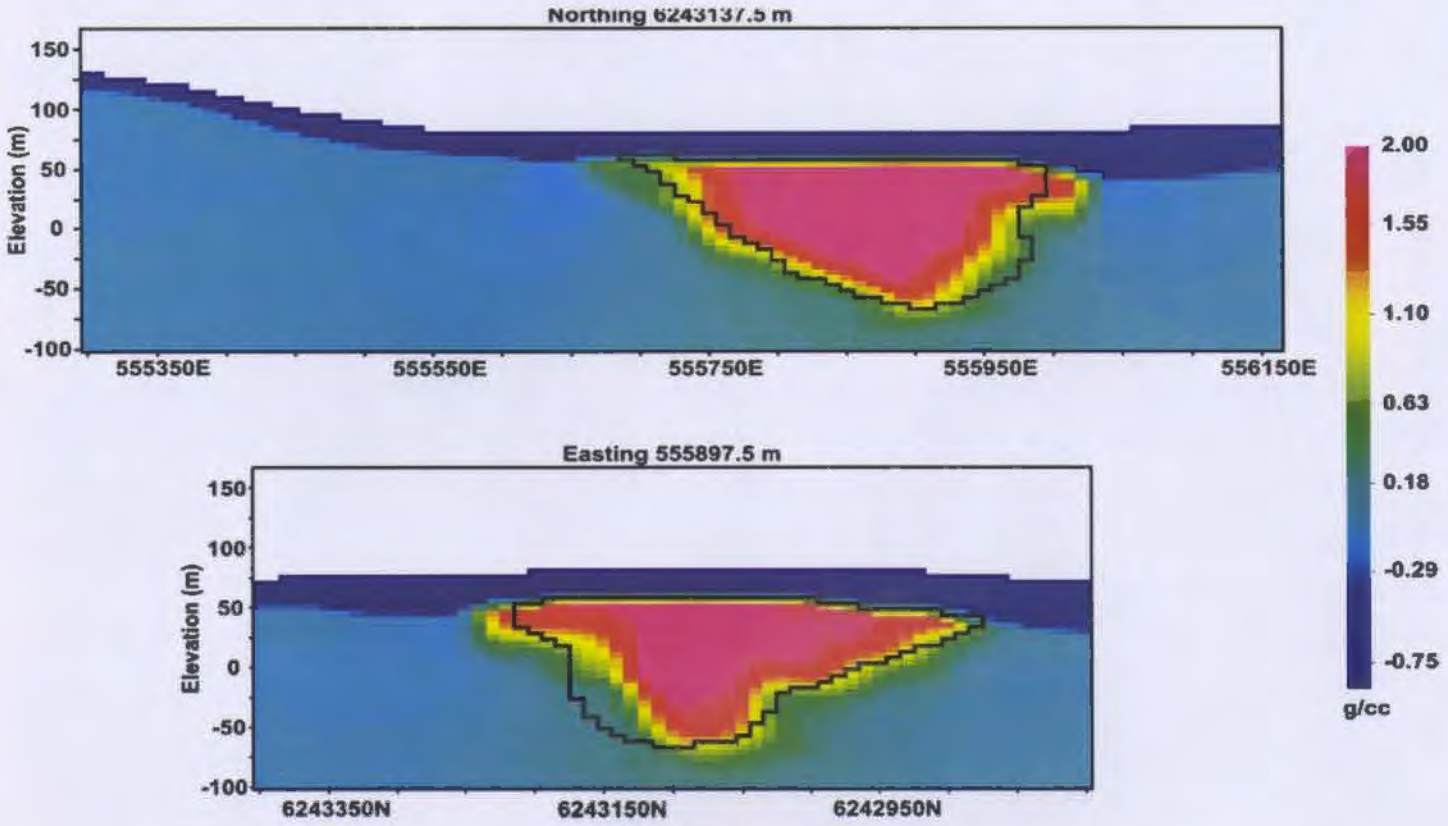

Figure 5.27: The density model DEN23 recovered from inversion INV23. Sections are along UTM northing 6243137.5m and easting 555897.5m (NAD83), with elevations relative to sea level. The known position of the Ovoid is shown in black. Scale can be inferred from coordinate annotations.

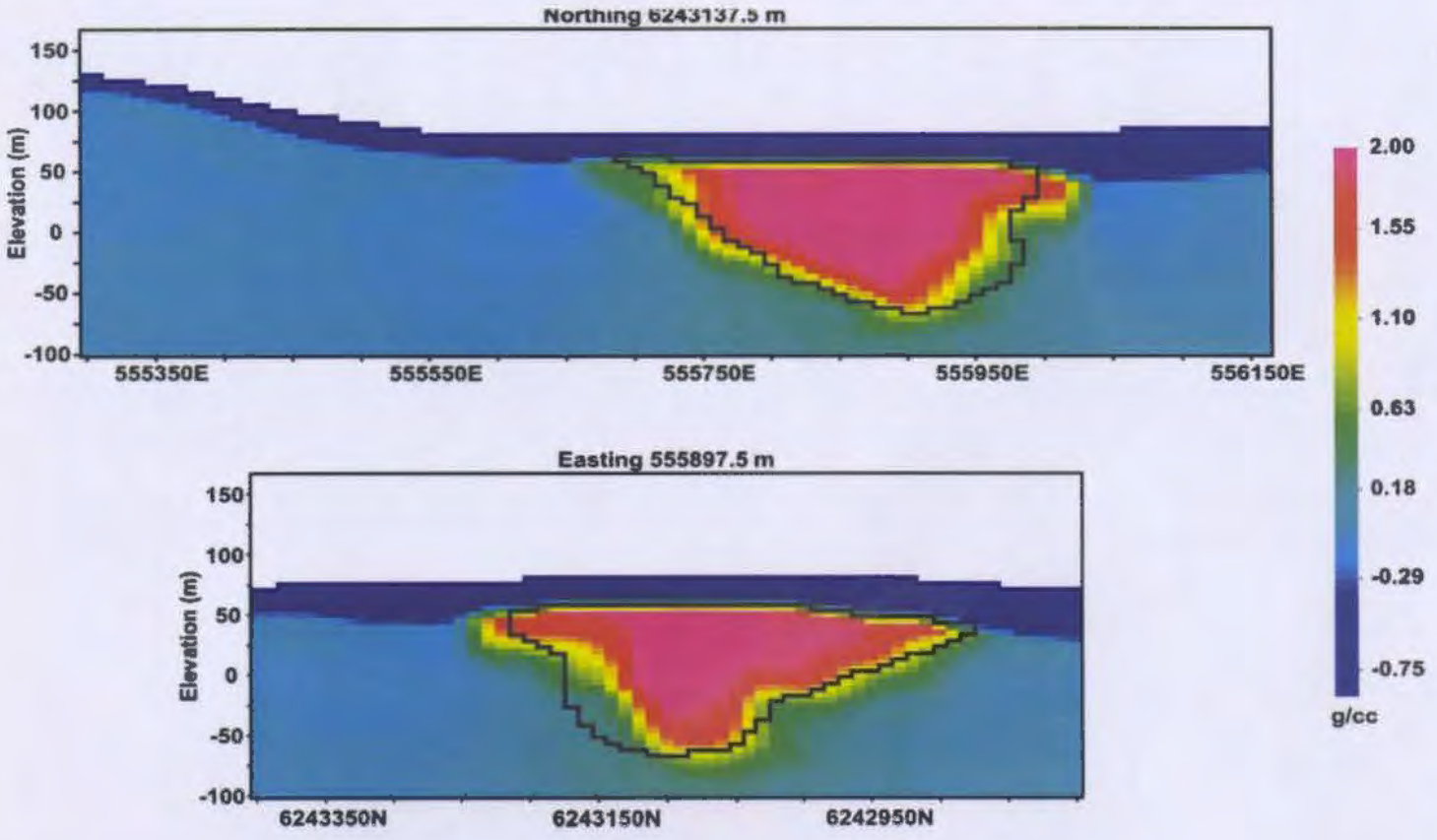

Figure 5.27: The density model DEN23 recovered from inversion INV23. Sections are along UTM northing 6243137.5m and easting 555897.5m (NAD83), with elevations relative to sea level. The known position of the Ovoid is shown in black. Scale can be inferred from coordinate annotations.

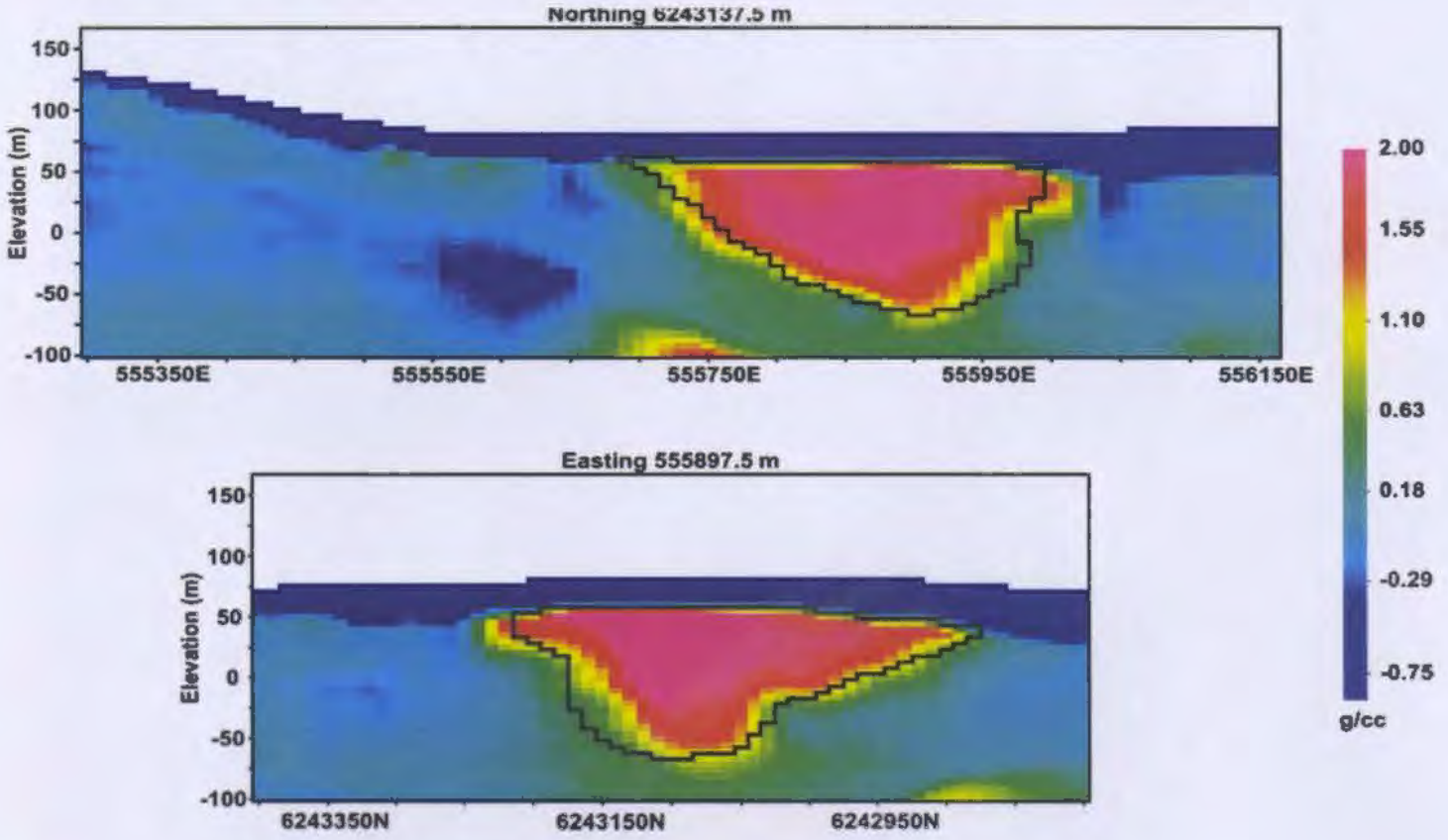

Figure 5.28: The density model DEN24 recovered from inversion INV24. The inversion was constrained using the density contrast model DM06 (Figure 5.26) as a reference model. Cells within the reference model were constrained using the WDAT03 weighing model. Sections are along UTM northing 6243137.5m and easting 555897.5m (NAD83), with elevations relative to sea level. The known position of the Ovoid is shown in black. Scale can be inferred from coordinate annotations.

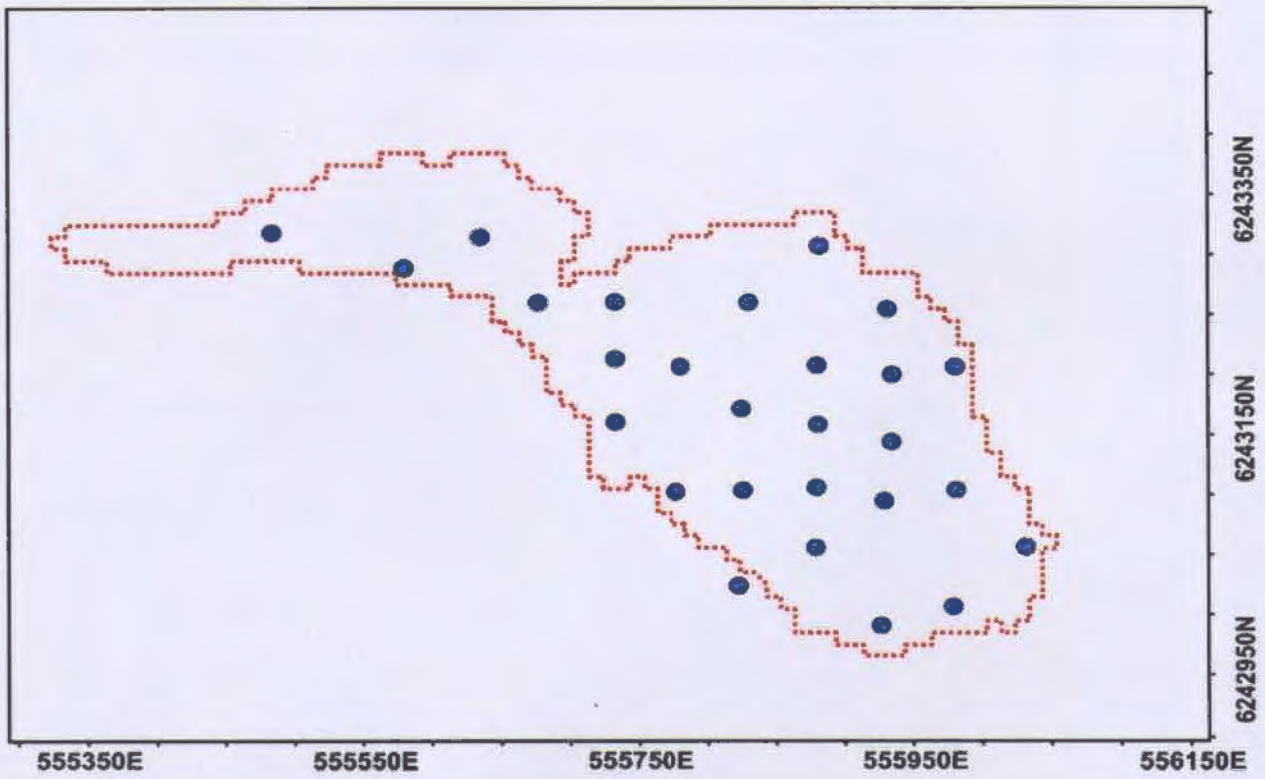

Figure 5.29: Position of the drill collar locations of the density logs used to generate the 25% decimated density model DM07. The MASU unit projected to the surface is shown by the red dotted line. Coordinates are in UTM northings and eastings (NAD83). Scale can be inferred from coordinate annotations.

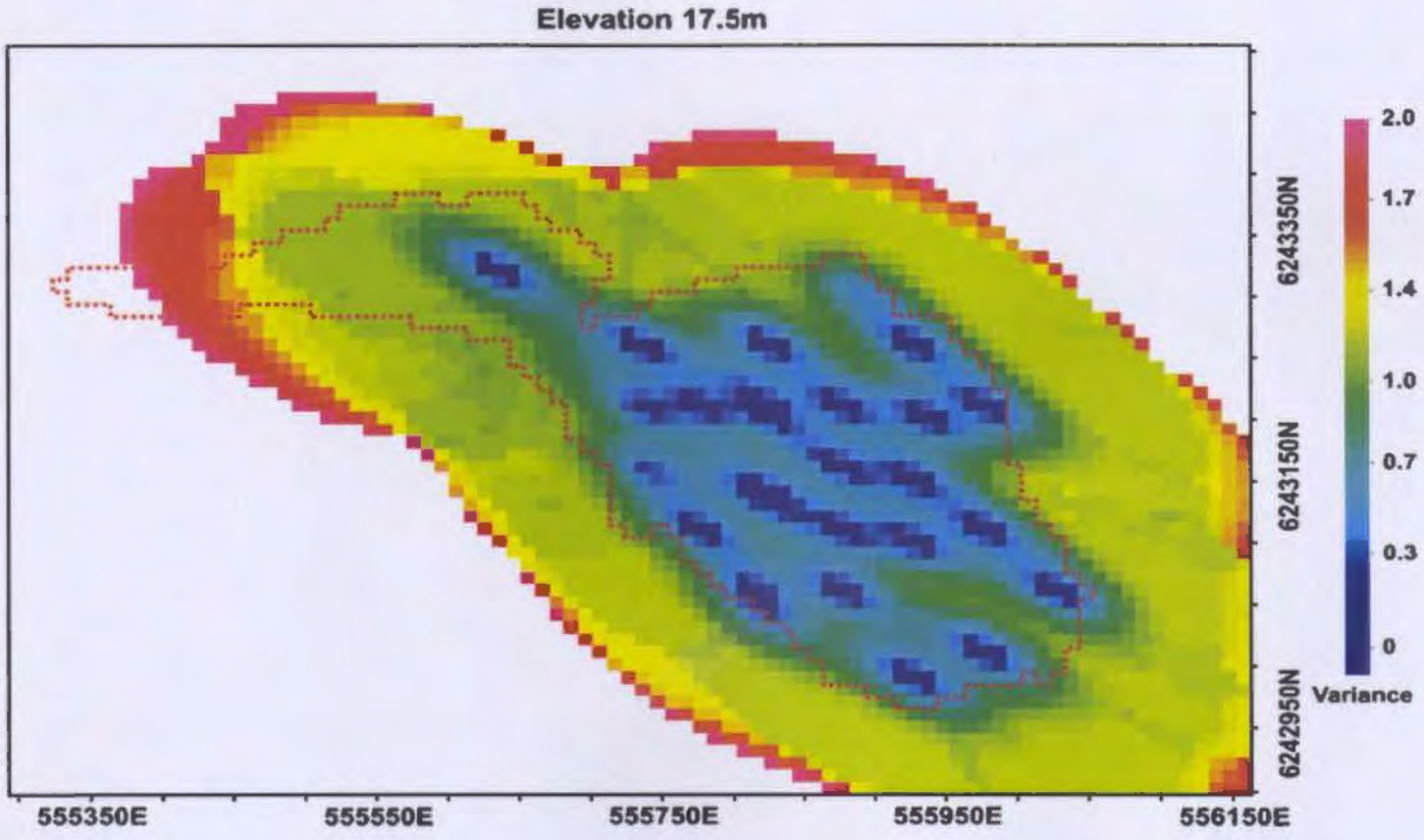

Figure 5.30: A horizontal slice at an elevation of 17.5m illustrating the cell variances obtained from Kriging 28 density logs. White areas containing no variances are assigned a no-data-value (NDV) in Gocad. The MASU unit projected to the surface is shown by the red dotted line. Coordinates are in UTM northings and eastings (NAD83). Scale can be inferred from coordinate annotations.

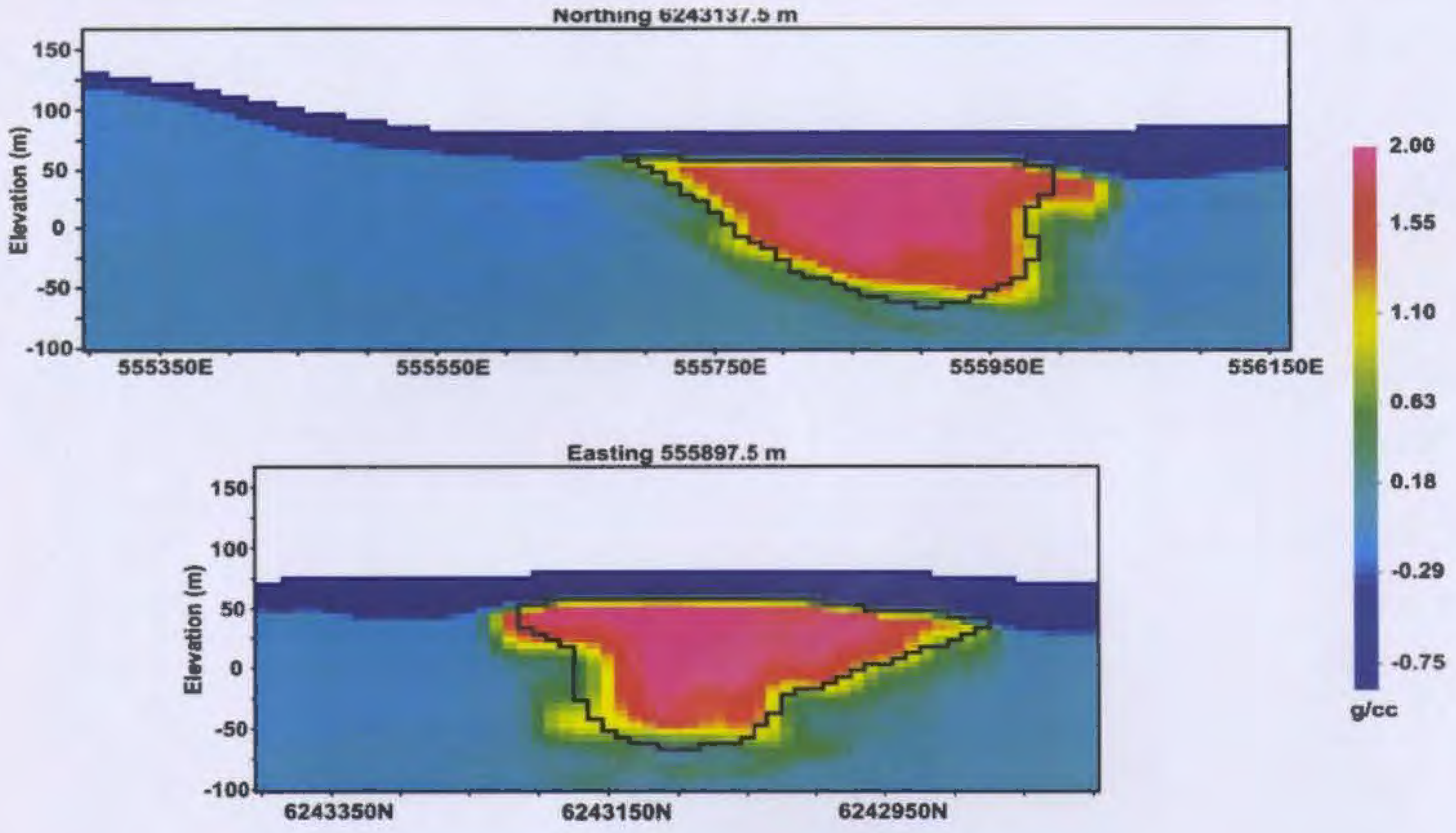

Figure 5.32: The density model DEN25 recovered from inversion INV25. Sections are along UTM northing 6243137.5m and easting 555897.5m (NAD83), with elevations relative to sea level. The known position of the Ovoid is shown in black. Scale can be inferred from coordinate annotations.

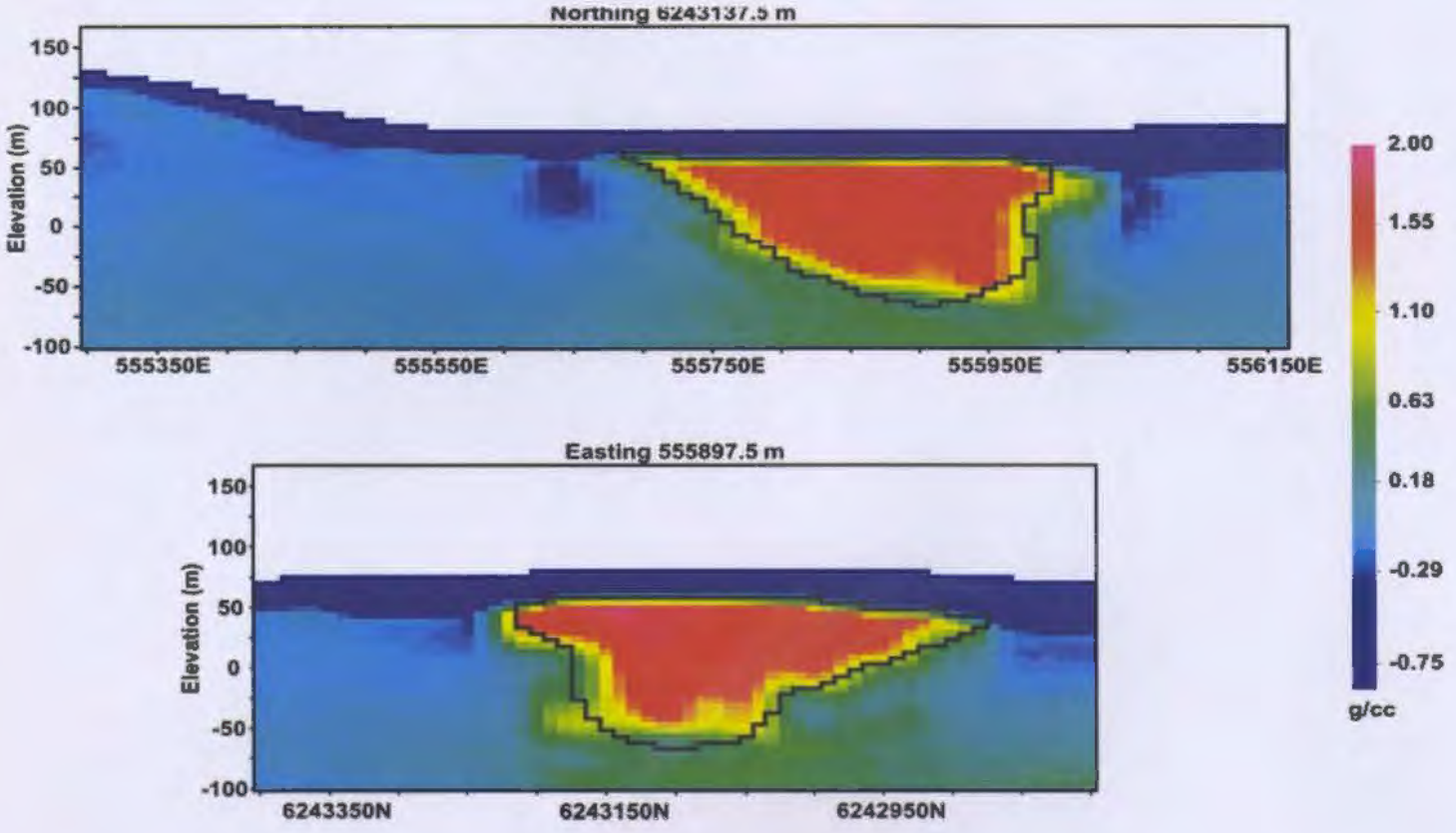

Figure 5.33: The density model DEN26 recovered from inversion INV26. The inversion was constrained using the density contrast model DM07 (Figure 5.31) as a reference model. Cells within the reference model were constrained using the WDAT04 weighing model. Sections are along UTM northing 6243137.5m and easting 555897.5m (NAD83), with elevations relative to sea level. The known position Ovoid is shown in black. Scale can be inferred from coordinate annotations.

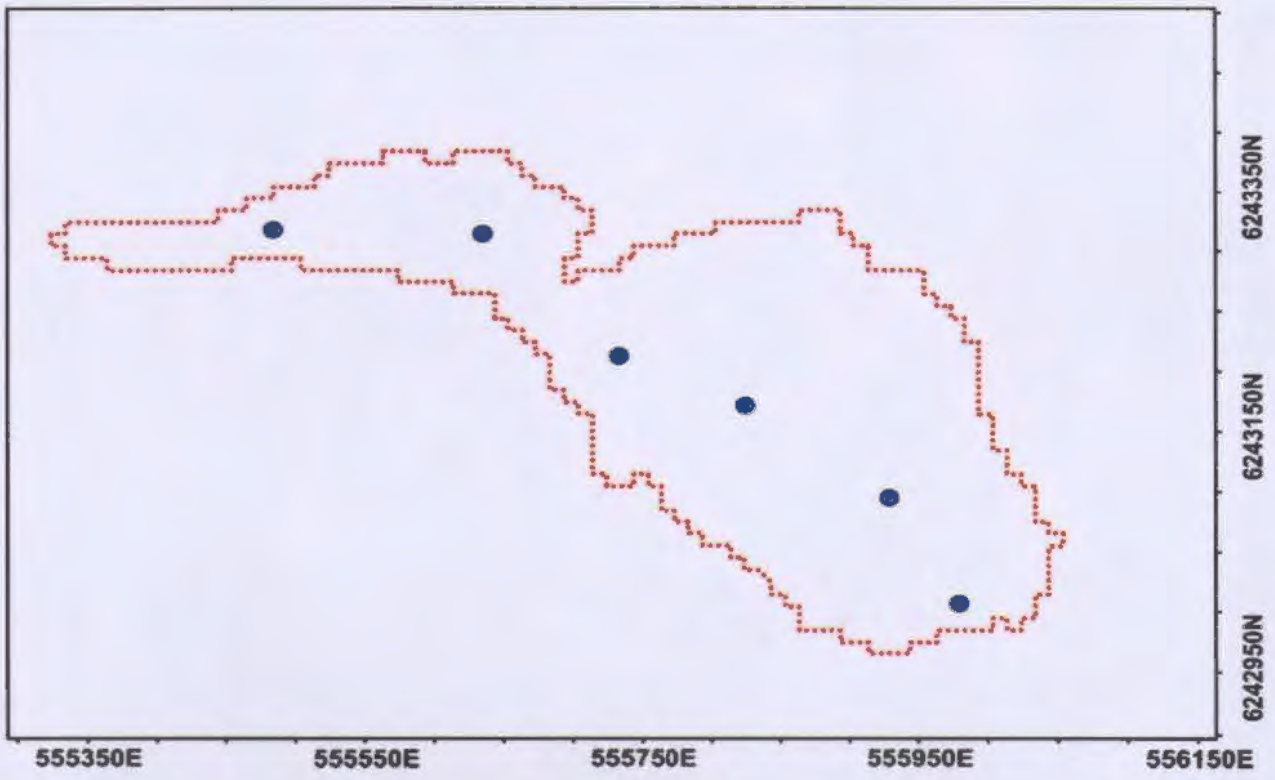

Figure 5.34: Position of the drill collar locations of the density logs used to generate the 5% decimated density model DM08.The MASU unit projected to the surface is shown by the red dotted line. Coordinates are in UTM northings and eastings (NAD83). Scale can be inferred from coordinate annotations.

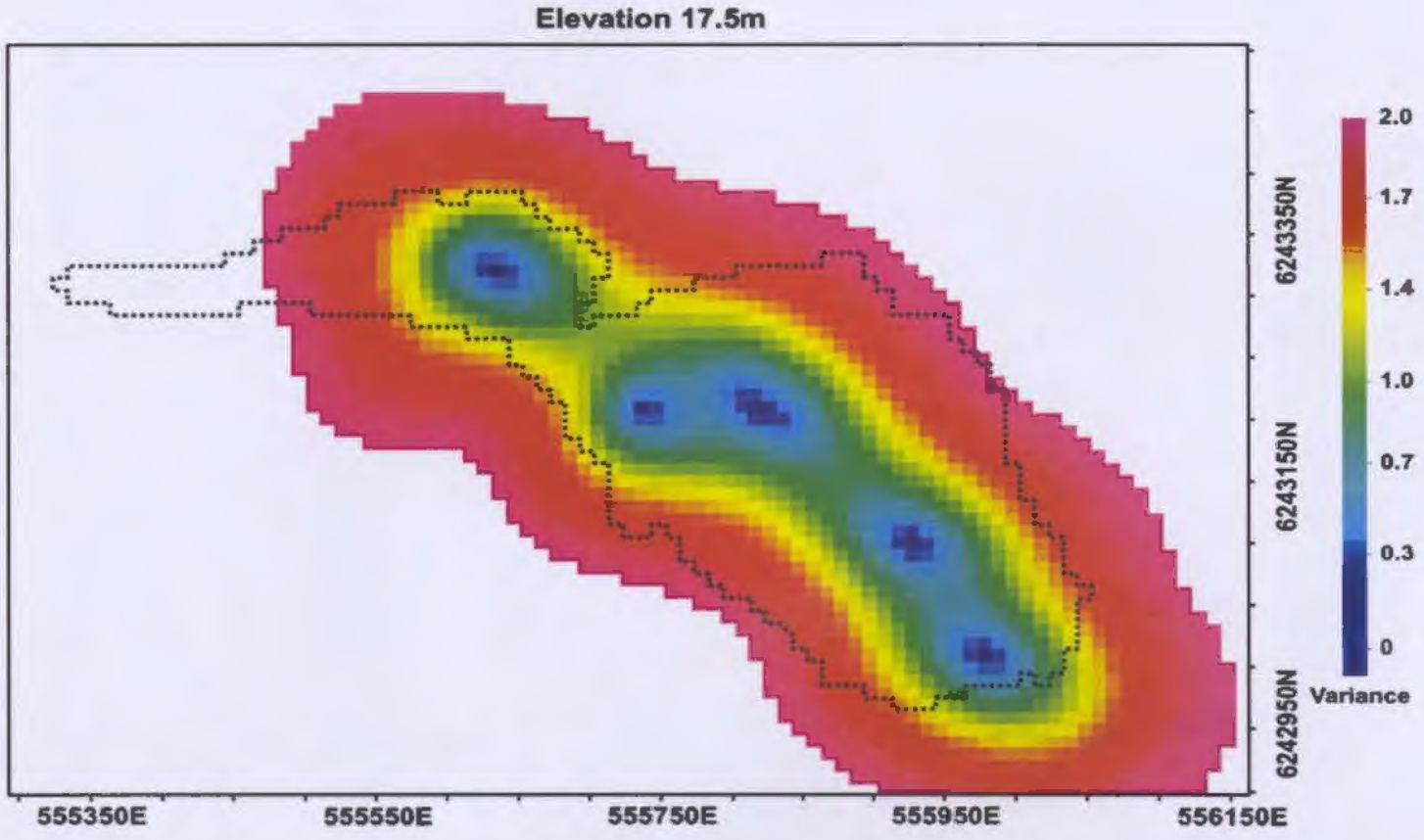

Figure 5.35: A horizontal slice at an elevation of 17.5m illustrating the cell variances obtained from Kriging 6 density logs. The white areas containing no variances are assigned a no-data-value (NDV) in Gocad. The MASU unit projected to the surface is shown by the black dotted line. Coordinates are in UTM northings and eastings (NAD83). Scale can be inferred from coordinate annotations.

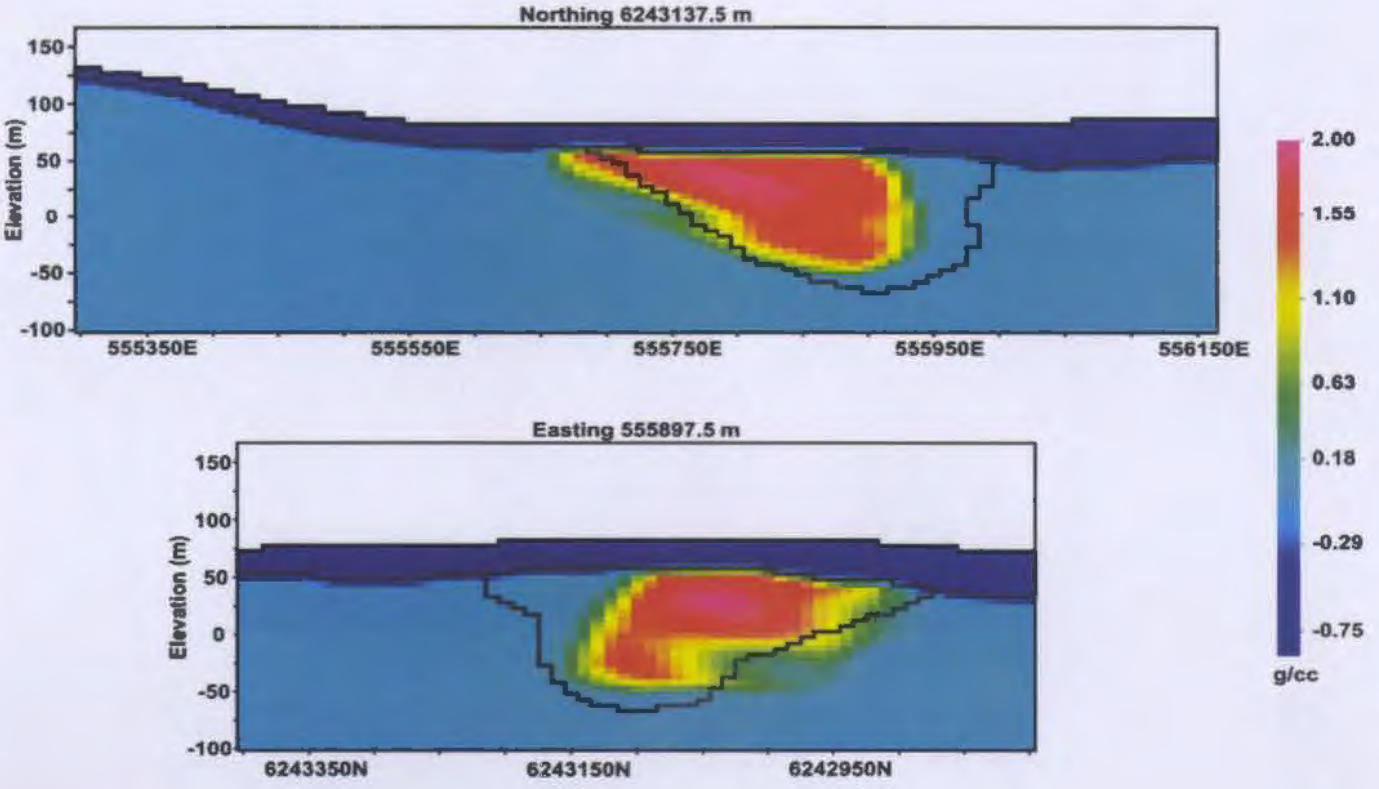

Figure 5.36: Sections along UTM northing 6243137.5m and easting 555897.5m illustrating the density model DM08 obtained from kriging the 6 drill logs illustrated in Figure 5.34. The OB region (RG01) was assigned a constant density of 1.92 g/cc and cells containing a variance range of 0.0 to 1.0 (Figure 5.35) are assigned a constant density of 2.81 g/cc The known position if the Ovoid is shown in black. Scale can be inferred from coordinate annotations.

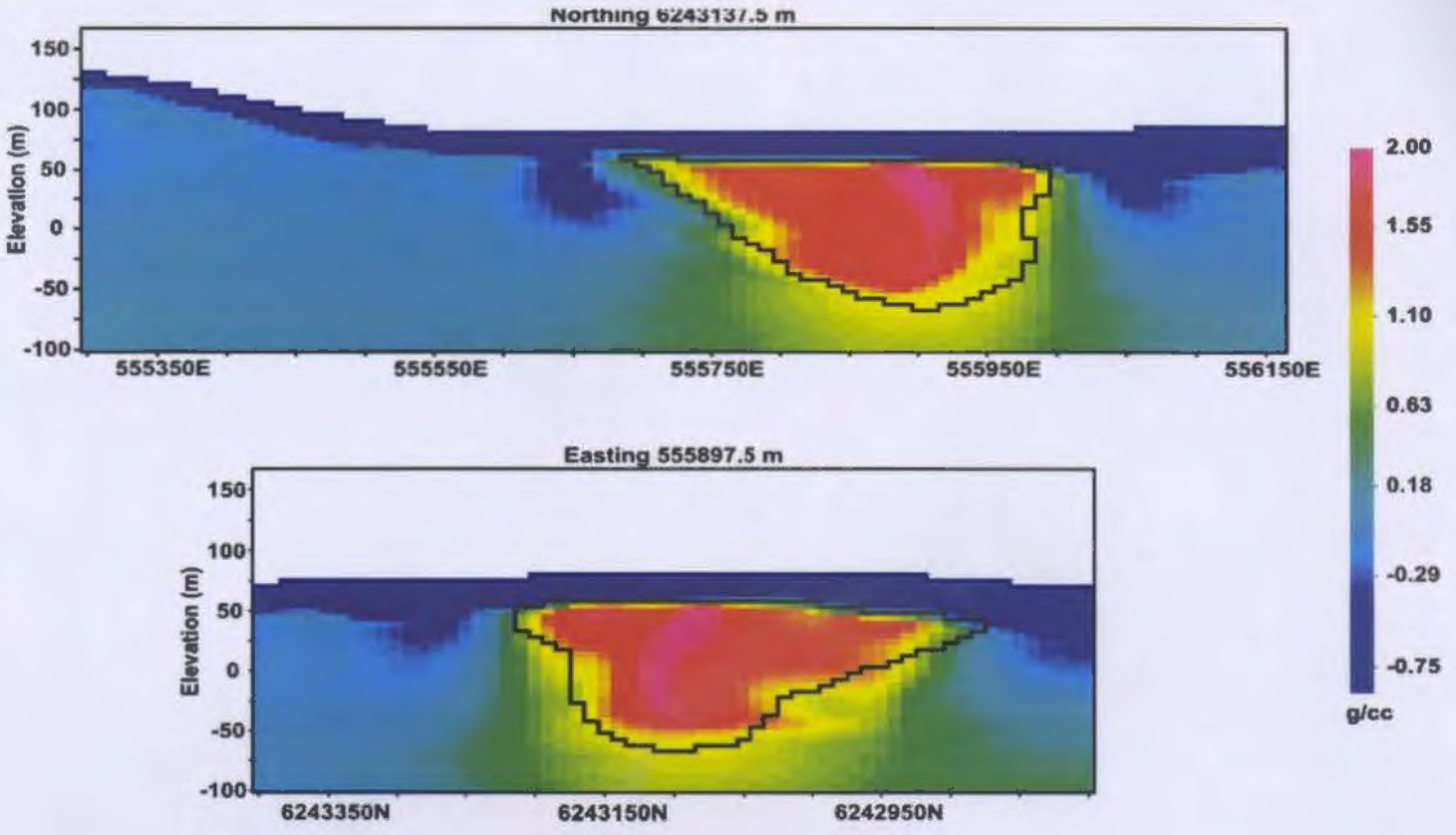

Figure 5.37: The density model DEN27 recovered from inversion INV27. The inversion was constrained using the density model DM08 illustrated in Figure 5.35 as a reference model. Sections are along UTM northing 6243137.5m and easting 555897.5m (NAD83), with elevations relative to sea level. The known position of the Ovoid is shown in black. Scale can be inferred from coordinate annotations.

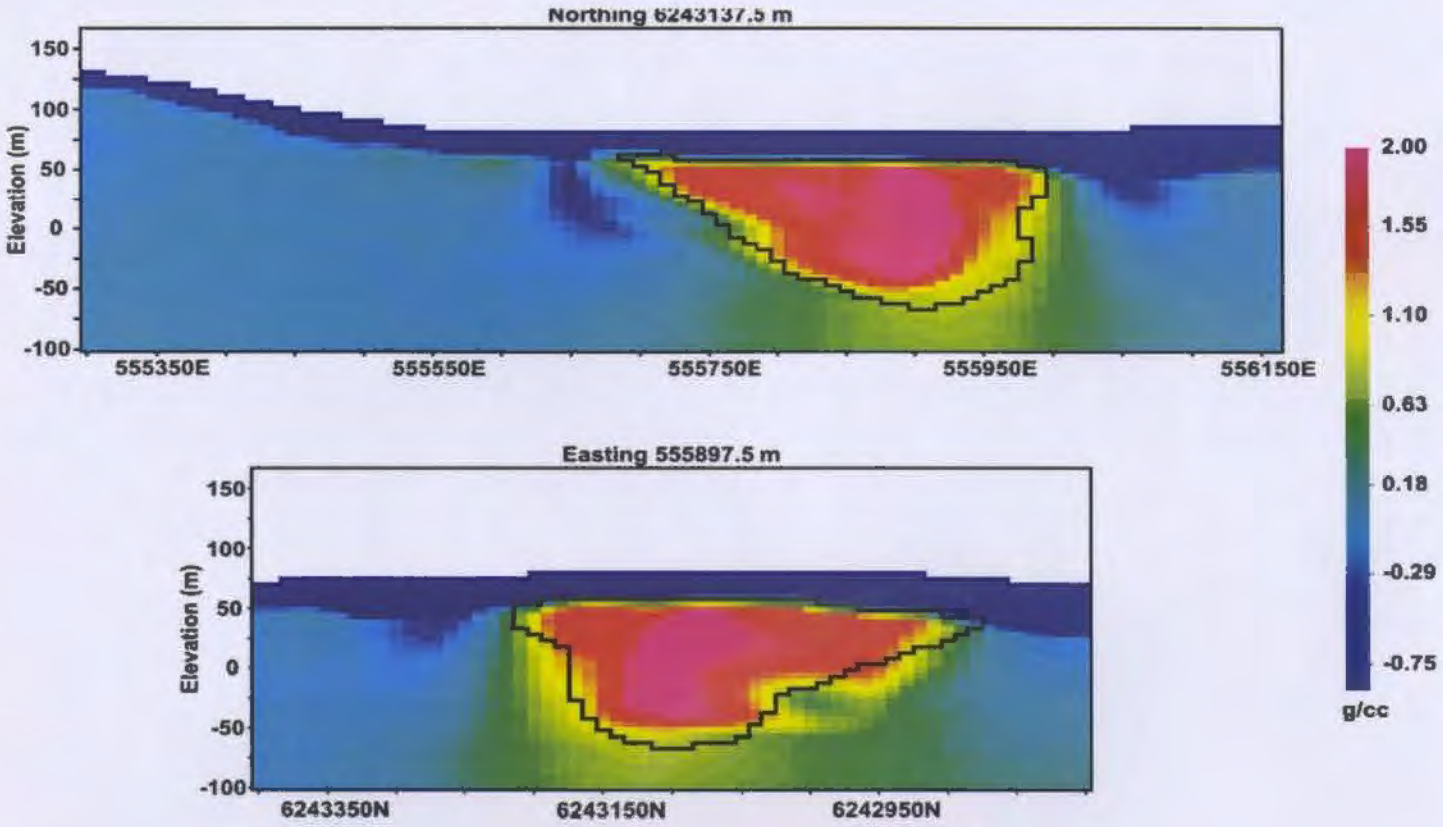

Figure 5.38: The density model DEN28 recovered from inversion INV28. The inversion was constrained using the density contrast model DM08 (Figure 5.36) as a reference model. Cells within the reference model were constrained using the WDAT05 weighing model. Sections are along UTM northing 6243137.5m and easting 555897.5m (NAD83), with elevations relative to sea level. The known position of the Ovoid is shown in black. Scale can be inferred from coordinate annotations.

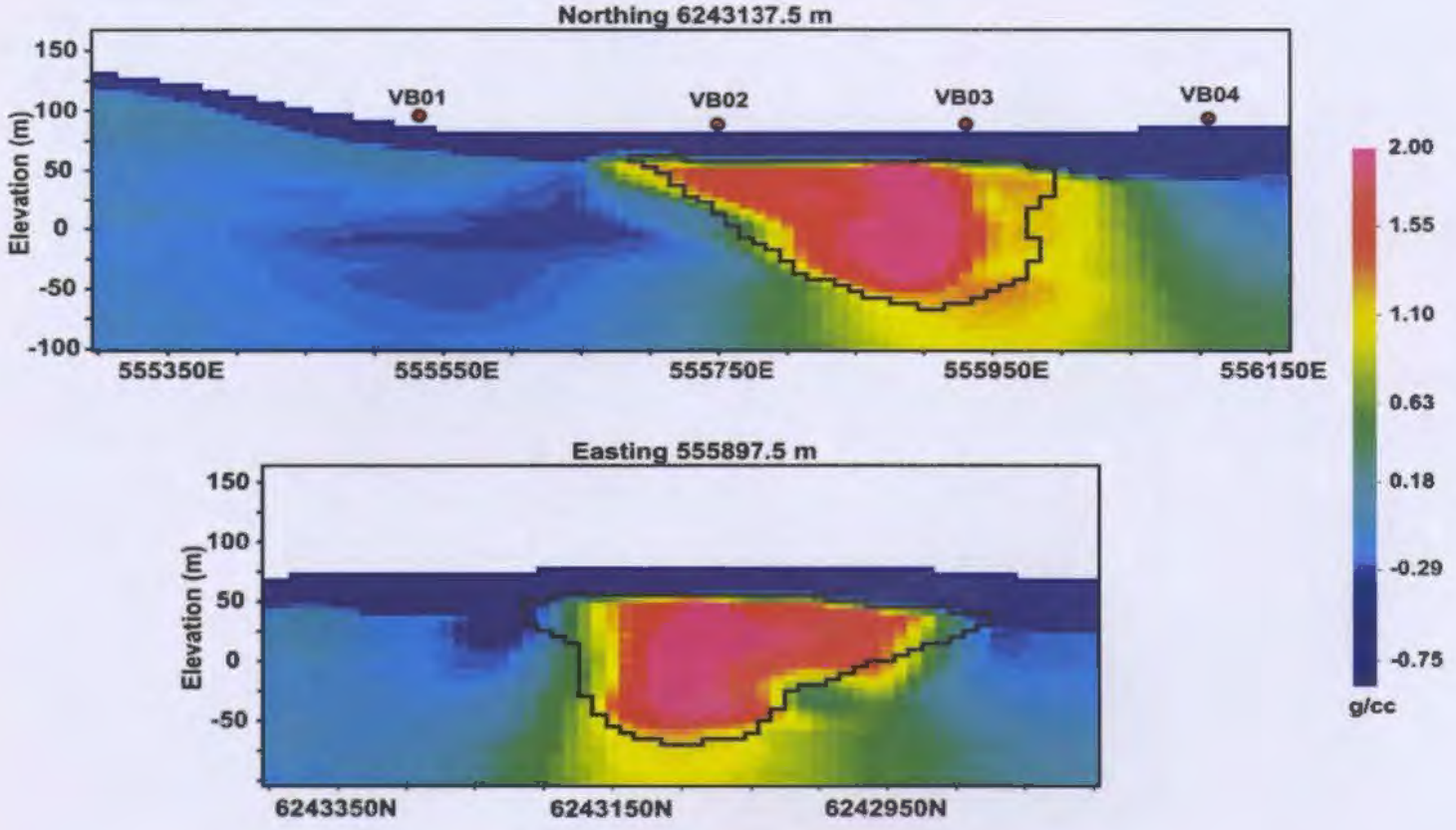

Figure 5.39: The density model DEN29 recovered from inversion INV29. The inversion was constrained using the density contrast model DM08 (Figure 5.36) as a reference model. Cells within the reference model were constrained using the WDAT05 weighing model. Sections are along UTM northing 6243137.5m and easting 555897.5m (NAD83), with elevations relative to sea level. The known position of the Ovoid is shown in black. Estimated position of gravity lines VB01, VB02, VB03 and VB04 perpendicular to east-west section are shown in red. Scale can be inferred from coordinate annotations.

Chapter 6: Results, conclusions and recommendations for further work

The final chapter in this study examines the results obtained from the gravity data and processing, density model construction and inversion results. The chapter primarily focuses on the impact of integrating geological models into the UBC-GIF inversion program. The chapter concludes with recommendations for further work.

6.1 Gravity Data and Processing

Many processing techniques were applied to the gravity data collected at Voisey's Bay to try and enhance the response of near surface geological features. The processing techniques were carried out in both frequency and spatial domains. Frequency domain methods included wavelength filtering and upward continuation. Spatial techniques applied to the gravity dataset included the removal of 1st and 2nd order polynomial surfaces. Upward continuation to a level of 3 km (Figure 2.22) was chosen to produce the best estimate of the regional field, of near surface geological features, since the residual anomalies are isolated and continuous from large scale regional features throughout Voisey's Bay. Gravity anomalies in the south are not well resolved due to the complexity of the geological units, coupled with the low density contrast between the gneisses and granites. Most of the southern anomalies have similar wavelengths making it difficult to visually interpret the data.

Similar processing techniques were used to separate the gravitational contribution of the Ovoid from the surrounding Voisey's Bay troctolite and enderbitic gneiss. The regional field was removed from the dataset over the Ovoid by upward

continuing the gravity field to level 500m. At a continuation level of 500m, there is no visible contribution from the Ovoid as illustrated in Figure 5.3. The upward continued field was then interpolated to the location of the collected gravity data using the vertical projection capabilities in Gocad. This method was used to eliminate additional data points generated from gridding an irregular dataset. The primary purpose of processing the dataset was to use the residual field as an input dataset in the UBG-GIF inversion program. Gridding datasets is a limitation imposed by processing packages and is not recommended when inverting gravity data. The estimated residual fields along lines VB01, VB02 and VB03 over the known position of the Ovoid have a maximum amplitude of 3.5 mGal (Figure 5.1).

6.2 Three-Dimensional Density Models

A three-dimensional model of the Ovoid and Mini-Ovoid was generated in Gocad using the surfaces and wireframes provided by VBNC. The model was constructed by generating cell regions based on the known position of the OB, ENGN, TR and MASU units. The TR and MASU regions were gridded in three dimensions using ordinary Kriging and variogram models derived from the drill hole data. The Kriged density model shown in Figure 3.11, demonstrates a significant density contrast between the MASU and ENGN regions (Figure 3.9B). The density contrast between the ENGN and TR regions (Figure 3.9B) are insignificant and not evident in the Kriged model (Figure 3.11). Slight density variations are observed within the Ovoid on the order of 0.20 g/cc. At an elevation of 62.5m (Figure 3.13A), a high density region exists containing densities greater than 1.70 g/cc located approximately at an easting and northing of 555825m and

6243250m. A second high density region is observed at a depth of 52.5m (Figure 3.13B) at a UTM easting and northing of 555825m and 6243100m. These two high density regions are connected at a depth of 32.5m (Figure 3.14B) into a single high density region extending to a depth of 12.5m (Figure 3.15B). These high average density anomalies are concentrated toward the center of the Ovoid. The density variations observed within the Ovoid provides further evidence that the deposit was not a result of gravitational settling occurring at the base of a magma chamber. Deposits driven by gravitational settling within magma would concentrate high densities toward the base of the chamber. The concentration of densities toward the center of the deposit agree with the theory that the Ovoid is a result of multiple waves of magma (Naldrett, 2004; Naldrett et al., 2000) through a complex conduit system (Evans-Lamswood et al, 2000; Evens-Lamswood, 1999).

A series of synthetic gravity datasets were generated to examine the gravitational field of the Kriged density model. Synthetic datasets FM01 and FM02 were generated from density models DEN02 and DEN03 in order to establish a background density which would be removed from reference models. Comparisons made between the synthetic datasets FM01 (Figure 5.1) and the residual gravity dataset (Figure 2.6) indicate that a reasonable estimate of the background density is 2.67 g/c. Comparisons between the location of the survey lines VB01, VB02, VB03 and VB04 and the synthetic dataset FM03 (Figure 5.2) indicates that the gravity data collected along line VB03 are offset approximately 70m east of the thickest section of the Ovoid. As a result, the maximum residual you would expect based on the Kriged density model is 0.50 mGal grater than the residual observed on the survey lines.

6.3 Gravity Inversions

Unconstrained gravity inversions (Figure 5.6 and Figure 5.8) provide a reasonable estimate of the location of the Ovoid but a poor estimate of the density variation. The poor density reproduction is primarily due to the lack of a low density overburden region and medium density cells being populated at a greater depth. Constraining the inversion to cells within the model region MESH01, known to be occupied by the Ovoid, only slightly improves the anomaly amplitude shown in Figure 5.9 and Figure 5.10. A major improvement in amplitude is observed when the simple two layer regional model DM05, consisting of low density overburden by denser bedrock, is incorporated into the inversion process as a reference model (Figure 5.11 and Figure 5.12) and furthermore when the overburden cells are weighted high using the weighting model WDAT01. A down side to weighting the overburden cells is that a smooth transition exists between the OB and MASU interface (Figure 5.13 and Figure 5.14). Smoothing is an inherent byproduct of minimum-structure style inversion programs. Setting the length scales to 0m eliminates the smoothing parameters but increases the complexity as shown in Figure 5.17. Reducing length scales slightly reduces the overall smoothing in the vertical and horizontal directions whereas a significant decrease in smoothing is observed when the depth weighting parameter *beta* is adjusted (Figure 5.18).

To generate a sharp density contrast at the OB-MASU interface a geologically meaningful model containing the sharp interface must be incorporated into the inversion process. Inverting the INDATA01 dataset using the Kriged model DM02 as a reference model in INV19 (Figure 5.19) does an excellent job approximating the outline of the Ovoid. However, the high density variations within the Ovoid are not well preserved and

are placed beneath the observation locations along line VB03. The spatial distribution of the initial gravity acquisition locations control the capacity of the inversion to correctly position recovered density anomalies. Inverting the INDATA02 datasets required the depth weighting parameters *beta* and *znot* to be set at 2.0 and 1.25. When the depth weighting parameters are set to default, the internal variations are recovered when the INVDATA02 dataset is inverted (Figure 5.22). Lower beta values, as shown in inversion trial INV20 (Figure 5.21), are not able to reproduce the internal variation of the Ovoid since the gzfor3d program was used to calculate the pseudo-gravity dataset INDATA02.

Decimated models DM06 and DM07 generated from Kriging 56 (Figure 5.26) and 28 (Figure 5.31) drill logs provide a good approximation of the geometry and amplitude of the Ovoid. Inverting the INDATA02 dataset using the DM06 and DM07 models as reference models provides a slight improvement when comparing the recovered anomalies to the Kriged density model illustrated in Figure 3.11. The decimated datasets do not resolve density variations inside the Ovoid due to averaging and smoothing adjacent cells during the Kriging process. The spatial distribution of the density dataset controls the vertical and horizontal resolution of the inversion. The greatest improvement was shown when 6 drill logs were used to create a reference model DM08 (Figure 5.36). The DM08 model was generated using a variogram derived from the gravity data and borehole data. Due to the lack of drill logs, the northernmost and easternmost edges of the Ovoid are not well defined from Kriging. However, inverting the pseudo-gravity INDATA02 dataset using DM08 (6 drill logs) as a reference model considerably improves the northern and eastern edges of the DM08 model (Figure 5.38). As a result, it can be concluded that inverting preliminary density models derived from density logs

using a detailed gravity dataset, similar to the distribution of INDATA02, can significantly improve early-stage geological models as drilling progresses. When a sparse gravity dataset is available, such as INDATA01, little improvement in the recovered density models is observed.

6.4 Conclusions

The results and conclusions can be summarized as follows;

(1) Good inversions require a relatively dense initial set of gravity observations.

(2) Good inversions require geological constraints such as bedrock-overburden interface, range of density contrasts and limits of deposit in the lateral and vertical directions.

(3) Inversions applied to gravity data with limited additional information can localize drilling targets. Incorporating even a modest amount of information from drilling can significantly improve recovered models when the proper parameters are set.

6.5 Recommendations for Future Work

The Kriged density model generated in this study was derived from a density dataset calculated from three conditional equations using regression analysis of the assay percentages of iron, sulphur and copper. Another approach which could be used to generate a density model of the Ovoid and Mini-Ovoid is to individually generate three-dimensional models of the percentage of each element. This approach would retain the

spatial characteristics of each element. The empirical equations derived by VBCN could then be applied to each cell within the mesh to construct the final density model. In addition, other multi-point geostatistical methods could be used to generate reference models.

Another recommendation would be to examine the cause of the high density regions observed within the Ovoid. The high density regions could have major implications on the Ovoid mineralization and could suggest pathways of high density fluids. These zones could be compared and correlated with other geochemical, geophysical and geological information. The final recommendation would be to study the effect of changing weights along the cell interfaces. The cell weights in the vertical direction may be adjusted to accommodate for sharp boundaries such as the OB-MASU interface encountered in this study.

References

Amelin, Y., Li, C., and Naldrett, A.J., 1999, Geochronology of the Voisey's Bay intrusion, Labrador, Canada, by precise U-Pb dating of coexisting bad-deleyite, zircon, and apatite: Lithos, **47**, 33-51.

Bhattacharyya, B.K., 1966, Continuous spectrum of the total-magnetic-field anomaly due to a rectangular prismatic body, Geophysics, **31**, 97-121

Blakely, R. J., 1995, Potential theory in gravity & magnetic applications: Cambridge University Press, Cambridge, United Kingdom (GBR).

Boersting Pedersen, L., 1977, Interpretation of potential field data, a generalized inverse approach: Geophys.Prospect., **25,** 199-230. A

Briggs, I. C., 1974, Machine contouring using minimum curvature: Geophysics, **39,** 39-48.

Dean, W. C., 1958, Frequency analysis for gravity and magnetic interpretation: Geophysics, **23,** 97-127.

Evans-Lamswood, D. M., Butt, D. P., Jackson, R. S., Lee, D. V., Muggridge, M. G., Wheeler, R. I. and Wilton, D. H. C., 2000, Physical controls associated with the distribution of sulfides in the Voisey's Bay Ni-Cu-Co deposit, Labrador; A special issue on Voisey's Bay Ni-Cu-Co deposit: Econ.Geol.Bull.Soc.Econ.Geol., **95,** 749-769.

Evans-Lamswood, D., 1998, Physical and geometric controls on the distribution of magmatic and sulphide bearing phases within the Voisey's Bay nickel-copper-cobalt deposit, Voisey's Bay, Labrador:

Farquharson, C.G., *Constructing piecewise-constant models in multi-dimensional minimum-structure inversions*, 76th Annual Meeting of the Society of Exploration Geophysicists, New Orleans, 1-6 October 2006.

Funck, T., and Louden, K., 1998, Wide-angle transect across the Torngat orogen from Churchill to Nain provinces: Secretariat LITHOPROBE Rept. **68**, 38-49.

Grav3D; *A Program Library for Forward Modelling and Inversion of Gravity Data over3D Structures, version 2.0* (2001). Developed under the consortium research project Joint/Cooperative Inversion of Geophysical and Geological Data, UBC-Geophysical Inversion Facility, Department of Earth and Ocean Sciences, University of British Columbia, Vancouver, British Columbia.

Hearst, R. B. and Morris, W. A., 2001, Regional gravity setting of the Sudbury Structure: Geophysics, **66,** 1680-1690.

Hinze, W. J., 2003, Bouguer reduction density, why 2.67? Geophysics, **68,** 1559-1560.

James, J. F., 2002, A student's guide to Fourier transforms: with applications in physics and engineering: Cambridge University Press.

Kitanidis, P. K., 1997, Introduction to geostatistics: applications to hydrogeology: Cambridge University Press.

Krige, D. G., 1976, A review of the development of geostatistics in South Africa: **24,** 279-293.

Li, C., Lightfoot, P. C., Amelin, Y. V. and Naldrett, A. J., 2000, Contrasting petrological and geochemical relationships in the Voisey's Bay and Mushuau intrusions, Labrador, Canada; implications for ore genesis; A special issue on Voisey's Bay Ni-Cu-Co deposit: Econ.Geol.Bull.Soc.Econ.Geol., **95,** 771-799.

Li, X. and Goetze, H., 1999, Comparison of some gridding methods: **18,** 898-900.

Li, Y. and Oldenburg, D. W., 1996, 3-D inversion of magnetic data: Geophysics, **61,** 394-408.

Li, Y. and Oldenburg, D. W., 1998a, 3-D inversion of gravity data: Geophysics, **63,** 109-119.

Li, Y. and Oldenburg, D. W., 1998b, Separation of regional and residual magnetic field data: Geophysics, **63,** 431-439.

Nagy, D., 1973, A chart for the computation of the gravitational attraction of a right rectangular prism: Pure Appl.Geophys., **102,** 5-14.

Nagy, D., 1966, The gravitational attraction of a right rectangular prism: Geophysics, **31,** 362-371.

Naidu, P. S. and Mathew, M. P., 1998, Analysis of geophysical potential fields: a digital signal processing approach: Elsevier.

Naldrett, A.J., Keats, H., Sparks, K., and More, R., 1996, Geology of the Voisey's Bay Ni-Cu-Co deposit, Labrador, Canada: Exploration and Mining Geology, **5**, 169-179.

Naldrett, A. J., Li, C., Asif, M. and Amelin, Y., 1998, The Voisey's Bay Ni-Cu-Co deposit, Labrador, Canada; a model for ore genesis; Geological Society of America, 1998 annual meeting: **30,** 14.

Naldrett, A. J., Asif, M., Kristic, S. and Li, C., 2000, The composition of mineralization of the Voisey's Bay Ni-Cu sulfide deposit, with special reference to platinum-group

elements; A special issue on Voisey's Bay Ni-Cu-Co deposit: Econ.Geol.Bull.Soc.Econ.Geol., **95,** 845-865.

Naldrett, A. J., 2004, Magmatic sulfide deposits; geology, geochemistry and exploration: Springer-Verlag, Berlin, Federal Republic of Germany (DEU).

Odegrad, M. E. and Berg, J. W., 1965, Gravity interpretation using the Fourier integral, Geophysics, **30,** 424-438.

Oldenburg, D. W., 1974, The inversion and interpretation of gravity anomalies: Geophysics, **39,** 526-536.

Pan, G. and Harris, D. P., 2000, Information synthesis for mineral exploration: Oxford University Press.

Parker, R. L., 1973, The rapid calculation of potential anomalies: Geophys J. Royal Astron. Sot., **31,** 447-455.

Press, S. J., 1989, Bayesian statistics : principles, models, and applications: Wiley.

Ramirez, R. W., 1985, The FFT, fundamentals and concepts: Prentice-Hall.
Ripley, E. M., Park, Y., Li, C. and Naldrett, A. J., 2000, Oxygen isotope studies of the Voisey's Bay Ni-Cu-Co deposit, Labrador, Canada; A special issue on Voisey's Bay Ni-Cu-Co deposit: Econ.Geol.Bull.Soc.Econ.Geol., **95,** 831-844.

Rivers, T., and Mengel, F., 1994, A cross-section of the Abloviak shear zone at Saglek Fiord, and a preliminary tectonic model for Torngat orogen: LITHOPROBE Rept. **36,** 171-184.

Ryan, B., 2000, Geological investigations in the type locality of the Nain plutonic suite (NTS 14C/12): Government of Newfoundland and Labrador. Geological Survey, St. John's, NL, Canada (CAN), 2000-1.

Ryan, B., Wardle, R. J., Gower, C. F., and Nunn, G.A.G., 1995, Nickel-copper sulphide mineralization in Labrador: The Voisey's Bay Discovery and its exploration implications: Newfoundland Department of Mines and Energy, Geological Survey, Current Research Rept. **97,** 1-14.

Serway, R. A., 1996, Physics for scientists & engineers, with modern physics: Saunders College Pub.

Silva, J. B. C., Medeiros, W. E. and Barbosa, V. C. F., 2001, Potential-field inversion; choosing the appropriate technique to solve a geologic problem: Geophysics, **66,** 511-520.

Skeels, D. C., 1967, What is residual gravity: Geophysics, **32,** 872-876.

Spector, A. and Grant, F. S., 1970, Statistical models for interpreting aeromagnetic data: Geophysics, **35,** 293-302.

Spiegel, M. R., 1999, Schaum's outline of theory and problems of advanced mathematics for engineers and scientists: McGraw-Hill.

Stein, M. L., 1999, Interpolation of spatial data: some theory for kriging: Springer.

Van Krenendonk, M.J., St-Onge, M.R., and Henderson, J.B., 1993, Paleo-proterozoic tectonic assembly of northeast Laurentia through multiple indentations: Precambrian Research, **63**, 325-347.

Telford, W. M., Geldart, L. P. and Sheriff, R. E., 1990, Applied geophysics: Cambridge University Press.

Zurflueh, E. G., 1967, Applications of two-dimensional linear wavelength filtering: Geophysics, **32,** 1015-1035.

Appendix A

Rock Codes and Density Statistics

Rock Code	VBNC Assigned Rock Name	Mean	Std. Deviation	Variance	Count
		(g/cc)			
AN	anorthosite	2.80	0.04	0.00	2
BBS2	basal breccia sequence Tr-5% sulphides	2.96	0.08	0.01	35
BBS3	basal breccia sequence 5-15% sulphides	3.04	0.09	0.01	139
BBS4	basal breccia sequence 15-40% sulphides	3.31	0.17	0.03	83
BBS5	basal breccia sequence 40-75% sulphides	4.46	0.26	0.07	5
BX	breccia	2.90	0.03	0.00	2
BX1	breccia barren	2.85	0.08	0.01	21
BX2	breccia Tr-5%	2.94	0.09	0.01	806
BX3	breccia 5-15%	3.03	0.11	0.01	2429
BX4	breccia 15-40%	3.23	0.18	0.03	1725
BX5	breccia 40-75%	3.54	0.24	0.06	33
CT1	chilled troctolite-barren	2.91	0.06	0.00	18
CT2	chilled troctolite Tr-5% sulphides	3.29	0.34	0.12	4
DIKE	dike	2.82	0.02	0.00	3
DNT	dunite	3.07	0.10	0.01	9
ENG1	enderbitic gneiss-barren	2.79	0.05	0.00	211
ENG2	enderbitic gneiss Tr-5% sulphides	2.82	0.09	0.01	196
ENGN	enderbitic gneiss	2.81	0.07	0.01	2340
FDIO	ferrodiorite	2.82	0.06	0.00	5
FEGB	ferrogabbro	2.96	0.09	0.01	84
FGB1	ferrogabbro-barren	2.94	0.11	0.01	160
FGB2	ferrogabbro Tr-5% sulphides	2.97	0.08	0.01	197
FGB3	ferrogabbro 5-15% sulphides	3.06	0.10	0.01	81
FGB4	ferrogabbro 15-40% sulphides	3.29	0.17	0.03	12
FLDK	felsic dike	2.72	0.07	0.00	9
FLT	fault	2.98	0.16	0.03	101
FM1	feeder melange-barren	2.92	0.05	0.00	24
FM2	feeder melange Tr-5% sulphides	2.97	0.08	0.01	209
FM3	feedermelange5-15%sulphides	3.09	0.17	0.03	85
FM4	feeder melange 15-40% sulphides	3.27	0.23	0.05	36
FM5	feeder melange 40-75% sulphides	3.80	0.18	0.03	3
G	gneiss	2.81	0.07	0.01	553
GB	gabbro	2.88	0.11	0.01	22
GPGN	garnetiferous paragneiss	2.82	0.12	0.01	915
GR	granite	2.72	0.10	0.01	471
GRGN	granite gneiss	2.76	0.03	0.00	3
HFZ	highly fractured zone	2.91	0.06	0.00	30
LBX2	leopard-textured breccia Tr-5% sulphides	2.92	0.07	0.00	13
LBX3	leopard-textured breccia 5-15% sulphides	3.18	0.18	0.03	62
LBX4	leopard-textured breccia 15-40% sulphides	3.38	0.16	0.03	129
LBX5	leopard-textured breccia 40-75% sulphides	3.50	0.12	0.02	37
LTT2	leopard texture troctolite Tr-5% sulphides	3.06	0.11	0.01	11
LTT3	leopard texture troctolite 5-15% sulphides	3.27	0.15	0.02	168
LTT4	leopard texture troctolite 15-40% sulphides	3.38	0.18	0.03	1164
LTT5	leopard texture troctolite 40-75% sulphides	3.60	0.15	0.02	186
MASU	massive sulfide	4.61	0.11	0.01	5222
MFDK	mafic dike	2.94	0.10	0.01	334

Rock Code	VBNC Assigned Rock Name	Mean	Std. Deviation	Variance	Count
		(g/cc)			
MGT1	marginal troctolite-barren	2.93	0.04	0.00	9
MGT2	marginal troctolite Tr-5% sulphides	2.94	0.08	0.01	64
MGT3	marginal troctolite 5-15% sulphides	2.92	0.03	0.00	9
MOG1	mafic orthogneiss-barren	2.79	0.04	0.00	17
MOG2	mafic orthogneiss Tr-5% sulphides	2.94	0.17	0.03	29
MOG3	mafic orthogneiss 5-15% sulphides	2.98	0.15	0.02	17
MOG4	mafic orthogneiss 15-40% sulphides	3.14	0.11	0.01	17
MONZ	monzonite	3.03	0.23	0.05	4
MT	magnetite	2.99	0.11	0.01	2
MYL	mylonite	2.84	0.09	0.01	17
MZ	mixed zone	2.94	0.13	0.02	234
NOG1	Nain orthogneiss-barren	2.85	0.12	0.01	34
NOG2	Nain orthogneiss Tr-5% sulphides	2.83	0.05	0.00	6
NOG3	Nain orthogneiss 5-15% sulphides	3.08	0.00	0.00	2
NOG4	Nain orthogneiss 15-40% sulphides	3.12	0.03	0.00	3
NT1	normal troctolite-barren	2.86	0.12	0.01	17
NT2	normal troctolite Tr-5% sulphides	2.90	0.06	0.00	160
OBX2	original fragmental breccia Tr-5% sulphides	3.04	0.14	0.02	33
OBX3	original fragmental breccia 5-15% sulphides	3.00	0.06	0.00	138
OBX4	original fragmental breccia 15-40% sulphides	3.04	0.11	0.01	30
OGB1	olivine gabbro-barren	2.91	0.07	0.00	31
OGB2	olivine gabbro Tr-5% sulphides	2.93	0.09	0.01	263
OGB3	olivine gabbro 5-15% sulphides	3.11	0.14	0.02	78
OGB4	olivine gabbro 15-40% sulphides	3.32	0.17	0.03	29
OGB5	olivine gabbro 40-75% sulphides	3.57	0.04	0.00	3
OLGB	olivine gabbro	2.90	0.03	0.00	4
ORGN	ortho gneiss	2.81	0.07	0.00	874
PEG	pegmatite	2.74	0.23	0.05	210
PRGN	paragneiss	2.82	0.17	0.03	643
PXT	pyroxenite	2.92	0.00	0.00	2
QPGN	quartzo-feldspathic paragneiss	2.77	0.11	0.01	327
QTZ	quartz	2.80	0.09	0.01	23
QV	quartz vein	2.75	0.16	0.02	67
QZDK	quartzo feldspathic dike	2.73	0.14	0.02	17
QZVN	quartzo feldspathic vein	2.69	0.09	0.01	100
RPGR	rapakivi granite	2.80	0.08	0.01	213
SHR	shear	2.99	0.12	0.01	17
SMAS	semi-massive sulfide	3.63	0.37	0.14	103
SRPT	serpentinite	2.95	0.09	0.01	9
SYNT	syenite	2.75	0.09	0.01	193
TBX1	troctolite breccia-barren	2.91	0.05	0.00	18
TBX2	troctolite breccia Tr-5% sulphides	2.98	0.10	0.01	644
TBX3	troctolite breccia 5-15% sulphides	3.08	0.13	0.02	829
TBX4	troctolite breccia 15-40% sulphides	3.29	0.19	0.04	705
TBX5	troctolite breccia 40-75% sulphides	3.69	0.25	0.06	9
TGM1	troctolite-gneiss melange-barren	2.86	0.09	0.01	47
TGM2	troctolite-gneiss melange Tr-5% sulphides	2.92	0.09	0.01	353

Rock Code	VBNC Assigned Rock Name	Mean	Std. Deviation	Variance	Count
		(g/cc)			
TGM3	troctolite-gneiss melange 5-15% sulphides	3.02	0.13	0.02	**52**
TR1	troctolite-barren	2.92	0.07	0.00	**850**
TR2	troctolite Tr-5% sulphides	2.95	0.10	0.01	**3004**
TR3	troctolite 5-15% sulphides	3.05	0.15	0.02	**1626**
TR4	troctolite 15-40% sulphides	3.31	0.21	0.04	**2269**
TR5	troctolite 40-75% sulphides	3.54	0.21	0.04	**568**
TRT1	transitional troctolite-barren	2.95	0.01	0.00	**3**
TRT2	transitional troctolite Tr-5% sulphides	3.00	0.09	0.01	**4**
TRT3	transitional troctolite 5-15% sulphides	3.18	0.11	0.01	**4**
UM	ultramafic	3.09	0.24	0.06	**362**
VBX3	vein breccia 5-15% sulphides	3.26	0.11	0.01	**19**
VBX4	vein breccia 15-40% sulphides	3.40	0.29	0.08	**127**
VBX5	vein breccia 40-75% sulphides	3.59	0.22	0.05	**11**
VT1	variable troctolite-barren	2.91	0.12	0.01	**79**
VT2	variable troctolite Tr-5% sulphides	2.93	0.08	0.01	**6565**
VT3	variable troctolite 5-15% sulphides	3.01	0.13	0.02	**3969**
VT4	variable troctolite 15-40% sulphides	3.24	0.19	0.04	**1081**
VT5	variable troctolite 40-75% sulphides	3.44	0.18	0.03	**425**
				Total =	**46058**

Appendix B

Repeated Density Calculations

Borehole ID	Easting (m)	Norting (m)	Elevation (m)	Calculation #1 (g/cc)	Calculation #2 (g/cc)
VB00518C	560956	6441121	-1331	3.24	3.25
VB00534	558985	6441140	-990	3.53	3.45
VB00534	558986	6441139	-966	2.99	2.97
VB00534	558987	6441138	-939	2.94	2.95
VB00534A	559004	6441218	-990	3.57	3.59
VB00534A	559004	6441214	-966	3.05	3.01
VB00535	558018	6441968	-820	3.48	3.52
VB00535	558019	6441967	-848	2.93	2.92
VB00536	558973	6441033	-955	2.96	2.95
VB00536	558972	6441030	-992	3.40	2.96
VB00537	559569	6441194	-1031	2.92	2.94
VB00538	560689	6440082	-1441	3.14	3.15
VB00539	560424	6448464	-592	2.93	2.91
VB00540	557276	6442506	-577	4.67	4.62
VB00540	557276	6442505	-522	3.04	3.02
VB00541	560764	6441134	-1273	2.85	2.86
VB00541	560764	6441131	-1230	2.91	2.94
VB00541B	560819	6441091	-1220	3.03	3.02
VB00541B	560829	6441084	-1361	3.06	3.08
VB00542	557283	6442531	-579	3.41	3.41
VB00542	557284	6442531	-535	4.62	4.61
VB00542	557285	6442531	-508	3.28	3.28
VB00543	557248	6442457	-593	3.25	3.32
VB00543	557249	6442456	-557	3.58	3.56
VB00543	557251	6442456	-519	4.60	4.61
VB00543	557253	6442456	-476	2.98	2.98
VB00544	557236	6442531	-501	2.99	3.02
VB00544	557235	6442530	-547	4.59	4.65
VB00544	557235	6442530	-568	3.63	3.62
VB00545	557394	6442502	-586	4.61	4.63
VB00545	557394	6442502	-563	2.95	2.95
VB00545	557394	6442502	-581	4.56	4.61
VB00546	557305	6442494	-517	3.20	3.20
VB00546	557305	6442494	-548	4.61	4.63
VB00546	557304	6442494	-578	4.61	4.60
VB00547	557362	6442429	-611	4.66	4.68
VB00547	557362	6442429	-575	3.30	3.31
VB00547	557363	6442428	-534	3.19	3.18
VB00548	557382	6442463	-552	3.15	3.14
VB00548	557383	6442463	-581	3.76	3.81
VB00548	557383	6442462	-608	4.59	4.57
VB00549	558095	6442080	-817	2.98	2.98
VB00549	558096	6442080	-845	2.92	2.92
VB00550	557662	6442313	-722	3.54	3.54
VB00550	557658	6442300	-673	3.31	3.28
VB00550	557656	6442292	-644	3.30	3.19

Borehole ID	Easting (m)	Norting (m)	Elevation (m)	Calculation #1 (g/cc)	Calculation #2 (g/cc)
VB01361B	560822	6441255	-1239	3.10	3.10
VB01461G	554892	6443030	-1576	3.60	3.29
VB01461G	554893	6443025	-1554	3.47	3.50
VB01552	557698	6442310	-657	3.23	3.19
VB01552	557698	6442309	-721	3.69	3.69
VB01553	557481	6442434	-553	2.92	2.96
VB01553	557481	6442433	-583	3.01	3.05
VB01553	557481	6442432	-610	3.49	3.43
VB01553	557482	6442432	-634	3.09	3.12
VB01555	561144	6441016	-1454	3.79	3.80
VB01555	561143	6441012	-1409	3.08	3.10
VB02556	556017	6442811	9	3.12	3.16
VB02557	556097	6442773	48	3.06	3.09
VB02557	556094	6442734	2	3.00	3.01
VB02557	556090	6442710	-29	3.25	3.14
VB02557	556086	6442693	-49	3.05	3.05
VB02557	556080	6442674	-73	3.01	3.00
VB02558	556144	6442789	30	2.88	2.92
VB02559	556164	6442744	15	3.07	3.07
VB02559	556232	6442719	-71	3.04	3.01
VB02559	556263	6442708	-110	3.03	3.01
VB02559	556292	6442698	-146	3.02	2.99
VB02560	556215	6442817	51	2.93	2.91
VB02560	556215	6442817	22	2.97	2.99
VB02562	556069	6442738	32	2.95	2.97
VB03581	556044	6442738	31	2.96	2.97
VB03581	556044	6442738	9	3.05	3.06
VB03581	556044	6442738	-8	2.93	2.95
VB03581	556044	6442738	-33	2.73	2.70
VB03582	556095	6442737	22	2.95	2.93
VB03582	556095	6442737	42	3.06	3.04
VB03582	556095	6442737	1	2.86	2.85
VB03582	556096	6442737	-19	3.01	3.03
VB03582	556096	6442737	-39	2.97	2.95
VB03582	556096	6442737	-61	3.28	3.29
VB03582	556096	6442736	-82	2.77	2.76
VB03583	556047	6442777	-39	2.78	2.78
VB03583	556046	6442776	-19	2.81	2.80
VB03583	556045	6442776	3	3.08	3.11
VB03583	556044	6442775	22	3.16	3.15
VB03584	554744	6443461	-88	2.91	2.91
VB03584	554743	6443453	-106	2.89	2.87
VB03584	554739	6443437	-142	2.75	2.75
VB03584	554738	6443429	-161	2.76	2.76
VB03585	556371	6442681	-205	3.03	3.02
VB03585	556372	6442681	-166	2.98	2.99

Borehole ID	Easting (m)	Norting (m)	Elevation (m)	Calculation #1 (g/cc)	Calculation #2 (g/cc)
VB03585	556373	6442681	-118	3.02	3.01
VB03585	556374	6442681	-76	2.94	2.93
VB03587	554832	6443439	-80	3.53	3.55
VB03588	553774	6443453	-188	4.57	4.56
VB03588	553774	6443441	-151	3.34	3.38
VB03588	553774	6443425	-103	3.11	3.09
VB03589	553772	6443462	-120	4.58	4.53
VB03589	553773	6443449	-94	3.02	3.04
VB03590	555015	6443422	-195	3.18	3.15
VB03591	553799	6443423	-198	4.58	4.59
VB03594	553802	6443466	-109	4.60	4.59
VB03596	553824	6443423	-215	2.91	2.92
VB03596	553824	6443417	-176	4.58	4.64
VB03597	553824	6443442	-145	2.88	2.92
VB03598	554947	6443443	-76	3.15	3.08
VB03599	553822	6443483	-140	4.60	4.62
VB03600	554994	6443447	39	2.88	2.87
VB03600	554996	6443420	4	3.64	3.66
VB03600	554998	6443393	-30	2.98	3.00
VB03601	553845	6443424	-192	4.53	4.60
VB03601	553846	6443422	-160	4.60	4.65
VB03602	555052	6443446	-46	3.55	3.57
VB03602	555054	6443424	-82	3.53	3.53
VB03603	553847	6443460	-181	2.91	2.94
VB03603	553847	6443453	-150	4.63	4.66
VB03604	554789	6443455	115	2.86	2.88
VB03604	554789	6443426	76	2.75	2.75
VB03604	554789	6443399	40	3.16	2.99
VB03605	554920	6443428	83	2.93	2.92
VB03605	554919	6443400	46	3.58	3.54
VB03605	554919	6443387	27	3.45	3.47
VB03606	553849	6443481	-103	2.96	2.96
VB03607	554823	6443397	163	2.94	2.94
VB03607	554823	6443375	129	3.33	3.33
VB03608	553876	6443460	-152	3.37	3.37
VB03609	554771	6443405	121	3.23	3.23
VB03609	554770	6443374	162	3.39	3.42
VB03610	553877	6443512	-154	4.72	4.72
VB03610	553876	6443489	-106	3.28	3.26
VB03610	553876	6443465	-55	2.75	2.75
VB03611	554768	6443399	91	2.95	2.94
VB03611	554765	6443368	130	3.31	3.27
VB03611	554763	6443336	172	2.86	2.83
VB03612	554967	6443461	20	3.03	3.02
VB03612	554968	6443438	47	2.86	2.85
VB03612	554969	6443410	77	3.28	3.25

Borehole ID	Easting (m)	Norting (m)	Elevation (m)	Calculation #1 (g/cc)	Calculation #2 (g/cc)
VB03612	554969	6443386	105	3.53	3.59
VB03612	554972	6443347	150	3.19	3.19
VB03613	553869	6443403	-251	2.90	2.91
VB03613	553868	6443398	-199	2.72	2.73
VB04206A	557312	6442558	-547	3.57	3.55
VB04544A	557236	6442531	-505	2.86	2.87
VB04544A	557235	6442530	-573	4.57	4.56
VB04614	555214	6443469	-143	2.91	2.90
VB04614	555215	6443458	-179	3.55	3.58
VB04615	553843	6443392	-183	4.68	4.61
VB04616	555150	6443382	-1	2.84	2.85
VB04617	555200	6443449	-117	3.19	3.25
VB04617	555200	6443440	-163	3.00	3.00
VB04618	553825	6443382	-220	2.75	2.76
VB04619	555200	6443381	-33	3.15	3.24
VB04620	553807	6443393	-210	4.54	4.20
VB04621	555082	6443408	58	2.92	2.92
VB04621	555083	6443408	18	3.37	3.40
VB04621	555084	6443408	-22	3.40	3.39
VB04621	555085	6443408	-58	3.00	2.98
VB04623	555079	6443341	114	3.00	2.99
VB04624	553939	6443375	-352	2.91	2.91
VB04624	553936	6443364	-319	3.09	3.11
VB04625	554933	6443375	163	3.18	3.16
VB04625	554932	6443347	119	2.90	2.90
VB04626	554957	6443369	161	3.28	3.29
VB04626	554969	6443336	117	2.91	2.94
VB04627	554927	6443397	149	3.16	3.16
VB04627	554928	6443370	110	3.13	3.15
VB04628	554794	6443388	167	3.28	3.27
VB04628	554764	6443388	137	3.52	3.55
VB04628	554724	6443387	98	3.25	3.20
VB04629	554974	6443375	170	3.09	3.10
VB04629	555002	6443358	139	3.02	2.98
VB04629	555028	6443343	110	2.89	2.88
VB04630	556576	6442237	-207	2.95	2.97
VB04630	556575	6442237	-163	2.90	2.90
VB04631	553845	6443384	-245	4.59	4.60
VB04631	553844	6443379	-197	4.65	4.66
VB04632	553841	6443347	-236	2.99	2.98
VB04633	553926	6443413	-298	2.98	2.99
VB04634	554010	6443388	-386	3.13	3.15
VB04635	553733	6443386	-234	4.56	4.56
VB04635	553731	6443370	-171	2.93	2.92
VB04636	553817	6443421	-165	4.60	4.62
VB04637	553731	6443362	-222	3.18	3.16

Borehole ID	Easting (m)	Norting (m)	Elevation (m)	Calculation #1 (g/cc)	Calculation #2 (g/cc)
VB04637	553729	6443353	-169	2.93	2.93
VB04638	553733	6443413	-219	4.63	4.58
VB04638	553731	6443398	-175	4.54	4.61
VB04639	553731	6443464	-230	4.60	4.62
VB04639	553728	6443432	-172	4.58	4.60
VB04639	553727	6443415	-139	3.16	3.13
VB04640	553728	6443437	-140	3.08	3.07
VB04640	553728	6443412	-102	3.12	3.12
VB04641	553777	6443394	-196	4.60	4.63
VB04642	553779	6443380	-223	2.91	2.92
VB04642	553778	6443372	-182	3.14	3.16
VB04643	553778	6443350	-289	2.95	2.95
VB04643	553779	6443346	-197	3.18	3.22
VB04644	553796	6443373	-210	4.58	4.59
VB04645	553796	6443353	-296	2.89	2.90
VB04645	553797	6443348	-252	3.18	3.19
VB04645	553798	6443343	-204	3.00	3.00
VB04646	553824	6443379	-263	2.86	2.87
VB04646	553823	6443367	-219	3.20	3.19
VB98433C	554762	6443188	-1164	3.46	3.54
VB98455A	557102	6443161	-512	3.45	3.46
VB98461B	554827	6443009	-1722	3.42	3.31
VB98461B	554834	6443002	-1663	3.43	3.44
VB98461C	554849	6443049	-1471	4.58	4.60
VB98462	556949	6443212	-480	3.52	3.56
VB98462	556949	6443211	-454	2.96	2.96
VB98464	559106	6442350	-798	2.93	2.94
VB98476	557029	6443145	-475	3.51	3.49
VB98479	553338	6443082	-449	2.74	2.75
VB98480	557121	6443047	-507	3.59	3.60
VB98482	553508	6443023	-554	3.00	3.01
VB98486	557621	6441779	-782	2.91	2.94
VB99487	553802	6443171	-681	2.88	2.86
VB99487	553808	6443143	-576	3.00	3.00
VB99489	557174	6443121	-525	3.65	3.67
VB99489	557174	6443120	-513	3.12	3.19
VB99492	558141	6441758	-846	2.92	2.92
VB99492	558143	6441752	-891	2.96	2.99
VB99494A	553803	6443105	-780	2.82	2.80
VB99494A	553804	6443100	-754	2.97	2.99
VB99494A	553805	6443097	-734	2.99	2.98
VB99501	554800	6443460	-518	2.93	2.93
VB99504	559750	6441572	-944	2.88	2.86
VB99504	559747	6441548	-1133	2.73	2.73
VB99508	554676	6443472	-111	3.08	3.07
VB99513	557071	6442431	-512	3.07	3.04

Borehole ID	Easting (m)	Norting (m)	Elevation (m)	Density #1 (g/cc)	Density #2 (g/cc)
VB99513	557072	6442419	-449	2.94	2.92
VB99518	561071	6441070	-1321	2.89	2.88
VB99518B	561076	6441175	-1371	2.98	2.97
VB99518B	561075	6441174	-1358	3.25	3.31
VB99521	557391	6442632	-588	3.66	3.69
VB99522	556976	6442612	-432	3.28	3.28
VB99523	557342	6442396	-496	2.96	2.95
VB99523	557341	6442396	-540	3.21	3.18
VB99523	557341	6442395	-569	3.22	3.21
VB99523	557341	6442394	-602	2.90	2.89
VB99525	557456	6442350	-556	2.86	2.88
VB99525	557456	6442349	-585	3.34	3.35
VB99525	557456	6442349	-611	2.88	2.89
VB99525	557457	6442348	-639	3.42	3.46
VB99526	557166	6442660	-533	3.21	3.20
VB99530	557818	6442414	-705	3.40	3.39
VB99531	557760	6442234	-717	3.31	3.34
VB99531	557756	6442228	-777	4.62	4.61
VB99532	557680	6442243	-675	2.94	2.92
VB99532	557682	6442240	-755	3.41	3.45
VB99533	556999	6442721	-459	3.40	3.39

Appendix C

Gravity Data: Ovoid Area

Line	Easting (m)	Northing (m)	Elevation (m)	Bouguer (mGal)
VB01	555534	6242870	74	46.13
VB01	555534	6242895	76	46.21
VB01	555534	6242920	77	46.27
VB01	555535	6242945	78	46.26
VB01	555535	6242971	78	46.37
VB01	555535	6242995	79	46.50
VB01	555536	6243020	79	46.42
VB01	555536	6243046	80	46.51
VB01	555537	6243070	81	46.55
VB01	555537	6243096	81	46.60
VB01	555537	6243118	82	46.67
VB01	555538	6243145	86	46.82
VB01	555538	6243170	90	47.01
VB01	555539	6243194	93	47.06
VB01	555539	6243219	97	47.37
VB01	555541	6243243	101	48.10
VB01	555541	6243268	103	48.66
VB01	555542	6243290	104	48.87
VB01	555540	6243317	103	48.61
VB01	555541	6243343	103	47.82
VB01	555539	6243368	107	47.45
VB01	555542	6243392	112	47.23
VB01	555542	6243417	118	47.03
VB01	555541	6243442	121	46.91
VB02	555738	6242865	69	46.57
VB02	555738	6242887	71	46.55
VB02	555739	6242914	73	46.68
VB02	555738	6242941	75	46.72
VB02	555739	6242965	77	46.95
VB02	555739	6242991	78	47.15
VB02	555739	6243015	79	47.29
VB02	555738	6243041	80	47.56
VB02	555739	6243065	80	47.95
VB02	555738	6243090	80	48.39
VB02	555739	6243114	80	48.77
VB02	555739	6243140	81	49.15
VB02	555739	6243163	80	49.36
VB02	555739	6243190	80	49.45
VB02	555740	6243218	80	49.38
VB02	555739	6243240	80	48.90
VB02	555739	6243265	81	48.07
VB02	555739	6243290	82	47.84
VB02	555738	6243314	83	47.59
VB02	555739	6243338	83	47.41
VB02	555739	6243365	84	47.24
VB02	555740	6243389	86	47.17

Line	Easting (m)	Northing (m)	Elevation (m)	Bouguer (mGal)
VB02	555739	6243414	87	47.00
VB02	555740	6243439	87	46.93
VB03	555930	6242869	71	47.51
VB03	555931	6242893	72	47.78
VB03	555931	6242921	75	48.00
VB03	555931	6242945	77	48.49
VB03	555932	6242970	79	48.94
VB03	555932	6242997	80	49.51
VB03	555932	6243022	81	50.06
VB03	555934	6243047	81	50.40
VB03	555934	6243074	81	50.74
VB03	555935	6243103	81	50.87
VB03	555935	6243129	81	50.94
VB03	555935	6243152	81	50.97
VB03	555935	6243185	81	50.45
VB03	555936	6243208	81	50.00
VB03	555937	6243237	79	49.19
VB03	555937	6243260	78	48.61
VB03	555937	6243283	77	48.15
VB03	555938	6243306	75	47.88
VB03	555939	6243333	74	47.68
VB03	555939	6243359	73	47.51
VB03	555939	6243385	73	47.42
VB03	555941	6243412	73	47.41
VB03	555941	6243437	73	47.31
VB04	556129	6242860	76	48.17
VB04	556130	6242884	76	48.02
VB04	556130	6242908	77	47.96
VB04	556131	6242933	79	48.01
VB04	556131	6242958	81	47.93
VB04	556131	6242983	82	47.94
VB04	556132	6243008	82	47.96
VB04	556133	6243033	83	48.04
VB04	556134	6243058	84	48.11
VB04	556133	6243083	84	48.05
VB04	556135	6243107	84	48.02
VB04	556134	6243135	84	48.10
VB04	556135	6243161	84	47.98
VB04	556135	6243186	83	47.93
VB04	556136	6243217	83	47.82
VB04	556136	6243245	82	47.85
VB04	556137	6243275	81	47.80
VB04	556138	6243301	79	47.77
VB04	556137	6243322	78	47.76